

Quantum Photonic Interfaces between Atomic and Telecommunication Wavelengths

Dissertation

zur Erlangung des Grades
des Doktors der Naturwissenschaften
der Naturwissenschaftlich-Technischen Fakultät II
– Physik und Mechatronik –
der Universität des Saarlandes

von

Andreas Lenhard



Saarbrücken
2015

Tag des Kolloquiums: 30.03.2015

Dekan: Univ.-Prof. Dr.-Ing. Georg Frey

Mitglieder des Prüfungsausschusses: Univ.-Prof. Dr. rer. nat. Jürgen Eschner
Univ.-Prof. Dr. rer. nat. Christoph Becher
Priv.-Doz. Dr. habil. Johannes A. L'huillier
Dr. rer. nat. Herbert Wolf

Abstract

In this thesis we study techniques based on nonlinear optical effects to establish interfaces for photons between the near infrared and telecom spectral region. We follow two approaches: Photon pairs generated by spontaneous parametric downconversion (SPDC) in an optical parametric oscillator (OPO) and quantum frequency conversion (QFC) of single photons.

The OPO is used to tailor the photonic state: One photon is resonant with a transition in $^{40}\text{Ca}^+$ while its telecom partner is used as herald. We investigate temporal correlations and time-energy entanglement of the photon pairs. To demonstrate the applicability for resonant excitation of atomic transitions we perform single photon spectroscopy of the Ca^+ $D_{5/2}$ - $P_{3/2}$ transition. Due to the temporal correlation we use the idler photon as a herald for the absorption process to demonstrate telecom-heralded absorption of a single photon.

The second approach is based on QFC of photons at 854 nm to the telecom O-band (1310 nm) by mixing with a pump field at 2453 nm in a nonlinear waveguide. A light source is developed to generate the pump field. An over-all QFC conversion efficiency of 8% is reached for coherent fields and single photons. Temporal shape and photon statistics of SPDC photons are preserved in the conversion process. We prove the conservation of time-energy entanglement during QFC and the violation of a Bell inequality. Via QFC of the herald photon, heralded absorption of a single photon by a single trapped calcium ion is demonstrated.

Zusammenfassung

Diese Dissertation befasst sich mit optisch nichtlinearen Effekten zur Entwicklung von Schnittstellen für Photonen zwischen dem nahinfraroten und Telekom Spektralbereich. Es werden zwei Ansätze verfolgt: Photonen-Paare, erzeugt durch spontane parametrische Abwärtskonversion (SPDC) in einem Optisch Parametrischen Oszillator und Quanten-Frequenzkonversion (QFC).

Der OPO dient zur Anpassung des photonischen Zustandes: Ein Photon ist resonant mit einem Übergang in $^{40}\text{Ca}^+$, sein Telekom-Partnerphoton dient zur Ankündigung. Wir untersuchen die zeitlichen Korrelationen und Zeit-Energie Verschränkung der Photonenpaare. Die Eignung für resonante Anregung wird durch Einzelphotonen Spektroskopie am Ca^+ $D_{5/2}$ - $P_{3/2}$ Übergang gezeigt. Aufgrund der zeitlichen Korrelationen verwenden wir das Idler-Photon bei Telekom Wellenlängen zur Ankündigung der Absorption eines einzelnen Signal-Photons.

Der zweite Ansatz basiert auf QFC von Photonen bei 854 nm ins Telekom O-Band (1310 nm) durch Mischung mit einem Pumpfeld bei 2453 nm in einem nichtlinearen Wellenleiter. Eine Lichtquelle zur Erzeugung des Pumpfeldes wurde entwickelt. Für kohärente Felder und einzelne Photonen wird eine Gesamteffizienz von 8% für die QFC erreicht. Zeitliche Form und Photonenstatistik sind beim Konversionsprozess erhalten. Wir zeigen die Konversion von Zeit-Energie Verschränkung und die Verletzung einer Bell-Ungleichung. Mittels QFC wird die Absorption eines einzelnen Photons durch ein einzelnes gefangenes Calcium-Ion durch ein Telekom-Photon angekündigt.

Contents

1	Introduction	1
1.1	Quantum Frequency Conversion	4
1.2	Spontaneous Parametric Downconversion	6
1.3	Single Ions	8
1.4	Scope and Outline of this Thesis	9
2	Theoretical Background	11
2.1	Nonlinear Optics	11
2.1.1	Coupled Wave Equations	13
2.1.2	Phase Matching	15
2.2	Quantum Theory of Light	19
2.2.1	Different Types of Light	19
2.2.2	Quantum Mechanical Model of DFG	24
2.2.3	Spontaneous Parametric Down-Conversion	26
3	Optical Devices and Materials	33
3.1	Lithium Niobate as Nonlinear Material	33
3.2	Nonlinear Optical Devices	37
3.2.1	Parametric Amplification	37
3.2.2	Optical Parametric Oscillation	40
3.3	Waveguides	47
3.3.1	Waveguide Nonlinear Optics	52
3.4	Waveguide Fabrication	56
4	Optical Parametric Oscillator	61
4.1	OPO Setup	61
4.1.1	Pumping System	62
4.1.2	OPO Resonator	64
4.2	Threshold and Output Power	66
4.3	Frequency Tuning and Linewidth	67
4.4	Summary	71

5	Photon Pairs	75
5.1	OPO-SPDC Source	75
5.1.1	Photon Properties	77
5.1.2	Narrowband Correlated Photon Pairs	82
5.2	Interaction with a Single Trapped Ion	87
5.2.1	Single Photon Spectroscopy	88
5.2.2	Telecom-Heralded Absorption	93
5.3	Franson Interferometry	95
5.3.1	Experimental Results	100
5.4	Summary	105
6	Quantum Frequency Conversion	109
6.1	Frequency Converter Setup	109
6.1.1	Waveguide Characterization	110
6.1.2	Linking the Labs	119
6.1.3	Telecom Photon Detection	120
6.2	Frequency Conversion of Coherent Fields	122
6.3	Frequency Conversion of SPDC Photons	130
6.4	Franson Interferometry of Converted Photons	142
6.5	Telecom-Converted Heralded Absorption	147
6.6	Summary	149
7	Quantum Networks	151
7.1	Telecom Single Photon Sources	153
7.2	Quantum Communication	155
7.3	Quantum Repeaters	163
7.4	Networks of Dissimilar Nodes	168
8	Summary and Conclusion	171
	Bibliography	175
	Publications	201

1 Introduction

One of the most far-reaching inventions in the 20th century was computer technology. Computers nowadays can be found in any aspect of daily life and revolutionized communication all over the world. In the middle of the 20th century with the first demonstrations of programmable universal computers, these consequences could hardly be imagined. Today we might have arrived at a similar turning point as quantum technologies become available for various applications.

Quantum information processing (QIP) today is vital field of quantum physics. Here, data is manipulated and transferred by means of quantum mechanical processes. QIP can be further divided in a few topics [1]: *Quantum cryptography* allows to establish a secret key between remote parties and reveal an eavesdropper. *Quantum teleportation* uses quantum mechanics to transfer a quantum state between two or more particles. *Quantum computing* uses quantum mechanics to enhance computational power of computers using superposition states and specialized algorithms.

The most widely used application so far is quantum cryptography. Cryptography is the art of encoding information in a way that only the addressed recipient can reveal its meaning while it is completely senseless for anybody else (c.f. [2]). In common procedures, sender and receiver share a secret key which is used to encode and decode the message. In general, the degree of secrecy depends on the length of the key. The most secure cryptography method is known as One-Time-Pad, where the key is completely random and has the same length as the message. In mathematical sense this procedure offers ideal secrecy. In practice this method is often not feasible due to the size of the key and the fact that both parties have to meet before communication to agree about the one time pad. Another class of methods is called public key encryption, where it is not necessary that the parties know each other. This is today commonly used in internet communication. Anyone who wants to receive a secret message generates a pair of keys. The public key is published and can be used by anybody for encoding the secret message, however decoding is afterwards only possible with the private key, kept by the recipient. The underlying algorithm uses large prime numbers for key generation. The secrecy relies on the fact that a large computational effort is necessary for the factorization of large prime numbers and hence to estimate the private key. At this point QIP comes into play. On the one hand, quantum computing offers an algorithm for fast factorization of prime numbers [3] which could make this kind of encryption obsolete in future. On the other hand quantum cryptography enables

methods for secure key distribution (unconditional security) [4].

Quantum cryptography means that we use *quantum key distribution* (QKD) to establish a secure key between the communicating parties and then use this secret key as a one time pad in a conventional way. Hence the problem is shifted from cryptography to QKD. In 1984 Bennett and Brassard proposed a scheme for QKD which is today known as BB84-protocol [4]. It was the first scheme that provides ideal security based on the fundamental laws of quantum physics. It relies on the exchange of single quanta (e.g. photons). As a quantum state cannot be cloned [5] it is not possible to make a copy of the quantum key. Furthermore, any measurement on a quantum system results in a projection of the wavefunction into a basis state which allows to identify an eavesdropper. The procedure was experimentally realized already a few years later [6]. The idea behind this protocol laid the foundation of many advanced QKD schemes [7].

As mentioned in the beginning, quantum computing offers algorithms that solve problems faster than classical algorithms. This has already been the historical motivation to develop a quantum computer. In 1982 Feynman pointed out that it gets difficult to simulate a complex quantum system on a classical computer as the computational requirements increase exponentially with the size of the quantum system to simulate. He suggested to use a quantum computer (i.e. a controllable quantum system) to simulate another quantum system [8]. This has already been realized experimentally for various problems [9]. A few years after Feynman, Deutsch proposed the universal quantum computer, in analogy to classical computing [10]. He theoretically showed that this machine indeed can solve some problems faster than a classical computer.

To understand how a quantum computer works, we have to introduce the concept of *Qubits*. In traditional computers a bit can only have the binary values of either 0 or 1. These states are usually represented as a low and high voltage level in an electronic circuit. In analogy, a quantum computer operates with qubits. For a qubit we use a binary quantum system with two basis states $|0\rangle$ and $|1\rangle$. We know from quantum physics that a system in general can also be prepared in a superposition of the basis states. Hence the qubit has the general form

$$|\Psi\rangle = \alpha |0\rangle + \beta |1\rangle \quad (1.1)$$

with the normalization condition $|\alpha|^2 + |\beta|^2 = 1$. On successful measurement, the wavefunction collapses to one the basis states. We here also have the possibility to collect several qubits to a common system to form a quantum register. The simplest example is a combination of two qubits:

$$|\Psi\rangle = c_{00} |00\rangle + c_{01} |01\rangle + c_{10} |10\rangle + c_{11} |11\rangle \quad (1.2)$$

A N -qubit register contains 2^N complex amplitudes c to describe the wavefunction. Thus, the amount of information grows exponentially with register size. Due to the superposition principle, several input states can be computed in a single operation

(quantum parallelism). Qubits can be realized in a manifold of ways. Usually one uses energy levels, or spin states in atomic systems. As these need to be prepared and stored locally in an experimental setup they are often referred to as *stationary qubits*. Another realization is the polarization state of photons. As photons can easily be transferred between remote locations they are called *flying qubits*. In general, qubits are manipulated in so-called quantum gates (c.f. [11]). We mainly distinguish between single-qubit gates (e.g. a rotation on the Bloch sphere) and two-qubit gates where two qubits interact. When several gates are combined, we can end up with a quantum circuit implementing a quantum algorithm on a quantum computer. To set up a system consisting of several qubits, entanglement is an essential tool for the qubits to interact. Fortunately, entanglement is not restricted to neighboring particles. In principle, different parts of a quantum computer can be distributed to remote locations if these are connected adequately [12]. This led to the idea of a quantum network [13] consisting of quantum nodes (hosting quantum computers, gates, memories, . . .) connected by flying qubits. One way to distribute the state of a system is emitting a photon which carries the information. The photons from different nodes then interact (e.g. via two-photon interference) and the nodes get entangled via entanglement swapping. The other way is based on absorption where the state of the photon is transferred to the node in the absorption process.

Progress in experimental implementations of QIP proved that trapped ions are promising candidates to realize quantum computers [14, 15]. The state of such an ion can be transferred to a photon [16, 17] and this photon can be distributed. However, we here face a problem for long-range state transfer. On the one hand, the photons must be resonant with a transition in the stationary atoms, demanding a wavelength usually in the ultraviolet (UV) to near infrared (NIR) spectral range. However, these wavelengths suffer considerable attenuation in optical fibers. Thus, on the other hand, we need telecom-compatible photons for long-range fiber transmission. To further increase the communication range *quantum repeaters* are necessary [18]. As losses and decoherence grow exponentially with distance, intermediate repeater stations have to be included into the quantum link. Entangled states are distributed as a resource for quantum communication between remote partners by means of entanglement swapping between the repeater nodes as well as entanglement distillation and storage at the nodes. The storage allows repeat-until-success strategies to transfer the entanglement over the whole chain of nodes. Further processing like distillation allows restoring fidelity and error correction. This drastically reduces the transfer time for long-range transmission at the cost of additional qubits and quantum nodes.

In this thesis I will present different techniques to establish interfaces bridging NIR and telecom wavelength bands. In detail, these are interfaces based on quantum frequency conversion and spontaneous parametric downconversion which will be introduced in the following sections. Afterwards, I will briefly discuss single trapped calcium

ions, which is the atomic quantum system mainly used in this thesis. The long-term motivation behind this work is to develop quantum repeater technologies for long-range interconnection of dissimilar quantum systems like trapped ions and solid-state quantum nodes.

1.1 Quantum Frequency Conversion

Nonlinear optics describes the interaction of electromagnetic fields with matter in a regime where the response by the displacement field cannot be described by a linear relation to the field strength but nonlinear terms have to be included [19]. This involves the generation of electromagnetic fields at new frequencies. However, as the observation of such effects demands high intensity optical fields, the invention of lasers allowed the first experimental generation of optical harmonics [20] only a few years after. Continuous improvement on specialized materials and techniques for phase-matching increased the efficiency of nonlinear effects and paved the way for a variety of applications. Today the state of the art material is lithium niobate [21] in combination with quasi-phasematching by periodic poling [22]. Motivated by high conversion efficiency at macroscopic power levels, first experiments with single-photon level coherent fields and non-classical states of light were realized in the early nineties. These were the foundations of the area of *Quantum Frequency Conversion* (QFC).

In general, QFC implies the manipulation of the optical frequency of quantum-mechanical light fields. The first proposal describes QFC of squeezed light to transfer the squeezing to different spectral regions [23] which was realized already two years later [24]. Regarding single photons, first reports on QFC focused on frequency *up-conversion*, i.e. the frequency is shifted towards higher values. The motivation was the absence of efficient single photon detectors for infrared wavelengths. Using sum-frequency-generation the photons can be transferred to the visible spectral region where efficient silicon based detectors exist [25]. To achieve reasonable conversion efficiency a high intensity of the pump field is necessary. With continuous wave fields and bulk nonlinear materials, first experiments used enhancement cavities for the pump (see e.g. [25]). The experimental setups became more feasible with improvements in the fabrication techniques of waveguide structures in lithium niobate [26]. With such integrated photonic structures, frequency conversion in a single pass is possible [27]. A milestone experiment on QFC of non-classical states of light was reported by Tanzilli and coworkers in 2005 [28]. Correlated photon pairs at the telecom C- and O-band were generated and the O-band photons were upconverted to the red spectral region. With the help of Franson-interferometry [29] the authors could show the entanglement between the original C-band and the converted red photons. This was the first experimental report on the conservation of the quantum state of a photon pair during frequency conversion. Another seminal experiment of QFC with single photons was

the upconversion of the emission of a single semiconductor quantum dot [30]. With such an upconversion-detection scheme the second-order correlation function could be measured and for the first time an antibunching could be observed which is a signature for single photons. In contrast to upconversion, the process of *downconversion* describes the frequency shift towards lower values which is also the main focus of this thesis. Early theoretical work models the ideal downconversion process and predicts downconversion of single photons with 100 % efficiency [31]. However, in experiments additional photons were generated forming a floor of uncorrelated noise. These effects are inherent to QFC in general but were investigated in detail for downconversion. First experiments by the group of Fejer aimed on the conversion of the emission of the NV-center in diamond to the telecom C-band. They observed a disturbance of the process by parametric fluorescence stimulated by the strong pump field as well as a broadband noise floor by parasitic conversion processes enabled by duty cycle errors of the quasi-phasematching [32]. A way out of this problem is to choose a pump wavelength that generates the noise in a region far away from the target wavelength. This can be done by splitting the conversion in two consecutive processes [32,33] with a long pump wavelength. Another noise source is Raman scattering of the pump field [34,35]. Recently these noise processes could be included to create a realistic model of the conversion process [36]. The choice of a pump wavelength significantly longer than the target wavelength, in combination with narrowband spectral filtering can help to reach a high signal to noise ratio. With these prerequisites the downconversion of quantum dot emission became possible [37]. In this paper, for the first time the conservation of coherence and emission statistics of the single photons could be demonstrated. At the same time another experiment [38] showed an additional fundamental application of QFC: The authors converted two emission lines of a single quantum dot to the same target wavelength. The interference of the converted light showed that QFC can be used to make photons from two different sources indistinguishable. Such a two-photon interference was proposed to allow the coupling of dissimilar systems to a hybrid quantum network [39]. More recently, the use of ultra short pump pulses paved the way for new applications of QFC. Tailoring the pump pulses allows temporal and spectral shaping of the single photons during the conversion process. Using for example linearly chirped pulses the spectral bandwidth of photons can be reduced [40]. With the same technique also the temporal shape and position of the output photons can be controlled allowing an implementation of time-bin entanglement [41]. The temporal shortening of the output photons can also be used to establish a quantum eraser technique. The photons can only be converted in presence of the ultra short pump pulse which then acts as a precise time-stamp for the generation of the output photon. The timing jitter of the following detector can thus be overcome and the phase of the photon is precisely determined. The converter erases additional which-way information and allowed the realization of atom-photon entanglement in a recent experiment [42]. The above

mentioned achievements show that QFC has developed to a powerful tool in quantum optics in recent years and paved the way for a plethora of applications.

Up to now I restricted the introduction of nonlinear interaction to effects based on second-order nonlinear susceptibility. However, one can also use higher orders of susceptibility as well as completely different effects to mediate a nonlinear interaction between photons. Of growing interest in recent time is four wave mixing (FWM). This process is based on third order nonlinearity and involves in general two pump fields, a signal and an idler field. In the sense of QFC two of these fields are strong coherent fields while the others are in the quantum regime. Depending on the application (e.g. up- or downconversion) one can choose which fields need to be strong. Here also energy conservation (matching of the wavelengths) as well as phase matching conditions have to be fulfilled. Usually, integrated optical elements are used to achieve the required high intensity. QFC was demonstrated in photonic crystal fibers [43–45] with reasonable efficiency. One drawback of this technique is that the frequency shift of the photons is less than what can be achieved with second-order nonlinear effects. The geometry is not limited to fibers, but there can also be waveguides fabricated for FWM [46, 47]. The materials of choice (Si or SiN) are compatible with standard chip-fabrication technologies and make these waveguides promising candidates for future integrated optical devices. Another emerging field is frequency conversion via resonant structures. One realization is that the input photon excites an optical mode of the cavity. Via opto-mechanical coupling energy is transferred to a mechanical mode. The photon is now in a lower-energy optical mode and coupled out of the resonator. Such schemes allow to implement up- and downconversion processes. They have been realized with single nanobeam cavities [48] which allow small frequency shifts or proposed by coupling two separate cavities which should allow arbitrary frequency shifts [49, 50]. A variant thereof proposes to use photonic crystal cavities [51]. A similar approach is based on microdisc optomechanical resonators. However, in this case electromagnetically induced transparency mediates wavelength conversion between near infrared and telecom wavelengths with experimentally demonstrated reasonable efficiencies [52]. Finally, a very effective method is to use resonant interaction with atomic transitions [53]. The drawback here is the restriction of the wavelengths to existing atomic transitions.

1.2 Spontaneous Parametric Downconversion

QFC, as described above based on second order nonlinear interaction, involves a strong classical pump field and a single photon state at the input of the nonlinear medium. The pump field stimulates the nonlinear process of frequency conversion of the photons. When there is no photon input but only the pump field, the conversion process is driven by vacuum fluctuations of the electromagnetic field and pump photons can

spontaneously decay into two photons at lower frequencies. This process is called *Spontaneous Parametric Downconversion* (SPDC). Both photons of the pair are created simultaneously and hence are temporally correlated. Depending on the generation process they can share even more correlations which gives rise for two-particle entanglement. The generation of photon pairs by SPDC was first proposed by Klyshko in 1967 [54] and could be experimentally observed almost at the same time by Harris and coworkers [55] (historically SPDC is also known as optical parametric fluorescence, OPF). A few years later the simultaneity of both photons of the pair could be experimentally verified [56]. SPDC sources became popular as a means to perform Einstein-Podolsky-Rosen (EPR) experiments [57] with photons. For such experiments, entangled particles are necessary. By properly choosing the phase matching conditions it is possible to generate photons with orthogonal polarization states. If the wavelengths of both photons of the pair are degenerate they can become indistinguishable and form a polarization entangled pair state. The first demonstration of such an EPR experiment with photons was in 1988 [58]. Since this time SPDC sources were continuously improved and clear violations of the EPR experiment observed [59]. Usually, the spectra of the SPDC photons are rather broad, which can be a drawback for some applications. A solution is to embed the nonlinear medium in a resonator. This enhances the generation efficiency and shapes the spectral and temporal envelope of the photon pairs [60] which paved the way for tailoring the properties of the photons on demand. Another application for photon pairs is to use them as a source for heralded single photons. This means, conditioned on the detection of one photon of the pair there must exist another photon in the other mode of the pair state. This effect was already demonstrated in the early days of SPDC sources [61]. Such a technique allows to deterministically generate a single photon state in spectral regions where no atomic sources exist. In particular, one can use a near infrared photon (which can efficiently be detected) to herald a photon at telecom wavelengths (where no atomic sources exist) [62–64]. Analog to QFC, an increase in efficiency can be achieved when the nonlinear material is micro-structured to form waveguides. In these structures the light intensity and modal overlap is increased. In this context, efficient SPDC sources have been demonstrated [64–66]. Instead of waveguides, devices like whispering gallery mode resonators can be employed to tailor photon properties [67]. Such resonating structures allow to generate the photons in distinct spatial and spectral modes. Today, SPDC sources have become a working horse in the lab to generate quantum states of light on demand with tailored properties.

In the previous descriptions emphasis was drawn on second-order nonlinear interaction. Similar to QFC, various other effects can be used to generate entangled photon pairs. One can exploit nonlinear interactions based on third order susceptibility. One way to realize this is FWM in a dispersion shifted fiber. Often, these fibers are arranged in Sagnac interferometers to generate polarization entangled pairs [68]. Another effi-

cient medium for this purpose are photonic crystal fibers which allow to tailor phase matching [69]. FWM is also possible in microstructures like waveguide devices [70] or silicon ring resonators [71]. A large increase in efficiency can be achieved by adding functional photonic structures to the waveguides. For example, an array of coupled resonators added to a waveguide (CROW geometry) can be used to slow down group velocity and increase the interaction length of the photons [72, 73]. These micro devices offer the opportunity to implement further components and thus build multiplexed sources [74] or single photon buffers [75] which are important elements for network technologies.

Historically, the first source of correlated photon pairs was not based on a nonlinear interaction but on an emission cascade in a single atom [76, 77]. A more recent variant is to use the exciton-biexciton emission cascade in a semiconductor quantum dot. With such quantum dot devices it is also possible to generate entangled photons at telecom wavelengths [78]. Finally, it is worth mentioning that SPDC processes can be cascaded to generate entangled states of more than two photons, e.g. photon triplets [79].

1.3 Single Ions

In the previous sections we focused on photons, their generation and properties. In regard of a quantum network we also need nodes where these photons can be processed and generated. Hence, I will here focus on quantum emitters, especially the single calcium ions used in this thesis. In 1998 DiVincenzo collected a list of criteria for physical hardware for a quantum computer [80]. This addresses the controllability, preparation, decoherence, measurement, gate operations and scalability of quantum bits. Although no quantum system fulfills all requirements sufficiently today, one of the most promising systems are trapped ions. The idea of trapping ions with radio frequency electric fields was suggested by Paul in the 1950s [81, 82]. In 1980, a single ion was trapped in a so-called Paul trap [83] for the first time. With the technique of trapping single ions, some of the DiVincenzo criteria could readily be fulfilled, like initialization [84], read-out [85] and long coherence time [86]. A first step towards scaling the system was achieved with the observation of ionic crystals in the trap [87]. However, to setup a quantum gate, entanglement between the particles is necessary. In 1995 Cirac and Zoller proposed to entangle the ions in the trap via their collective quantized motion [88] which was experimentally demonstrated a few years later [89]. This initiated the implementation of basic computational elements with trapped ions like universal quantum gates [90, 91], the c-NOT gate [89] or a geometric phase gate [92], as well as algorithms like Deutsch-Josza [93] or the Grover algorithm [94]. Another fundamental building block for quantum computing and quantum networks is the interconnection of remote particles. With ions the deterministic teleportation of massive particles could first be demonstrated [95, 96] and ions stored in remote traps have been

entangled [16,97]. The list of achievements shown here proves the feasibility of trapped ions for QIP and quantum networking.

1.4 Scope and Outline of this Thesis

The aim of this thesis was to introduce quantum nonlinear optic effects as basic building blocks for quantum repeater and quantum networking technology. At the beginning of this work, QFC was an emerging field. However many important effects were only theoretically expected but had not been demonstrated, yet. In this time we could drastically increase conversion efficiency by introducing ridge waveguides. Hence we were the first to demonstrate QFC of true single photons from a quantum dot and the preservation of anti-bunching and coherence [37]. The work in this thesis goes one step further, by bridging the gap between a NIR transition in a single trapped calcium ion and the telecom wavelength region with an entangled photon pair state. Two approaches were demonstrated: We have set up an optical parametric oscillator (OPO), operated below threshold as SPDC source. The OPO is used to tailor the photonic state resonant with the ion and have a photon in the telecom band as herald. In the second approach we developed a frequency converter to bridge the NIR to telecom band spectral regions. This involved setting up the pump laser, the converter and characterization and optimization of all devices. The capability of the converter has been demonstrated with coherent field as well as SPDC photons. Temporal properties of the photons, single photon character as well as time-energy entanglement of the SPDC photons were conserved in the conversion process, as demonstrated in this thesis. A major goal, which was achieved independently with both approaches, was heralded absorption of a single photon by a single ion. For the first time we could use a telecom photon as a herald, which never interacted with the ion itself. This paves the way for remote heralding the state transfer in a quantum node, here exemplified using a calcium ion.

We will begin the thesis by introducing the theoretical background necessary to explain the observed effects in chapter 2. This includes basic nonlinear optics and phase matching, as well as an introduction to quantum optics.

In chapter 3, this theory is modified for integrated optical devices and further theoretical background for OPOs is introduced. Chapter 4 addresses the OPO later used as a pump source for the frequency converter.

In chapter 5, first another OPO is introduced as SPDC source. We will show the temporal and spectral properties of the photons and demonstrate means to generate narrowband photon pairs. In that chapter, we also introduce Franson interferometry which is used as a tool to demonstrate the time-energy entanglement between the dissimilar photons of the OPO. With this source we were able to perform single photon

spectroscopy of an optical transition in calcium. The highlight is the absorption of resonant single photons in a single calcium ion, heralded by telecom photons and the observation of correlated quantum jumps.

In chapter 6, we will start with a detailed introduction of the frequency converter setup. A first characterization of the operation parameters is performed with weak laser fields. Then the conversion of photons from a SPDC source is demonstrated. The temporal shape and correlations are preserved and the application as heralded single photon source is investigated, both for narrowband and broadband source photons. Then, for the first time, we were able to demonstrate the Franson interference for downconverted photons proving the preservation of time-energy entanglement in QFC with high fidelity. A complete measurement framework for first order interference of the photons and the pair state is performed. Finally, this chapter is closed with another telecom heralded absorption experiment at a single calcium ion.

The final chapter 7 puts the former results into the context of quantum networks, repeaters and quantum communication. Therefore, relevant schemes are introduced and it is outlined, how these can benefit from the results of this thesis. This chapter also serves as an outlook for future applications of the demonstrated techniques.

The thesis is closed with a summary of the results in chapter 8.

2 Theoretical Background

In this chapter I will introduce the models and fundamental equations to describe the nonlinear interactions between three optical fields. In the following sections the quantum mechanical description of states of light and the nonlinear interaction is introduced. In the end the discussion focuses on single photon and photon pair states and their properties.

2.1 Nonlinear Optics

The introduction into nonlinear optics given here mainly follows the textbook of Boyd [98]. In general, electromagnetic fields are described by Maxwell's equations. For fields inside matter these can be written as:

$$\nabla \cdot \vec{D} = \rho \quad (2.1)$$

$$\nabla \cdot \vec{B} = 0 \quad (2.2)$$

$$\nabla \times \vec{E} = -\frac{\partial \vec{B}}{\partial t} \quad (2.3)$$

$$\nabla \times \vec{H} = \frac{\partial \vec{D}}{\partial t} + \vec{J} \quad (2.4)$$

For the materials we usually have to deal with in nonlinear optics we can make a few assumptions to reduce these equations. We are looking for solutions in regions without free charges, i.e. $\rho = 0$, and without free currents, i.e. $\vec{J} = 0$. Furthermore all nonlinear materials used in this work are nonmagnetic, leading to $\vec{B} = \mu_0 \vec{H}$. Here μ_0 is the permeability of space. Hence the interaction between light and matter can be fully described via the electric fields. We therefore use the following relation between the electric field \vec{E} and the displacement field \vec{D} :

$$\vec{D} = \epsilon_0 \vec{E} + \vec{P} \quad (2.5)$$

where ϵ_0 is the vacuum permittivity and \vec{P} is the dielectric polarization. This polarization generally depends on the electric field in a nonlinear manner. Mathematically the i -th component of the polarization vector can be expanded into a power series:

$$P_i = \underbrace{\epsilon_0 \chi_{ij}^{(1)} E_j}_{P_i^{(1)}} + \underbrace{\epsilon_0 \chi_{ijk}^{(2)} E_j E_k}_{P_i^{(2)}} + \underbrace{\epsilon_0 \chi_{ijkl}^{(3)} E_j E_k E_l}_{P_i^{(3)}} + \dots \quad (2.6)$$

The parameters $\chi^{(n)}$ are called n -th order susceptibilities. For $n > 1$ they describe the strength of nonlinear interactions. In the case of scalar fields these are constants depending on the material, optical frequencies and polarization. For the general case of vector treatment they become tensors of rank $n + 1$.

The optical field applied to the nonlinear medium can be split into a linear combination of plane waves with frequencies ω_m and amplitudes \vec{A}_m :

$$\vec{E} = \sum_m \vec{A}_m e^{i(\vec{k}_m \cdot \vec{r} - \omega_m t)} + c.c. \quad (2.7)$$

Here \vec{k}_m is the wavevector of field component m . The description of the field can be simplified by merging the spatial oscillation and the amplitude to $\vec{E}(\omega_m) = \vec{A}_m e^{i\vec{k}_m \cdot \vec{r}}$ and allowing negative frequencies (for the summation that means $\omega_{-n} = -\omega_n$). Then the components in equation 2.6 can be written in the following form:

$$P_i^{(1)}(\omega_m) = \epsilon_0 \sum_j \chi_{ij}^{(1)}(\omega_m) E_j(\omega_m) e^{-i\omega_m t} \quad (2.8)$$

$$\begin{aligned} P_i^{(2)}(\omega_m + \omega_n) &= \epsilon_0 \sum_{jk} \sum_{(mn)} \chi_{ijk}^{(2)}(\omega_m + \omega_n, \omega_m, \omega_n) \\ &\times E_j(\omega_m) E_k(\omega_n) e^{-i(\omega_m + \omega_n)t} \end{aligned} \quad (2.9)$$

$$\begin{aligned} P_i^{(3)}(\omega_m + \omega_n + \omega_o) &= \epsilon_0 \sum_{jkl} \sum_{(mno)} \chi_{ijkl}^{(3)}(\omega_m + \omega_n + \omega_o, \omega_m, \omega_n, \omega_o) \\ &\times E_j(\omega_m) E_k(\omega_n) E_l(\omega_o) e^{-i(\omega_m + \omega_n + \omega_o)t} \end{aligned} \quad (2.10)$$

From the above equations it becomes obvious that the first order polarization term $P_i^{(1)}$ contains only terms with frequencies ω_m which implies that it only oscillates with the same frequency as the original electrical field. This is the regime of linear optics. For higher order terms $P_i^{(n)}$ new frequency terms can be found that are combinations of the frequencies of all involved electrical fields. Thus second order nonlinear phenomena are also described as three-wave mixing processes. The effects of nonlinear polarization become weaker with increasing order. The nonlinear effects utilized in this thesis all rely on the second order polarization. Hence polarization terms higher than the second order will be neglected for the rest of the thesis.

In detail this second order nonlinear interaction introduced in Eqn. 2.9 involves the following processes for the interaction of two optical fields with frequencies ω_1 and ω_2 : There can be polarization terms proportional to $e^{\pm i2\omega_1 t}$ or $e^{\pm i2\omega_2 t}$ which are the second harmonic of ω_1 and ω_2 , respectively. This process is called Second Harmonic Generation (SHG). Terms with $e^{\pm i(\omega_1 + \omega_2)t}$ oscillate with the sum of the original frequencies of the electrical fields and the process is called Sum Frequency Generation (SFG). There is also an oscillation $e^{\pm i(\omega_1 - \omega_2)t}$ with the difference frequency belonging to the process of

jk	11	22	33	23,32	31,13	12,21
l	1	2	3	4	5	6

Table 2.1: Scheme for contracted matrix notation of the nonlinear coefficient.

Difference Frequency Generation (DFG). Finally there is also a non-oscillating term, known as Optical Rectification (OR).

Usually the strength of a nonlinear interaction is not described by the susceptibility but a new tensor $\mathbf{d} = d_{ijk}$ is introduced. This nonlinear coefficient is related to the susceptibility by $d_{ijk} = \chi_{ijk}^{(2)}/2$. By suppressing the frequency arguments of the coefficient and assuming that the dispersion of the susceptibility can be neglected, the Kleinman symmetry condition [99] is valid. This reduces the number of independent elements according to the following relation:

$$d_{ijk} = d_{jki} = d_{kij} = d_{ikj} = d_{jik} = d_{kji} \quad (2.11)$$

For convenience the notation is then simplified by introducing a contracted matrix d_{il} according to the rules given in table 2.1. Then the nonlinear polarization for SFG can be expressed by:

$$\vec{P}^{(2)}(\omega_3) = 4\epsilon_o \begin{pmatrix} d_{11} & d_{12} & d_{13} & d_{14} & d_{15} & d_{16} \\ d_{21} & d_{22} & d_{23} & d_{24} & d_{25} & d_{26} \\ d_{31} & d_{32} & d_{33} & d_{34} & d_{35} & d_{36} \end{pmatrix} \begin{pmatrix} E_x(\omega_1) E_x(\omega_2) \\ E_y(\omega_1) E_y(\omega_2) \\ E_z(\omega_1) E_z(\omega_2) \\ E_y(\omega_1) E_z(\omega_2) + E_z(\omega_1) E_y(\omega_2) \\ E_x(\omega_1) E_z(\omega_2) + E_z(\omega_1) E_x(\omega_2) \\ E_x(\omega_1) E_y(\omega_2) + E_y(\omega_1) E_x(\omega_2) \end{pmatrix} \quad (2.12)$$

If one restricts the process to fixed propagation and polarization directions the nonlinear coefficient can be reduced to a single scalar called the effective nonlinear coefficient d_{eff} .

2.1.1 Coupled Wave Equations

In linear optics the propagation of optical fields is usually described by wave equations. Similar equations will be derived for nonlinear interaction in the following. First we take the curl of Maxwell equation 2.3 with the simplifications mentioned above and then use equation 2.4 to eliminate the dependence on the magnetic field. With that one can obtain:

$$\nabla \times \nabla \times \vec{E} + \mu_0 \frac{\partial^2}{\partial t^2} \vec{D} = 0 \quad (2.13)$$

Next the displacement field can be replaced by the polarization via equation 2.5. Using the identity $\nabla \times \nabla \times \vec{E} = \nabla (\nabla \cdot \vec{E}) - \nabla^2 \vec{E} = \nabla^2 \vec{E}$ leads to:

$$\nabla^2 \vec{E} - \frac{1}{c^2} \frac{\partial^2}{\partial t^2} \vec{E} = -\frac{1}{\epsilon_0 c^2} \frac{\partial^2 \vec{P}}{\partial t^2} \quad (2.14)$$

This is an inhomogeneous wave equation describing an oscillating field \vec{E} with a driving term on the right hand side controlled by \vec{P} . Splitting the polarization into a linear and a nonlinear part results in a wave propagating with speed c/n through the medium, driven by the nonlinear part of the polarization:

$$-\nabla^2 \vec{E} - \frac{n^2}{c^2} \frac{\partial^2}{\partial t^2} \vec{E} = -\frac{1}{\epsilon_0 c^2} \frac{\partial^2 \vec{P}^{NL}}{\partial t^2} \quad (2.15)$$

Analogous to equation 2.7 the fields \vec{E} , \vec{D} and \vec{P} can be expanded to plane waves with frequency components ω_m to have the final form of the nonlinear wave equation:

$$\nabla^2 \vec{E}_m - \frac{n^2(\omega_m)}{c^2} \frac{\partial^2}{\partial t^2} \vec{E}_m = -\frac{1}{\epsilon_0 c^2} \frac{\partial^2 \vec{P}_m^{NL}}{\partial t^2} \quad (2.16)$$

A general solution of the homogeneous wave equation is a linear combination of plane waves as introduced earlier. In the inhomogeneous case the driving term will slowly change the amplitude of the waves while propagating through the nonlinear medium. For the amplitude of the nonlinear polarization in the case of DFG it can be found [100]:

$$P_3 = 4\epsilon_0 A_1(z) A_2^*(z) e^{i(k_1 - k_2 - k_3)z} \quad (2.17)$$

Where we restricted the propagation to a single dimension for the sake of simplicity. Substituting the equations 2.7 and 2.17 into the wave equation 2.16 leads to:

$$\frac{d^2 A_3}{dz^2} + 2i \frac{n(\omega_3) \omega_3}{c} \frac{dA_3}{dz} = \frac{-4d_{\text{eff}} \omega_3^2}{c^2} A_1(z) A_2^*(z) e^{i(k_1 - k_2 - k_3)z} \quad (2.18)$$

Using the slowly varying amplitude approximation $\left| \frac{d^2 A_3}{dz^2} \right| \ll \left| k_3 \frac{dA_3}{dz} \right|$ the first term on the left hand side can be dropped. The same procedure can be performed for all three fields resulting in the so called coupled wave equations:

$$\frac{dA_1}{dz} = i \frac{2\omega_1}{n_1 c} d_{\text{eff}} A_3 A_2 e^{-i\Delta k z} \quad (2.19)$$

$$\frac{dA_2}{dz} = i \frac{2\omega_2}{n_2 c} d_{\text{eff}} A_3^* A_1 e^{i\Delta k z} \quad (2.20)$$

$$\frac{dA_3}{dz} = i \frac{2\omega_3}{n_3 c} d_{\text{eff}} A_1 A_2^* e^{i\Delta k z} \quad (2.21)$$

Here the difference of the wavevectors

$$\Delta k = k_1 - k_2 - k_3 \quad (2.22)$$

is known as the phase mismatch. The intensity of the fields at a position z can be derived from these amplitude equations by:

$$I_j = 2\epsilon_0 n_j c |A_j(z)|^2 \quad (2.23)$$

The equation for each field amplitude depends on the amplitudes of both other fields. This is the reason for denoting them coupled mode equations. This coupling can be phenomenologically understood as the stimulation of the decay of field 1 to field 3 under the presence of field 2 and vice versa. There is no analytical solution for these equations. However, they can be integrated numerically via finite element methods.

2.1.2 Phase Matching

In special cases analytical solutions can be found to calculate the intensity. Assuming no pump depletion, i.e. the amplitudes A_1 and A_2 can be taken constant during the interaction, equation 2.21 can be integrated to yield the amplitude behind a crystal of length L :

$$A_3(L) = \frac{2id_{\text{eff}}\omega_3}{n_3c} A_1 A_2^* \int_0^L e^{i\Delta k z} dz = \frac{2id_{\text{eff}}\omega_3}{n_3c} A_1 A_2^* \left(\frac{e^{i\Delta k L} - 1}{i\Delta k} \right) \quad (2.24)$$

The generated field thus has an intensity:

$$I_3 = \frac{8d_{\text{eff}}^2\omega_3^2 I_1 I_2}{n_1 n_2 n_3 \epsilon_0 c^2} \left| \frac{e^{i\Delta k L} - 1}{\Delta k} \right|^2 \propto L^2 \frac{\sin^2(\Delta k L/2)}{(\Delta k L/2)^2} \equiv L^2 \text{sinc}^2\left(\frac{\Delta k L}{2}\right) \quad (2.25)$$

Hence the effects of wavevector mismatch is fully included in the $\text{sinc}^2\left(\frac{\Delta k L}{2}\right)$ term. This function is plotted in Fig. 2.1. The intensity has its maximum for vanishing wavevector mismatch ($\Delta k = 0$) and decreases with increasing Δk . For a fixed $\Delta k \neq 0$, after a certain length $L_{\text{coh}} = 2.783/\Delta k$ the intensity drops to half of its initial value. This effect is due to the generated field running out of phase with its driving polarization.

To achieve maximum conversion efficiency the phase mismatch has to be kept minimal. In the following some techniques will be introduced to achieve this. Regarding the DFG process the conservation of energy is fulfilled by definition of the process $\omega_3 = \omega_1 - \omega_2$. The condition of perfect phase matching of the wavevectors can also be expressed in terms of the frequency:

$$\frac{n_3\omega_3}{c} = \frac{n_1\omega_1}{c} - \frac{n_2\omega_2}{c} \quad (2.26)$$

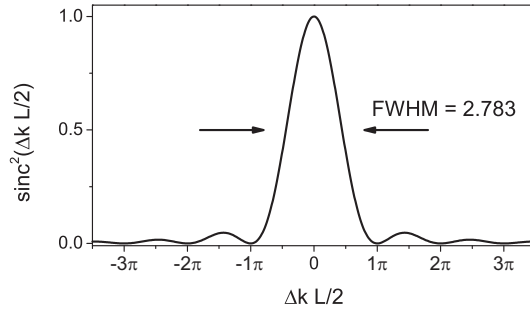


Figure 2.1: Plot of the sinc^2 -function that describes the dependence of the DFG intensity on the wavevector mismatch.

Together with energy conservation this introduces special requirements on the refractive index which cannot be fulfilled in general due to material dispersion. One technique called birefringent phase matching exploits the anisotropy of the refractive index in some crystalline materials. For certain frequency combinations and nonlinear materials a geometry can be found where the involved fields are arranged as ordinary and extraordinary beams with different polarizations and thus different dispersion curves. By tilting the crystal with respect to the crystal's optical axes and the incident beams as well as changing the crystal temperature the value of Δk can be reduced. More details about birefringent phase matching can be found in textbooks about nonlinear optics [98, 100, 101]. The disadvantages of this technique are the restrictions on geometry that cannot be fulfilled for all processes in general and the problem of walk-off, because the Poynting vector and the propagation vector of the fields have different directions. The technique of quasi phase matching avoids these problems and is used in all devices throughout this thesis.

Quasi phase matching

In Fig. 2.2a the problem of phase matching is again illustrated for the example of SHG. The fundamental wave of the optical field produces a polarization wave at twice the frequency traveling through the nonlinear medium. This polarization spreads with the fundamental field generating it. However, the polarization generates the second harmonic optical field which travels the medium with a velocity determined by the refractive index. Thus fundamental and second harmonic waves will run out of phase. After the coherence length destructive interference will occur, as illustrated in Fig. 2.2a, between the first and the last wavelet. To overcome this an additional phase shift could compensate the phase mismatch at this position and avoid destructive interference. A phase shift of π in the coupled amplitude equations corresponds to a sign change of the amplitude. Such a sign flip could be assigned to the nonlinear susceptibility or the

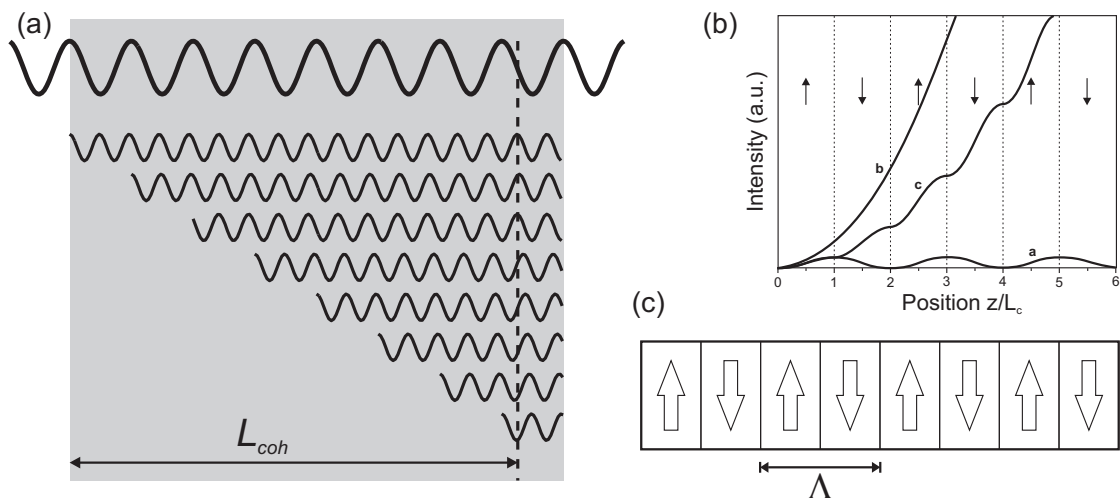


Figure 2.2: a) Demonstration of phase matching issue for the example of second harmonic generation. The fundamental wave ω generates wavelets with frequency 2ω traveling through the medium with different velocity. After the length L_{coh} destructive interference between the first and the last wavelet reduces conversion efficiency. b) Comparison between different phase matching conditions in DFG: **a** shows the case where no phase matching technique is applied, **b** shows the curve for perfect phase matching ($\Delta k = 0$) and **c** illustrates quasi phase matching. c) Domain inversion with period Λ can be used for quasi phase matching.

d_{eff} parameter.

The theoretical approach follows the descriptions in [22,98]. In quasi phase matching (QPM) the sign of the nonlinear $d(z)$ coefficient is varied along the crystal position. This can be expressed with a function $g(z) = d(z)/d_{eff}$ which in general can take any value between $-1 \dots 1$ within the crystal length L . The amplitude of the generated field (eqn. 2.24) could be integrated to:

$$A_3(L) = \frac{2i\omega_3}{n_3c} A_1 A_2^* d_{eff} L G(\Delta k) \quad (2.27)$$

Where the function $G(\Delta k)$ is the Fourier transform of $g(z)$:

$$G(\Delta k) = \frac{1}{L} \int_0^L g(z) \exp(-i\Delta k z) dz \quad (2.28)$$

Usually QPM is realized by periodic variation of the nonlinearity and $g(z)$ can be

expanded in a series as:

$$g(z) = \sum_{m=-\infty}^{\infty} G_m e^{iK_m z} \quad (2.29)$$

$$K_m = \frac{2m\pi}{\Lambda} \quad (2.30)$$

where K_m is the grating vector of order m corresponding to a quasi phase matching period of Λ/m . Assuming this K_m is approximately the phase mismatch Δk it will dominate the integration (eqn. 2.27) resulting in an amplitude:

$$A_3(L) = \frac{-2\omega_3}{n_3 c} A_1 A_2^* L d_{\text{eff}} G_m e^{-\Delta k' L/2} \text{sinc}(\Delta k' L/2) \quad (2.31)$$

The additional grating vector leads here to an effective mismatch

$$\Delta k' = k_1 - k_2 - k_3 - K_m \quad (2.32)$$

Obviously this effective mismatch can vanish by appropriately tailoring K_m . Equation 2.31 behaves similar to eqn. 2.24 with respect to the effective mismatch and a lower effective nonlinearity $d_{\text{eff}} G_m$. In practice the QPM will be realized by periodic poling of ferroelectric crystals leading to a rectangular wave of period Λ with values ± 1 for $g(z)$ (illustrated in Fig. 2.2c). The duty cycle D describes the ratio between the length l of a section with positive d compared to the period $D = l/\Lambda$. For perfectly matched $\Delta k' = 0$ it can be found:

$$G_m = \frac{2}{\pi m} \sin(\pi m D) \quad (2.33)$$

$$d = \frac{2d_{\text{eff}}}{\pi m} \quad (2.34)$$

The highest nonlinearity can thus be achieved for first order QPM ($m = 1$) and a duty cycle that maximizes the sin-function (i.e. $D = 0.5$). It is worth mentioning that QPM reduces the nonlinear coefficient by a factor of $\frac{2}{m\pi}$. The output power is thus lower compared to the case of perfect phase matching. Compared to birefringent phase matching in QPM one is free to choose the crystal orientation. Thus a geometry can be chosen that allows for the highest nonlinear coefficient of the material and additionally avoids walk-off effects. In practice these advantages usually overcompensate the lower coefficient.

All devices used in this work rely on first order QPM ($m = 1$). For the sake of simplicity for the rest of the thesis phase mismatch always denotes the effective mismatch (eqn. 2.32) and the prime will be omitted ($\Delta k' \rightarrow \Delta k$). Furthermore the effective nonlinearity d_{eff} will now include the reducing factors due to QPM ($\frac{2}{\pi} d_{\text{eff}} \rightarrow d_{\text{eff}}$).

2.2 Quantum Theory of Light

Light is an electromagnetic wave and can thus be treated with a wave-description, at least at high intensities. However, it is also known that light can show particle-like behavior in certain experiments. These light particles are called photons and are carriers of a single quantum of energy $\hbar\omega$ from the electromagnetic field. Quantum theory has thus to combine both quantum nature and wave-like effects. The experiments presented in this thesis involve laser light, single photons and photon pair states. We will first distinguish between these different forms of light and later find quantum physical descriptions for them.

2.2.1 Different Types of Light

In a first example we consider a monochromatic light beam with a long-term average power P that is registered with an ideal photon detector. In a quantum picture this beam consists of a stream of photons. We now use the detector to count the number of photons arriving in a certain time interval T . Observation at short integration times or low photon flux then reveals the graininess of the beam. As the photon is the elementary quantum of light it cannot be divided further. That means when the average photon number in the integration time is smaller than one there will be time bins with no detection and other bins where photons are detected. Actually the photon number distribution in a certain time interval follows statistics depending on the nature of the light. Thus measuring the statistics will be a means to distinguish different types of light. Figure 2.3 illustrates photon number distributions for three different statistics. Comparing the plots shows that photons in the case of chaotic light tend to form bunches of multiple photons, resulting in rather high photon numbers. The photon numbers in the case of coherent light seem to be more randomly distributed. Finally, in the last case of single-photon emission there exist no photon numbers exceeding the value of one and the light is called anti-bunched.

First we regard light emitted by a thermal source which is a typical example for chaotic light. It can be shown that the probability $P(n)$ to measure n photons in a time bin with an average photon number $\langle n \rangle$ is described by a Planck probability distribution [102]:

$$P_{\text{Planck}}(n) = \frac{\langle n \rangle^n}{(1 + \langle n \rangle)^{1+n}} \quad (2.35)$$

Its variance is

$$(\Delta n)_{\text{Planck}}^2 = \langle n \rangle^2 + \langle n \rangle. \quad (2.36)$$

Next we consider a perfectly coherent light beam with time-invariant average photon flux. Such a beam can be generated by a single-mode laser operated far above threshold. In this case the photon number fluctuations on short time scales are described by

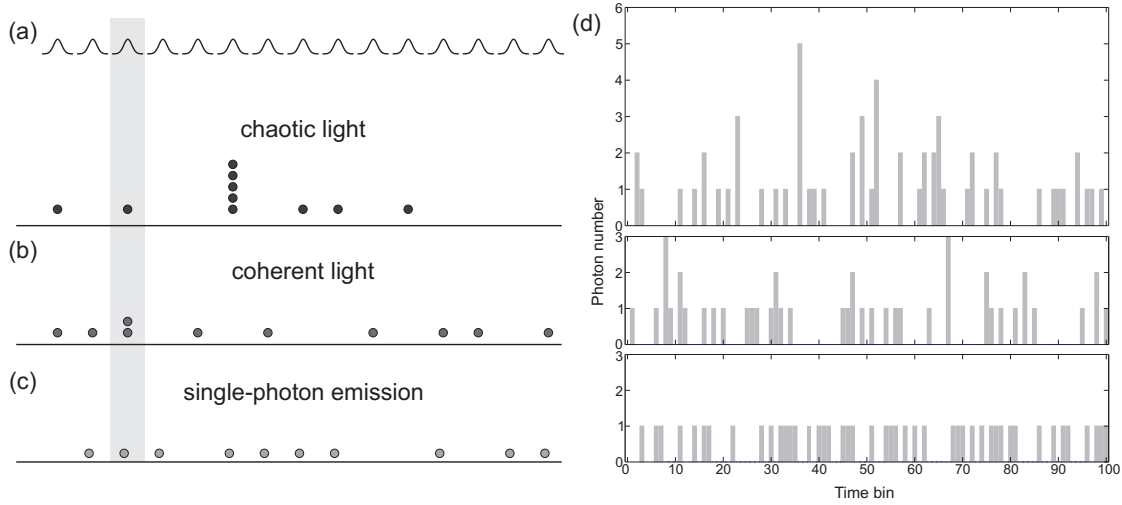


Figure 2.3: Illustration of photon statistics. A pulse train is sketched with an average photon number of $2/3$ photons per pulse. a) shows a simulated photon distribution for chaotic light with a super-Poissonian statistics. b) shows the distribution for coherent light with Poissonian statistics and c) illustrates emission of a single-photon emitter with sub-Poissonian statistics. In all three plots the same average photon number is assumed. d) illustrates again the distribution with these three statistics with a mean value of 0.5 photons per time-bin.

Poissonian statistics [1]:

$$P_{\text{Poisson}}(n) = \frac{\langle n \rangle^n}{n!} e^{-\langle n \rangle} \quad (2.37)$$

with a variance of

$$(\Delta n)_{\text{Poisson}}^2 = \langle n \rangle. \quad (2.38)$$

Finally, anti-bunched light which is generated by ideal quantum emitters is described by a fixed number of photons per time-bin. In this ideal case the variance is zero. To distinguish the photon statistics the variance can be used: If the variance is larger than the average value, $(\Delta n)^2 > \langle n \rangle$, the statistics is called super-Poissonian, the equality $(\Delta n)^2 = \langle n \rangle$ holds for Poissonian statistics and for $(\Delta n)^2 < \langle n \rangle$ it is called sub-Poissonian. Actually there is no classical counter-part for the last distribution and the observation of sub-Poissonian statistics is a signature for the quantum nature of the light [1]. For comparison, the photon number distribution for these three cases is plotted in Fig. 2.4 for different average photon numbers. To determine the photon statistics a naive way would be to just count the photons in several pulses. However photon number resolving detectors [103] are not readily available for high photon numbers. Nevertheless there are techniques to estimate the distribution by measurements with binary detectors [104,105] and to observe non-classical statistics even with a single

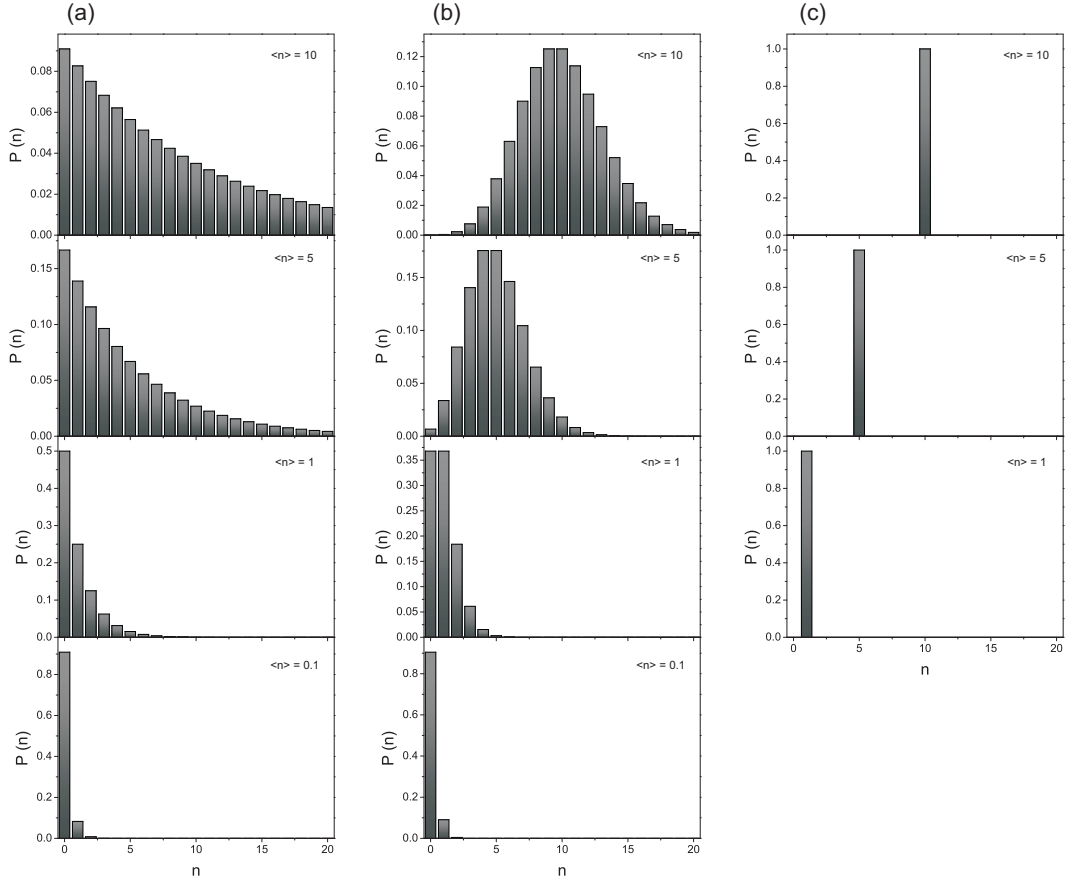


Figure 2.4: Photon number distribution for different types of light: a) chaotic light, b) coherent light, c) Fock state. The average photon number decreases from 10 to 0.1 from top to bottom.

detector [106]. However the most common technique to reveal non-classical light is the intensity correlation measurement in a Hanbury-Brown Twiss interferometer [107]. This will be introduced later in more detail.

Photon Number States

The heart of quantum description of light is the quantum harmonic oscillator. Its solution shows an energy spectrum with equally spaced levels, separated by a single quantum of energy. In analogy for the photon number state $|n\rangle$ (Fock state) the electromagnetic field can be described by a ladder occupied by n photons. The Hamiltonian of the quantum harmonic oscillator can be written in the form [102]:

$$\hat{H} = \frac{1}{2}\hbar\omega (\hat{a}\hat{a}^\dagger + \hat{a}^\dagger\hat{a}) = \hbar\omega \left(\hat{a}^\dagger\hat{a} + \frac{1}{2} \right) \quad (2.39)$$

In the case of a light field the ladder operators are generation (\hat{a}^\dagger) and annihilation (\hat{a}) operators of photons. For the Fock state their effect is:

$$\hat{a} |n\rangle = \sqrt{n} |n-1\rangle \quad (2.40)$$

$$\hat{a}^\dagger |n\rangle = \sqrt{n+1} |n+1\rangle \quad (2.41)$$

$$\hat{a} |0\rangle = 0 \quad (2.42)$$

It is also convenient to define the number operator \hat{n} with:

$$\hat{n} = \hat{a}^\dagger \hat{a} \quad (2.43)$$

$$\hat{n} |n\rangle = n |n\rangle \quad (2.44)$$

With these tools the number state representation can be applied to any system described by a Hamiltonian equivalent to the simple quantum harmonic oscillator [1]. In the case of light fields the photon number representation describes the system by the number of energy quanta excited, i.e. the number of photons excited at an angular frequency ω . The photon number state $|n\rangle$ represents a quantized field containing n photons of frequency ω . The ground state $|0\rangle$ is called vacuum state. The creation operator \hat{a}^\dagger then adds another photon of frequency ω to the field and increases its energy by $\hbar\omega$.

Coherent States

The number states form a complete base in the Fock space. An arbitrary light field can now be described as a superposition of photon number states. Thus we can also describe coherent light with this formalism. A coherent state $|\alpha\rangle$ is characterized by its (classical) complex field amplitude α . In the photon number representation it can be written as:

$$|\alpha\rangle = \exp(-|\alpha|^2) \sum_{n=0}^{\infty} \frac{\alpha^n}{\sqrt{n!}} |n\rangle \quad (2.45)$$

The coherent state is an eigenstate of the annihilation operator:

$$\hat{a} |\alpha\rangle = \alpha |\alpha\rangle \quad (2.46)$$

Projecting the coherent state on the photon number state results in the photon number distribution:

$$\langle n|\alpha\rangle = e^{-\frac{|\alpha|^2}{2}} \frac{\alpha^n}{\sqrt{n!}} \quad (2.47)$$

which is a Poissonian distribution. This means that these coherent states have Poissonian photon statistics and indeed describe coherent light fields. Finally we can also calculate the expectation value for the photon number operator of a coherent state:

$$\langle \alpha|\hat{n}|\alpha\rangle = \alpha^* \alpha \quad (2.48)$$

which is proportional to the classical intensity of the coherent field.

Second Order Coherence

To distinguish between the above mentioned types of light one usually measures the degree of second order coherence. In practice this is done with a Hanbury Brown-Twiss setup [107]. The principle is illustrated in Fig 2.5. The setup consists of a 50:50

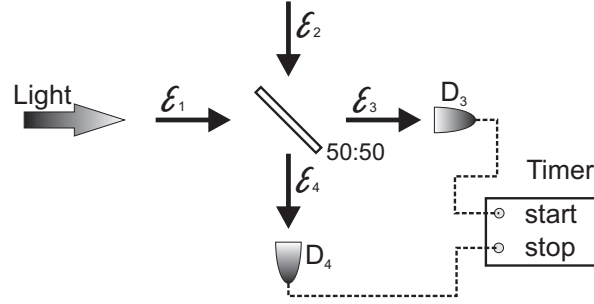


Figure 2.5: Measurement setup for second order coherence function (after [1]).

beamsplitter with two input modes ($\mathcal{E}_1, \mathcal{E}_2$) and two output modes ($\mathcal{E}_3, \mathcal{E}_4$). At each output port there is a single photon detector. The times of detection events are registered with a timer (time tagging electronics). Each output mode of the beamsplitter is a superposition of both input modes. For single-photon input we can exchange the field by the annihilation operators ($\mathcal{E}_i \rightarrow \hat{a}_i$). This results in outputs [1]:

$$\hat{a}_3 = (\hat{a}_1 - \hat{a}_2) / \sqrt{2} \quad \hat{a}_4 = (\hat{a}_1 + \hat{a}_2) / \sqrt{2} \quad (2.49)$$

We can then define the second order correlation function $g^{(2)}(\tau)$ by:

$$g^{(2)}(\tau) = \frac{\langle n_3(t) n_4(t + \tau) \rangle}{\langle n_3(t) \rangle \langle n_4(t + \tau) \rangle} = \frac{\langle \hat{a}_3^\dagger(t) \hat{a}_4^\dagger(t + \tau) \hat{a}_4(t + \tau) \hat{a}_3(t) \rangle}{\langle \hat{a}_3^\dagger(t) \hat{a}_3(t) \rangle \langle \hat{a}_4^\dagger(t + \tau) \hat{a}_4(t + \tau) \rangle} \quad (2.50)$$

This function contains the number of coincidences when a photon is registered in output 3 at time t and at output 4 at time $t + \tau$ and is normalized by the number of detection events in each mode.

To characterize a single light field the second input port is usually left open ($\mathcal{E}_2 = |0\rangle$) which simplifies the last equation. The degree of second order coherence of a light field is then the value of the second order correlation function at zero delay $g^{(2)}(0)$. Assuming the input light in the state $|\Psi\rangle$ this results in [1]:

$$g^{(2)}(0) = \frac{\langle \Psi | \hat{n}(\hat{n} - 1) | \Psi \rangle}{(\langle \Psi | \hat{n} | \Psi \rangle)^2} = \frac{\langle \hat{n}(\hat{n} - 1) \rangle}{\langle \hat{n} \rangle^2} \quad (2.51)$$

It can be shown that for any classical light the degree of second order coherence has a lower boundary: $g^{(2)}(0) \geq 1$. We can then distinguish three classes of light:

- **bunched light:** $g^{(2)}(0) > 1$
- **coherent light:** $g^{(2)}(0) = 1$
- **antibunched light:** $g^{(2)}(0) < 1$

Furthermore, chaotic light is limited to values $g^{(2)}(0) \leq 2$. To demonstrate the non-classical character of a light source the emission should have a degree of second order coherence of $g^{(2)}(0) < 1$ for a single mode. Measuring the correlation between two modes of a single source can result in $g^{(2)}(0) > 2$. Bunched light that exceeds the classical limits can be generated with entangled pair sources. Antibunched light is a signature of single photon sources.

2.2.2 Quantum Mechanical Model of DFG

The process of difference frequency generation was introduced earlier in this chapter involving classical light fields. In the case of single photons or other non-classical states of light a quantum optical description of this process is desirable. In the photon picture DFG means that a high energy photon (signal) splits into two photons with lower energy (pump and idler). This process is stimulated by a strong field at the pump wavelength. Please note that the labeling of the fields here is different from literature. The stimulating field with high power is named pump, the original single photon field is called signal and the output field is called idler. The process is typically illustrated in an energy level diagram which shows the conservation of energy (see Fig. 2.6a). However these are not real energy levels, the fields are not resonant with any transition and the material should be transparent for all fields. The process can be expressed with the help of the generation and annihilation operators of the three fields in an interaction Hamilton operator as first introduced by Ou [31]:

$$\hat{H} = i\hbar\eta\hat{a}_s\hat{a}_p^\dagger\hat{a}_i^\dagger - i\hbar\eta^*\hat{a}_p\hat{a}_i\hat{a}_s^\dagger \quad (2.52)$$

Here η is the coupling constant of the process. Usually the pump field is a strong classical light field. Hence its photon operators can be replaced by the classical field amplitude for the pump field:

$$\hat{H} = i\hbar\eta\hat{a}_s\hat{a}_i^\dagger A_p^* - i\hbar\eta^* A_p\hat{a}_i\hat{a}_s^\dagger \quad (2.53)$$

The time evolution of an operator \hat{O} can be calculated by the Heisenberg equation of motion:

$$\frac{d\hat{O}}{dt} = \frac{i}{\hbar} [\hat{H}, \hat{O}] \quad (2.54)$$

Following the derivation of [23] this results in the equations of motion for the photon operators in the DFG process:

$$\frac{d\hat{a}_s}{dt} = -\eta^* A_p \hat{a}_i, \quad \frac{d\hat{a}_i}{dt} = \eta A_p^* \hat{a}_s \quad (2.55)$$

which have the solutions:

$$\hat{a}_s(\tau) = \hat{a}_s(0) \cos(|\eta A_p| \tau) - e^{i\Phi_p} \hat{a}_i(0) \sin(|\eta A_p| \tau) \quad (2.56)$$

$$\hat{a}_i(\tau) = \hat{a}_i(0) \cos(|\eta A_p| \tau) + e^{i\Phi_p} \hat{a}_s(0) \sin(|\eta A_p| \tau) \quad (2.57)$$

Here Φ_p is the pump phase defined by $\Phi_p = \eta A_p^* / |\eta A_p|$. When the relation $|\eta A_p| \tau = \pi/2$ is fulfilled the fields are completely converted to the other mode: $\hat{a}_s^{\text{out}} = -e^{i\Phi_p} \hat{a}_i(0)$ and $\hat{a}_i^{\text{out}} = e^{i\Phi_p} \hat{a}_s(0)$. To compare these results with the classical equations for intensity we have to calculate the evolution of the expectation value of the photon number operator:

$$\langle n_s(\tau) \rangle = \langle n_s(0) \rangle \cos^2(|\eta A_p| \tau) + \langle n_i(0) \rangle \sin^2(|\eta A_p| \tau) \quad (2.58)$$

$$\langle n_i(\tau) \rangle = \langle n_i(0) \rangle \cos^2(|\eta A_p| \tau) + \langle n_s(0) \rangle \sin^2(|\eta A_p| \tau) \quad (2.59)$$

This evolution is illustrated in Fig. 2.6. If the input of the DFG process is a single photon Fock state $|n_s(0), n_i(0)\rangle = |1, 0\rangle$ it can be converted with unity efficiency to the output state $|n_s(\tau_{\text{opt}}), n_i(\tau_{\text{opt}})\rangle = |0, 1\rangle$ after the optimum interaction time $\tau_{\text{opt}} = \pi/2 |\eta A_p|$. This means that the quantum state is preserved while the frequency of the photon is altered.

With the help of the equations above we can define the conversion efficiency η_{QFC} which corresponds to the probability of a single photon being converted in the QFC

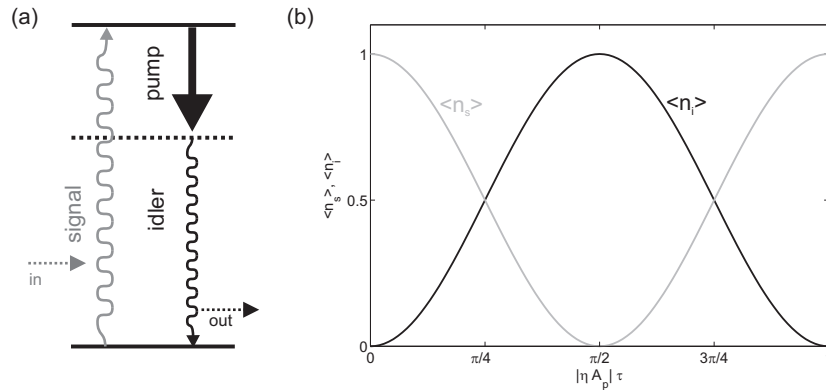


Figure 2.6: a) Energy level diagram of downconversion process. b) evolution of the expectation value of the photon number operator.

process:

$$\eta_{\text{QFC}} = \frac{\langle n_i(\tau) \rangle}{\langle n_s(0) \rangle} = \sin^2(|\eta A_p| \tau) = \sin^2(|\eta| \sqrt{P_p} \tau) \quad (2.60)$$

The description given here for the QFC process, according to Ou [31], holds only for an ideal case. We assumed only three modes involved in the interaction which however is a good approximation for the experiments described in this thesis as all fields will be continuous wave with frequency bandwidths much smaller than the acceptance bandwidth of the QFC process and thus in a single frequency and spatial mode. However the theory had been extended to the more general multi-mode case by Brecht [108]. A more realistic scenario also involves losses and noise sources. This has been implemented by Blum [36, 105] including the generation of photons in the output mode by processes that are uncorrelated to the QFC process. The most prominent noise sources are spontaneous parametric down-conversion (see section 2.2.3) and Raman scattering of the pump field [34]. The model by Blum includes a Hamiltonian for each noise process and for photon loss. It is based on a Heisenberg-Langevin formalism and can be used to evaluate the influence of noise photons on the statistics of QFC photons. The results can be compared with our experimental data [109].

2.2.3 Spontaneous Parametric Down-Conversion

In a general way the parametric process for single-mode signal and idler fields can be described by a simple interaction Hamiltonian:

$$\hat{H}_I = i\hbar\chi\hat{a}_s^\dagger\hat{a}_i^\dagger + H.c. \quad (2.61)$$

The time evolution of the quantum state $|\Psi(t)\rangle$ can be described in the interaction picture by:

$$|\Psi(t)\rangle = \hat{U}(t)|\Psi(0)\rangle = \exp\left(-i\hat{H}_I t/\hbar\right)|\Psi(0)\rangle \quad (2.62)$$

In the low gain regime for $|\eta| = |\chi t| \ll 1$, then the state can be approximately written as:

$$|\Psi(t)\rangle \approx (1 - |\eta|^2/2)|0\rangle + \eta|1_s, 1_i\rangle + \eta^2|2_s, 2_i\rangle \quad (2.63)$$

This state obviously describes a system that has the same numbers of photons in the signal and the idler mode. The first term includes the vacuum field. The next term contains a pair of photons. The following terms describe higher order pairs whose contributions decrease with increasing order with respect to the efficiency parameter η . Such parametric processes can be realized in many ways for example by nonlinear optic interactions or multi-photon transitions in atoms.

Here we want to focus on parametric down-conversion as second order nonlinear interaction. It is similar to the frequency conversion process described earlier. However,

here only the pump field is present at the beginning of the nonlinear medium and the pump photons spontaneously decay into signal and idler photons with lower energy ($\omega_3 \rightarrow \omega_1 + \omega_2$). The derivation of the SPDC pair state follows the book of Ou [110]. Hence we start with the nonlinear interaction Hamiltonian:

$$\hat{H}_I = \frac{1}{2} \int d^3\mathbf{r} \vec{P}^{NL} \vec{E} = \frac{1}{2} \int d^3\mathbf{r} E_i \int dt_1 dt_2 \chi_{ijk}^{(2)} E_j E_k \quad (2.64)$$

$$\begin{aligned} \hat{H}_I = & \int_{\omega_p} d^3\mathbf{k}_3 \int_{\omega_0} d^3\mathbf{k}_1 d^3\mathbf{k}_2 \sum_{\nu_1, \nu_2, \nu_3} \chi_{ijk}^{(2)}(\omega_1, \omega_2, \omega_3) \mathbf{e}_{\nu_1 i} \mathbf{e}_{\nu_2 j}^* \mathbf{e}_{\nu_3 k}^* \hat{a}_3 \hat{a}_1^\dagger \hat{a}_2^\dagger \\ & \times \exp(i(\omega_1 + \omega_2 - \omega_3)) \int d^3\mathbf{r} \exp(i\Delta\mathbf{k}\mathbf{r}) + H.c. \end{aligned} \quad (2.65)$$

In order to calculate the time evolution of the state we need the time integral of the Hamiltonian. At this point we make some assumptions to simplify the expression: The system reaches a steady state after the interaction, thus we can extend the integration boundaries to infinity. Furthermore at this point we take the conservation of energy into account reducing the exponential term to a delta function. Finally we regard a certain process with quasi phase matching in a collinear geometry. This implies fixed polarizations of the involved fields and allows a one-dimensional treatment. This leads to the expression:

$$\begin{aligned} \frac{1}{i\hbar} \int_{-\infty}^{\infty} \hat{H}_I(\tau) d\tau = & \xi \int_{\omega_p} d\omega_3 \int_{\omega_0} d\omega_1 d\omega_2 \delta(\omega_1 + \omega_2 - \omega_3) \\ & \times \hat{a}_p(\omega_3) \hat{a}_s^\dagger(\omega_1) \hat{a}_i^\dagger(\omega_2) h(L\Delta k) + H.c. \end{aligned} \quad (2.66)$$

$$\text{with } h(x) = \exp(-ix/2) \text{sinc}(x/2) \quad (2.67)$$

Here $\Delta k = [n_p/\lambda_p - n_s/\lambda_s - n_i/\lambda_i - 2\pi/\Lambda_{\text{QPM}}]$ is the phase mismatch, L is the interaction length and $\xi \propto \chi^{(2)}$ is a constant describing the nonlinear interaction strength. For the initial state we assume a classical, coherent pump field α_p and vacuum in both signal and idler mode:

$$|\Psi_0\rangle = |\alpha_p(\omega)\rangle \otimes |0_s, 0_i\rangle \quad (2.68)$$

The time evolution generates the following final state:

$$\begin{aligned} |\Psi\rangle &= \hat{U}(\infty, -\infty) |\Psi_0\rangle = \exp\left[\frac{1}{i\hbar} \int_{-\infty}^{\infty} \hat{H}_I(\tau) d\tau\right] |\Psi_0\rangle \\ &\approx \left[1 + \frac{1}{i\hbar} \int_{-\infty}^{\infty} \hat{H}_I(\tau) d\tau\right] |\Psi_0\rangle \\ &= |\alpha_p(\omega)\rangle \otimes [|0_s, 0_i\rangle \\ &+ \xi \int_{\omega_p} d\omega_3 \int_{\omega} d\omega_1 d\omega_2 h(L\Delta k) \delta(\omega_1 + \omega_2 - \omega_3) \alpha_p(\omega_3) | \omega_{1s}, \omega_{2i} \rangle] \end{aligned} \quad (2.69)$$

The exponential function was approximated by its first order Taylor expansion. Thus the generation of multi-pair states is neglected here. In the case of a narrowband pump field, which is usually fulfilled for continuous wave pumping, the operator for the coherent pump field reduces to a single mode $\alpha_p(\omega) = V_p \delta(\omega - \omega_p)$. Here V_p is the pump amplitude. The the state simplifies to:

$$|\Psi\rangle_{\text{PDC}}^{(cw)} = |0_s, 0_i\rangle + \zeta \int d\omega_1 d\omega_2 \Phi(\omega_1, \omega_2) |\omega_{1s}, \omega_{2i}\rangle \quad (2.70)$$

where ζ is a normalization constant and

$$\begin{aligned} \Phi(\omega_1, \omega_2) &= V_p \delta(\omega_1 + \omega_2 - \omega_p) \varphi(\omega_1) \\ \varphi(\omega_1) &\propto h(L\Delta k) \end{aligned} \quad (2.71)$$

describing the spectral properties of the created photons.

Properties of SPDC Photons

Knowing the quantum optical description of the SPDC photon pair state we can derive some of its properties that are accessible in experiments. These are expressions for the photon rates as well as first and second-order correlation functions. With the help of the electric field operator of mode m

$$\hat{E}_m(\mathbf{r}, t) = \frac{1}{\sqrt{2\pi}} \int d\omega_m \hat{a}(\omega_m) e^{i(\mathbf{k}_m \mathbf{r} - \omega_m t)} \quad (2.72)$$

we can calculate the first order correlation function giving the coherence properties:

$$\Gamma_m(\tau) = \left\langle \hat{E}_m^\dagger(\mathbf{r}, t) \hat{E}_m(\mathbf{r}, t + \tau) \right\rangle \quad (2.73)$$

This results in

$$\Gamma_s(\tau) = |\zeta|^2 I_p \int d\omega_1 |\varphi(\omega_1, \omega_p - \omega_1)|^2 e^{-i\omega_1 \tau} \quad (2.74)$$

$$\Gamma_i(\tau) = |\zeta|^2 I_p \int d\omega_1 |\varphi(\omega_1, \omega_p - \omega_1)|^2 e^{-i(\omega_p - \omega_1)\tau} = e^{i\omega_p \tau} \Gamma_s^*(\tau) \quad (2.75)$$

Here I_p is the flux of pump photons. This means both modes have the same coherence properties. The coherence functions are complex conjugates of each other and differ by a phase factor. Generally the spectrum is the Fourier transform of the coherence function and thus described by $|\varphi(\omega_1, \omega_p - \omega_1)|^2$ which mainly depends on the phase matching function $h(L\Delta k)$ up to normalization constants. The rate of downconverted photons is then given by the absolute square of the electromagnetic field amplitude of the photons $\left\langle \hat{E}_m^\dagger(\mathbf{r}, t) \hat{E}_m(\mathbf{r}, t) \right\rangle$. This is the coherence function at zero delay ($\Gamma_m(0)$) resulting in:

$$R_m(\mathbf{r}, t) = |\zeta|^2 I_p \quad (2.76)$$

Thus $|\zeta|^2$ can be identified as a normalization constant, corresponding to the efficiency of converting a pump photon to a signal and idler photon. This constant combines all effects affecting efficiency, like mode coupling or material nonlinear coefficient.

The previous equations described properties of the individual modes. However, both modes together form a common state which can also be investigated in more detail. Due to the simultaneous generation process of signal and idler photons we know, there is a temporal correlation between them. A coincidence detection between these modes can reveal the temporal shape of the photons. The coincidence detection of a signal and idler photon can be calculated with the help of the second order (cross-) correlation function:

$$\begin{aligned} G^{(2)}(\tau) &= \left\langle \hat{E}_i^\dagger(\mathbf{r}_i, t) \hat{E}_s^\dagger(\mathbf{r}_s, t + \tau) \hat{E}_s(\mathbf{r}_s, t + \tau) \hat{E}_i(\mathbf{r}_i, t) \right\rangle \\ &= \left\| \hat{E}_s(\mathbf{r}_s, t + \tau) \hat{E}_i(\mathbf{r}_i, t) |\Psi\rangle_{\text{PDC}} \right\|^2 \end{aligned} \quad (2.77)$$

The measured coincidence rate R_c additionally depends on the detection efficiencies β_m and is given by integrating the correlation function over the detector time resolution T_R :

$$R_c = \beta_s \beta_i \int_{T_R} d\tau G^{(2)}(\tau) = \beta_s \beta_i \int_{T_R} d\tau \left| \frac{\zeta V_p}{2\pi} \tilde{g}(\tau - \Delta z/c) \right|^2 \quad (2.78)$$

$$\text{with } \tilde{g}(\tau) = \int d\omega_1 \varphi(\omega_1) e^{-i\omega_1 \tau} \quad (2.79)$$

In the derivation we included the spatial dependence of the system as the distance of the source to the different detectors. The factor $\Delta z = z_s - z_i$ accounts for this unbalanced distance for signal and idler mode. In practice this includes not only the optical path of the photons from source to detector but also the electrical path of the detection signal from the detectors to the time tagging electronics.

The second order correlation function shows a peak at a time corresponding to the simultaneous creation of a signal and an idler photon. As the function $\tilde{g}(\tau)$ is connected to the spectral function $\varphi(\omega_1)$ the temporal width of the correlation signal is proportional to the inverse of the photons spectral bandwidth: $T_c \propto 1/\Delta\omega_{\text{PDC}}$. The shape and width of this correlation peak are determined by the spectral properties of the photons. In the case that the detector resolution is much worse than the coherence time $T_R \gg T_c$ the temporal shape of the peak will be washed out by detector timing jitter. The coincidence rate refers to the rate of correlated detection events in a specified time window.

Narrow-band spectral filters can be used to reduce spectral width and thus increase coherence of the photons. In that case, the above equations can be adopted by modifying the spectral function $\varphi(\omega_1, \omega_2)$. The intrinsic spectrum of the photons has to be convoluted with the transfer function of the filters inside this function [111]. In such a

regime ($T_c > T_R$) we are able to resolve the temporal shape of the coherence function in experiment. A side effect of filtering is the reduction of photon and coincidence rates as not all generated photons can pass the filter. In general it is also possible to use asymmetric filtering with different bandwidths and spectra in signal and idler mode. In this case not all detected photons can contribute to the coincidence rate as some photons do not have a partner as it was rejected by the filter.

Heralded Single Photons

If we resume the basic description of parametric down-conversion state (eqn. 2.63):

$$|\Psi(t)\rangle = (1 - |\eta|^2/2) |0_s\rangle |0_i\rangle + \eta |1_s\rangle |1_i\rangle + \eta^2 |2_s\rangle |2_i\rangle + \dots \quad (2.80)$$

And now assume to detect a single photon in the signal mode, the measurement will collapse the state to:

$$\langle 1_s | \Psi(\tau) \rangle = (1 - |\eta|^2/2) \langle 1_s | 0_s \rangle |0_i\rangle + \eta \langle 1_s | 1_s \rangle |1_i\rangle + \eta^2 \langle 1_s | 2_s \rangle |2_i\rangle + \dots = \eta |1_i\rangle \quad (2.81)$$

This is a single photon state in the idler mode. This process is called heralded single photon generation as the detection of one partner of a photon pair heralds the existence of its twin photon in the other mode. Sometimes devices exploiting this process are also referred to as deterministic single photon source as an event signaling the presence of a single photon is available.

In practice usually binary single photon detectors are used that cannot distinguish between one or more than one photon per mode. If we use such a detector in a heralded single photon source, the higher order photon number states will also result in a herald signal on detection which means we do not reach an ideal single photon state. However we can generate antibunched light. If we start with the basic SPDC state from eqn. 2.62 it can be shown [110] that after normal ordering the operator can be expressed as a series:

$$|\Psi\rangle = \sum_{k=0}^{\infty} \frac{\nu^k}{\mu^{k+1}} |k\rangle_s |k\rangle_i \quad (2.82)$$

where ν and μ are constants depending on the conversion efficiency. If we now consider only one field, e.g. the idler, it is necessary to trace out the other field with the following density operator:

$$\hat{\rho} = \sum_{n=0}^{\infty} P_n |n\rangle_s \langle n|_s \quad (2.83)$$

It can be shown [112] that the probability distribution P_n can have the form

$$P_n = \frac{\exp(-n\beta\hbar\omega_s)}{1 - \exp(-\beta\hbar\omega_s)} \propto \frac{\langle k \rangle^n}{(\langle k \rangle + 1)^{n+1}} \quad (2.84)$$

which is a Boltzmann distribution. Hence each field of the SPDC process has the same statistics as a thermal source. This is a purely quantum mechanical effect which arises from the amplification of vacuum fluctuations [112]. Due to these statistics we expect the observation of bunching in an HBT experiment when looking at signal or idler photons individually. Theoretically, the expected value of $g^{(2)}(0) = 2$ is reached for a pure state only, while a value between $1 \leq g^{(2)}(0) \leq 2$ is expected for multi-mode fields [110]. Such a bunching peak in second order coherence could be observed experimentally [113]. The deviation from the ideal value of 2 can be used as a measure for the number of contributing modes. We expect a value of $g^{(2)}(0) = 1 + 1/N$ with N being the effective number of modes.

Anyway we can use SPDC sources to generate antibunched light. Heralding the idler field by detection of a signal photon reduces the number of vacuum detection events. This means in the resulting idler state the ratio of $|0\rangle_i$ is greatly reduced. The width of the original thermal distribution depends on the pump power of the SPDC process. This means at low pump powers higher order photon numbers can be neglected. When due to the heralding also the vacuum component can be neglected such a modified thermal statistic can reach sub-poissonian width. Indeed has antibunching been experimentally demonstrated in heralded detection [67].

If the temporal resolution of the detection system is below the coherence time of the photons ($T_R < T_c$), we cannot resolve the temporal structure of the correlation function. Anyway, it is possible to gather information about the purity of the pair generation process. There are approximations to estimate probabilities for multi-pair generation. This involves heralded detection in the experiment. The anti-correlation parameter α as introduced by Grangier and coworkers [114]:

$$\alpha = \frac{R_{123}R_1}{R_{12}R_{13}} \quad (2.85)$$

has a lower limit of $\alpha \geq 1$ for classical states of light. Thus a value of $\alpha < 1$ is a signature for non-classical photon statistics. Determining it involves a three-fold coincidence measurement with one photon of the pair as herald and its twin send to a HBT interferometer. Then R_1 is the heralding rate, R_{12} and R_{13} are the detection rates in the HBT interferometer conditioned on the detection of a herald event and R_{123} is the three-fold coincidence rate. In a similar way an approximation for the second order correlation at zero delay can be found [65]:

$$g^{(2)}(0) \approx 2 \frac{P(2)}{P^2(1)} = 4 \frac{R_{123}R_1}{(R_{12} + R_{13})^2} \quad (2.86)$$

Here we assumed the value $g^{(2)}(0)$ is dominated by the probabilities $P(1)$ of having one or $P(2)$ for finding two photons simultaneously in the field. Here, higher order contributions are neglected. Furthermore, we assume $P(2) \ll P(1)$ and equal detection

efficiencies for detectors 2 and 3. It is possible to determine the $g^{(2)}(0)$ -value in this manner, even when the detector timing resolution is not enough to reveal the temporal shape of $g^{(2)}(\tau)$ completely as long-term averaging effects are partly suppressed.

3 Optical Devices and Materials

In this chapter I will summarize the optical and material properties of lithium niobate which is the optical nonlinear medium in the quantum frequency conversion experiments. In the previous chapter the fundamental aspects of nonlinear optics were introduced. Here this description is continued in more detail to introduce the fundamental aspects of optical parametric amplification and oscillation. These are the foundation of the working principle of optical parametric oscillators. The experimental setup of these oscillators will be presented later in chapters 4 and 5. In the third part of this chapter I will introduce waveguides and the nonlinear optical interaction in such devices. Therefore the coupled amplitude equations derived in the previous chapter have to be adapted. The device details for the particular waveguides used in the experiments can be found in section 6.1.1. At the end of this chapter fabrication techniques for waveguides will be briefly introduced.

3.1 Lithium Niobate as Nonlinear Material

The description of the material properties of lithium niobate (LN) here mainly follows a seminal review paper [21]. The crystal is an isotypus of lithium tantalate and thus these materials share similar properties. Lithium niobate does not appear naturally but is one of the first crystals synthesized for nonlinear optics [115]. It shows large pyroelectric, piezoelectric, electro-optic and photoelastic coefficients. This enables applications in amplitude and phase modulators and other integrated optical devices. It also features large nonlinear coefficients and birefringence which allows its usage in nonlinear devices via birefringent phase matching. However, lithium niobate is also ferroelectric which paved the way for quasi phase matching (QPM) by periodic poling. With the development of this technique it started to become one of the most popular nonlinear materials [115].

The nonlinear properties and the ferroelectricity are connected to the crystalline structure of lithium niobate, shown in Fig. 3.1. At room temperature it consists of planar sheets of oxygen atoms in a distorted hexagonal close-packed configuration [21]. This configuration forms octahedral interstices. These octahedral structures are filled with lithium atoms, niobium atoms or are empty (in the order Nb, vacancy, Li, ... in c^+ -direction). The Li and Nb atoms are shifted out of the symmetry plane of the oxygen octahedrons. This charge separation causes a spontaneous polarization

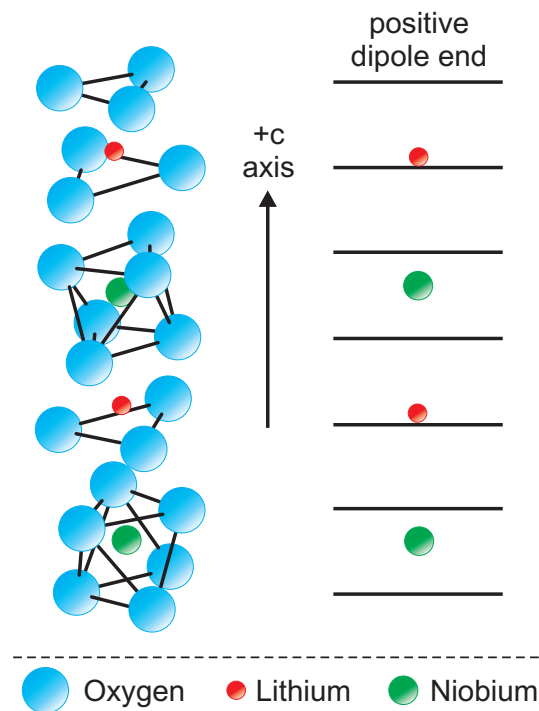


Figure 3.1: Structure of lithium niobate for the ferroelectric phase, after [21].

and is origin of the ferroelectricity. When lithium niobate is heated above its Curie temperature of 1210°C , the Li atoms lie in an oxygen layer, the Nb atoms are centered between two oxygen layers and the material is in its paraelectric phase [21].

Ferroelectric lithium niobate is a member of the trigonal crystal system due to a three-fold rotation symmetry around the c -axis. It shows an additional three-fold mirror symmetry and can thus be attributed to the $3m$ point group [21]. This symmetry defines the crystallographic c -axis in the hexagonal unit cell. The c^+ direction of this axis is defined by the face of the crystal becoming positively charged on cool-down. The coordinate system to describe tensor elements is usually Cartesian with the z -axis parallel to the crystal c -axis, the x -axis parallel to one of the hexagonal a -axes and the y -axis in one of the mirror symmetry planes. Thus an z -cut crystal means a sheet that is cut normal to the z -axis.

Congruent lithium niobate is grown with the Czochralski method. Congruent in this case means that the composition of species in the original melt equals the composition of the final crystal. This increases the homogeneity of the crystal. However, this is not the same as the stoichiometric composition given by the chemical formula LiNbO_3 but there is a slight excess of niobium ions [116].

Already in 1966 optically induced inhomogeneities have been observed in lithium niobate [117]. These are named photorefractive effects today and include the change

of the refractive index of an optical material induced by incident light. In lithium niobate defect centers can exist in the crystal lattice either due to unwanted doping with impurities or intrinsically due to niobium ions sitting at lithium sites or due to lithium vacancies. Such defects can be origin of optically induced free charge carriers. These charges might diffuse to non-irradiated regions of the crystal and trapped there. This local variation of electric field and charge density changes the refractive index locally [118]. The result is a spatial distortion of a light beam passing the crystal. The photorefractive effects are sensitive to short wavelength light leading to aberrations of high power visible beams. A well known further problem is the blue- and green-induced infrared absorption [119,120]. One way to overcome such effects is to operate the crystal at elevated temperatures which increases the mobility of the charge carriers and reduces the lifetime of the traps. A more feasible method is the doping of the crystal reducing the number of defects. It has been shown that doping lithium niobate with MgO or ZnO drastically reduces the susceptibility to photorefractive effects [119–122]. Typical doping concentrations are 5-7 mol%.

Electric Field Poling

In the sketch of the lithium niobate crystal structure shown in Fig. 3.1 all Li^+ ions are positioned above the oxygen triangles with respect to the c -axis. The shift of the Li^+ and Ni^- ions with respect to the oxygen octahedra results in permanent electric dipole moments in each unit cell. This causes the ferroelectricity of lithium niobate. If all ions in a certain volume are shifted in the same direction the microscopic dipole moments add to a macroscopic spontaneous polarization. Such a volume is then referred to as ferroelectric domain, in analogy to ferromagnetic materials with all magnetic moments in a domain being aligned to one direction [123]. Actually the energy of the ions along the c -axis follows a double-well potential [124]. Hence there is another stable position of the ions just below the oxygen triangles. At room temperature the thermal energy is not large enough for the ions to toggle to the other minimum of the double well potential. However, an externally applied electric field may allow the Li^+ ions to tunnel. The position is stable also after switching off the external field. This effect is exploited by periodic poling techniques to achieve QPM in lithium niobate [118,124]. A domain with flipped polarization has the same effect as flipping the whole crystal structure in this volume, i.e. the c^+ surface becomes c^- and vice versa. Thus the d_{31} and d_{33} tensor elements change their signs in the flipped domain.

Linear and Nonlinear Optical Properties

Lithium niobate is transparent between 0.34 and 5.5 μm with two more small peaks around 6 μm and 7 μm with significant transmission [125]. During growth process there is a contamination of the crystal with hydrogen resulting in an additional absorption

peak due to OH-vibrations which can be found around 2826 nm for MgO-doped lithium niobate [126]. According to its crystal structure, lithium niobate is uniaxially birefringent. In the whole transparency range the birefringence is negative ($\Delta n = n_e - n_o < 0$). The refractive index can be calculated with the help of Sellmeier equations. There exist a couple of publications with slightly different values. However, the equations by Gayer and coworkers [127] for 5% MgO doped LN turned out to fit best to the OPO results and according to comment from the manufacturer [128] the equations of Jundt for congruent LN [129] are a good approximation for the ridge waveguides. The Sellmeier coefficients are summarized in Fig. 3.2.

	n_e MgO:LN [127]	n_o MgO:LN [127]	CLN [129]
a_1	5.7560	5.653	5.355830
a_2	0.0983	0.1185	0.100473
a_3	0.2020	0.2091	0.206920
a_4	189.32	89.61	100
a_5	12.52	10.85	11.34927
a_6	$1.320 \cdot 10^{-2}$	$1.970 \cdot 10^{-2}$	$1.5334 \cdot 10^{-2}$
b_1	$2.860 \cdot 10^{-6}$	$7.941 \cdot 10^{-7}$	$4.6290 \cdot 10^{-7}$
b_2	$4.700 \cdot 10^{-8}$	$3.134 \cdot 10^{-8}$	$3.8620 \cdot 10^{-8}$
b_3	$6.113 \cdot 10^{-8}$	$-4.641 \cdot 10^{-9}$	$-0.8900 \cdot 10^{-8}$
b_4	$1.516 \cdot 10^{-4}$	$-2.188 \cdot 10^{-6}$	$2.6570 \cdot 10^{-5}$

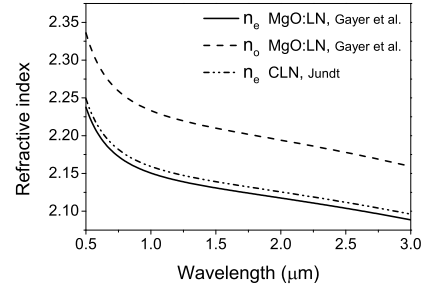


Figure 3.2: Dispersion curves of lithium niobate. The Sellmeier coefficients for the extraordinary n_e and ordinary refractive index n_o of 5% MgO-doped LN can be found in [127] and the refractive index n_e for congruent LN in [129]. The graph shows the calculated data according to the equations in the particular publication.

As LN crystal symmetry belongs to the $3m$ point group, the nonlinear tensor (eqn. 2.12) reduces to [101]:

$$\mathbf{d} = \begin{pmatrix} 0 & 0 & 0 & 0 & d_{31} & -d_{22} \\ -d_{22} & d_{22} & 0 & d_{31} & 0 & 0 \\ d_{31} & d_{31} & d_{33} & 0 & 0 & 0 \end{pmatrix} \quad (3.1)$$

which has only three non-vanishing components. The values of these coefficients are usually derived in SHG experiments and depend on the doping of LN as well as the wavelengths of the nonlinear process. Furthermore, even for the same experimental parameters the exact values differ for different publications. Some values are summarized in table 3.1. According to the so-called Miller's rule [130, 131] the nonlinear coefficient

Material	λ (nm)	d_{22}	d_{31}	d_{33}	Ref.
CLN	852		4.8	25.7	[131]
	1064		4.6	25.1	[131]
	1064	2.1	4.4	27.2	[132]
	1313		3.2	19.5	[131]
5%MgO:LN	852		4.9	28.4	[131]
	1064		4.4	25.0	[131]
	1313		3.4	20.3	[131]

Table 3.1: Nonlinear coefficients of congruent LN and doped LN at different wavelengths. The values of the tensor elements are given in pm/V.

for a certain process can be approximated by known values at other wavelengths:

$$d = d' \frac{(n^2(\lambda_1) - 1) \cdot (n^2(\lambda_2) - 1) \cdot (n^2(\lambda_3) - 1)}{(n^2(\lambda'_1) - 1) \cdot (n^2(\lambda'_2) - 1) \cdot (n^2(\lambda'_3) - 1)} \quad (3.2)$$

Assuming the second harmonic generation process (1064 nm + 1064 nm \rightarrow 532 nm) in [131] and with the help of eqn. 3.2 we can calculate the effective nonlinear index for the OPO process (1079 nm - 1926 nm \rightarrow 2453 nm) as $d_{\text{eff}} = 21.1$ pm/V. For the QFC process (854 nm - 2453 nm \rightarrow 1310 nm) in waveguides the results is $d_{\text{eff}} = 22.0$ pm/V.

As shown in the data of table 3.1, the coefficient d_{33} has the highest value and is only slightly influenced by crystal doping. Thus QPM usually takes advantage of this coefficient. Therefore all three involved fields have to be polarized along the crystal z-axis, i.e. perpendicular to the surface of a z-cut crystal with in-plane propagation direction.

3.2 Nonlinear Optical Devices

In this section the optical parametric oscillator (OPO) will be introduced. The gain mechanism in such an OPO is parametric amplification which hence will be described first.

3.2.1 Parametric Amplification

In this chapter we want to revisit the coupled wave equations (2.19, 2.20, 2.21) to find solutions for practical applications. First let's consider a DFG interaction in a crystal of length L . As boundary conditions we assume

$$A_1(0) = A_{10} \quad A_2(0) = A_{20} \quad A_3(0) = A_{30} \quad (3.3)$$

The field A_1 should be very strong ($|A_{10}| \gg |A_{20}|, |A_{30}|$) so it can be treated as constant during the whole interaction (this is called the no pump depletion approximation). In this case the equations 2.20 and 2.21 can be integrated with the following general solution [98, 124]:

$$A_2(z) = A_{20}e^{i\Delta kz/2} \left[\cosh gz - \frac{i\Delta k}{2g} \sinh gz \right] + \frac{i\kappa_2 A_{10}}{g} A_{30}^* e^{i\Delta kz/2} \sinh gz \quad (3.4)$$

$$A_3(z) = A_{30}e^{i\Delta kz/2} \left[\cosh gz - \frac{i\Delta k}{2g} \sinh gz \right] + \frac{i\kappa_3 A_{10}}{g} A_{20}^* e^{i\Delta kz/2} \sinh gz \quad (3.5)$$

with the coupling parameters $\kappa_j = \frac{2\omega_j d_{\text{eff}}}{n_j c}$. We here further introduce the following parameters:

$$\Gamma^2 = \kappa_2 \kappa_3 |A_{10}|^2 \quad \text{and} \quad g = \sqrt{\Gamma^2 - \left(\frac{\Delta k}{2}\right)^2} \quad (3.6)$$

g is called the gain coefficient. The above expressions describe the general case of difference frequency generation with a non-depleted pump field. Next we want to consider the case when, apart from the strong pump field, there is only one weak field present at the beginning of the nonlinear medium, i.e. we use the boundary conditions $A_1(0) = A_{10}, A_2(0) = A_{20}, A_3(0) = 0$. The equations then reduce to

$$A_2(z) = A_{20}e^{i\Delta kz/2} \left[\cosh gz - \frac{i\Delta k}{2g} \sinh gz \right] \quad (3.7)$$

$$A_3(z) = \frac{i\kappa_3 A_{10}}{g} A_{20}^* e^{i\Delta kz/2} \sinh gz \quad (3.8)$$

which is often used in the following form for the case of perfect phase matching ($\Delta k = 0, g = \Gamma$):

$$A_2(z) = A_{20} \cosh \Gamma z \quad (3.9)$$

$$A_3(z) = i \sqrt{\frac{n_2 \omega_3}{n_3 \omega_2}} \frac{A_{10}}{|A_{10}|} A_{20}^* \sinh \Gamma z \quad (3.10)$$

The amplitude A_2 grows monotonically in the crystal and the field thus experiences amplification retaining its initial phase evolution. Additionally, a field A_3 with the difference frequency $\omega_3 = \omega_1 - \omega_2$ is generated and is also amplified. This process is called Optical Parametric Amplification (OPA). Historically, the field A_1 is called pump, the amplified field A_2 is called signal and the newly generated field A_3 is called idler.

An important measure for the efficiency of the amplification is the gain that the signal field experiences in a single pass through the nonlinear medium. The gain is defined via the ratio of the powers before and after the OPA interaction. These powers

are proportional to the absolute square of the amplitudes (compare eqn. 2.23).

$$\begin{aligned} \frac{P_2(L)}{P_2(0)} &= \frac{|A_2(L)|^2}{|A_{20}|^2} =: 1 + G \\ &= 1 + \Gamma^2 L^2 \frac{\sinh^2(gL)}{(gL)^2} \end{aligned} \quad (3.11)$$

Here G defines the parametric gain. In the case of small gain ($g \ll \Delta k/2$) this simplifies to [100]:

$$G \approx (\Gamma L)^2 \operatorname{sinc}^2\left(\frac{\Delta k L}{2}\right) \xrightarrow{\Delta k=0} \Gamma^2 L^2 \quad (3.12)$$

Figure 3.3 shows a numerical calculation of the OPA process for the operation conditions of the OPO as presented in chapter 4.

In this section the process of difference frequency generation was analyzed with different boundary conditions. The signal field will experience an amplification and its power increases at the cost of the strong pump field. Additionally the idler field is amplified and can even be created when it has not been present at the beginning of

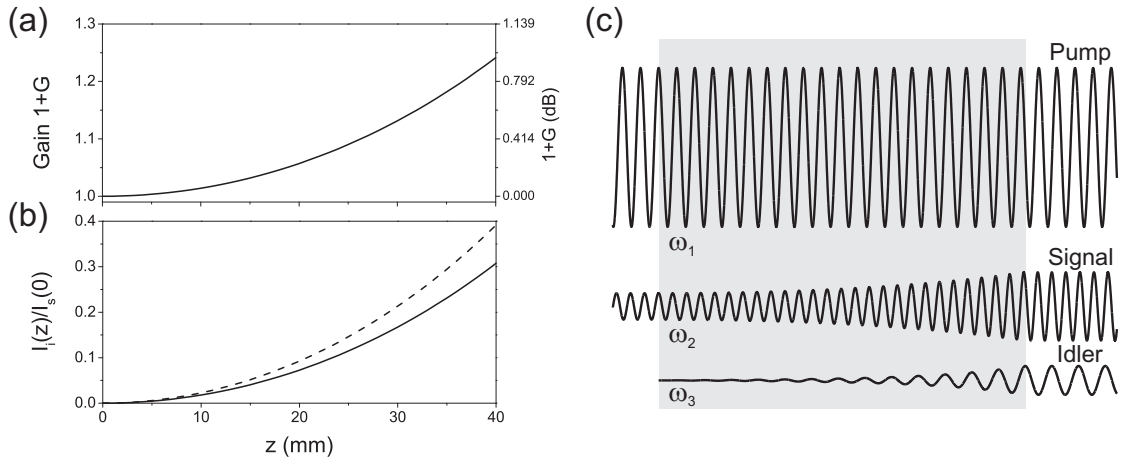


Figure 3.3: Optical parametric amplification: a) shows the gain of the signal field during the passage through the nonlinear medium. b) shows the output intensity of the idler field, normalized to the signal intensity at the beginning of the crystal. The dashed line shows the data of the solid curve multiplied with the wavelength ratio λ_i/λ_s to account for the lower photon energy of the idler field. For the calculations in a) and b) the following parameters were used: $\lambda_p = 1079$ nm, $\lambda_s = 1926$ nm, $\lambda_i = 2453$ nm, $n_{p,s,i}$ according to [127], $d_{\text{eff}} = 16$ pm/V, $I_{10} = 2.5\text{W}/3.02 \cdot 10^{-9}\text{m}^2$, $\Delta k = 0$. c) shows a sketch of the OPA process where the signal amplitude is amplified and the idler field is generated with the assumption of an undepleted pump field.

the process. Finally we take a look at the case where only the pump field is incident in the nonlinear medium ($|A_{10}| \gg A_{20} = A_{30} = 0$). However, according to quantum mechanical theory of light there is always a vacuum field present and here this field can feed the signal mode. Thus the vacuum mode will experience parametric amplification within the boundary conditions given by energy conservation and phase matching. In analogy to lasers this can be seen as spontaneous DFG. It is often called optical parametric fluorescence (OPF). Obviously the equations 3.4 and 3.5 vanish and a quantum mechanical treatment is necessary to describe this process. Actually, this is the same process we introduced as spontaneous parametric down conversion (SPDC, see sec. 2.2.3).

3.2.2 Optical Parametric Oscillation

In the previous section parametric amplification was introduced as a method to amplify an optical field and to generate a new field via the process of difference frequency generation. Calculating the gain for OPA under realistic conditions shows that it is rather low even for high pump powers (Fig. 3.3). One way to overcome this lack of efficiency is to feed back the signal wave resulting in several passages through the nonlinear medium. Therefore the nonlinear medium can be placed inside an optical resonator that feeds back the signal field. A device exploiting such an effect is known as Optical Parametric Oscillator (OPO). Optical parametric oscillation was first reported in 1965 [133] and the first continuous wave OPO was demonstrated only a few years later [134]. QPM was introduced to OPOs almost three decades later [135, 136].

In analogy to lasers, OPOs consist of three principal elements: a pump source that delivers the power for the generated light; a gain medium which in this case uses the nonlinear process of OPA for amplification; a feedback resonator that recycles the generated light fields for further amplification. The pump source is a laser field at frequency ω_1 . This can either be pulsed or continuous wave. The gain medium is a nonlinear crystal that supports difference frequency generation phase matched for the desired wavelength combinations. In this work emphasis is placed on quasi phase matched lithium niobate and continuous wave OPOs. A criterion to distinguish different kinds of OPOs is the cavity design. It can be singly resonant (SRO), i.e. only the signal (or idler) field can oscillate, doubly resonant (DRO) where both signal and idler oscillate, or even triply resonant (TRO) where additionally the pump field oscillates. There is also an intermediate design where signal (or idler) and the pump field are resonant, often described as pump enhanced singly resonant OPO (PESRO). The number of resonating fields influences output power and efficiency as discussed below. We use a PESRO design for the first setup of the OPO and then change the cavity to a SRO design for final operation in the experiments.

Oscillation Threshold

In analogy to lasers the oscillating field experiences gain on every round trip in the resonator. However, it also suffers losses due to absorption in the nonlinear material and transmission through the cavity mirrors. A net amplification thus requires the gain exceeding the losses. As shown in equations 3.11 and 3.6 the gain of the OPA process depends on the intensity of the pump field. Similar to a laser there is a pump power threshold where the oscillation in an OPO starts and output power is generated effectively. To calculate the minimum pump power threshold we assume perfect phase matching ($\Delta k = 0$). The fractional amplitude loss per round trip can be defined as

$$l_j = 1 - R_j e^{-\alpha_j L} \quad (3.13)$$

Here j denotes all resonating fields, R_j is the corresponding total mirror reflectivity and α_j the total absorption loss. To calculate the steady state threshold condition in general, we demand the field amplitudes to reproduce themselves after each round trip. Adding these loss coefficients to the OPA equations 3.7 and 3.8 leads to the following threshold condition [98]:

$$\cosh \Gamma L = 1 + \frac{l_s l_i}{2 - l_s - l_i} \quad (3.14)$$

For low gain the approximation $\cosh(\Gamma L) \approx 1 + \frac{1}{2}\Gamma^2 L^2$ can be used. It can be seen that a DRO has a significantly lower threshold than a SRO due to the additional resonance of the second field. With the low-gain approximation, the threshold condition for a singly resonant OPO is

$$(\Gamma L)^2 = 2l_s = 2(1 - R_s e^{-\alpha_s L}) \quad (3.15)$$

Without loss of generality we assume the signal field to be resonant (the equations also hold for an idler resonant SRO by exchanging the indices). This condition results in a pump power at threshold $P_{p,\text{thr}}$ for plane waves of [100]:

$$P_{p,\text{thr}} = A \frac{\epsilon_0 n_s^2 n_p c \lambda_p^2}{\pi^2 d_{\text{eff}}^2 L^2 (1 - \delta^2)} (1 - R_s e^{-\alpha_s L}) \quad (3.16)$$

where A is the beam area and δ is the degeneracy parameter defined by

$$\omega_s = \frac{1}{2}\omega_p (1 + \delta) \quad \omega_i = \frac{1}{2}\omega_p (1 - \delta) \quad (3.17)$$

Usually the pump and signal field are focused in the nonlinear medium to increase intensity and overlap. To account for these tightly focused Gaussian beams the equation for threshold pump power has to be modified [100]:

$$P_{p,\text{thr}} = \frac{\epsilon_0 n_s^2 c \lambda_p^3}{\pi^2 d_{\text{eff}}^2 L (1 - \delta^2) \bar{h}_m(B, \xi)} (1 - R_s e^{-\alpha_s L}) \quad (3.18)$$

Here the function $\bar{h}_m(B, \xi)$ is the gain reduction factor [137] which will be discussed later. Obviously this parameter has to be maximized to reduce the threshold power.

The starting process of the OPO is induced by optical parametric fluorescence. When the pump field is switched on, no other fields are present to allow parametric amplification. However, photons are generated by SPDC. Some of these photons will be generated in a cavity mode and can start a first round trip. Then the basic conditions for OPA are fulfilled and this weak signal field will be amplified until the threshold condition is reached.

OPO Design Rules

As mentioned earlier, the optical fields are usually focused into the nonlinear medium and thus the treatment as infinite plane waves has to be replaced by Gaussian beams. A similar approach was introduced to describe the propagation of optical fields in laser resonators [138]. In analogy, a paraxial wave equation can be derived from 2.15 for each frequency component [98]. The solutions of these equations describe beams with a Gaussian transverse profile propagating in z -direction. The waist size $w(z)$ is then given by:

$$w(z) = w_0 \sqrt{1 + \left(\frac{z}{z_R}\right)^2} \quad (3.19)$$

$$z_R = \frac{\pi w_0^2}{\lambda} = b/2 \quad (3.20)$$

where w_0 is the beam waist, i.e. $1/e^2$ -radius of the intensity distribution at the focal point (here at $z = 0$). The Rayleigh length z_R equals the distance from the focus where the area of the beam has doubled. The confocal parameter b is twice the Rayleigh length. The shape of a Gaussian beam is plotted exemplary in Fig. 3.4a.

A function $\bar{h}(B, \xi)$ can be introduced [137] including the parameters that can be optimized in the nonlinear interaction, namely the birefringence (described by B) and the focusing (described by ξ). The parameter $\xi = L/b$ connects the confocal parameter of the Gaussian beam with the crystal length L . The function $\bar{h}(B, \xi)$ can be calculated numerically and is shown in Fig. 3.4b for the case of vanishing birefringence ($B = 0$). It has a maximum $\bar{h}(0, \xi) \approx 1$ for $\xi = 2.84$ (Boyd-Kleinman criterion). Thus for a given crystal length there exists an optimal focusing that maximizes conversion efficiency.

From this fact one can deduce a design rule for an OPO. For a given crystal length L first calculate the confocal parameter $b = L/\xi$ ($b = 14.1$ mm for $L = 40$ mm). Then the beam waist can be calculated for the pump wavelength ($w_0 = 49.2$ μm for $\lambda_p = 1079$ nm). In a next step a stable resonator has to be designed [138] where the beam waist for the signal field in the nonlinear medium fits best to the calculated waist for the pump field. This ensures a maximum in overlap and efficiency [98]. Finally

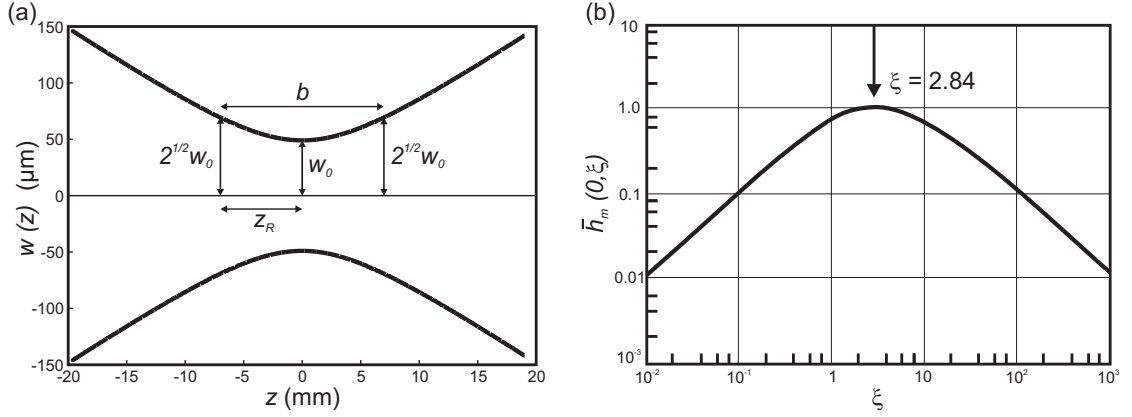


Figure 3.4: a) Gaussian beam calculated with parameters: $w_0 = 49 \mu\text{m}$, $\lambda = 1079 \text{ nm}$.
 b) Function of the gain reduction factor assuming vanishing birefringence, according to [137].

the coupling of the pump field into the resonator has to be chosen to fit the calculated beam waist accordingly. As shown in Fig. 3.4b a small deviation of the actual focusing parameter from the optimum does not decrease the efficiency much as the function $\bar{h}(0, \xi)$ only decreases slowly. Thus in practice a slightly smaller waist can be chosen to compensate thermal lensing effects at high pump powers [139].

Output Power

Under steady-state conditions above oscillation threshold the resonant signal field has approximately constant intensity over the cavity length. The idler field is generated inside the nonlinear medium and its power thus increases within the crystal. Accordingly we have to take into account the depletion of the pump field due to the energy transfer from pump to idler. This effect can be quantified by the value of the power conversion efficiency $\tilde{\eta}$, which gives the ratio of pump power converted to idler power. Alternatively, it can be measured in the value of the photon conversion efficiency η which gives the probability of a pump photon being converted to an idler photon:

$$\tilde{\eta} = \frac{P_i}{P_p - P_{thr}} \quad (3.21)$$

$$\eta = \frac{\lambda_i}{\lambda_p} \frac{P_i}{P_p - P_{thr}} \quad (3.22)$$

Furthermore, we introduce the normalized pump power $\tilde{P}_p = P_p/P_{thr}$ which is the number of times the pump power exceeds threshold. The conversion efficiency can also

be calculated theoretically under the assumption of Gaussian beams [100]:

$$\eta = 1 - \left[\frac{1}{\tilde{P}_p} + \int_0^{\ln \tilde{P}_p} e^{-x} \cos^2 \Psi(x) dx \right] \quad (3.23)$$

Here the function Ψ can only be calculated numerically:

$$\frac{\sin^2 \Psi(x)}{\Psi^2(x)} = \frac{e^x}{\tilde{P}_p} \quad (3.24)$$

With the efficiency the normalized idler output power \tilde{P}_i can readily be obtained by:

$$\tilde{P}_i = \eta \tilde{P}_p \quad P_i = \eta P_p \quad (3.25)$$

The efficiency and output power is plotted in Fig. 3.5 as a function of the normalized pump power for plane wave and Gaussian beam approximation. In both cases the

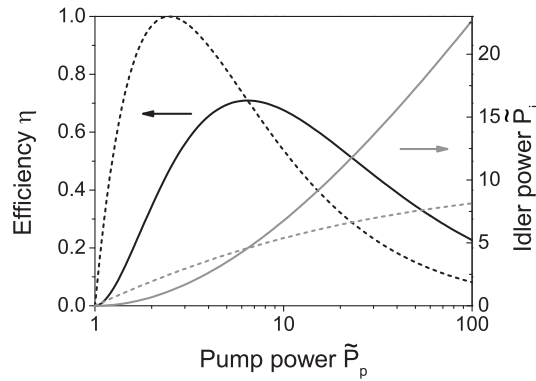


Figure 3.5: OPO conversion efficiency (black curves) and idler power (gray curves) calculated for Gaussian beam approximation (solid lines) and plane wave approximation (dashed lines), according to [100].

efficiency shows a peak value. The decrease of efficiency for high powers is due to pump back-conversion by sum frequency generation of signal and idler. However, the idler output power increases monotonically with the pump power. For plane waves 100 % conversion can be achieved whereas this is not possible for Gaussian beams due to the weaker intensity in the wings of the distribution [100].

Wavelength Tuning

Restricted by the law of energy conservation the process of difference frequency generation allows to generate any wavelength that is longer than the pump wavelength.

However, to achieve reasonable gain the phase matching condition has to be fulfilled. In the case of an OPO, material absorption and finite bandwidth of mirror reflectivities further influence the tuning. However, this is a major difference to a laser system where the tuning bandwidth is limited by the availability of electronic transitions in the active material.

Hence the output frequency of an OPO can be controlled through the phase matching condition. For QPM-based OPOs coarse wavelength tuning is achieved with the choice of the poling period. Usually an OPO crystal contains several channels with different poling period lengths. By translating the crystal in lateral direction through the cavity beam path a particular channel and QPM period can be chosen. Fine tuning is then achieved by changing the temperature of the nonlinear medium due to the temperature dependence of the refractive index. Due to gain competition effects the OPO will oscillate on the mode with the highest overall gain which is usually found at $\Delta k = 0$. By inserting the operation parameters in this condition

$$\Delta k = \frac{n_p(\omega_p, T) \omega_p}{c} - \frac{n_s(\omega_s, T) \omega_s}{c} - \frac{n_i(\omega_i, T) \omega_i}{c} - \frac{2\pi}{\Lambda} := 0 \quad (3.26)$$

and with the knowledge of temperature and wavelength dependence of the refractive index described by Sellmeier equations, the OPO frequencies (ω_s, ω_i) can be calculated, as shown in Fig. 3.6. By changing the phase matching conditions a wavelength tuning range of several 100 nm can be covered. Another way to externally control the phase

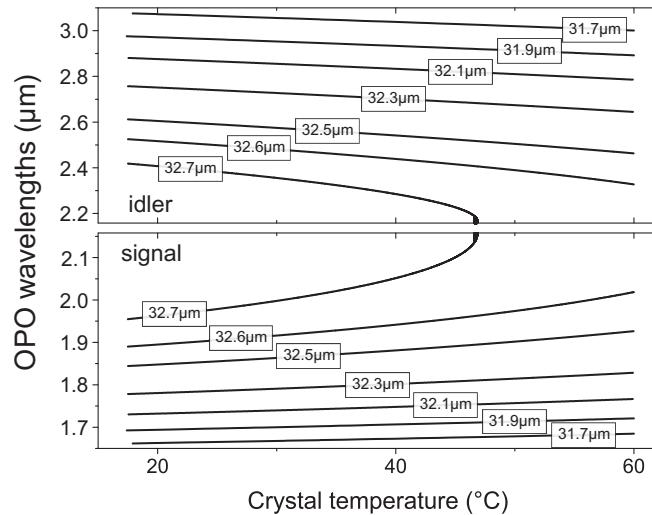


Figure 3.6: OPO wavelength tuning via crystal temperature for different poling periods. The curves were calculated with the help of Sellmeier equations [127] of MgO:LN for a pump wavelength of 1078.9 nm.

matching condition is to tune the pump frequency ω_p . This allows on the one hand a wide signal/idler tuning range in the case of a broad pump laser wavelength tuning range. On the other hand it offers a way of very fast tuning as the OPO output frequency directly follows the variation of the pump frequency.

As mentioned in the beginning there is not only the parametric gain that determines the operation wavelength but the OPO resonator has also to be taken into consideration. This results in effects on a smaller frequency scale and is thus exploited for fine tuning the OPO wavelengths. Actually, the OPO can only oscillate at a frequency that is simultaneously a longitudinal mode of the cavity. In detail it will oscillate on that particular mode which has the lowest threshold [140]. For fixed temperature, poling period and pump wavelength the parametric gain is proportional to $\text{sinc}^2(\Delta k L/2)$ which has a width in the order of 1 THz for the OPO wavelength combinations used in the frequency conversion experiments. Thus the OPO tends to oscillate close to this maximum. To tune the OPO within this gain curve an etalon can be inserted into the OPO resonator. The transmission function of the etalon periodically modulates the losses in the OPO and thus its oscillation threshold. By multiplying the transmission and gain functions, an effective gain curve can be inferred as shown in Fig. 3.7a. Tilting the etalon reduces its free spectral range and thus shifts the transmission peaks. In detail it also changes the length of the OPO cavity and shifts its resonances, too. Fig. 3.7a shows a calculation where a tilt by 20° shifts the effective gain maximum in the order of 100 GHz. Actually, fine tuning up to 70 GHz with an etalon could be demonstrated [141].

Even finer tuning is possible via the variation of the OPO cavity length, e.g. by a piezo transducer attached to one of the mirrors, shifting the cavity modes relative to the parametric gain curve. The OPO further oscillates in the mode with the highest gain, however the frequency of this mode is tuned. For fixed pump frequency signal and idler are thus shifted to opposite directions. An example for the cavity mode structure compared to the etalon and the parametric gain is shown in Fig. 3.7b. The tuning range is here limited by the arrival of an adjacent cavity mode at the gain maximum. The oscillation may abruptly change its frequency to the mode with higher gain. This effect is called mode-hop. Fine-tuning via cavity length allows high resolution setting of frequency and can be used for spectroscopy applications and frequency stabilization [141–143]. Finally, an intracavity etalon is not only used to tune the OPO but it also increases its stability. Due to the additional modulation of the mode structure, a mode-hop to a neighboring longitudinal mode is unlikely because of the decreased effective gain there. Thus, the main reason to insert an etalon into the OPO cavity in our case is to prevent mode-hops and stabilize the output frequency.

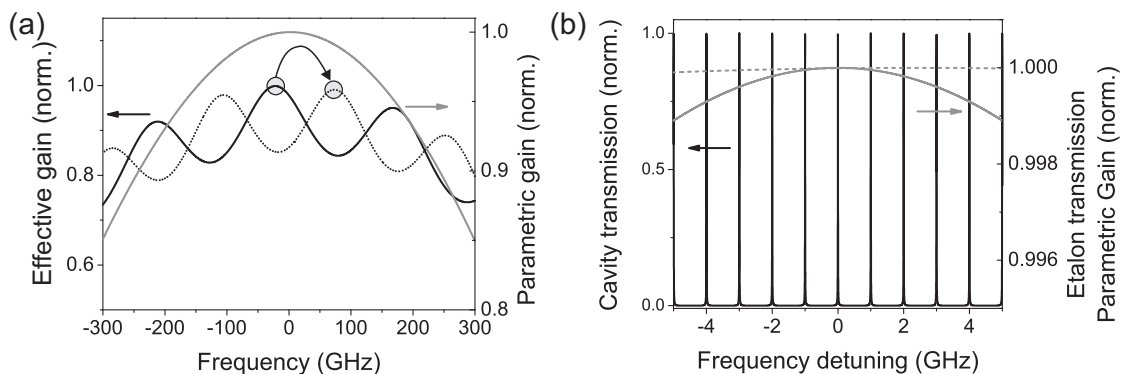


Figure 3.7: a) shows the normalized parametric gain (gray curve) and the product of etalon transmission and gain (black curves); shown are two tilt angles of the etalon (0° solid line; 20° dotted line). This results in a tuning of the OPO wavelength by about 100 GHz. b) shows the longitudinal modes of the OPO cavity (black) and the parametric gain and etalon transmission (gray). The gain is approximately constant and even the etalon transmission is almost flat. Parameters for calculation: $\lambda_p = 1078.9$ nm, $\lambda_s = 1917$ nm, $\lambda_i = 2468$ nm, $\Lambda = 32.6$ μm , $T = 30.3^\circ\text{C}$, thickness etalon 500 μm , $\text{FSR}_{cav} = 1$ GHz, Sellmeier equations [127].

3.3 Waveguides

Waveguides (WG) are devices with the capability to guide light by confining its electromagnetic fields. Usually light propagation is limited to a small cross-section and one can take advantage of certain spatial mode profiles and the high intensity. Waveguides are employed in passive devices to guide light (e.g. fibers) or in active elements (e.g. modulators, couplers). In the next section the basic principles of waveguides will be introduced. Later, nonlinear processes will be included in order to discuss integrated frequency converters.

Dielectric, Rectangular Waveguides

One basic approach to introduce wave guiding is to start with geometric optics. First we consider an interface between two dielectric media with different indices of refraction. For a light beam coming from the medium with higher refractive index there exists a critical angle of incidence where the beam will be totally reflected. Its value depends on the ratio of the refractive indices of the media. Sandwiching a layer of high refractive index material between two layers of lower index allows waveguiding by periodically reflecting the beam at the opposing interfaces around the core layer. This geometry is known as the dielectric slab waveguide. On every reflection the beam experiences a phase shift. In the steady state case, constructive interference between all beams

traveling the same direction and angle is required. Thus only certain spatial modes can be effectively guided in such a structure [144]. A more fundamental approach to describe waveguiding is to solve Maxwell's equations with the boundary conditions given by the device geometry. For the basic case of dielectric slab waveguides this leads to the same results as the geometric optics approach [145] in regard of mode number or cut-off frequency. However, the geometric optics approach cannot provide the field distributions which is necessary to understand the nonlinear coupling of the modes.

In the following a solution for the electromagnetic field distribution in rectangular dielectric waveguides will be derived. A full description of this solution was given by Marcuse [146]. The rectangular geometry is a very good approximation for the waveguides used throughout this thesis. The description of a strip of dielectric material surrounded by dielectric media with other refractive indices shows no analytical solution in general. However, there exist solutions for an approximate layout, shown in Fig. 3.8. Here we have split the geometry into five regions: The waveguide core with refractive

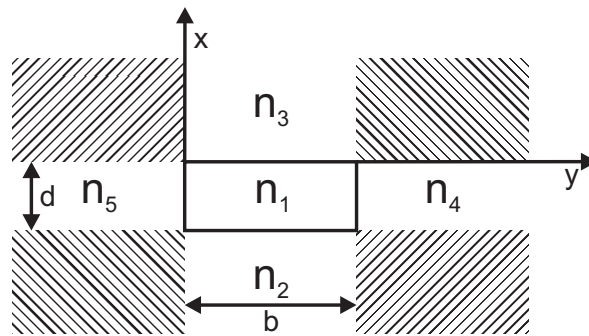


Figure 3.8: Layout for the rectangular dielectric waveguide geometry, according to Marcuse [146].

index n_1 , the substrate n_2 and surrounding layers $n_3 \dots n_5$. The shaded regions are neglected as they only contain an insignificant part of the intensity. The solution of the rectangular geometry consists of the independent solutions for the slab waveguide in the two perpendicular dimensions. This approximation is valid for modes far away from cut-off frequency as they experience a high confinement in the core region. The cut-off frequency is the lowest frequency for which propagating waveguide modes can exist. We further assume to deal with nonmagnetic materials and neglect free charges and material absorption. This simplifies Maxwell's equations. Without loss of generality we consider monochromatic fields propagating in z-direction (i.e. perpendicular to the

plain of drawing in Fig. 3.8). So we can drop the oscillatory terms:

$$e^{i\omega t} \cdot e^{-i\beta z} \quad (3.27)$$

Here β is the propagation constant which can be seen as the effective wavenumber for the propagation of the optical field in a certain mode of the waveguide. Two kinds of solutions can be distinguished: E_{pq}^x -modes are polarized predominately in x-direction, whereas E_{pq}^y -modes are polarized predominately in the y-direction ($p, q = 0, 1, 2, \dots$ are the order of the mode in x- and y-direction) [146]. These are comparable to quasi-TM and quasi-TE modes, known from fiber optics [147]. Pure TM or TE modes have vanishing longitudinal field components, i.e. TM modes have $E_x, H_y, E_z \neq 0$ while for TE modes $H_x, E_y, H_z \neq 0$. With all these assumptions Maxwell's equations for the \mathbf{E} and \mathbf{H} field can be written as [146]:

$$E_x = \frac{-i}{K_j^2} \left[\beta \frac{\partial E_z}{\partial x} + \omega \mu_0 \frac{\partial H_z}{\partial y} \right] \quad (3.28)$$

$$E_y = \frac{-i}{K_j^2} \left[\beta \frac{\partial E_z}{\partial y} - \omega \mu_0 \frac{\partial H_z}{\partial x} \right] \quad (3.29)$$

$$H_x = \frac{-i}{K_j^2} \left[\beta \frac{\partial H_z}{\partial x} - \omega n_j^2 \epsilon_0 \frac{\partial E_z}{\partial y} \right] \quad (3.30)$$

$$H_y = \frac{-i}{K_j^2} \left[\beta \frac{\partial H_z}{\partial y} + \omega n_j^2 \epsilon_0 \frac{\partial E_z}{\partial x} \right] \quad (3.31)$$

with the parameter $K_j = \sqrt{n_j^2 k^2 - \beta^2}$. The index j defines the region $1 \dots 5$ of the geometry. The solution is then calculated piecewise for each region with continuity required at the boundaries between neighboring regions. Then the general solution for the waveguide core (region 1) can be found [146]:

$$E_x = \frac{iA}{\kappa_x \beta} (n_1^2 k^2 - \kappa_x^2) \sin(\kappa_x(x + \xi)) \cos(\kappa_y(y + \eta)) \quad (3.32)$$

$$H_x = 0 \quad (3.33)$$

$$E_y = \frac{-iA\kappa_y}{\beta} \cos(\kappa_x(x + \xi)) \sin(\kappa_y(y + \eta)) \quad (3.34)$$

$$H_y = iA \sqrt{\frac{\epsilon_0}{\mu_0}} n_1^2 \frac{k}{\kappa_x} \sin(\kappa_x(x + \xi)) \cos(\kappa_y(y + \eta)) \quad (3.35)$$

$$E_z = A \cos(\kappa_x(x + \xi)) \cos(\kappa_y(y + \eta)) \quad (3.36)$$

$$H_z = -A \sqrt{\frac{\epsilon_0}{\mu_0}} n_1^2 \frac{\kappa_y k}{\kappa_x \beta} \sin(\kappa_x(x + \xi)) \sin(\kappa_y(y + \eta)) \quad (3.37)$$

Here A is the amplitude, $k^2 = \omega^2 \epsilon_0 \mu_0$ is the vacuum wavenumber and $K_1^2 = n_1^2 k^2 - \beta^2 = \kappa_x^2 + \kappa_y^2$; ξ and η are phase parameters to fulfill the continuity condition at

the boundaries. Similar sets of equations can be derived for the other regions of the geometry as discussed in [146]. For guided modes the field evanescently vanishes outside the core region. Furthermore the continuity conditions lead to the following eigenvalue equations:

$$\tan(\kappa_x d) = \frac{n_1^2 \kappa_x (n_3^2 \gamma_2 + n_2^2 \gamma_3)}{n_3^2 n_2^2 \kappa_x^2 - n_1^4 \gamma_2 \gamma_3} \quad (3.38)$$

$$\tan(\kappa_y b) = \frac{\kappa_y (\gamma_4 + \gamma_5)}{\kappa_y^2 - \gamma_4 \gamma_5} \quad (3.39)$$

which can be used to derive κ_x and κ_y as they only depend on the geometry, refractive indices and the γ_j parameters:

$$\gamma_2 = \sqrt{(n_1^2 - n_2^2) k^2 - \kappa_x^2} \quad (3.40)$$

$$\gamma_3 = \sqrt{(n_1^2 - n_3^2) k^2 - \kappa_x^2} \quad (3.41)$$

$$\gamma_4 = \sqrt{(n_1^2 - n_4^2) k^2 - \kappa_y^2} \quad (3.42)$$

$$\gamma_5 = \sqrt{(n_1^2 - n_5^2) k^2 - \kappa_y^2} \quad (3.43)$$

There can be several solutions for the above equations. Each of these solutions represents a guided mode of the WG. After the κ_x and κ_y are known, the phase parameters can be calculated with the relations:

$$\tan(\kappa_x \xi) = -\frac{n_3^2 \kappa_x}{n_1^2 \gamma_3} \quad (3.44)$$

$$\tan(\kappa_y \eta) = -\frac{\gamma_5}{\kappa_y} \quad (3.45)$$

and finally one obtains the propagation constant β and the effective refractive index n_{eff} of the mode:

$$\beta = \sqrt{n_1^2 k^2 - (\kappa_x^2 + \kappa_y^2)} \quad (3.46)$$

$$n_{\text{eff}} = \frac{\beta}{k} \quad (3.47)$$

To calculate the power transmitted through the waveguide, the normal component of the energy flux density S_z has to be integrated over the xy-plane:

$$P = \iint \mathbf{S} \cdot \hat{\mathbf{z}} \, dx dy \quad (3.48)$$

with the time-averaged Poynting vector $\mathbf{S} = \frac{1}{2} \text{Re}(\mathbf{E} \times \mathbf{H}^*)$.

With the help of mathematical software (Matlab) numerical values can now be calculated for the equations derived above. The waveguide chip (*WS-0854-000-A-C-C-S008*, SN. 3071124) used for the QFC experiments in this thesis was fabricated by NTT electronics. According to the manufacturer [128], the waveguide core consists of Zn-doped lithium niobate that is bonded onto undoped lithium tantalate (LT) serving as substrate. At all other sides the core is surrounded by air. The core has a thickness of $9\ \mu\text{m}$, a width of $15 - 16\ \mu\text{m}$ and a length of $40\ \text{mm}$. For the refractive index the Sellmeier equations of Jundt [129] fit best for the core, whereas for the substrate equations from Dolev [148] are used. As these devices will be used for frequency conversion experiments, emphasis is placed on the three interacting wavelength of $854\ \text{nm}$, $1310\ \text{nm}$ and the pump field at $2453\ \text{nm}$. The polarization for the nonlinear interaction is restricted to the x-direction, while wave guiding is possible for all polarizations. The results are summarized in figure 3.9. According to the calculations, the waveguide supports guided modes with transverse mode numbers $p = 0, 1$ and $q = 0, \dots, 16$ for the pump wavelength. For the other wavelengths even higher order modes are possible. With increasing mode number the part of the intensity distribution leaking out of the core

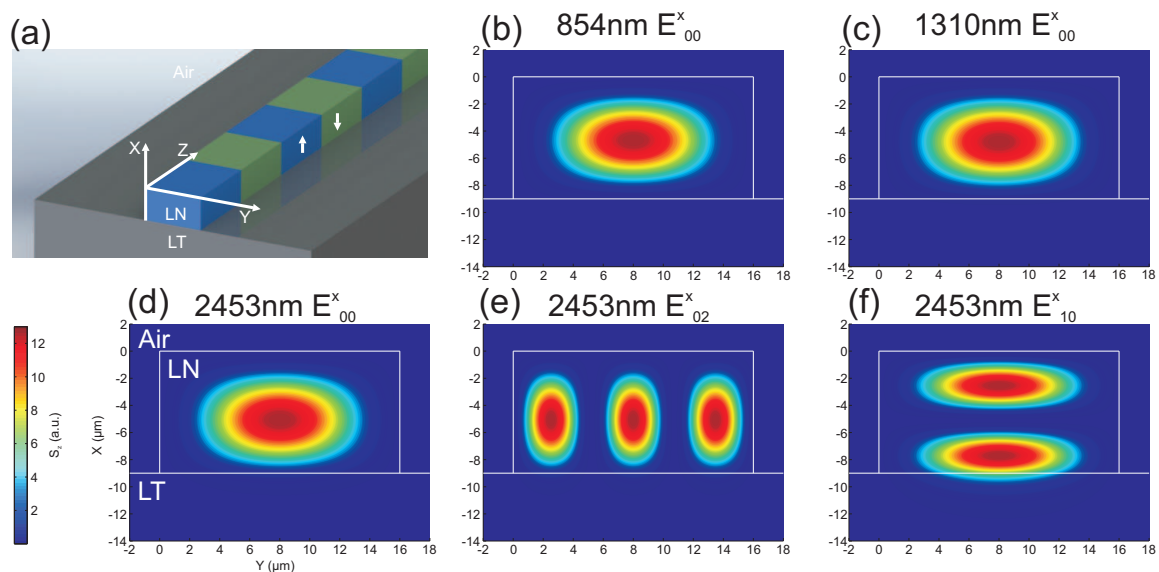


Figure 3.9: a) shows a schematic drawing of the waveguide outline in the coordinate frame used in the calculations. b)-f) show different spatial modes for the waveguide with polarization along the x-direction. In every graph the time-averaged z-component of the Poynting vector is plotted. b)-d) show the fundamental 00-modes for wavelengths of $854\ \text{nm}$, $1310\ \text{nm}$ and $2453\ \text{nm}$, respectively. e) and f) show higher order modes for a wavelength of $2453\ \text{nm}$. The color scale is the same for all plots and shows arbitrary units. Details about the calculations can be found in the text.

region increases. For the 00-mode of the pump field 98.5 % of the intensity is inside the core region. This value is even higher for the lower wavelengths. Nearly all the rest of the power leaks into the substrate (region 2). This is due to the higher contrast of refractive index between the core and the air regions. As will be shown in the next section a high overlap of the modes of the interacting fields will help to increase conversion efficiency. This overlap is illustrated in Fig. 3.10. This figure shows a cut through

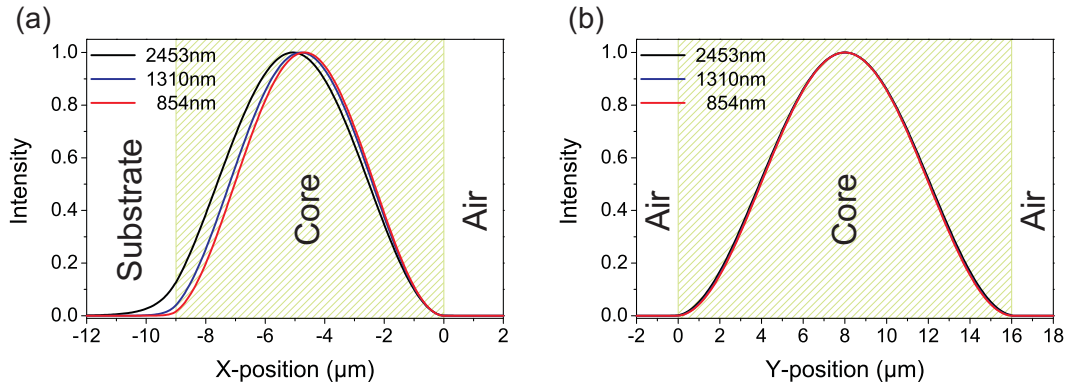


Figure 3.10: Cut through the intensity distribution parallel to the x-axis at $y = -d/2$ (a) and y-axis at $x = b/2$ (b). In (b) there is a high degree of overlap for all wavelengths. The modes are shifted towards the substrate depending on wavelength (a). The shaded area shows the dimensions of the core region.

the intensity distribution of the fundamental 00-mode at the center of the waveguide for the three different wavelengths. There is a high overlap in y-direction due to the high refractive index contrast between the core and the surrounding air layers. In x-direction an asymmetry is visible and the center of mass of the intensity distribution is shifted towards the substrate. This shift and the width of the distribution increase with wavelength.

3.3.1 Waveguide Nonlinear Optics

The fundamentals of nonlinear optics were already presented in section 2.1 and the process of difference frequency generation was also discussed in section 3.2 for bulk nonlinear media. These equations have to be slightly modified to account for additional effects in integrated optics. Finally this will result in the coupled mode equations replacing the coupled amplitude equations in bulk nonlinear optics. Particularly, plane wave or Gaussian beam approximations can be used for bulk optics whereas the intensity distribution in the waveguide modes has now to be taken into account. The

derivation here follows the book of Suhara [124]. First the expression for the electric field can be split into several parts, depending on the coordinate components:

$$\mathbf{E}_m(\mathbf{r}, t) = A_m(z) \mathcal{E}_m(x, y) e^{i\omega_m t} e^{-i\beta_m z} + c.c \quad (m = 1, 2, 3) \quad (3.49)$$

Again, we can drop the temporal oscillation. The index m represents the different fields: pump ($m = 1$), signal ($m = 2$) and idler ($m = 3$). The field distribution of the modes is included in the vector $\mathcal{E}_m(x, y)$. It is normalized to unity intensity. By introducing normalization constants C_m it can thus be related to the electric fields calculated in the previous section via

$$\mathcal{E}_m(x, y) = C_m \mathbf{E}_m(x, y) \quad (3.50)$$

$$C_m = \left[\frac{1}{2} \iint \text{Re}(\mathbf{E}_m \times \mathbf{H}_m^*) \cdot \hat{\mathbf{z}} \, dx dy \right]^{-\frac{1}{2}} \quad (3.51)$$

Similar to the equations for bulk interaction (2.19, 2.20, 2.21) we can now introduce the coupled mode equations for waveguide devices [124]:

$$\frac{\partial A_1}{\partial z} = -\alpha_1 A_1 - i\kappa_1 A_2 A_3 e^{-i\Delta\beta z} \quad (3.52)$$

$$\frac{\partial A_2}{\partial z} = -\alpha_2 A_2 - i\kappa_2 A_3^* A_1 e^{+i\Delta\beta z} \quad (3.53)$$

$$\frac{\partial A_3}{\partial z} = -\alpha_3 A_3 - i\kappa_3 A_1 A_2^* e^{+i\Delta\beta z} \quad (3.54)$$

In waveguides the optical fields experience loss not only due to material absorption but also due to scattering at interface roughness. To account for this, additional loss terms ($-\alpha_m A_m$) were introduced. Furthermore the wavevector mismatch Δk was replaced by the mismatch of propagation constants $\Delta\beta$ to consider the dispersion effects of the waveguide. The third modification concerns the modal overlap by introducing the coupling coefficients κ_m :

$$\kappa_1 = \frac{\omega_1 \epsilon_0}{2} \iint \mathcal{E}_1^*(x, y) \mathbf{d}_Q \mathcal{E}_3(x, y) \mathcal{E}_2^*(x, y) \, dx dy \quad (3.55)$$

$$\kappa_2 = \frac{\omega_2 \epsilon_0}{2} \iint \mathcal{E}_2^*(x, y) \mathbf{d}_Q \mathcal{E}_3(x, y) \mathcal{E}_1^*(x, y) \, dx dy \quad (3.56)$$

$$\kappa_3 = \frac{\omega_3 \epsilon_0}{2} \iint \mathcal{E}_3^*(x, y) \mathbf{d}_Q \mathcal{E}_2(x, y) \mathcal{E}_1(x, y) \, dx dy \quad (3.57)$$

These include the spatial distribution of all electric fields involved in the nonlinear interaction as well as the tensor of the material nonlinearity \mathbf{d}_Q . With the help of the effective nonlinear coefficient d_{eff} this material property is the same for all modes and can be written outside the integral. In this case the coupling coefficients only scale with mode frequency:

$$\kappa_1/\omega_1 = \kappa_2/\omega_2 = \kappa_3^*/\omega_3 := \kappa \quad (3.58)$$

Including the modes of the dielectric waveguide into this formalism the coupling coefficients can be calculated with the help of the normalization factors:

$$\begin{aligned}
 \kappa_1 &= \frac{\omega_1 \epsilon_0 d_Q}{2} \iint \mathcal{E}_{1x}^*(x, y) \mathcal{E}_{3x}(x, y) \mathcal{E}_{2x}^*(x, y) \, dx dy \\
 &= \frac{\omega_1 \epsilon_0 d_Q}{2} \underbrace{C_1 C_2 C_3 \iint E_{1x}^*(x, y) E_{3x}(x, y) E_{2x}^*(x, y) \, dx dy}_{:=J_1} \quad (3.59)
 \end{aligned}$$

and analog for κ_2 and κ_3 .

In the following, the coupled mode equations (3.52, 3.53 and 3.54) will be numerically solved. The waveguide geometry is the same as used before (16 $\mu\text{m} \times 9 \mu\text{m}$; LN core, LT substrate). The wavelengths are $\lambda_1 = 2453 \text{ nm}$, $\lambda_2 = 1310 \text{ nm}$ and $\lambda_3 = 854 \text{ nm}$ corresponding to the difference frequency conversion process of the calcium ion emission to the telecom O-band. In a first step the coupling coefficient can be calculated according to equation 3.59. If all fields are guided in the fundamental 00-mode, the coupling integral will have the numerical value of $|J_1| = 7.524 \cdot 10^8 \text{ 1/m(V/A)}^{3/2}$. As starting values we assume that no idler field is present ($P_{1310}(0) = 0$) and we have a signal power of $P_{854}(0) = 1 \text{ nW}$. The results are presented in Fig. 3.11 for different parameter conditions. Within the waveguide the signal field (λ_3) is depleted in order to create the idler field (λ_2). When the signal field is completely converted, the process reverses its direction and the idler field is converted back to signal. This behavior repeats and the power oscillates between the signal and idler mode. The point of maximum difference frequency conversion shifts with the available pump power as illustrated in Fig. 3.11a. Thus a low pump power can be compensated with a large interaction length. However, the maximum efficiency is limited by losses. Assuming a fixed waveguide length and pump power, increasing loss will reduce the achievable maximum conversion efficiency (Fig. 3.11b). The power where maximum conversion efficiency is reached only slightly changes. Thus a long waveguide device naturally limits the efficiency due to unavoidable losses. The devices used in this thesis have a fixed length of 40 mm and transmission losses below 0.2 dB/cm for all wavelengths in use (according to the manufacturer). The efficiency is determined by the nonlinear coupling of the involved fields. In accordance with equation 3.59 there are two values to be taken into account. One is the overlap integral which involves the geometry and field distribution. It reaches its maximum value if all fields are guided in their 00-mode. The absolute value of the overlap integral is drastically reduced in the case when modes with even and odd mode-numbers are mixed. The electric fields corresponding to these modes have different symmetries with respect to the waveguide geometry and thus parts can cancel by integrating the field distributions. A comparison for different values of the overlap integral can be found in Fig. 3.11d. The other parameter is the nonlinear coefficient d_{eff} . It depends on material and wavelength but in practice it can

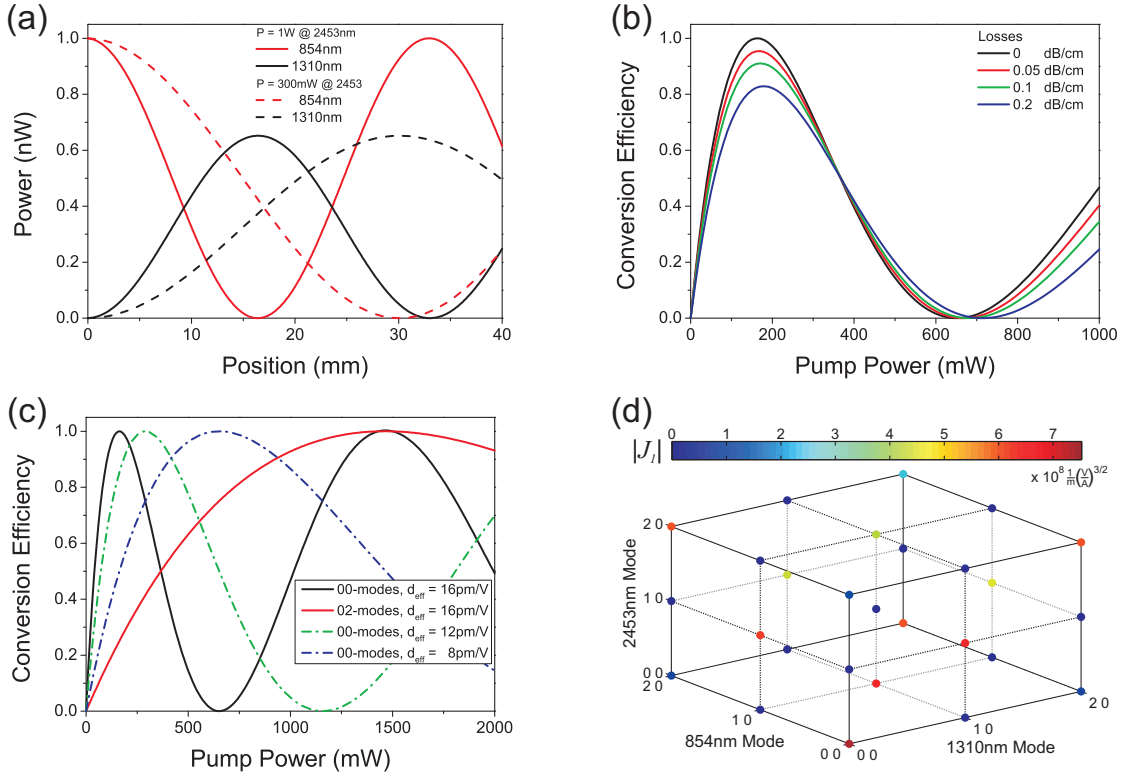


Figure 3.11: Numerical solutions of the coupled mode equations. a) Shows the signal (854 nm) and idler (1310 nm) power variation along the waveguide for different pump powers (1 W, solid lines; 0.3 W, dashed lines). Pump wavelength 2453 nm, losses $\alpha_i = 0$, $d_{\text{eff}} = 14$ pm/V, all 00-modes. b) shows the effect of losses on the conversion efficiency as a function of pump power. $d_{\text{eff}} = 14$ pm/V, 00-modes, waveguide length 4 cm. c) shows the effect of modal coupling. The coupling coefficient is varied due to the interaction of different modes (solid lines) and the nonlinear coefficient is varied (dash-dotted lines). For the 02-modes the overlap integral is $|J_1| = 2.511 \cdot 10^8$ 1/m(V/A)^{3/2}. $\alpha_i = 0$, length 4 cm. d) illustrates the overlap integral for different mode combinations.

also be reduced due to imperfect periodic poling. Both d_{eff} and κ appear as a product term in the coupled mode equations and hence their effect on the conversion is the same. This is illustrated in Fig. 3.11c. A reduction of the coupling shifts the point of maximum conversion towards higher pump powers. Thus a low coupling can in theory be compensated by increasing the pump power. In practical case the power is limited so that increasing the coupling is a main goal for efficient frequency conversion. According to the simulated curves, a pump power of 210 mW should be enough to achieve maximum conversion in the best case for the process under investigation.

3.4 Waveguide Fabrication

In this section different techniques for waveguide fabrication will be briefly introduced. Results on first steps of waveguide fabrication within the scope of this thesis will be presented.

Waveguide fabrication techniques can be divided into two classes: Techniques that result in a modification of the properties of LN in order to form guiding channels, and techniques including the removal of material to create a refractive index step. Actually, combinations of both approaches are also possible. One popular technique for LN waveguide formation is the in-diffusion of Ti-atoms into the bulk material [149, 150]. The waveguide outline is defined by lithographic techniques combined with a titanium film sputtered onto a positive mask. Treatment of the sample at high temperatures leads to a diffusion of Ti-atoms into the LN. The Ti-doping locally increases the refractive index. The concentration profile due to the diffusion process results in a refractive index profile, accordingly. The change in refractive index is in the range of $10^{-2} - 10^{-3}$. The process takes effect on ordinary and extraordinary index, allowing the guidance of both TE and TM modes [149]. The drawback of this procedure is the weak and smooth refractive index profile which leads to a significant dependency of the modal profile on the wavelength. This introduces to a rather low modal overlap regarding the large wavelength spread involved in frequency conversion. Furthermore, Ti increases the susceptibility of the material to photorefractive effects [151], disturbing applications at visible wavelengths. However, it finds widespread applications at telecom wavelengths especially in optical modulators [152].

The technique of annealed proton exchange (APE) waveguide fabrication [153, 154] also starts with a lithography process after which a metal mask covers the areas which should not be affected by the following steps. Then the sample is immersed in benzoic acid where H^+ ions substitute the Li^+ ions, resulting in an exclusive increase of the extraordinary refractive index. Thus waveguiding is restricted to TM modes. At this point the smooth refractive index profile is comparable to the one resulting from Ti diffusion technique. A subsequent annealing promotes further diffusion of H^+ from the sample surface towards bulk regions, partly restoring the original material properties in the surface layers. This increases the profile and mode symmetry and the overlap. Additionally the susceptibility for refractive effects of the original material is partly re-established. Latest insights in the APE process open the door for tailored integrated optic devices for nonlinear optic applications [27]. Both the Ti-diffusion and the APE technique allow for quasi phase matching.

High-energy implantation of ions can influence the crystal lattice properties of LN. This can result in a variety of effects depending on ion energy, dose and species [155]. Especially, this can be used to increase the refractive index. Usually this kind of implantation is not used to directly define waveguide channels but an extensive layer with

lower refractive index is created in bulk material. Waveguides can then be established with additional techniques usually by machining or etching.

The afore mentioned techniques lack of modal overlap or polarization independent guiding. Both drawbacks can be overcome with high-contrast refractive index steps, created by material removal and by tailoring the interface between LN and air. This can result in ridge waveguide structures described theoretically in the previous section. The devices used in this thesis are fabricated in the following steps. First a wafer of LN is adhered to a LT substrate by direct heterobonding. The LN is polished and lapped to final waveguide height. Next QPM is established by periodic poling. Then a wafer dicing saw is used to cut air-trenches into the material to define ridge waveguides [156]. The blade polishes the waveguide sidewalls simultaneously to the cutting process. Finally the device is finished by polishing the end facets and the application of anti-reflective coating. The drawback of this technique is that only straight, linear geometries can be produced. This limits the applications for integrated optic devices. The advantages are the polarization independent guiding, high modal overlap and low propagation losses. Nonlinear interaction in such waveguides could be demonstrated with high efficiency [157, 158]. However, the process is difficult and expensive for which reason it has not found widespread use yet.

A versatile tool for waveguide fabrication in lithium niobate are ultrashort laser pulses. As source usually titanium sapphire lasers are employed, generating pulses in the near infrared spectral region with durations below 100 fs. Depending on the intensity a variety of different processes can be observed. The most popular techniques are summarized as direct laser writing [159]. Either the extraordinary refractive index can be increased by the interaction of the laser pulses with the material or both ordinary and extraordinary refractive index can be decreased. With these effects waveguides can be formed with low refractive index steps. However, when the intensity of the laser pulses is increased, material can be removed [160]. In this operation regime waveguiding structures with high refractive index contrast can be formed. The application of laser pulses for material processing of lithium niobate offers a very fast and flexible way to create 2D waveguiding structures. However, up to now the quality of waveguides regarding losses can not yet compete with the other methods mentioned in this thesis.

Another method for material removal is etching. Lithium niobate can either be etched chemically or by physical processes. Chemical etching usually involves hydrofluoric acid and mixtures thereof [161]. Unfortunately the etching rate is sensitive to crystal orientation which makes it less feasible in combination with periodic poling [162]. In our group we pursued a dry-etching approach including reactive ion etching. The fabrication process invented in the framework of the diploma thesis of Benjamin Weigand [145] will now be briefly discussed. The first steps involve bonding of LN on LT and polishing of the LN layer as introduced above. Then layers of chromium and copper are sputtered onto the c^- -side of the LN wafer (Cu later acts as an adhesive layer for the

mask). The next step is the masking of the sample. A negative photo-resist is applied. In a lithographic process the waveguide geometry is defined in the resist. Here a resin specialized for galvanic applications is used which can be coated in very thick layers. Due to the pyroelectric effects in LN the following hard bake of the resist had to be optimized not to destroy the sample which includes slow temperature ramps and mounts that allow charge equalization. After developing of the resist and removal of the unwanted parts the sample is brought into a galvanic bath where nickel is deposited on the copper layer of the LN surface. This Ni-mask can be made very thick allowing the masking even in long-running etching processes and thus etching of deep trenches. Afterwards the actual etching is performed. We use reactive ion etching (ECR-RIE) in a plasma consisting of Ar and SF₆. By increasing the HF-power of the plasma and the Argon concentration the physical effect can be increased and chemical etching effects decreased. After the RIE process the metal mask can be dissolved by acid without pitting the LN. With this process waveguide structures with a height of 6 μm and steep sidewalls angles of 75° could be fabricated. A scanning electron microscopy (SEM) image of fabricated structures is shown in Fig. 3.12. Up to now the waveguiding could not be demonstrated due to problems in the initial bonding and polishing steps. First attempts were undertaken to form a guiding layer by implantation of high-energy ions. A sample was illuminated successively with oxygen ions (O²⁺) at energies of 5 MeV, 5.5 MeV and 6 MeV and doses of 10¹⁴ ions/cm² each. The implantation was performed at the tandem accelerator of RUBION in Bochum. This procedure should generate vacancies and hence a layer with decreased refractive index in a depth around 2.7 μm. The next processing step was not reactive ion etching, but laser micro structuring of the materials (Photonik Zentrum Kaiserslautern, [163,164]). For this end, pulses with

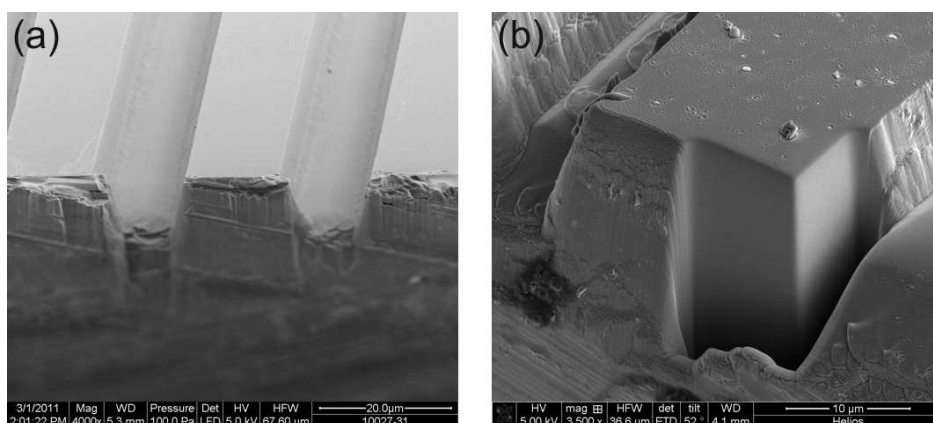


Figure 3.12: SEM images of fabricated waveguide structures, reproduced from [145]. a) shows a view on an array of waveguides. b) shows a close-up image of one waveguide after additional machining of facet and sidewall by FIB.

picosecond duration at a wavelength of 355 nm were used. This wavelength is close to the absorption edge of lithium niobate and makes two-photon absorption feasible. With these parameters the interaction can be described with standard models for ultrashort-pulse interactions with matter [165]. The pulses are slightly longer than the femtosecond pulses usually employed, having the side effect of additional heat input. This results in melting of the material followed by solidification, reducing surface roughness. After laser micro structuring the surface of the ion-implanted samples, waveguiding could be observed recently [166]. Subsequent research included the post processing of the etched structures by focused ion beam milling (FIB) to increase sidewall steepness and for facet polishing, as shown in Fig. 3.12b. FIB also allows the fabrication of photonic microstructures in combination with the etched waveguides [167]. Furthermore the material indium tin oxide (ITO) was investigated as a promising substrate layer [168]. ITO is a conducting oxide and transparent in a wide wavelength range. Its electrical and dielectric properties can be adjusted in the growth process. The electrical conductivity opens interesting applications for electro-optic devices. The waveguide fabrication is ongoing work.

4 Optical Parametric Oscillator

For the quantum frequency conversion experiments a classical pump field is necessary to stimulate the downconversion process. For the three near infrared transition wavelengths of Ca^+ -Ions at 850 nm, 854 nm and 866 nm, pump wavelengths of 2419 nm, 2455 nm and 2557 nm are required in order to convert them to the telecom O-band at 1310 nm. Thus a tunable light source is necessary that covers this range of pump wavelengths. At the same time, a narrow linewidth and stable frequency is recommended to avoid influence on the spectral shape of the converted photons. Recently, commercial systems became available that could fulfill these requirements. Such systems can consist of semiconductor discs (e.g. lasers from Fraunhofer-Institut für angewandte Festkörperphysik IAF, Freiburg) or Cr:ZnS/Se crystals (IPG Photonics, laser of SFTL series). However, as lasers at such wavelengths were not readily available at the beginning of this thesis work, we decided to build an optical parametric oscillator (OPO) that can be tailored to our demands. The following chapter describes the design and setup of the OPO and presents exemplary experiments to demonstrate its performance. Eventually these properties will be compared with the requirements for quantum frequency conversion experiments.

Parts of this work were done in cooperation with Elisabeth Zscherpel and presented earlier in her Master-Thesis [169]. Further details about the setup can be found in [169].

4.1 OPO Setup

The pump wavelength for the OPO was chosen at 1080 nm. The crystal properties and mirror coatings of the cavity were designed to generate idler wavelengths between 2300-3100 nm via difference frequency generation. This covers all wavelengths mentioned in the previous, introductory section. The corresponding signal wavelengths in the range 1650-2000 nm are planned to be used in future conversion experiments. The OPO consists of a master oscillator power amplifier (MOPA) system as a pump source. The nonlinear optical crystal offers several poling periods to support QPM over a large wavelength range. This crystal is surrounded by a ring cavity providing the feedback for the signal field. Both parts, the pump source and the OPO resonator will be described in detail in the next sections.

4.1.1 Pumping System

The idea of increasing the versatility of the light source also influenced the choice of the pump laser. From equation 3.18 we see that the threshold of the OPO reduces when it is operated close to degeneracy of signal and idler wavelengths. Hence for such a design a low pump power is necessary. Hence we here aimed at a pump wavelength above $1 \mu\text{m}$. We decided to use a laser that is tunable around 1081 nm due to the fact that this wavelength could also be used to pump a frequency conversion process to convert photons from a Nitrogen Vacancy center in diamond (637 nm) to the telecom C-band in a future experiment. In a first stage we use an external cavity diode laser (ECDL, Toptica DL100 pro design) that is tunable between 1073.9 nm and 1088.9 nm. The emission is directly coupled to a polarization maintaining fiber resulting in an output power of more than 80 mW behind the fiber. However, this power is not enough to operate a singly resonant OPO above its oscillation threshold. Thus the light is coupled to a Ytterbium-doped fiber amplifier (YDFA, Keopsys KPS-STD-BT-YFA-40-SLM-PM-111-HIP-FA-FA) to increase the power, preserving the tuning range. Behind the amplifier the output beam can be split into two arms to pump two independent OPOs in future experiments. A sketch of the complete pump setup can be found in Fig. 4.1.

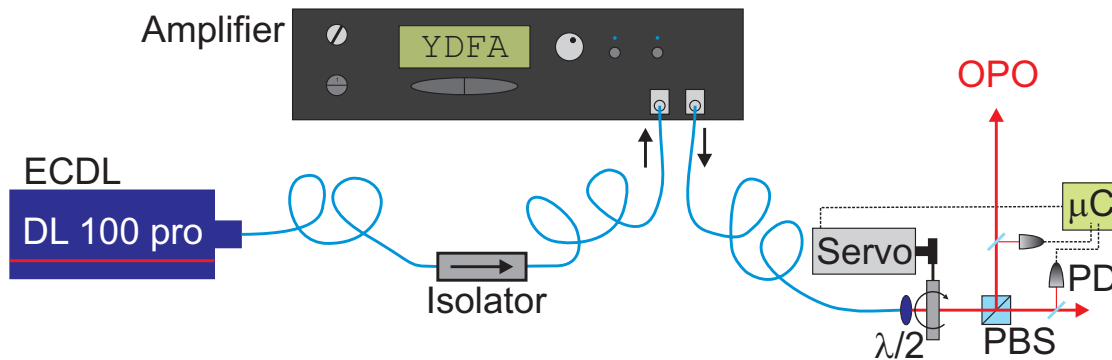


Figure 4.1: Setup of the pumping system for the OPO, including the polarization stabilization. PD: photodiodes, PBS: polarizing beam splitter, $\lambda/2$: half-wave plate, μC : microcontroller circuit.

The amplifier delivers an output power of more than 10 W which is high enough to pump the OPO well above threshold. The output power is proportional to the setting current of the amplifier (Fig. 4.2a) allowing fine tuning of the power. The total output power has a stability better than 1 % RMS over a typical run-time of 10 h (see inset of Fig. 4.2a). This power measurement is performed using a polarization independent detector. However, the difference frequency process in the OPO is polarization sensitive.

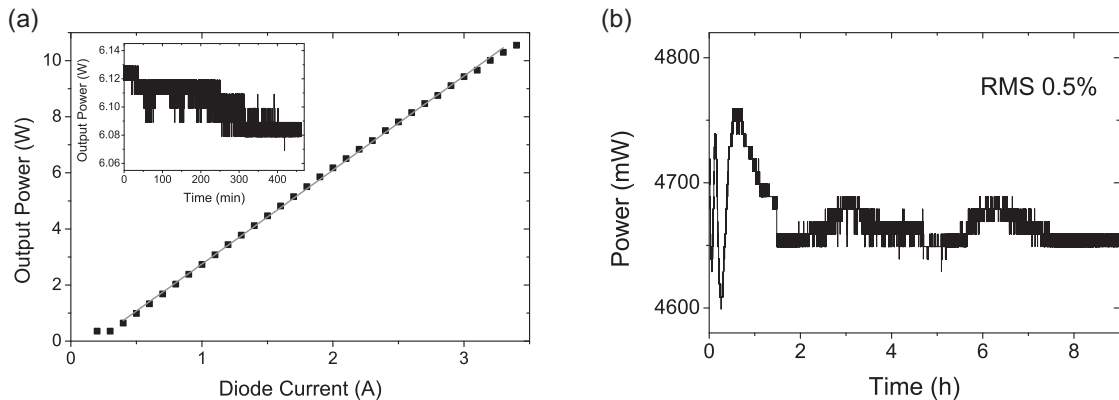


Figure 4.2: Output power characteristics of the fiber amplifier: (a) the output power shows a linear dependence on the current setting with a slope of 3.35 W/A . The inset shows a long-term measurement of the total optical output power with an RMS stability of 0.23% . (b) Long-term power measurement behind polarizing beam splitter. With the active stabilization the power fluctuations including polarization effects are decreased. A RMS stability of 0.5% can be reached.

In detail this means that the pump field needs to exhibit a linear, vertical polarization corresponding to the c-axis of the nonlinear crystal in the OPO cavity. The polarization is perpendicular to the plane of beam propagation in the cavity. The diode laser generates a linearly polarized output coupled to a polarization maintaining fiber with a measured polarization contrast exceeding 25 dB . The amplifier is equipped with polarization maintaining fibers as well and should thus deliver a linear polarization at the output. However, this was not the case in practice due to some fabrication tolerances inside the amplifier which could not be completely eliminated by the manufacturer. This results in slow drifts of the polarization axis at the output of the fiber. Behind the polarizing beamsplitter this leads to a variation of power. To compensate for these drifts we introduced an intensity stabilization by inserting a motorized half-wave plate in the beam. Behind the polarizing beam splitter small amounts of light are sampled on photodiodes to measure the ratio of both polarization components. A microcontroller circuit uses this information to correct the polarization state by rotating the waveplate. This setup allows to stabilize the output power in both arms behind the beamsplitter to any splitting ratio. Without stabilization RMS fluctuations of the power behind the polarizer worse than 8% were observed. The active stabilization reduced this value to 0.5% (see Fig. 4.2b), close to the intrinsic power fluctuations of the amplifier of 0.23% (see Fig. 4.2a).

During the installation of the OPO we encountered another problem of the pumping system. Operating the amplifier at high powers has sometimes lead to a failure of the

diode in the ECDL which in consequence had to be replaced. To protect the diode laser it was necessary to reduce back-reflections from the amplifier by inserting an additional fiber in-line isolator. By this, the ECDL failure issue could be overcome but it had led to a damage of some components inside the amplifier. Due to these obstacles the complete OPO system had to be rebuilt several times. Thus the following specifications and graphs show measurements from different versions of the OPO setup.

4.1.2 OPO Resonator

As a nonlinear medium we chose periodically poled MgO-doped lithium niobate (PPLN) as this is the state of the art material with the highest optical nonlinearity in the near-infrared spectral region. We decided to adopt an existing OPO design [143] to the new wavelength requirements. The crystal was fabricated by HC Photonics and has a length of 40 mm and a facet outline of $8.4 \text{ mm} \times 0.5 \text{ mm}$. It offers 7 poling periods ($\Lambda_1 \dots \Lambda_7 = 31.7, 31.9, 32.1, 32.3, 32.5, 32.6$ and $32.7 \text{ }\mu\text{m}$) and its facets are anti reflective coated for pump (1068–1088 nm), signal (1650–2000 nm) and idler (2352–3135 nm) wavelengths. The crystal is mounted on a 4-axis stage to align it relative to the beam path and it is temperature controlled by a peltier element and a PID-controller (Newport N325B). Thus coarse wavelength tuning is possible by changing the poling period via translating the crystal perpendicular to the beam path and afterwards adjusting the phase matching by the temperature.

Once the crystal length is known, the optimum beam waist is given by the Boyd-Kleinman-criterion [137]. The cavity geometry was designed to fit this value. For coupling the pump light we use a lens with a focal length of 84 mm resulting in a beam waist radius of $30.9 \text{ }\mu\text{m}$. This corresponds to a confocal parameter of 5.56 mm and a Boyd-Kleinman parameter of 7.2 for 40 mm crystal length. This parameter is close to the efficiency maximum. Analogue to the former designs [140, 143], the ring cavity consists of two plane and two plano-concave mirrors with a radius of curvature of 50 mm. The cavity geometry was optimized with the help of the software SARA (Software Assisted Resonator Analysis, Photonikzentrum Kaiserslautern) resulting in the setup depicted in Fig. 4.3. As shown in the figure by means of the overlap of the diameter for sagittal and tangential plane, the design allows for an astigmatism-free beam-path inside the nonlinear medium.

The mirrors are highly reflective for the signal wavelength (HR 1650-2000 nm) and have an anti-reflection coating for the pump (AR 1081 nm) and idler wavelengths (AR 2300-3100 nm) allowing a singly resonant operation with maximum output of the desired idler field (mirror coatings by Layertec GmbH). A set of mirrors with high reflectivity coating for both signal and pump field is also available which was used to build a pump enhanced single resonant OPO cavity for initial setups. There exists also a set of mirrors for the singly resonant design with partial transparency for the

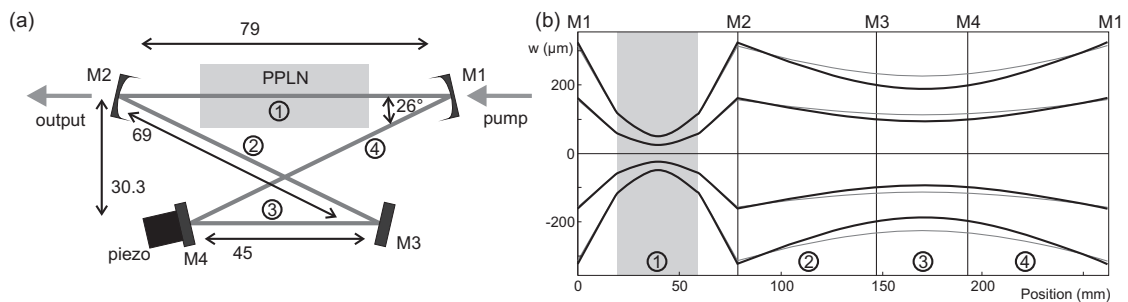


Figure 4.3: Schematic of the OPO cavity: (a) Shows a view of the beam path in the ring resonator. All dimensions are given in mm. (b) Shows a copy of the screen from the SARA software. The lines indicate the beam waist as a function of the position along the beam path. The black curves show the beam in the tangential plane whereas the gray curves describe the sagittal plane. The inner curves correspond to $1/e$ -radius and the outer ones to the FWHM.

signal wavelengths (not applied in this thesis). The mirror $M4$ is mounted on a piezo transducer to fine-tune the cavity length. Behind the OPO an uncoated CaF-lens ($f = 100$ mm) is used to colimate the output beam.

Additionally, an etalon can be inserted in the second focal plane of the resonator, i.e. centered between the two plane mirrors. The etalon introduces additional loss to neighboring modes and thus increases their oscillation threshold. In that way mode-hops can be effectively suppressed and the frequency stability of the OPO output is improved. As an etalon we use an uncoated plane-parallel glass plate (reflectivity ≈ 4 %) with a thickness of $500 \mu\text{m}$ and a free spectral range around 200 GHz. It can be tilted around the horizontal axis for frequency tuning.

In the OPO we observe parasitic nonlinear processes like the sum frequency mixing (SFG) of the pump field with the signal or idler. Such effects can be partially phase-matched due to random duty-cycle errors of the quasi phase matching grating [170]. In our case this results in the generation of red light with wavelengths between 665-710 nm (SFG of pump and signal) and 730-800 nm (SFG of pump and idler). As the coating for the OPO mirrors is not specified in this spectral range, a small amount is transmitted at each mirror. Behind $M3$ this light is collected, spectrally filtered by interference filters and then coupled to a multimode fiber. With the knowledge of the pump wavelength and a measurement of this red wavelength, the exact idler wavelength can be calculated. This offers an easy access to the spectral properties of the OPO without the necessity of a mid-IR spectrometer.

4.2 Threshold and Output Power

A basic characteristic of an OPO is its output power. In Figure 4.4 the idler power for different pump powers is shown. This curve was measured at an idler wavelength of 2468 nm, close to the final value for the QFC experiments. To increase frequency stability, the etalon was inserted in the resonator which resulted in a single longitudinal mode operation even at output powers above 1 W. For the calculation of

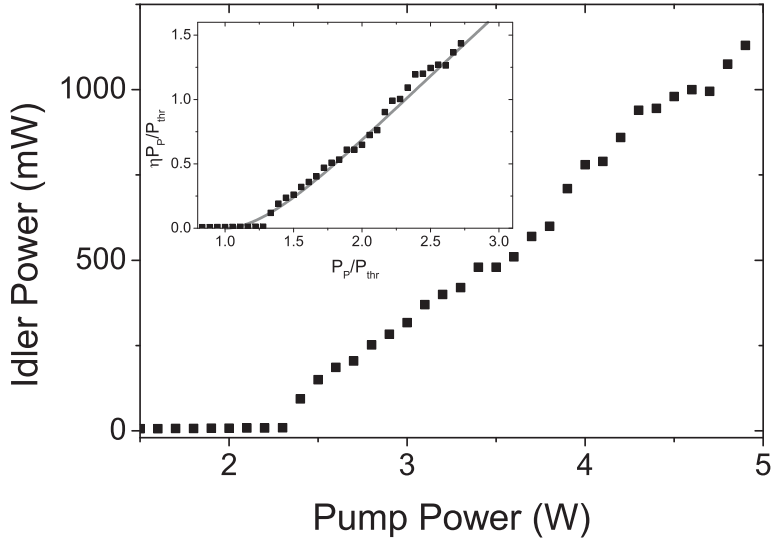


Figure 4.4: Idler output power vs. pump power. In this measurement the etalon was inserted which increases the threshold and reduces output power. The inset shows the same experimental data normalized to compare with the theoretical curve.

the threshold under ideal conditions [171] the following assumptions were used: Ideal focusing condition ($\xi = 2.84$) with a beam waist radius of $49.2 \mu\text{m}$, nonlinear coefficient $d_{eff} = 13.4 \text{ pm/V}$, reflectivity of 0.5 % for each crystal facet (given by the coating manufacturer) and 99.9 % reflectivity for all four cavity mirrors, i. e. $(1 - R_S)(1 - R_F) = 0.999^4 \cdot 0.995^2 = 0.986$. According to equation 3.18 this results in a pump power at threshold of 1129 mW. The actually observed threshold value is around 2 W as can be seen in Fig. 4.4. The calculations did not include absorption losses in the crystal or the effects of the intracavity etalon. However, this cannot fully explain the discrepancy. In the succeeding setups of the OPO after the pump laser failures different threshold values were reached. This indicated that the cavity alignment plays an important role, as expected. There are some degrees of freedom like the transverse position of the crystal that cannot be adjusted after setting up the cavity

as the crystal mount does not support this additional degree of freedom in translation. Another unknown parameter is the quality of the quasi phase matching. A deviation of the poling period from the optimum duty cycle reduces the effective nonlinear coefficient resulting in lower parametric gain and thus higher threshold.

In spite of the high threshold the OPO reaches a very high conversion efficiency. The slope of the data in Fig. 4.4 gives the power conversion efficiency $\tilde{\eta} = P_i/(P_p - P_{thr})$. In the data shown above this is 40 %. However, a more significant measure is the photon conversion efficiency which corresponds to the probability of a pump photon being converted to an idler photon. This can be calculated from $\tilde{\eta}$ by including the ratio of photon energies, respectively their wavelengths: $\eta = \lambda_i P_i / \lambda_p (P_p - P_{thr}) = 0.91$. This rather high value was confirmed by measurements of the pump power depletion behind the OPO. This means that nearly all available pump photons are downconverted to signal and idler photons. In detail, the efficiencies are a function of the pump power. To compare the experimental data with the theoretical curve (see eqn. 3.23 and Fig. 3.5), the normalized pump power is introduced: $\tilde{P}_p = P_p/P_{thr}$. Hence the normalized output power can be calculated with the help of the efficiency: $\tilde{P}_i = \eta \tilde{P}_p$. Using equation 3.23 the optimum efficiency can be calculated and the idler power thus compared with experimental data (see inset of Fig. 4.4). Using a threshold value of 1.8 W, the theoretical model fits best to the the data.

4.3 Frequency Tuning and Linewidth

The output wavelength of an OPO can be tuned by changing the phase matching conditions or cavity resonance. Coarse tuning is possible by translating the crystal in the resonator and thus bringing one of the seven possible poling channels into the optical axis. Then a certain wavelength can be chosen by the crystal temperature. With this technique, idler wavelengths between 2311 nm and 2870 nm with the corresponding signal wavelengths of 1731 to 2030 nm have been achieved, as shown in Fig. 4.5. The tuning curves can be calculated theoretically by solving the phase matching equation, including the wavelength dependent refractive index of the material. The refractive index was calculated with the help of Sellmeier equations for MgO-doped lithium niobate (extraordinary index, [127]). From the almost perfect overlap of the theoretical model with the experimental data in Fig. 4.5, a tuning range down to signal wavelengths of 1650 nm and idler wavelengths up to 3120 nm can be estimated including the two poling periods with the shortest periodicity. For the periods 32.1 to 32.5 μm tuning without a gap is possible in a temperature range between 20 and 45 °C. For shorter periodicity this is possible with temperature tuning between 20 and 70 °C. For the QFC experiments the OPO has to be set to a poling period of 32.6 μm and a temperature around 27.5 °C. The OPO was designed to be operated slightly above room temperature making temperature stabilization more feasible. In principle the OPO can

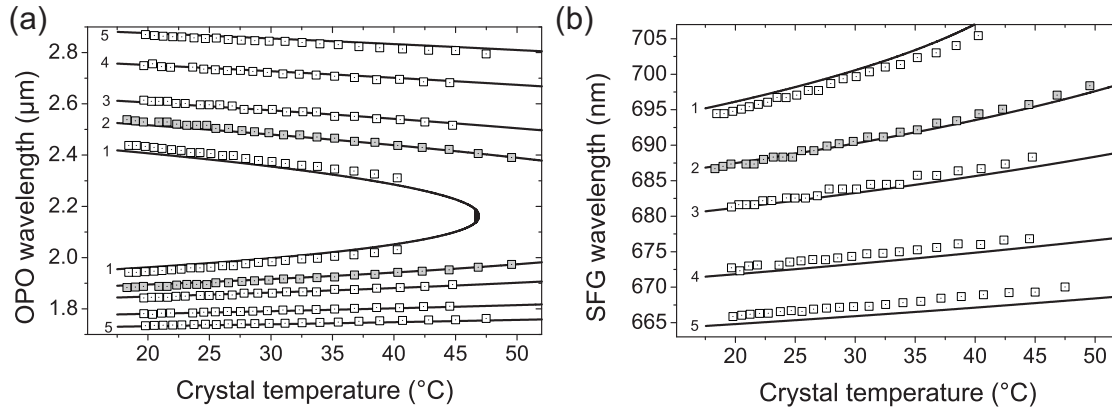


Figure 4.5: OPO tuning curves: (a) Signal and idler wavelengths vs. crystal temperature for different poling periods. These values are calculated from the measured SFG signal, shown in (b). The solid lines show theoretical calculations with Sellmeier equations [127] and a pump wavelength of 1078.9 nm. The numbers 1...5 indicate the poling periods 32.7, 32.6, 32.5, 32.3 and 32.1 μm . The period of 32.6 μm is used throughout the QFC experiments and therefore highlighted by gray filled squares.

be set to any wavelength in the above mentioned range. In the end this is limited by the resolution and stability of the temperature controller.

For fine-tuning of the output frequency, the mirror $M4$ is mounted on a piezo actuator to slightly change the cavity length. This changes the free spectral range and thus the resonance frequency of the cavity. The OPO output frequency will follow the resonance until it jumps to a neighboring mode with higher gain. Experimentally, a continuous tuning range of 1040 MHz was achieved. The fine-tuning properties were measured by recording the red sum frequency signal of the OPO with the help of a wavelength meter (High Finesse WS-6). This wavemeter has a relative resolution of 50 MHz and an absolute accuracy of 200 MHz.

Another way to tune the OPO externally is changing the pump frequency. The ECDL allows coarse tuning of the pump wavelength by manual tilting the grating as well as fine-tuning by a piezo that is attached to the grating. The gain bandwidth of the amplifier is broad enough to cover the tuning range of the diode laser. Thus also fast tuning of the OPO pump wavelength is possible. Tuning the pump laser via its piezo a maximum mode-hop free scan range of 54 GHz could be observed. The OPO output frequency should follow this tuning. However this could not be observed experimentally due to limitations of the wavemeter. The minimum tuning speed of the diode laser is too fast for proper sampling of the OPO wavelength by the wavemeter.

After the discussion of different ways to tune the output wavelength of the OPO,

another important figure of merit is the stability of the OPO wavelength. A prerequisite for a stable output frequency is a stable design of the OPO setup. This includes mechanical stability of the individual components, a housing that shields the resonator from environmental influences and a stable crystal temperature control. Additionally, the output stability of the OPO depends on the input stability, respectively the stability of the pumping system. In Fig. 4.6a a simultaneous measurement of the OPO frequency and power is shown. As there was no spectrometer available for the idler wavelength range, we use the red parasitic radiation (SFG of pump and signal), together with a suitable wavelength meter for precision frequency measurements. At this point we are only interested in the relative frequency excursions and therefore use the long-term average value as reference. As can be seen in the figure, the peak to peak frequency fluctuations are below 250 MHz within a ten hours measurement. The RMS fluctuation of the power is 0.9 % which is in the order of the pump laser power stability.

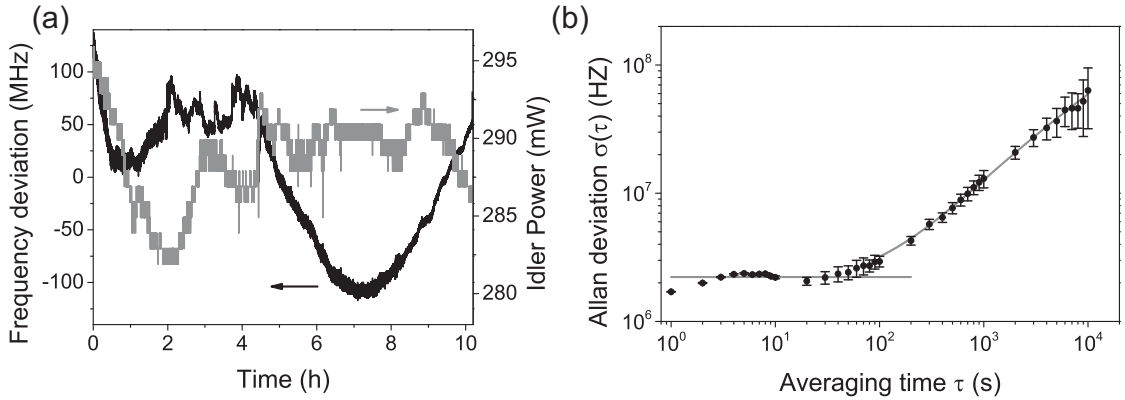


Figure 4.6: Frequency stability of the OPO: (a) variation of the OPO output frequency (black curve) and power (gray curve) over time. (b) Allan variance calculated from the data of (a); the solid lines depict a linear and a square root slope to model the noise sources for short and long-term fluctuations, respectively. Idler wavelength $\lambda_i = 2486$ nm.

To reveal the noise sources affecting the stability of the OPO on different time scales, we calculated the Allan variance $\sigma_y^2(\tau)$:

$$\sigma_y^2(\tau) = \frac{1}{2(N-1)} \sum_{i=1}^{N-1} (y_{i+1}(\tau) - y_i(\tau))^2 \quad (4.1)$$

Here N is the total number of samples, $\tau = t_{i+1} - t_i$ is the time interval between two measurements and $\{y_i\}$ is the set of frequency deviations from the mean value measured

at times $\{t_i\}$. Practically, this means the data from Fig. 4.6a can be used to create sets with different averaging times by calculating the average value of a certain amount of successive samples [172]. The Allan deviation $\sigma_y(\tau)$ of the long-term measurement depending on averaging time is shown in Fig. 4.6b. For integration times above 200 s the slope of the data points can be well fitted by a square-root function ($\propto \tau^{1/2}$). This is a well-known signature for random walk frequency noise [173]. This kind of drift is usually related to fluctuations of the environmental conditions of the oscillator. On timescales below 10 s the data curve is almost constant. This regime is often described as flicker floor [172]. Thus there is no systematic noise source present disturbing the OPO output. Integration times below 1 s are hardly accessible with our wavemeter due to the minimum sampling rate. To investigate the stability on shorter time scales a common procedure is a beat measurement with a reference light source. The beat signal can be detected at high speed with a fast photo diode. In this sense we could use a second OPO of the same design as reference. In a former experiment we employed this technique to characterize another OPO with the help of a frequency comb down to integration times below 10^{-5} s [141].

We can define the linewidth of an OPO as the time averaged excursion of its output frequency. The Allan variance provides a measure of such average frequency fluctuations. Thus we here can use the Allan deviation as an approximation for the linewidth of the OPO. It has to be noted that in this approach the linewidth depends on the observation time. Regarding Fig. 4.6b we can define the linewidth of the OPO to be about 2 MHz for an integration time of a few seconds and slightly increasing with integration time.

The frequency tuning techniques described in the beginning of this section can also be exploited to actively stabilize the output wavelength. Therefore, in general a device is necessary that measures the frequency or at least compares its fluctuations relative to a reference and then feeds an error signal back to compensate for the frequency change. In previous works we already used the frequency of the pump laser [143] or the wavemeter [141] as reference. The last seems feasible with this OPO, too. The wavemeter continuously measures the current wavelength and compares it to a preset reference value. The complete feedback control is implemented in software emulating a PID-controller (software supplied with the wavemeter). The error signal generated by the PID software controls an analogue voltage source at the wavemeter device. After amplifying with a high voltage amplifier (TEM-Messtechnik miniPIA 103) the voltage is fed to the piezo to vary the OPO cavity length. The OPO output frequency, measured with the wavemeter, is shown in Fig. 4.7. To interpret this data one has to keep in mind that here the measurement device is also used as a reference for the stabilization. This means the data can only reveal the fluctuations of the OPO relative to the wavemeter. The peak to peak fluctuations are now below 57 MHz. The stabilization reduced the

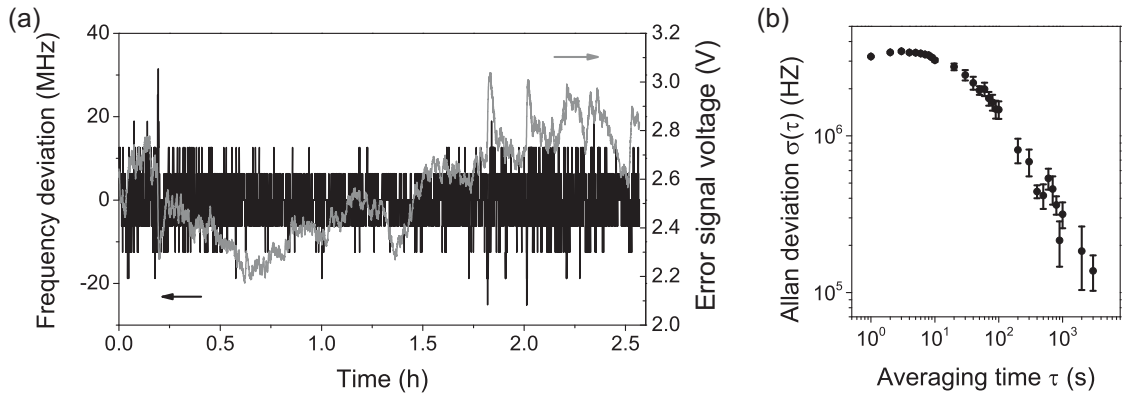


Figure 4.7: Frequency stability of the stabilized OPO: (a) variation of the OPO output frequency (black curve) and the output voltage, i.e. the error function (gray curve) over time. (b) Allan variance calculated from the data of (a). Idler wavelength $\lambda_i = 2486$ nm.

RMS frequency fluctuations from 63.6 MHz (Fig. 4.6) down to 5.6 MHz (Fig. 4.7a). We can also calculate the Allan deviation as shown in Fig. 4.7b. These values can not be referred to an absolute stability but qualitatively demonstrate that the OPO follows the feedback mechanism. Their continuous decrease shows the capability of the stabilization for long time scales. A quantitative result could be achieved by comparing the OPO output with an external frequency reference and not the wavemeter which is used for stabilization. In Fig. 4.7a the output voltage of the wavemeter is shown, which is a measure for the error function of the feedback loop of the stabilization. For these results of wavelength stability we have to keep in mind that the idler wavelength could not be measured directly but we used the sum frequency signal. This includes also fluctuations of the pump wavelength. Initial measurements of the pump laser frequency stability showed that it is more stable than the OPO output and we can in a first approximation attribute all fluctuations of the sum frequency signal to the OPO.

4.4 Summary

In the current chapter the design and most significant properties of an optical parametric oscillator, pumped by a diode laser fiber amplifier system have been presented. In particular the OPO can be tuned from 2311 to 2870 nm at the idler wavelength with an output power exceeding 1 W in a single longitudinal mode. In regard of frequency down-conversion of light at the wavelength of the 854 nm transition in Ca^+ ($3^2\text{D}_{5/2} \leftrightarrow 4^2\text{P}_{3/2}$), this OPO tuning range will allow to cover a wavelength interval between 1216 nm and 1355 nm, including the telecom O-band. In the best case max-

imum QFC efficiency is expected at a pump power around 210 mW in the waveguide (see Fig. 3.11). Taking into account transmission and coupling loss this can easily be reached with the OPO with some overhead left. The detailed discussion about coupling efficiency can be found in section 6.1.1.

Long-term measurements revealed high stability for both output power and wavelength. Special attention is drawn to the wavelength region around 2450 nm which is necessary as a pump wavelength for the quantum frequency conversion experiments. Furthermore, a maximally allowed value of frequency excursion can be defined by the filter bandwidth behind the frequency conversion setup. The width of the most narrow filter for telecom O-band available in our lab (fiber Bragg grating) is 145 GHz FWHM. During a common measurement time of 8 h the fluctuations of the OPO should not exceed this limit. Indeed the OPO outperforms this value by nearly two orders of magnitude. A detail more relevant in practice are mode hops. In case of a mode hop the output wavelength of the OPO suddenly changes by a multiple of OPO cavity FSR. Such a change in wavelength can drastically change the phase matching conditions in a subsequent QFC process and should thus be avoided. As the presented long-term measurements show, no such mode hops appeared. The QFC measurements of chapter 6 indeed revealed that the OPO can be operated on a single longitudinal mode for several days without interruption. The ability to stabilize the output wavelength to a wavemeter further reduces frequency fluctuations and would even allow to directly address an atomic transition with the help of frequency conversion. In regard of the frequency conversion experiments we can think of a scenario that a narrow-line telecom light field should be upconverted to an atomic transition. In this case the OPO as pump source must not broaden the converted spectrum and the OPO can be used to tune the target wavelength. Hence the requirements on linewidth and frequency stability are given by the properties of the atomic transition. For example the transition in calcium at 854 nm has a bandwidth of 22 MHz. From the Allan variance measurement we find an upper limit for the short-term linewidth in the low MHz range. To address such an atomic transition in a long-term measurement an active stabilization is necessary. The stabilization to a wavemeter resulted in frequency excursions in the low MHz range, too. Hence the requirements for such an experiment are fulfilled.

The above mentioned stability could be important for future experiments like frequency upconversion where telecom single photons are converted towards the absorption line of the Ca ion at 854 nm. In this case a narrowband feature at a fixed wavelength has to be addressed. The OPO can be used to hit this narrow resonance due to its stability and tunability, at least in principle. Future improvements of the OPO should include the exchange of mirror M3 with a partially reflecting mirror to gain access to the signal field. At the time of writing this thesis a second OPO is set up which is a copy of the described one, with the same mirror set and crystal. Output coupling

mirrors are available with slightly different reflection curves to optimize the signal output coupling for a certain wavelength range (e.g. around 1690 nm). A coherent field around 1690 nm can be generated serving as pump for downconversion experiments with Silicon-Vacancy (SiV) centers in diamond. Their emission around 738 nm could thus be converted to the telecommunications O-band. Ideally both OPOs can be operated simultaneously with the same pump laser. This would allow to run two QFC experiments in parallel that even share the same master-oscillator. This paves the way to convert two dissimilar quantum systems (SiV and Ca^+) independently to the same telecom wavelength.

5 Photon Pairs

Photon pairs generated by spontaneous parametric downconversion (SPDC) form a non-classical state of light described by a collective state wavefunction (see. section 2.2.3). Of special interest in quantum information technology are the strong temporal correlations of these photons investigated in this chapter. On the one hand, the temporal correlation enables the deterministic generation of heralded single photons. In addition these photons can be entangled and are therefore an elementary tool for quantum network and quantum repeater scenarios. Commonly the photons are entangled in their degree of polarization, i.e. the photons of a pair are orthogonally polarized. Instead we here report on time-energy entanglement.

We use an optical parametric oscillator, operated below threshold to generate such pair states. In this chapter we will introduce the source and present the properties of the photons, especially their temporal and spectral characteristics. Furthermore, spectral filter systems to produce narrowband correlated photon pairs in the MHz-regime compatible to atomic resonances will be introduced. The first and second-order coherence properties of the photon pairs are measured in single- and two-photon Franson-type interference experiments. With these preconditions fulfilled, we demonstrate the absorption of a single photon by a single trapped calcium ion heralded by a telecom photon.

5.1 OPO-SPDC Source

The photon pair states described in this chapter were generated by an optical parametric oscillator operated far below its oscillation threshold. This OPO was originally developed as a highly stable, high power light source [141, 174]. It was first used as source of the pump field for the quantum frequency conversion process of quantum dot emission to the telecom O-band [37]. As a pump source for the OPO we use a frequency doubled solid state laser system (Coherent Verdi V-10). It delivers a continuous wave single mode, single frequency output at 532 nm with a power of up to 10 W. The pump laser has a monolithic design which offers high passive stability for frequency and power [141]. The OPO was developed following the design rules explained in section 3.2.2. The heart of the device is a crystal of periodically poled stoichiometric lithium tantalate. Previous experiments revealed the sensitivity of lithium niobate to photorefractive effects, induced especially by green light [175, 176]. Lithium

tantalate here is the better choice. Furthermore, the crystal was doped by 1 mol% of MgO and hence showed no photo-induced effects, even at high pump powers. The crystal has a length of 30 mm and the end facets are cut under an angle of 2° to reduce etalon effects and are anti-reflective coated for pump, signal and idler wavelengths. Quasi phase matching is realized by six equally spaced poling periods between $\Lambda_1 = 8.1\mu\text{m} \dots \Lambda_6 = 8.6\mu\text{m}$. The crystal is placed in a four-mirror bow-tie type ring cavity. The mirrors are coated for a high reflectivity at the signal field between 790–995 nm and high transmission at the pump (532 nm) and idler wavelengths (1100–1600 nm). One of the mirrors is mounted on a piezo translator to change the resonator length. Fine tuning of the wavelengths can be realized via crystal temperature and cavity length. In this configuration gap-less tuning could be realized between 1202–1564 nm for the idler and 806–954 nm for the signal wavelength. The oscillation threshold can be as low as 0.9 W and a single-mode single frequency output power exceeding 1 W for the idler field could be achieved. Details can be found in [141, 174, 175].

To use the OPO as a photon pair source, access to both signal and idler fields is necessary. Thus one of the cavity mirrors was exchanged by an output-coupling mirror with a reflectivity of 97 % for the signal wavelengths. These additional losses increase the oscillation threshold (e.g. from 0.9 W to 2.5 W at 895 nm). However, with increased pump power it is still possible to generate high single frequency output powers above 1 W for now both signal and idler field. The OPO is still in a singly resonant operation mode.

If the pump power is reduced below threshold, the losses exceed the round trip gain and there is no feedback for the signal field. Signal and idler photons are generated by spontaneous parametric down conversion (SPDC). In the SPDC process the spectral and temporal shape of the generated photons' wave packet is in first order determined by the phase matching conditions. However, in the case of an OPO the nonlinear medium is embedded in a cavity and thus the photons can only be generated in resonant cavity modes. This resonance effect allows for enhancement of the down conversion process and shaping of the wave packet. This was first observed and described by Ou and Lu [60, 177]. As a result, OPOs became a popular source for narrowband photon pairs. Many sources are designed at the point of frequency degeneracy and thus such OPOs are operated in a doubly resonant scheme. However singly resonant OPOs can be used as pair sources as well. In our OPO only the signal field is resonant. Due to the frequency correlation of the photons the influence of the cavity will also be visible in the spectrum of the idler photons (which are not resonant) [178]. In the next section the experimental results for these properties will be presented.

5.1.1 Photon Properties

As introduced above, we can assume the spectrum of the signal photons to be a product of the phase matching spectrum and the transmission spectrum of the OPO cavity. The resonator spectrum is described by an Airy function, i.e. in first approximation a train of Lorentzian peaks. The distance between these peaks is known as the free spectral range (FSR) which is inversely proportional to the cavity round trip time. The cavity length was designed to give a FSR around 1 GHz. The width of the peaks is given by the finesse \mathcal{F} of the cavity:

$$\mathcal{F} = \frac{\pi\sqrt{|r|}}{1-|r|} \quad (5.1)$$

With a total mirror reflectivity of $r = 0.999^3 \cdot 0.97$ this leads to $\mathcal{F} = 186$ and a cavity linewidth of $\delta\nu = \frac{FSR}{\mathcal{F}} \approx 5.4$ MHz. This is an approximation where we neglected losses in the cavity. Additional loss would decrease the finesse and increase the linewidth. Thus the spectrum should be composed of lines separated by 1 GHz, each having a width of a few MHz. The resolution limit of the single photon grating based spectrometers in our lab is around 30 GHz and thus not capable for resolving the fine structure. We only measure the envelope of the spectrum as can be seen in Fig. 5.1. The shape of the spectrum is asymmetric and differs from the ideal sinc^2 -shape which can be explained by inhomogeneities in the poling structure. It has a width of 275 GHz (FWHM). As there is no direct access to the spectral fine structure we next investigate

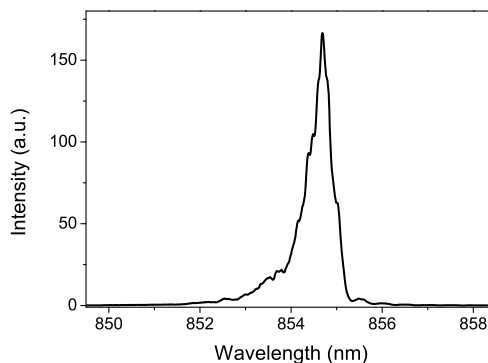


Figure 5.1: Spectrum of the OPO signal photons, measured below threshold.

the temporal shape of the photons. In the photon picture of the SPDC process, a pump photon decays into a signal and an idler photon, i.e. both photons are created at the same time. In our OPO the idler photon will immediately leave the cavity while the corresponding signal photon will have a chance to be reflected at the output coupling

mirror followed by another cavity round trip. Thus the detection of an idler photon can define the starting time for a measurement of the temporal correlation between the photons. The correlation of idler and signal detection events will reveal the temporal characteristics of the photons determined by the cavity, i.e. the round trip time and the cavity decay time. The experimental setup is shown in Fig. 5.2a. To reduce the

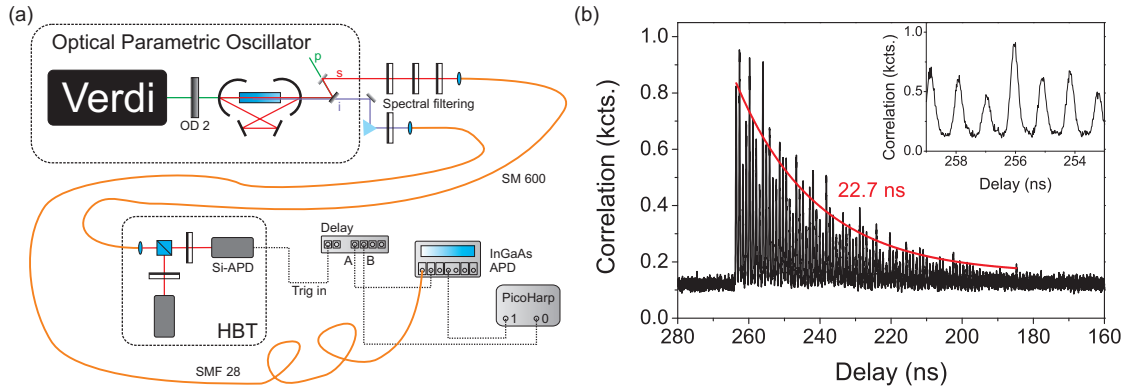


Figure 5.2: Time correlation measurement of the OPO photon pairs. a) shows the experimental setup. b) shows the result of the correlation. The inset is a close-up view of the comb structure.

multi-pair contribution the OPO was operated with a very low pump power of 0.5 mW. Behind the OPO, broad-band spectral filters were used to suppress the pump laser as well as noise photons from unwanted processes. The photons were coupled to single-mode fibers and guided to the detectors. The signal photons were registered with a silicon avalanche photo diode (APD, Perkin Elmer SPCM-AQRH-14). This APD was installed in a HBT interferometer, i.e. at the beam splitter half of the signal photons are lost for this particular measurement. The electronic detection signal of the APD is used as a trigger for a delay generator (Highland Technologies T560). A copy of this pulse was sent to the correlation electronics (Picoquant Pico Harp 300) and marks the detection time of the signal photon. After a certain delay time, another pulse is sent to an InGaAs single photon avalanche detector (SPAD, IdQuantique id201). This detector can only be operated in a gated mode. That means, the detection pulse of the signal photon triggers the gates for the detection of an idler photon. The idler photons are optically delayed by a fiber before being detected by the InGaAs-SPAD. The setting of the delay generator was varied continuously to scan the gate of the InGaAs-SPAD over the peak structure. The gate of the SPAD was set to 5 ns. Its detection output was recorded by the second channel of the correlation electronics.

After recording the detection events for 5400 s the lists with the detection time tags were correlated to calculate the second order correlation function. The result is shown in Fig. 5.2b. The expected structure of a pulse train is clearly visible. The pulses have an average distance of 939 ps which corresponds well with the designed cavity length 1 ns (FSR 1 GHz). Furthermore, the envelope of the peak structure resembles the exponential cavity decay. An exponential fit gives a time constant of $\tau_d = 22.7$ ns for the cavity decay time. From this value we can calculate the linewidth of a single mode: $\delta\nu = \frac{1}{2\pi\tau_d} = 7$ MHz in agreement with our initial estimation for the cavity linewidth. In summary, shape of the correlation function consists of a comb of peaks, separated by the round-trip time of the resonator. The width of the peaks is determined by the total spectral bandwidth of the SPDC photons. The height of the peaks shows an exponential decaying envelope which corresponds to the cavity decay time. The time constants derived from this shape agrees very well with the expectations. There also exist theoretical descriptions of correlation functions from an OPO [178] fitting well to our experimental findings. However, the shape of each individual peak in Fig. 5.2b is still not fully resolved as in our measurement it is resolution limited due to the detector timing jitter (350 ps for the Si-APD, 250 ps for the InGaAs-SPAD).

To gain more insight into the structure of the photons we proceed with a high resolution method. By sending the photons through a Michelson interferometer we can measure the first order coherence function containing both temporal and spectral information. Details about the interferometer can be found in [179]. It offers a maximum path length difference of 1.7 ns and a minimum step size of 7 fs. A sketch of the setup is shown in Fig. 5.3a. For different delays the output count rate was recorded while the

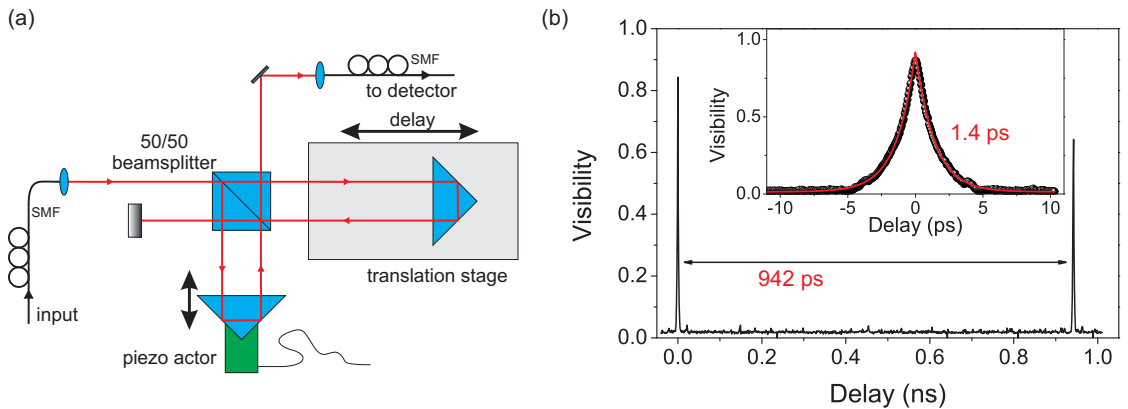


Figure 5.3: Interferometric measurements of the SPDC photons. a) shows a sketch of the Michelson interferometer setup. b) shows the interferogram of the photons. The inset shows a high-resolution scan of the first peak.

piezo arm of the interferometer was continuously scanned. By fitting the fringes in the count rate, the visibility can be calculated. The interferogram (displayed in Fig. 5.3b) describes the visibility as a function of the optical delay. The graph shows the raw-data without any noise subtraction, so the maximum visibility of 0.9 is mainly limited by dark counts and interferometer alignment. The main graph shows a long-range scan of the delay. There is one peak at zero delay and another peak appears at a delay of 942 ps. This delay corresponds to the round trip time of the OPO cavity, confirming the time correlated photon counting results. The inset shows a high resolution scan of the first peak. A bi-exponential fit of the peak reveals a coherence time of 1.4 ps which corresponds well to the measured spectral width of 275 GHz (FWHM).

Another point worth mentioning is that we here indeed observed the interference of single photons with themselves. In this particular measurement the average detected count rate was 17 kcts./s which corresponds to an average temporal distance of 26 μ s between consecutive photons. This is about three orders of magnitude larger than the maximum delay in the interferometer. Thus one can claim that simultaneously never more than, on average, one photon was present in the interferometer. The observed interferogram thus resembles the wave packet and coherence properties of any single photon of the signal field.

To prove the single photon character of the emission, the standard procedure is to measure the heralded second order correlation function. The experimental setup is sketched in Fig. 5.4a. It is similar to the time correlation measurement but now the idler photons are split by a 50/50 fiber beam splitter and each output is attached to an InGaAs-SPAD. Both SPAD are triggered by the detection of a signal photon. Thus the detection of a photon in a signal mode heralds the presence of an idler photon. The gate width was set to 50 ns. However, there is one issue with this standard procedure to take into account. The coherence length of the photons of 1.4 ps is much shorter than the detector timing jitter of 250 ps. The resulting experimental data is in general a convolution between the second order correlation function and the instrument response function. To simulate this, first an idealized temporal wavepacket $f(t)$ was generated consisting of a train of Lorentzian peaks with 1.4 ps width and 940 ps separation and a height determined by an exponential envelop of 22.7 ns decay time. The ideal $g^{(2)}$ -function is then calculated with the help of the autocorrelation of the wavepacket normalized to unity as $g^{(2)}(\tau) = 1 - \mathcal{F}(\mathcal{F}(f(\tau)) \cdot \mathcal{F}^*(f(\tau)))$ (\mathcal{F} here denotes Fourier transformation). This function has a central dip going down to zero with maximum contrast. Then this function is convoluted with an Lorentzian function of 250 ps width according to the timing jitter. The result is shown in Fig. 5.4b. The jitter washes out the very narrow anti-bunching dips. In particular, the resulting dip goes only down to 0.99. Obviously, such small dips will be lost in the shot noise of the detection when recorded for a reasonable integration time. The experimental measurement result for such a $g^{(2)}$ -function is shown in Fig. 5.4c. The function here has

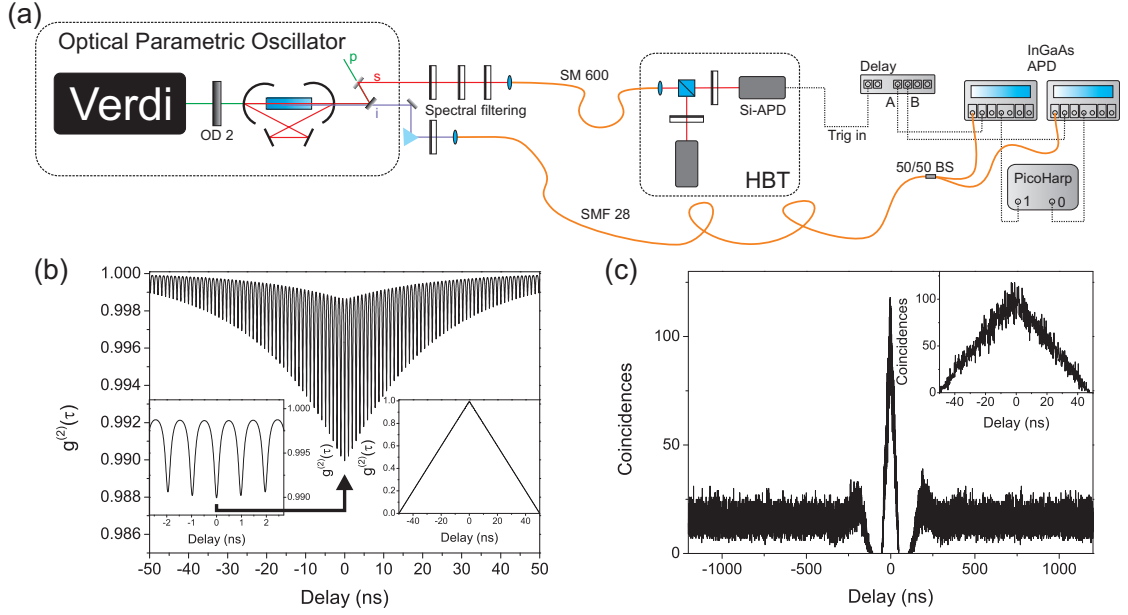


Figure 5.4: Heralded $g^{(2)}$ measurement. a) sketch of the experimental setup. b) simulated $g^{(2)}$ -function for free-running detectors including timing jitter. The left inset shows a close-up around zero delay. The right inset shows the same function for a gated measurement. The fringes are hardly visible. Please note the scale bars of the plots. c) experimental results for heralded $g^{(2)}$ -function.

a triangular shape. This is due to the rectangular shape of the detection gates. If two such gates are correlated (autocorrelation function) the result is a triangle where the baseline has twice the width of the original rectangle. This fact can also be included in the simulation as shown in the inset of Fig. 5.4b. The resulting dips in the triangle are hardly visible. Nevertheless we can use the experimental data to calculate a value for $g^{(2)}(0)$ and the anti-correlation parameter α , according to equations 2.86 and 2.85. The results for two different pump powers are summarized in table 5.1. At these low pump powers the source obviously delivers single photons with high purity.

P[mW]	t (s)	N_{herlad}	N_{coinc}	N_1	N_2	α	$g^{(2)}(0)$
0.1	18405	25840620	4449	4100159	5156877	0.005	0.005
5	3638	208835752	38790	13051217	18848215	0.033	0.032

Table 5.1: Heralded second order correlation measurements of the idler photons. P: pump power; t: measurement time; N_{herlad} : number of heralding events; N_{coinc} : number of triple coincidences; N_j : detection events on SPAD j .

5.1.2 Narrowband Correlated Photon Pairs

In the previous section the photons were characterized as generated from the OPO. The results proved that they are emitted in multiple spectral modes. The coherence length could be drastically increased if a single mode was cut out from the spectrum. In the experiments carried out for narrowband single photon generation the OPO was set to a signal frequency around 350.863 THz (854.443 nm) at a transition in Ca^+ -ions. The corresponding idler wavelength is around 1411.242 nm. One goal is to generate photons resonant with the afore mentioned transition. Thus the following requirements for a spectral filter can be summarized: A single mode should be transmitted, i.e. the pass-band should be broader than the 7 MHz measured for a mode. Further, the pass-band should be smaller than the FSR of the OPO to suppress neighboring modes. The rejection region should be broader than the width of the OPO spectrum. For the filtered mode the transmission should be as high as possible to not lose photons. Finally, tuning of the filter center is desirable to compensate for drifts.

In telecommunication applications there exist fiber based optical filter systems like wavelength division multiplexers for coarse wavelength separation and fiber Bragg gratings (FBG) which can also be used for narrow filtering. The filter used in our case for the OPO is based on the latter devices which thus should be introduced briefly. The fibers have the same layout as usual single mode fibers but their core is slightly doped (e.g. with germanium) to make it photo-sensitive [180]. This photosensitivity can be exploited to optically induce refractive index changes in the fiber core: either by direct laser writing or holographic techniques the fiber can be exposed to light and a periodic pattern is imprinted in the refractive index. In analogy to dielectric coatings on bulk optics surfaces, such Bragg structures can be used to tailor the reflectivity. Whereas the thickness of dielectric coatings is limited mechanically, very long structures are possible in fibers. Hence FBG can be designed to have a very narrow reflection bandwidth. A fiber optic circulator can be used in combination with the FBG to separate the reflected signal from the ingoing one, the rejected part of the spectrum is transmitted through the FBG fiber. For standard applications these FBG are usually limited to a few GHz in bandwidth. To fabricate much more narrow FBG filters a phase shift can be introduced in the grating structure [181, 182]. This results in a very narrow transmission peak inside the reflection region. In this manner, filters down to the MHz regime are commercially available. One drawback is that the rejection bandwidth of such a phase shifted FBG is rather small. The disadvantages of both FBG can be compensated: when they are combined the standard FBG can be used for coarse filtering with practically unlimited rejection bandwidth and the reflected signal can be sent to a phase shifted FBG for narrowband filtering. The FBG can be tuned via temperature, changing the elongation of the Bragg structure. The device used here to filter the idler photons (AOS Ultra Narrow Transmission filter)

is customized for our wavelengths and based on the afore described combination of two FBG. To characterize the FBG system, the OPO is operated above threshold. In this case, the linewidth is in the low MHz regime and the mode hop free tuning range is 1 GHz. In this way, the filter transmission spectrum can be recorded with the OPO by stitching together several measurements. A part of the OPO emission is separated before coupling the rest to a fiber and used as power reference. By measuring the transmitted power behind the filter, the transmission can be calculated. The result is shown in Fig. 5.5a. The fit shows a maximum transmission of 13 % including insertion loss. The filter has a bandwidth of 1.56 GHz with a Lorentzian shape.

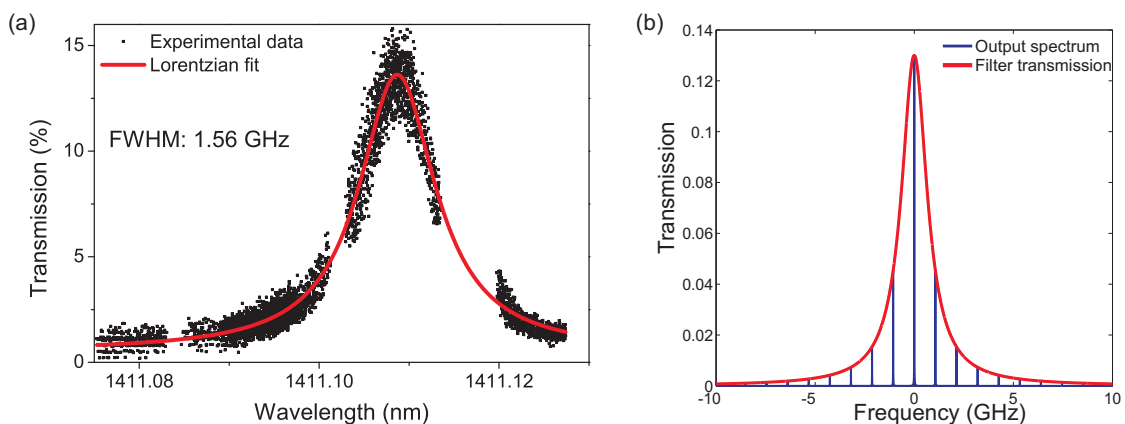


Figure 5.5: Characterization of the narrowband filter system for the idler photons. a) shows a transmission spectrum including insertion loss. b) shows the simulated transmission of the OPO spectrum through the filtering system.

Both numbers for transmission and width are below the initial specifications (1.2 GHz FWHM, 50 % transmission). The low transmission introduces additional loss in the idler channel reducing the coincidence rates and the signal to noise ratio in correlation measurements. Numerical simulations of the spectrum show, when operating the OPO as SPDC source, in best case 44.6 % of the photons transmitted through the filter stem from the central OPO mode, the rest from neighboring modes (see Fig. 5.5b). This automatically limits the achievable signal to background ratio. The measurement illustrated in Fig. 5.5a can be repeated for different FBG temperature settings. With this data the tuning curve can be measured (Fig. 5.6a). The total tuning range exceeds an interval of 90 GHz around 1411.3 nm. As mentioned earlier, the tuning capability is necessary to compensate for frequency drifts of the OPO. Figure 5.6b shows a long-term measurement of the frequency of the OPO pump laser. Obviously after two hours of warm-up time during which the frequency drastically decreases the

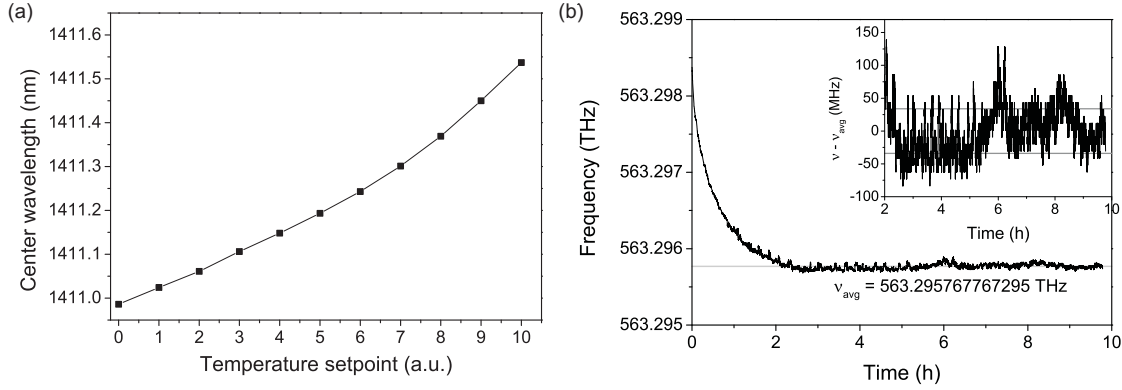


Figure 5.6: a) demonstrates the tuning capability of the center linewidth for the FBG filter system. b) shows a long-term measurement of the OPO pump laser frequency. After two hours of warmup it is stable. The inset shows the frequency deviation from the long-term average value during the stable operation period.

laser stabilizes. After warm-up in this example we have an average pump frequency of $\nu_p = 563.295767$ THz ($\lambda_p = 532.2115$ nm) with a standard deviation of only 34 MHz. The later goal of these experiments is the interaction of the OPO signal photons with a single Ca^+ -ion. The transition of interest ($4^2P_{3/2} \leftrightarrow 3^2D_{5/2}$) has a transition frequency of 350.862887 THz ($\lambda_{Ca} = 854.4433$ nm). This frequency was determined by probing the transition with a stabilized diode laser and measuring its wavelength with a wavemeter (High Finesse WS-7). Accordingly, using these two values we can calculate the frequency of the idler photon $\nu_i = \nu_p - \nu_{Ca} = 212.432879$ THz ($\lambda_i = 1411.2338$ nm). The FBG filter system can then be set to this value. An active stabilization scheme between filter and pump laser is not necessary here because the frequency fluctuations of the laser are much smaller than the transmission bandwidth of the filter. The photons transmitted through the FBG filter system were later detected by a superconducting single photon detector (SSPD).

Up to now in this section the narrow-band filtering of the idler photons was described. The detection rate of the unfiltered signal photons is by two orders of magnitude higher compared to the narrowband filtered idler photons. A correlation measurement between them would suffer from high background due to uncorrelated detection events. Thus for the characterization of the source it is necessary to filter out a single mode in the signal branch, too. Therefore, an existing system of filtering cavities was used [183, 184]. It consists of two cascaded Fabry Perot cavities of different length. The cavities are actively stabilized to an atomic reference. The combination of linewidth and FSR of both resonators is designed to emulate the $4^2P_{3/2} \leftrightarrow 3^2D_{5/2}$ transition in a calcium ion in central wavelength and the linewidth of 22 MHz. Thus the signal photons of the OPO were coupled to a single mode fiber (90 m of SM600 fiber) and sent to the lab (AG

Eschner) where the filtering system was installed. Behind the cavities the transmitted photons were detected with a silicon APD (Perkin Elmer SPCM-AQRH-15). The overall transmission of the filtering system is limited by attenuation of the fiber channel and especially the mode-matching to the filtering cavities. The coupling to the filters was optimized for a different concurrent experiment and could not be changed which resulted in rather low coupling ratio for the experiments described here. These losses reduce the over-all coincidence rate and heralding efficiency. We measured an over-all transmission of 2.1 % between the OPO and the detector. This includes 27.3 % for fiber coupling and transmission to the ion lab, 60 % transmission of the filter cavities and 13 % transmission for the bypass path between fiber and cavities. This last number can be increased to nearly 100 % by optimizing the beam path for this particular experiment. The transmission of the fiber is low because it was originally intended to transmit shorter wavelengths.

To measure the temporal correlation between the narrow-band filtered OPO photon pairs, the signal photons behind the filter cavities were detected with the silicon APD. The idler photon behind the FBG filter was detected with the SSPD and the electronic signal was sent to the lab where the filtering cavities were set up (AG Eschner). There the detection signals of both photons were recorded with a time tagging electronics (Picoquant Pico Harp 300) and correlated afterwards. The wavelength of the central OPO mode has to fit the filter window of only 22 MHz. However, the fluctuations of the signal frequency are larger than this (peak to peak fluctuations of 160 MHz were observed in [141, 174]) as will be shown in more detail in the next section. For this initial experiment the OPO frequency was thus permanently scanned over the filter resonance. These correlations were carried out for different OPO pump powers. The results are illustrated exemplarily in Fig. 5.7 for two powers values. The temporal shape of the photons is now determined by the OPO spectrum and the whole filtering system. The signal photons are filtered down to 22 MHz by the cavities while for the idler photons a single line is cut out from the OPO frequency comb that was described in the beginning of the chapter. Both filters will cause an exponentially decaying temporal shape of the wave packet. In the correlation this results in a convolution of both curves:

$$\begin{aligned}
 f(t) &= \int_{-\infty}^{\infty} \Theta(t-x) \exp\left(\frac{-(t-x)}{\tau_1}\right) \Theta(x) \exp\left(\frac{-x}{\tau_2}\right) dx \\
 &= \frac{\tau_1 \cdot \tau_2}{\tau_2 - \tau_1} \left[\exp\left(\frac{-t}{\tau_2}\right) - \exp\left(\frac{-t}{\tau_1}\right) \right]
 \end{aligned} \tag{5.2}$$

Here $\Theta(x)$ is the Heaviside function. Thus equation 5.2 can be used as a fit to the data. As shown in Fig. 5.7 it describes the experimental data quite well. The fit parameter for the longer decay is around 20 ns for all powers which is consistent with the OPO cavity ring down time measured earlier. The second time constant is 7 ns

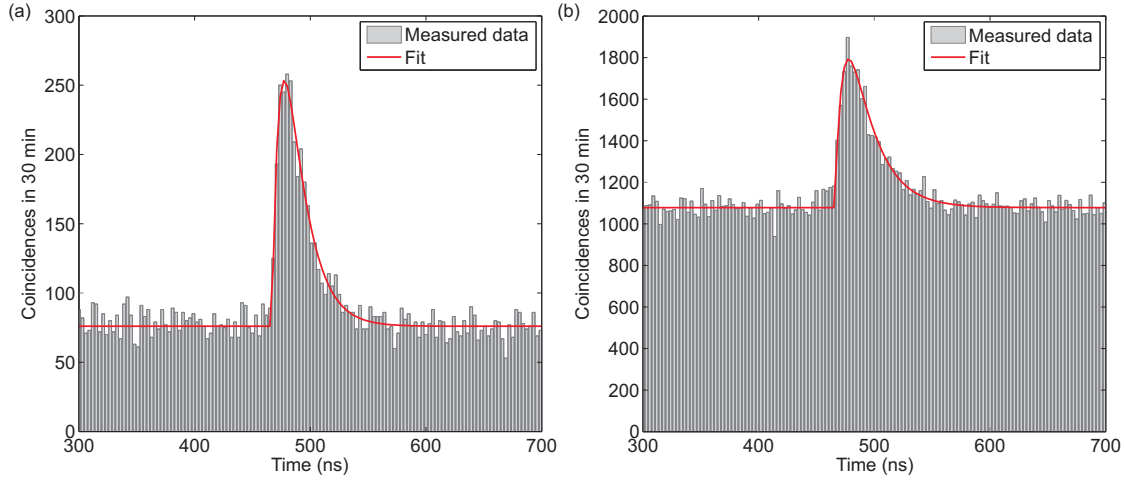


Figure 5.7: Correlation of narrow-band filtered photon pairs for pump powers of a) 300mW and b) 1200mW. The integration time was 30 min and for the graph a bin size of 3 ns was used. The red line shows a fit to the data.

corresponding to the filter cavity bandwidth. In addition, further parameters of the photon pair source can be derived from the fit data. The offset of the fit equals the number of accidental coincidences per time bin. The area of the fit curve without the offset gives the number of signal coincidences. By integrating signal and offset over a common interval (here we use the full $1/e$ width) and dividing both numbers we can calculate the signal to background ratio (SBR). The noise in the measurement is mainly statistical shot noise and thus described by the square root of the count number. This can be used as error for the calculated numbers. The signal to noise ratio (SNR) hence is the ratio between signal counts and this shot noise. Figure 5.8 shows some of these experimentally derived values for different OPO pump powers. As expected, the coincidence rate depends linearly on the pump power. It has a slope of $6.13 \cdot 10^{-4}$ coinc./($s \cdot mW \cdot MHz$) which results in $5 \cdot 10^{-3}$ pairs/($s \cdot mW \cdot MHz$) corrected for detection efficiency. This value is small compared to state of the art OPO pair sources [185]. This is due to the losses in both filtering systems as described earlier. The measured SBR decreases approximately hyperbolically with power which means that true coincidences will be more and more lost in accidental correlations. An additional, more systematic source of errors in these measurements is the fact that the single photon wavelength is continuously scanned over the resonance. Hence the filter cavity can only be passed in short time intervals during a scan cycle whereas the idler photons are permanently registered due to the much broader filter width of the FBG. This effect can be estimated by integrating the count rate behind the filter in a long term measurement and comparing this average value with the average peak count rate. For a representative measurement this results in a duty cycle of 0.24. Thus for ideal

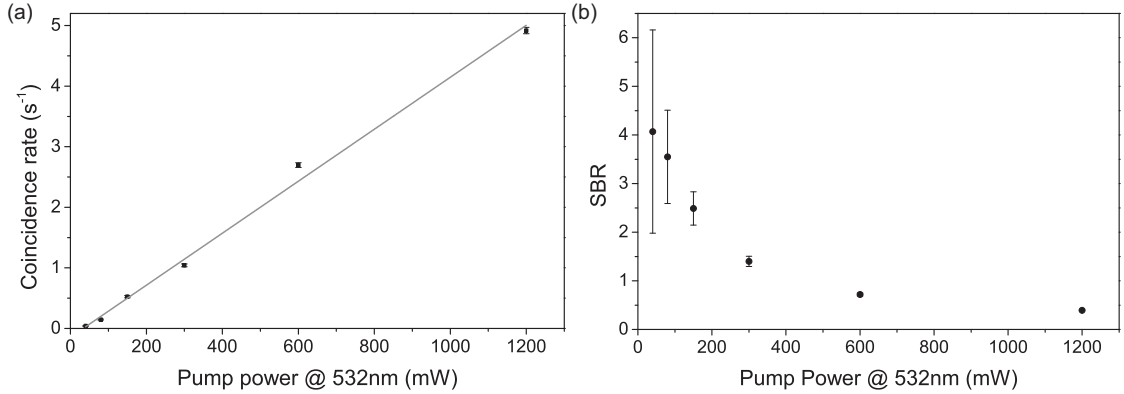


Figure 5.8: Results of the narrowband filtered SPDC correlation measurements. a) shows the coincidence rate together with a linear fit. b) shows the signal to background ratio (SBR) as a function of the pump power.

resonance the coincidence rate should be at least a factor of four higher than values measured here. The relatively low coincidence rate is mainly caused by the losses. On the idler side only 13 % of the photons reach the detector while on the signal side even more photons are lost due to the transmission over several fibers with a total length of more than 100 m and the coupling to the filtering cavities (approximately 98 % of the photons are lost).

In this section we saw that we can generate narrowband photon pairs bridging the near infrared spectral region with the telecom bands. There is a temporal correlation between these photons that can be exploited to establish a heralded telecom single photon source with low $g^{(2)}(0)$ -values, as demonstrated. Furthermore, these photons are compatible with atomic transitions in the NIR. Hence we next investigate the absorption of the signal photon by a single atom. The correlated telecom partner photon can serve as a herald for this transition as will be shown in the next section.

5.2 Interaction with a Single Trapped Ion

In the previous section the properties of the single photons generated by the OPO were investigated in detail. It turned out that after narrowband filtering to a single mode, the photons are compatible with an atomic transition in calcium. In this section experiments demonstrating the interaction of single photons with a single trapped ion are presented. In particular, spectroscopy of the 854 nm transition of $^{40}\text{Ca}^+$ with single photons and finally the absorption of single 854 nm photons was heralded by the detection of 1411 nm telecom compatible photons were performed.

5.2.1 Single Photon Spectroscopy

The frequency fluctuations of the pump laser, as already shown in Fig. 5.6b, are larger than the width of the 854 nm transition in calcium. The OPO signal photons suffer further frequency distortion due to cavity stability and influence of environmental effects on their generation process: In earlier experiments with the OPO above threshold, the effect of the lab air condition could be clearly identified [174]. We can expect to see a similar influence for the operation below threshold. Thus, for effective interaction with the ion the signal wavelength has to be stabilized to the atomic transition. The setup can be found in Fig. 5.9. We split the photons by a 50/50 fiber based beam splitter

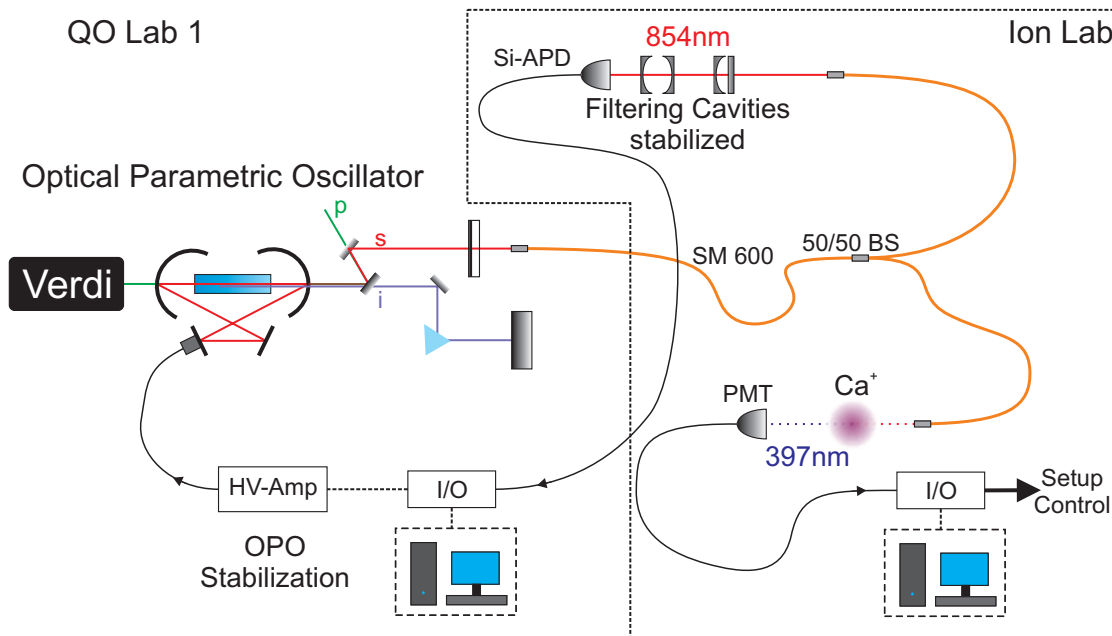


Figure 5.9: Setup for linewidth measurement

and couple one half of the signal photons to the filtering cavities and the other half is coupled to the ion. We neglect the idler photons for this experiment. We use the filtering cavities as a reference to stabilize the OPO output. The locking of the OPO to the filtering cavities was realized by a side-of-fringe stabilization. This means the signal wavelength was first scanned over the resonance to measure the transmission of the filter reference. Assuming stable single photon generation rate and staying on one side of the Lorentzian transmission profile there is a unique relation between count rate and frequency. Stabilizing to a fixed frequency thus means stabilizing the transmitted count rate. The APD was connected to a data acquisition card (DAQ, National

Instruments NI USB-6009) controlled by a homemade LabView program. The counts were integrated for 50 ms. A homemade PID controller was implemented in software. It compared the current count rate with a set-value and calculated an error signal. The controller included two independent integrators reacting on short timescales to compensate for distortions and long time scales to compensate for drifts. Both were combined appropriately to the integral part of the controller. Additionally, there was an interface to manually influence the control-loop. Finally the error signal was sent back to the DAQ to generate an analogue voltage output. This signal was linearly amplified using a homemade high voltage amplifier and connected to the piezo transducer at the OPO cavity. As mentioned earlier, the filtering cavities are actively stabilized to the calcium transition. By shifting the frequency of the locking laser with an acousto-optic modulator (AOM), a constant frequency offset can be established between the cavity resonance frequency and the atomic transition. Hence the filter resonance can be tuned over the Ca^+ transition via the AOM frequency. As the signal photons are actively stabilized to the filters they will also be scanned over the transition [186].

The pump power of the OPO was set to 300 mW resulting in a maximum detected count rate of 8100 cts./s on filter resonance with an average background rate of 154 cts./s. Figure 5.10a shows a long-term record of the rate measured by the DAQ system. The setpoint was chosen at 3600 cts./s here. The long-term average value of the count rate is indeed 3600 cts./s with a standard deviation of 707 cts./s. We

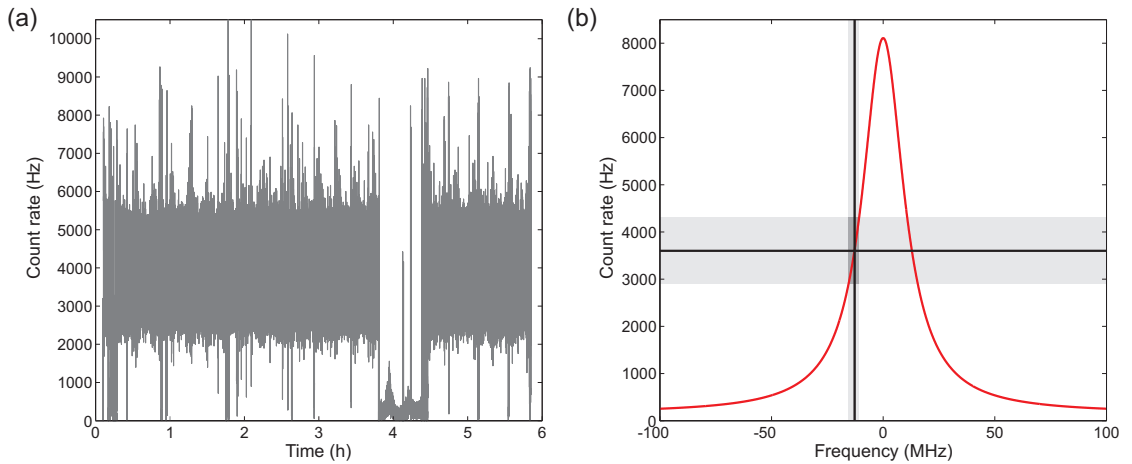


Figure 5.10: Frequency Stabilization of the OPO photons. a) shows a time trace of the count rate measured behind the filter cavities. b) shows the calculated transmission profile of the filter normalized to the average peak count rate in a). The horizontal black line indicates the long-term average count rate and the vertical line is the corresponding frequency. The shaded areas indicate the standard deviations around the black lines.

attribute the long-term drifts to the influence of air condition, as mentioned above, while for the short-term fluctuation no source could be clearly identified. Figure 5.10b shows a calculated profile of the filter transmission, scaled with the actually measured count rates. The crossed lines indicate the set-point while the shaded regions show the standard deviation intervals. In particular, a rate of 3600 cts./s here corresponds to a frequency offset of -12.8 MHz. The standard deviation of 707 cts./s translates to a frequency variation of 2.7 MHz. The setpoint was chosen to realize an approximately linear relation between count rate and frequency. In Fig. 5.10a after around 4 h of measurement time the count rate dropped to the dark count level. Here the filtering cavities fell out of lock (to the atomic resonance) and the measurement had to be interrupted. The time was used for check-up and optimization of the setups before continuing.

Detection of Quantum Jumps

To observe the interactions between photons and the single ion we decided to search for quantum jumps. In the following, this procedure will be explained in more detail. A scheme of the energy levels of $^{40}\text{Ca}^+$ is illustrated in Fig. 5.11.

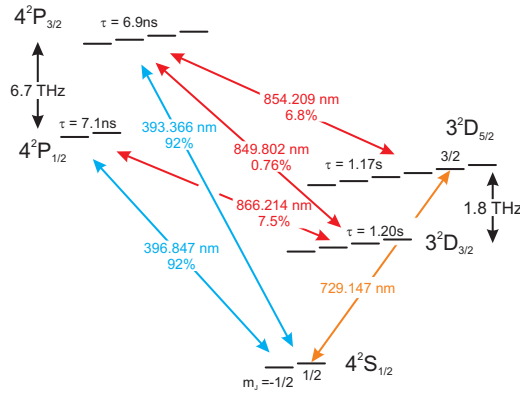


Figure 5.11: Detailed level scheme of $^{40}\text{Ca}^+$. Wavelengths measured in air. Reproduced from [187].

The sequence for initialization of the ion and detection of quantum jumps is illustrated in Fig. 5.12 (The level $3^2\text{D}_{3/2}$ was ignored here for clarity). In the beginning the ion is prepared in the ground-state ($\text{S}_{1/2}$, $m = -\frac{1}{2}$) by optical cooling and optical pumping (Lasers at 729 nm, 854 nm and 866 nm switched on). This initialization succeeds with an efficiency of 99.6 %. In the next step a sequence of four laser pulses at 729 nm ($40 \mu\text{s}$) transfers the population into the meta-stable $\text{D}_{5/2}$ manifold with a

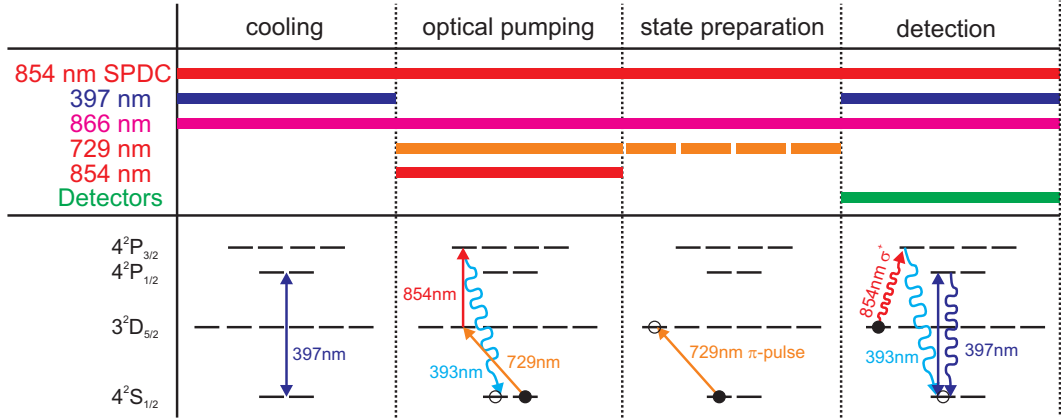


Figure 5.12: Sequence of laser emission for ion control and the detection of quantum jumps in $^{40}\text{Ca}^+$.

probability of 99.99 % with 99.2 % of the population ending in the $m = -\frac{5}{2}$ sub-level. Due to the quadrupole character of the transition to the ground state ($D_{5/2} \rightarrow S_{1/2}$), the state has a relatively long lifetime of 1.17 s. After this initialization the absorption and detection sequence follows. To this end, the lasers at 397 nm (driving the transition $S_{1/2} \rightarrow P_{1/2}$) and 866 nm ($D_{3/2} \rightarrow P_{1/2}$) are switched on. A gating circuit interrupts the detection during the initialization and now activates it. If a photon at 854 nm is now absorbed, the ion will be excited to the $P_{3/2}$ state. With a probability of 94.2 % it then will decay into a state involved in the cooling cycle, i.e. into $S_{1/2}$ (93.5 %) or $D_{3/2}$ (0.7 %). As there is now population in the cooling cycle, fluorescence at 397 nm will be generated. This onset of fluorescence serves as evidence for the absorption of a photon. The fluorescence is collected by two high aperture laser objectives (HALO) and detected with two photomultiplier tubes (PMT). The over-all detection efficiency is 1 %. The detection cycle is continued for 50 ms. The probability for spontaneous decay ($D_{5/2} \rightarrow S_{1/2}$) during this time is 4.2 %. After the detection interval the ion is again prepared in the ground state and the sequence starts from the beginning. The starting time of a sequence and the detection events of the PMT are recorded by time tagging electronics.

We chose to detect the absorption via quantum jumps as this technique offers a high detection probability. As described, the population will decay with 94.2 % probability into the cooling cycle. Caught in this cycle many 397 nm photons will be scattered. Thus the probability of detecting any of them grows with ongoing detection cycle time. One drawback is the rather low repetition rate of the sequence due to the detection interval time.

In the post-processing, we consider the time of occurrence of fluorescence as the ab-

sorption time of the photon. The time delay between the beginning of the detection cycle and the absorption event is the current lifetime of the $D_{5/2}$ state. This measurement is repeated many times and a histogram of the time delays is generated. The exponential decay time of this histogram is the effective lifetime of the $D_{5/2}$ state. As mentioned earlier, the natural lifetime in $D_{5/2}$ is 1.17 s. If a 854 nm photon is absorbed, the population can decay into the ground state within 7 ns drastically reducing the effective lifetime. The absorption probability of a photon depends on the spectral shape of both photon and transition. On resonance the lifetime thus should be clearly reduced compared to the spontaneous decay. The inverse value of the lifetime in consequence is a measure for the strength of absorption.

We can exploit this fact to measure linewidth and shape of the transition via single photon spectroscopy. Therefore we measure the effective lifetime for various frequency detunings as shown in Fig. 5.13. To exclude systematic errors and long term drifts

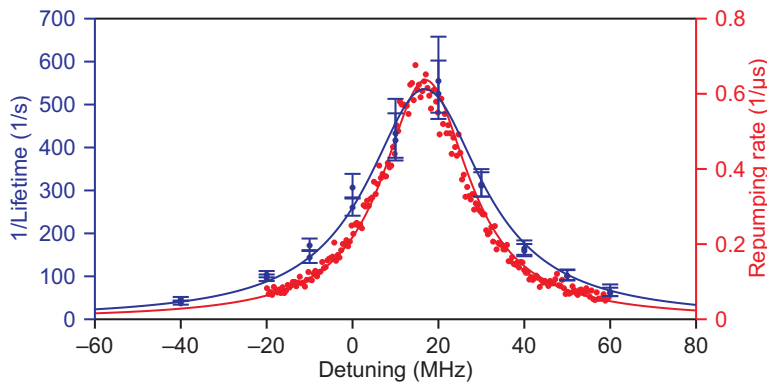


Figure 5.13: Spectroscopy of the calcium transition at 854 nm. The red line shows a reference measurement with a narrowband laser. The blue data show the inverse value of the effective lifetime for different frequency detunings. The measurement was repeated several times starting red- or blue-detuned, indicated by overlapping data points.

during the measurement, the data acquisition was repeated four times. Every series included one measurement starting from red detuning to blue detuning and back again. The data is fitted with a Lorentzian function with a width of 34.05 ± 0.91 MHz. The fit shows a frequency offset of 17 MHz in accordance with the offset introduced by the side of fringe stabilization scheme. The resulting line is again a convolution of the natural Lorentzian linewidth (22.986 ± 0.063 MHz, [188]), the linewidth of the single photons (7.2 ± 1.1 MHz) and the frequency fluctuations due to the stabilization process (5.4 MHz). If we assume all these noise sources and the single photon width

to have Lorentzian shape, the values can be added to yield the convoluted linewidth. Hence we expect a value of 21.45 ± 2.01 MHz as natural linewidth of the transition. This agrees well with the literature value of 23 MHz within the error bars [188]. For comparison, we repeated the measurement with a narrowband diode laser (see red data in Fig. 5.13) which does not suffer distortion by our side of fringe stabilization and has a lower intrinsic linewidth. With the laser we find a width of 24.6 MHz confirming the results.

This result demonstrates that we can use the OPO to generate narrowband single photons, compatible with atomic transitions. The stabilization of the OPO is well suited to fine-tune and stabilize the photon frequency. In the end we were able to directly address an atomic transition and perform single photon spectroscopy. The frequency dependent reduction of the effective lifetime of the $3^2D_{5/2}$ -state is a clear indication of the OPO's single photons interacting with the ion.

5.2.2 Telecom-Heralded Absorption

For the spectroscopy of the atomic transition at 854 nm we did not exploit any properties of the photon pair state. Nevertheless, according to the operation parameters, the OPO generated optical fields at the single photon level. The spectroscopy showed that the transition in Ca^+ can be directly addressed with a selected spectral mode of the OPO. We already know from the previous results (see sec. 5.1.2) about the temporal correlation between the signal and idler photons. The experiment in this section will demonstrate the preservation of this correlation in the absorption process.

The experimental setup can be found in Fig. 5.14. It is similar to the setup for spectroscopy of the Ca-transition. Now we set the frequency of the signal photons to center the resonance with the 854 nm transition to achieve maximum absorption probability. The idler photons are filtered by the FBG system to cut out essentially the frequency mode corresponding to the resonant signal mode. The idler photons are detected by a SSPD. The detection events are recorded by a time tagging electronics. The quantum jumps on the other hand are recorded as described earlier. In the post processing the point in time of the onset of quantum jumps is correlated with the idler detection times. The result is shown in Fig. 5.15. The central peak clearly proves a temporal correlation between the idler photon and the quantum jumps in the single calcium ion. The detection events were integrated for 310 min and 9034 coincidences were found (0.49 coincidences per second). However, this signal sits upon 1876516 background coincidences (per $7 \mu\text{s}$ time bin) resulting in a SBR of $4.81 \cdot 10^{-3}$ and a signal to noise ratio (SNR) of 6.59. The poor temporal resolution of the quantum jump detection scheme does not allow to resolve the temporal structure in the correlation peak. In this measurement the coincidence rate is rather high (compare sec. 6.5) but also the background is large. This SBR is limited mainly by the filtering of the

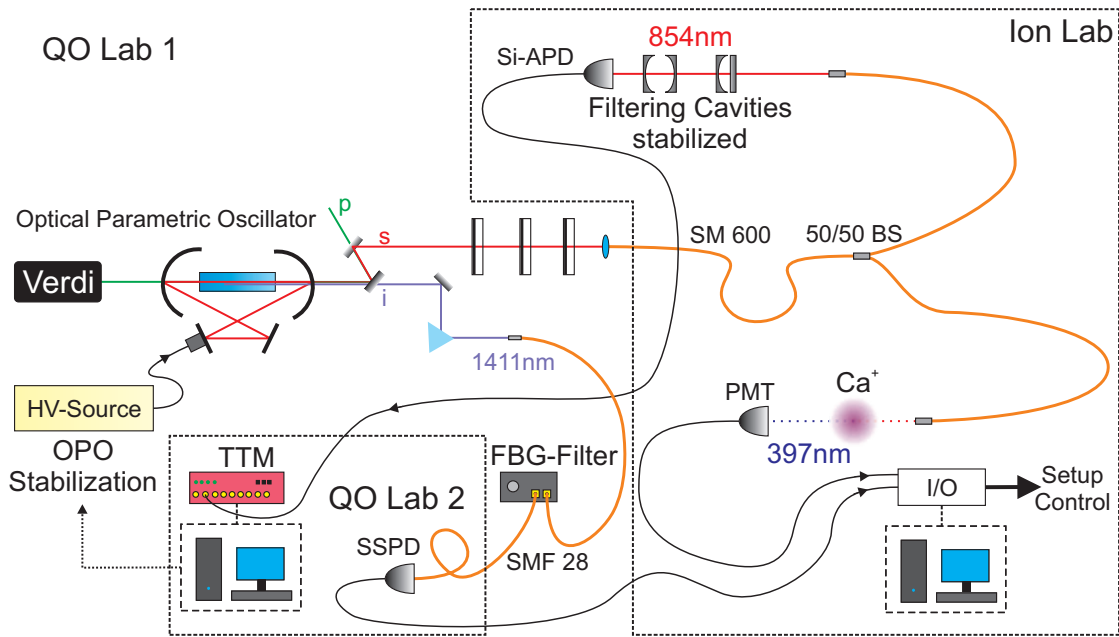


Figure 5.14: Setup for the telecom-heralded absorption measurement.

idler photons in the FBG. As shown earlier, the neighboring modes are also partially transmitted through this filter, mainly contributing to the background of uncorrelated photons. The coincidence rate is mainly limited by the absorption efficiency of the ion ($4.8 \cdot 10^{-5}$, spatial mode matching of the 854 nm photons to the ion). We can derive an estimate for the heralding efficiency from the correlation data. The probability to observe a true absorption event within $7 \mu\text{s}$ after detecting a telecom photon is

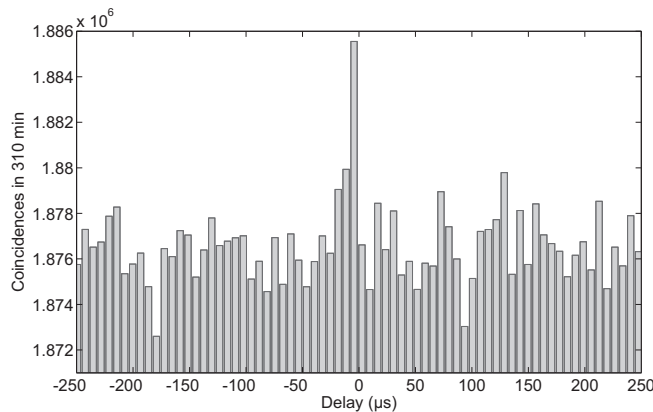


Figure 5.15: Correlation measurement between idler photons and quantum jumps (bin-size $7 \mu\text{s}$).

$4.79 \cdot 10^{-3}$ (ratio between true coincidences and total coincidences in central time bin). We can compare our results with a former report on heralded absorption in trapped Ca^+ [184] which is actually the only report so far. In that experiment a much higher pair rate (ca. 3000 s^{-1}) for narrowband photons was reached while we can estimate 8 s^{-1} for our settings. For the heralding probability, according to our definition, we can deduce a value of 89 % from the data given in [184], exceeding our result by two orders of magnitude. We can only partly attribute this discrepancy to our low filter efficiency for the herald.

With our experiment we demonstrated that the temporal correlation between the photons of the pair can be transferred to the ion-photon system by the absorption process. For the first time, we could establish this temporal correlation between the ion and a photon at a telecom wavelength. Such a heralded absorption procedure is a basic building block for quantum networks as it is based on atom-photon interaction. In our case, as the heralding photon is at a telecom wavelength, low-loss transfer of the herald in optical fibers is possible. This in principle allows heralding the state transfer in the atomic qubit over large distances.

5.3 Franson Interferometry

The superposition principle is a result common to the solutions of the wave equation leading to interference of optical fields when a wave packet is superimposed by a spatially or temporally shifted copy of itself. This effect can also be observed with non-classical states of light, e.g. single photons, due to interference of the wave function. Furthermore, photon-pair states can also be brought into interference as first suggested by Franson [29]. The basic idea is illustrated in Fig. 5.16a. The setup consists of a SPDC source generating pairs of signal and idler photons. For each mode there is an unbalanced interferometer with delay $T_{A/B}$. If the delay is smaller than the single photon coherence time, oscillations in the count rate on each individual detector, i.e.

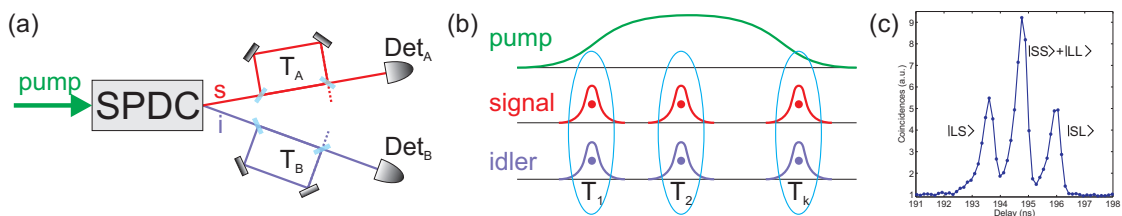


Figure 5.16: a) Setup for Franson experiment, b) timing sequence and coherence. Pictures adapted from [110]. c) Temporal distribution of the coincidences, demonstrating the path entanglement.

interference fringes, can be observed on varying the delay. For the Franson experiment, in both interferometers the delays are chosen to be much larger than the single-photon coherence time T_c but smaller than the pump coherence time ($T_c \ll T_{A/B} < T_p$) and are equally unbalanced ($T_A \approx T_B$). In this configuration, no intensity oscillations are observed on delay variation, i.e. single photon interference is suppressed. Each photon can now independently travel the short S or long L path of the interferometer before reaching the detector. Hence a photon in mode A can be described with the following state:

$$|1\rangle_A \longrightarrow \frac{1}{\sqrt{2}} (|S\rangle_A + e^{i\omega_A T_A} |L\rangle_A) \quad (5.3)$$

For the sake of simplicity, we attributed the whole phase to the long path and will use the abbreviation $\Phi_j = \omega_j T_j$. Accordingly the pair state can be expressed in the following way:

$$|\Psi\rangle = [|S_A S_B\rangle + e^{i(\Phi_A + \Phi_B)} |L_A L_B\rangle + e^{i\Phi_B} |S_A L_B\rangle + e^{i\Phi_A} |L_A S_B\rangle] / 2 \quad (5.4)$$

For equally unbalanced interferometers the photons described with the first two terms will arrive simultaneously at the detectors, as shown in Fig. 5.16c. A coincidence detection, together with the post-selection of the first two terms, can thus entangle the path of both photons. The postselected pair state can then be written as

$$|\Psi\rangle = [|S_A S_B\rangle + e^{i(\Phi_A + \Phi_B)} |L_A L_B\rangle] / \sqrt{2} \quad (5.5)$$

To derive the coincidence probability we project this state into the coincidence base

$$\begin{aligned} P_{AB} &= \left| \frac{1}{\sqrt{2}} (\langle S_A S_B | \Psi \rangle + \langle L_A L_B | \Psi \rangle) \right|^2 \\ &= \frac{1}{2} |1 + e^{i(\Phi_A + \Phi_B)}|^2 = \cos^2 \left[\frac{\Phi_A + \Phi_B}{2} \right] \end{aligned} \quad (5.6)$$

This means the coincidence detection probability is a function of the combined phase ($\Phi_A + \Phi_B$) of both interferometers (i.e. the detunings of the interferometers T_A and T_B). In the experiment we thus expect the observation of interference fringes in the coincidence rate when scanning the phase of the interferometers. The detection probability derived above predicts an interference visibility of 100 %. This means in the case of constructive interference both photons of the pair always leave the interferometers at the same output port (to the detector or the other exit). For destructive interference the photons leave their interferometers at opposite ports. Deriving the coincidence probability including all four path combinations, i.e. without the post-selection process (eqn. 5.5), results in a similar expression as eqn. 5.6 but the visibility is limited to 50 % in that case. Hence a visibility exceeding 50 % is a signature for an entangled state [189].

The basic expression above, demonstrating the interference effect, only considers a single spectral mode for each photon. For a more realistic treatment we have to take the spectral properties of the SPDC state into account. This will result in the introduction of coherence effects.

We here follow the multi-mode treatment of the pair state as outlined in [110]. The fields at the detectors are then given by:

$$\hat{E}_A = \left(\hat{E}_s(t) + \hat{E}_s(t - T_A) \right) / 2 \quad , \quad \hat{E}_B = \left(\hat{E}_i(t) + \hat{E}_i(t - T_B) \right) / 2 \quad (5.7)$$

with

$$\hat{E}_k(t) = \frac{1}{\sqrt{2\pi}} \int \hat{a}_k(\omega) e^{-i\omega t} d\omega \quad (k = s, i) \quad (5.8)$$

The two-photon coincidence can be calculated:

$$\Gamma_{AB}^{(2)}(t, t + \tau) = \left\langle \hat{E}_A^\dagger(t) \hat{E}_B^\dagger(t + \tau) \hat{E}_B(t + \tau) \hat{E}_A(t) \right\rangle \quad (5.9)$$

In principle two cases have to be distinguished for coincidence detection: If the temporal resolution of the detection system is too bad to resolve the individual peaks ($|L_A S_B\rangle, |S_A S_B\rangle, |L_A L_B\rangle, |S_A L_B\rangle$), photons from distinguishable paths will contribute to the count rate and reduce the interference visibility [110]. Here we will consider the other case where the time-bin with entangled photons ($|S_A S_B\rangle + |L_A L_B\rangle$) can be clearly separated from the distinguishable paths ($|L_A S_B\rangle, |S_A L_B\rangle$). In this case the coincidence count rate is given by [110]:

$$R_{AB}^{(2)} \propto 1 + \underbrace{F(T_A - T_B)}_I \cdot \underbrace{\left| \gamma_p \left(\frac{T_A + T_B}{2} \right) \right|}_{II} \cdot \underbrace{\cos[\omega_p (T_A + T_B) / 2 + \phi_0]}_{III} \quad (5.10)$$

We can identify three independent parts of this equation influencing the coincidence rate in the experiment. In part II the expression $\gamma_p(\tau)$ is the first-order coherence function of the pump field. In our case, we operate in a regime with a delay much shorter than the pump coherence (i.e. $T_A, T_B \ll T_p$). Hence in first approximation we assume the pump coherence as constant and set $\gamma_p = 1$. Part I describes the envelope of the coincidence rate when the delay of the interferometers is coarsely detuned, i.e. it describes the amplitude of the visibility. Thus we can identify the function $F(\tau)$ as the two-photon coherence function of the pair state. In detail,

$$F(\tau) = \frac{\int_{-\infty}^{+\infty} g_A(t) g_B^*(t + \tau) dt}{\int_{-\infty}^{+\infty} g_A(t) g_B^*(t) dt} \quad (5.11)$$

describes the convolution between the first order single-photon coherence functions $g_j(t)$ of the signal and idler mode. This is the dominating part of the two-photon visibility in the Franson experiment:

$$V = F(\Delta T) \quad (5.12)$$

We can measure this function in the experiment by (coarsely) detuning the path lengths differences of the interferometers against each other (ΔT) and deriving the interference visibility for each detuning. Finally, part III contributes for the phase-dependence of the coincidences. The phase factor ϕ_0 accounts for a constant phase offset and is added to describe a general solution. This means the coincidence rate depends on the sum of the phases in both interferometers via their individual detunings ($\omega_p (T_A + T_B)$). In the experiment we thus expect to see oscillations of the coincidence rate on variation of the phases in the interferometers. Due to the proportionality via the pump frequency, this part reacts very sensitive on the detuning. In the experiment we need to introduce fine tuning of the interferometer position to resolve these oscillations. In summary,

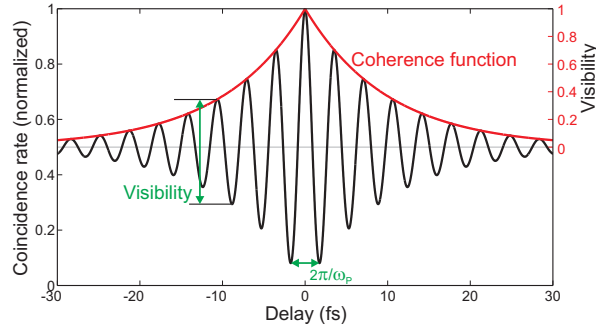


Figure 5.17: Coincidence rate as a function of the combined path length detuning of both interferometers in the Franson experiment. The envelope of the coincidence rate is an effect of the two-photon coherence function.

this means that the coincidence fringes can be observed only for unbalanced delays that are much shorter than the first order coherence time of the pump field (part II) and for differences in interferometer delays smaller than the single photon coherence length $|\Delta T| = |T_A - T_B| \ll T_c$ (part I). The experimental procedure can be visualized with the help of figure 5.17. When the phase in the interferometers is varied, we can observe oscillations in the coincidence rate (black line). The experimental findings for that are shown in Fig. 5.20b. Then we can calculate the visibility of the fringes via the minimum and maximum of the coincidence rate:

$$V = \frac{R_{\max} - R_{\min}}{R_{\max} + R_{\min}} \quad (5.13)$$

The coincidence rate and hence the visibility depend on the two-photon coherence function (part I in eqn. 5.10). In the figure we can identify this coherence in the envelope of the fringes (red line). In contrast to the image in Fig. 5.17, the coherence time in the experiment is much longer than an oscillation period. Thus we coarsely

detune the phase (i.e. the interferometer path detuning) and measure the visibility for each step. This relation between visibility and the interferometer detuning, as shown in Fig. 5.19, is the first order coherence function of the pair state. The observation of fringes with a visibility exceeding 50 % in the Franson experiment is a signature for time-energy entanglement and a visibility exceeding 70.7 % is a violation of the Bell inequalities, as we will see below.

Bell Inequalities

In 1964 John Bell derived an inequality to prove if quantum mechanics is a local realistic theory [190]. Locality means that the result of a measurement on one system is independent of the measurement on another, spatially separated, system in the past. Realism means that the outcome of a measurement is determined independently of the measurement process. It was assumed that there exist local hidden variables that connect two systems, especially in the case of the EPR paradox [57], which cannot be observed in the measurement process. Bell's inequality is a mathematical formalism of this assumptions and gives an upper bound for measurement outcomes following local realism. In 1969 Bell's inequality was modified to bring it into a form that is experimentally accessible [191], known as the CHSH variant of Bell's inequality. The violation of the inequality could be demonstrated with photons emitted by an atomic cascade [192] showing that the idea of local hidden variables is not compatible with quantum theory.

The violation of the CHSH inequality could also be demonstrated with entangled photons from a pair source. Usually polarization entanglement is exploited for such tests [193]. However, the results from Franson type experiments can also be used to test Bell's theorem for energy-time entangled photons [194]. The CHSH inequality can be written as:

$$S = E(\Delta\phi_s, \Delta\phi_i) + E(\Delta\phi_s, \Delta\phi'_i) + |E(\Delta\phi'_s, \Delta\phi_i) - E(\Delta\phi'_s, \Delta\phi'_i)| \leq 2 \quad (5.14)$$

where $\Delta\phi_{s,i}$ are the phases in the signal and idler interferometers, respectively. The functions $E(\Delta\phi_s, \Delta\phi_i)$ are the correlation coefficients depending on the coincidence rates $R_{\pm\pm}(\Delta\phi_{s,i})$. The index \pm accounts for one of the two output ports of each interferometer.

$$E(\Delta\phi_s, \Delta\phi_i) = \frac{R_{++}(\Delta\phi_{s,i}) - R_{+-}(\Delta\phi_{s,i}) - R_{-+}(\Delta\phi_{s,i}) + R_{--}(\Delta\phi_{s,i})}{R_{++}(\Delta\phi_{s,i}) + R_{+-}(\Delta\phi_{s,i}) + R_{-+}(\Delta\phi_{s,i}) + R_{--}(\Delta\phi_{s,i})} \quad (5.15)$$

The quantum mechanical description of [194] derives to the coincidence rate in a general way:

$$R_{j,k}(\Delta\phi_s, \Delta\phi_i) = \alpha [1 + jkV \cos(\Delta\phi_s + \Delta\phi_i)] \quad (5.16)$$

Here $j, k = \pm 1$ introduces a sign change depending on the combination of detectors used in the two interferometers, α is a normalization constant and V is the maximum

achievable visibility. This results in a correlation function of

$$E(\Delta\phi_s, \Delta\phi_i) = V \cos(\Delta\phi_s + \Delta\phi_i) \quad (5.17)$$

The maximum value for the Bell parameter S is reached for the phases $\Delta\phi_s = -\pi/4$, $\Delta\phi'_s = \pi/4$, $\Delta\phi_i = 0$ and $\Delta\phi'_i = \pi/2$ [194]. This results in

$$S_{\max} = V \cdot 2\sqrt{2} \quad (5.18)$$

Hence there is an upper bound for the visibility to fulfill the CHSH inequality (eqn. 5.14) of

$$V \leq \frac{1}{\sqrt{2}} \approx 70.7\% \quad (5.19)$$

This means the observation of a visibility in the Franson experiment exceeding the above value is a violation of the Bell inequality. Thus the time-energy entanglement can not be described by local realistic theory with hidden variables. This outcome has already been demonstrated for interferometers with large spatial separation via telecom photons [195].

For the sake of completeness it is necessary to mention that there exist loopholes that render the proves of violation of Bell's theorem insufficient. The detection events of both photons must be well separated in space-time, i.e. it must not be possible that any signal traveling from one detector to the other with the speed of light or less can influence the detection of the later event. A more serious blemish in the experiment is the so-called detection loophole. In general detectors operate with efficiencies below 1, i.e. not every photon is detected. This means that possibly only these photons cause an event that support a certain experimental outcome and all other photons will be lost. Usually fair sampling is assumed which involves that every photon is detected with the same probability. However, the detection efficiency can be included in the CHSH inequality and a new equation derived [196] with efficiency dependent boundary condition. Thus a minimum efficiency is necessary to show the violation, which is hard to reach in practice. Only few experiments succeeded in this so far, e.g. [197, 198]. In the case of the Franson experiment demonstrated in this thesis, a post-selection of the data is necessary to distinguish between the different path combinations by cutting out the central peak in the correlation function. This selection establishes the entanglement. However, parts of the data is selected here and the same arguments from the detection loophole apply.

5.3.1 Experimental Results

Parts of the results presented here have already been discussed and published earlier in the master thesis of Matthias Bock [199].

As a source of photon pairs again the OPO pumped at 532 nm is used. It is set to an idler wavelength of 1310 nm corresponding to the central wavelength of the telecom O-band. This results in a signal wavelength around 895 nm (close to the cesium D_1 transition $6^2P_{1/2} \leftrightarrow 6^2S_{1/2}$). The Franson interference involves two unbalanced interferometers with the restriction that the path delay must be larger than the signal and idler coherence time to suppress single photon, first order interference effects. The OPO is used without narrowband spectral filtering to achieve the highest possible photon rate and to have a short coherence time. Additionally, the resonator is blocked by inserting a metal shield in the second beam waist of the ring cavity. This suppresses the cavity ring down effect and reduces the temporal structure of the photon wave packet to the first peak of the comb. This is necessary to prevent the correlation of photons with different delays. The drawback is that around 97 % of the generated signal photons are lost due to the reflectivity of the output coupling mirror while the rate for the idler photons is unaffected. This asymmetric filtering decreases the SBR due to uncorrelated detection events. For the signal photons the same Michelson interferometer (MI) as earlier for the coherence measurements (section 5.1.1) is used. Its setup is described in detail in [179]. The maximum possible delay is 1.7 ns. Coarse tuning can be realized via a motorized translation stage and for fine tuning the phase, a piezo transducer is used to shift one of the mirrors (see Fig. 5.3). A reference measurement with the OPO above threshold shows a maximum visibility of 85 %. This is limited by the spacial overlap of both arms in the interferometer and distortions of the polarization state due to residual birefringence of some optical components.

The experimental setup is shown in Fig. 5.18. For the idler photons an equally unbalanced interferometer had to be set up. As the photons have telecom wavelengths, it is desirable to build a fiber based interferometer out of standard telecom components. It has the layout of a Mach-Zehnder interferometer (MZI) consisting of two fiber beam splitters. The phase can be modulated by a variable phase shifter (Phoenix photonics

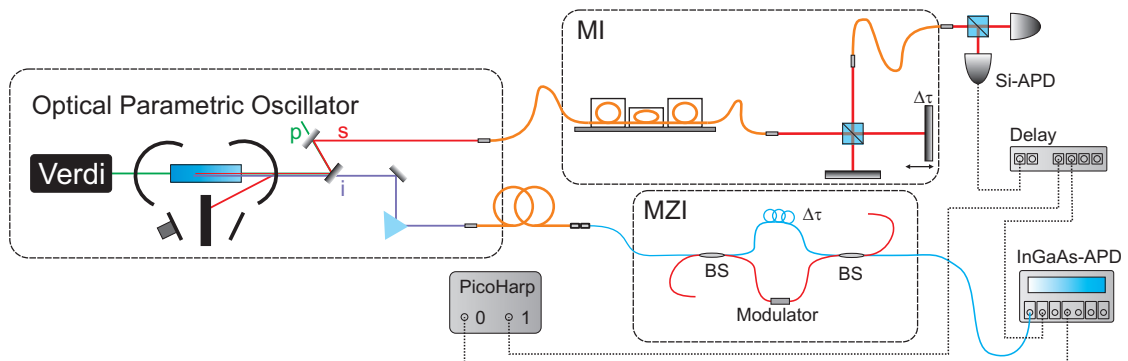


Figure 5.18: Sketch of the setup for the Franson experiment.

VPS-15-SM-1-1). With this device phase shifts of more than 49π could be realized at the telecom O-band. However, this modulator introduces an over-all delay of 11.98 ns, especially due to the length of its input and output fibers. As this delay is much larger than the maximum available for the signal photons, it was partially compensated by a fiber cut to the appropriate length in the second arm of the MZI. This results in an over-all delay of 1.14 ns between the two arms of the MZI. For this interferometer, a reference measurement with the OPO above threshold gives a maximum visibility of 90 % which is probably limited by fiber mating losses and the polarization control in both fiber arms. In the experimental procedure the delay of the MI hence has to be matched to the MZI via the motorized translation stage. The phase can then be modulated either via the piezo in the signal branch or the phase shifter in the idler branch.

A silicon APD (Perkin Elmer SPCM-AQR-14) was connected to one of the outputs of the MI. During the measurement this APD was installed in an Hanbury-Brown Twiss setup and thus for our purpose half of the signal photons were lost before detection. The detection signal of the APD triggered a delay generator which sent a copy of the pulse to a time tagging module (Picoquant Pico Harp 300). After an appropriate delay another pulse was sent to an InGaAs-SPAD (IdQuantique id201) to open a gate for detection of the idler photon behind one port of the MZI. The detection signal of the SPAD is also recorded with the time tagging module. A correlation measurement reveals the temporal structure of the two-photon wave packet. As illustrated in Fig. 5.16c it consists of three peaks corresponding to different combination of paths in the interferometers where the central peak involves both $|SS\rangle$ and $|LL\rangle$ and thus corresponds to the path-entangled state. We record this coincidence function for each phase value. As the intrinsic gate width of the SPAD is too large to directly cut out the central peak we sum up the coincidences in this peak in the post processing. In this way we derive the coincidence rate for each phase value. In the experiment the phase is scanned continuously by applying a voltage ramp to the piezo and/or the phase modulator. The detection events are recorded continuously and stored in a series of data files with one second integration time each. Hence each file corresponds to a certain phase value. Every single file is later analyzed by calculating the second order correlation function. The number of coincidences in a well defined interval around the central peak is summed up and this sum serves as data point for this certain time step. Thus a time trace of the coincidence rate can be retrieved. This trace shows the interference fringes of the pair wave function. Similar to the single photon coherence, this time trace can be fit with a sinusoidal function and the visibility is given by the minimum and maximum values of the fit.

To first find the point of zero delay (i.e. equally unbalanced interferometers), the visibility was measured at different positions of the MI. The result should be the con-

volution of the first order coherence functions of signal and idler single photons (see eqn. 5.11). At zero delay the visibility will reach its maximum value. The result is shown in Fig. 5.19. The solid line shows a theoretical model which is the Fourier trans-

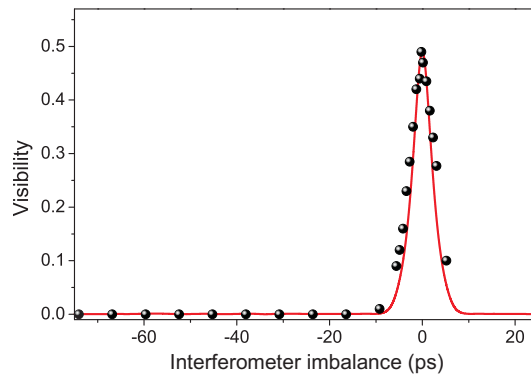


Figure 5.19: Visibility of the Franson experiment for different interferometer delays ΔT . The solid curve shows a theoretical model of measurement outcome.

form of the square of the signal spectrum (we here assume the same spectral shapes for signal and idler mode). The peak visibility is fitted to the experimental data. It has a width of 4 ± 0.2 ps (full- $1/e$ -width). A reference measurement of the signal $g^{(1)}$ function had a width of 1.87 ± 0.2 ps. It is worth mentioning here that the spectrum and hence the coherence properties slightly change with the OPO output wavelength due to different phase matching conditions. In particular the coherence time increases with the signal wavelength (e.g. from 1.4 ps at 854 nm to 1.9 ps at 895 nm) for the spectral range covered by the OPO due to flattening of the dispersion curve of lithium tantalate. Due to the above mentioned convolution theorem we expect the coherence of the pair wave function to have twice the width of the signal photon coherence in a first approximation. Within the error bars the experimental data agrees well with this estimation.

To achieve highest visibility, the setup and operation parameters can be further optimized. The details can be found elsewhere [199]. First, care has to be taken to have a clear polarization state of both photons in the interferometers. The visibility also depends on the pump power. It decreases with increasing pump power in a hyperbolic dependence [199] due to the increasing contribution of multi-photon events. A weak pump seems desirable, but there is a lower limit due to rare occurrence of coincidences demanding for long integration times which is in conflict with the stability of the setup. In particular, we found a pump power of 1 mW to be a good compromise and used this for further measurements. In the post-processing, there is also potential for opti-

mization regarding position and width of the coincidence window. The optimal values were found by continuously varying these variables [199]. Obviously the visibility will be low for large windows as coincidences from neighboring peaks leak into the window and the height of the central peak exponentially decreases, while the background (e.g. dark counts) is constant. However, for narrow windows the coincidence rate is again very low and thus affected by detection noise.

With the above mentioned parameters optimized (i.e. polarization in the MI, gate width and position Fig. 5.20a), a high-visibility measurement can be performed. The phase was continuously scanned via the piezo in the MI. The integration time for each data point was chosen at 1 s. The resulting coincidence rate as a function of measurement time, i.e. as a function of the phase is shown in Fig. 5.20b. A sinusoidal

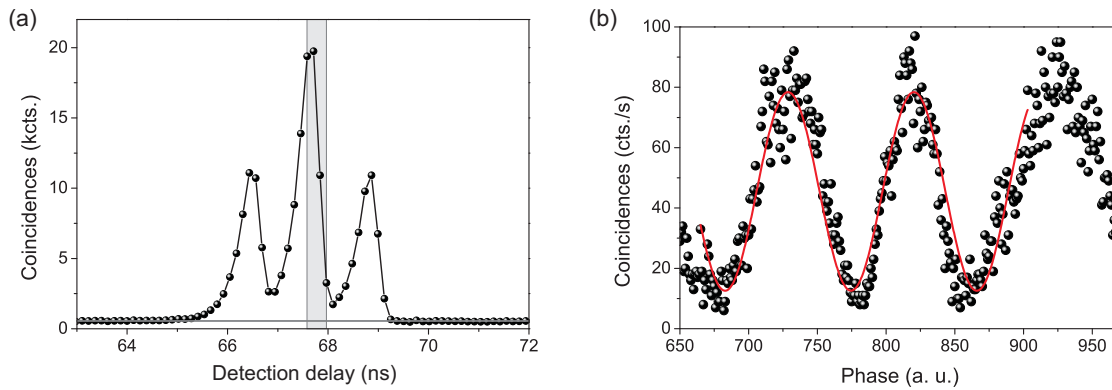


Figure 5.20: Optimized parameters for Franson interference. a) Long-term average temporal correlation function. The gray shaded area indicates the gate, selected in post-processing. The horizontal gray line indicates the background level. b) Coincidence fringes with the maximum visibility of $72.3 \pm 1.2 \%$ calculated from the fit data. Data fit by sine function (solid line).

fit results in a visibility of $72.3 \pm 1.2 \%$. This clearly violates the Bell inequalities by 1.3 times the measurement error interval. The value given above is derived from the raw data. Usually, noise subtraction is included into the post processing. From the long-term average we can estimate a background count rate of 1.78 cts./s for the coincidences (indicated as horizontal line in Fig. 5.20a). After subtracting this value from each data point a new fit results in a visibility of $75.2 \pm 1.2 \%$. The visibility is ultimately limited by the product of the visibilities of each individual interferometer for the single photon case to a value of $V_{\max} = 0.9 \cdot 0.85 = 0.765$. This shows that the result is consistent with the results from the preparatory work and that we are limited

by the individual interferometer visibilities.

We can compare the results of our measurement with earlier published data. The first report on a Franson experiment with high visibility is published in [200]. The authors used frequency degenerate photons at NIR wavelengths. They achieved a raw visibility of 80.4 %. Another experiment [195] used frequency degenerate photons at the telecom O-band to perform a violation of the Bell inequalities over long distances. They reached a raw visibility of 85.3 % which increased to 95.5 % after subtracting accidental coincidences. There is also an experiment that investigated frequency non-degenerate photon pairs [28] which resulted in a raw visibility of 86.4 % and a net visibility of 96.2 % after noise subtraction. In summary all these demonstrations show a raw visibility between 80-90 % which is only slightly higher than our result. In all these publications the authors claim to end up with visibilities exceeding 90 % after subtracting accidental coincidences. They further state that the final discrepancy left to reach 100 % can be explained by imperfect interferometer alignment. In our experiment we tested this interferometer alignment in preparatory work and derived a maximum visibility of 76.5 % for the Franson experiment, limited by the measurement apparatus. Indeed we reached this value after subtracting the accidental coincidences. In the same way as the other authors we can thus claim to have produced a nearly maximally time-energy entangled state with our photon pair source. In comparison with the cited experiments our interferometers seem to offer a poor alignment or overlap of the beam paths. The alignment could be optimized later as demonstrated with the results in section. 6.4. Anyway our result not only exceed the visibility threshold for entangled states of 50 %, but it also violates the Bell inequality significantly by exceeding a visibility of 70.7 %.

One challenge for future experiments involving Franson interferometry is to optimize the alignment of the interferometers. This seems to be the limiting factor for the present results. It is worth mentioning again the losses for the signal field. The OPO was blocked to generate photons with low coherence time and without the comb-like temporal shape, leading to 97 % photon loss. If we wanted to use all photons, the delay in the interferometer had to be drastically increased (single mode coherence length 22.7 ns; cavity ring-down time). This would be technically challenging for the MI design. A more feasible improvement is in the detection part. If we used a single APD which is not mounted in a HBT-setup the detection rate would double. This already increases the coincidence rate by a factor of four. This in turn would allow to reduce the pump power and hence the background.

5.4 Summary

In this chapter a source of photon pairs, generated by spontaneous parametric down-conversion in an optical parametric oscillator was presented. The cavity of the OPO

acts as a temporal and spectral filter for the generated photons. This could be proved in coherence and cavity ring-down measurements, enabled by the temporal correlation between signal and idler photons. To generate narrowband, correlated photon pairs a single mode of the spectrum needs to be cut out. This was realized by additional external filtering systems, i.e. a FBG for the telecom and Fabry-Perot cavities for the signal photons. The resulting modes have a width of 7 MHz while the temporal correlation is preserved. The OPO is also feasible as a source of heralded single photons at telecom wavelengths which has been demonstrated in a heralded $g^{(2)}$ -measurement. In a Franson interference experiment we demonstrated the time-energy entanglement between the unfiltered photons. Furthermore, the maximum visibility violates the Bell inequalities and hence proves the invalidity of local realism for our system. In a first step towards quantum networks, we demonstrated single photon spectroscopy of a transition in a single trapped calcium ion. With these preconditions (temporal correlation, spectral shape and wavelength as well as time-energy entanglement), we are able to demonstrate interactions between the photons and a single ion. In particular, the absorption of a resonant signal photon was heralded by a telecom-compatible idler photon. Although the idler photon never interacted with the ion, we can see a temporal correlation between its detection and the state transition in the ion. This experiment forms a basic building block for quantum repeater schemes.

An ongoing improvement to increase the count rates for signal photons and signal/idler coincidences is an advanced filtering. At the moment, the filtering cavities employed for the signal photons are located in another lab. Losses occur by fiber attenuation and especially the mode matching from the fiber to the cavity. We designed new solid-state etalons based on high-reflection coated biconvex lenses [201]. These devices can be installed behind the OPO output to select a single mode with low losses. Due to the coating parameters these lenses can be used for the whole signal tuning range of the OPO.

The large tuning range due to multiple poling periods is also an outstanding property of this SPDC source. In our configuration gap-less tuning could be realized between 1202-1564 nm for the idler and 806-954 nm for the signal wavelength. Thus our OPO can cover the telecom O-, E-, S- and C-band and simultaneously the NIR region where especially transitions in quantum dots (InAs/GaAs [202], In(Ga)As-QD [203]) or atomic transitions (e.g. Ca^+ : 850 nm, 854 nm, 866 nm, Cs: 852 nm, 894 nm) exist. Of special interest is the D_1 transition in cesium at 894.593 nm ($6^2P_{1/2} \leftrightarrow 6^2S_{1/2}$; [204]). We already demonstrated doppler-free saturation spectroscopy of this transition with the OPO above threshold [199]. With the experience from the calcium spectroscopy it seems feasible to also address the cesium transition with single photons from the OPO. The special feature in our case is, that pumping the OPO at 532 nm, the corresponding idler wavelength is at 1313.844 nm, close to the center of the telecom O-band. Quantum

memories are an essential element for quantum repeaters and there exist schemes to use cesium for such a memory [205]. Regarding future experiments in Saarbrücken with quantum dots around 900 nm wavelength, similar herald wavelengths are expected. There will be further research on quantum memories, based on solid-state systems in Saarbrücken in future. One possible realization is Nd:YSO [206] which has a transition at 883 nm. Again, this wavelength is accessible with an idler partner photon in the telecom O-band. All these opportunities make the OPO a versatile pair source to connect the NIR with the telecom spectral region.

6 Quantum Frequency Conversion

In this chapter the results of frequency down conversion between 854 nm and the telecom O-band at 1310 nm will be presented. In the first section the setup of the frequency converter is discussed and particular parts are explained in detail. A first characterization of the frequency conversion process is performed with attenuated coherent fields as signal input. In the remaining part of the chapter we focus on the conversion of photons from a SPDC source. The preservation of temporal correlations in the conversion process arises special interest. Thus this device is also suitable as a heralded telecom single photon source. The results from Franson interferometry further prove the preservation of time-energy entanglement. With these preconditions the absorption of a single photon by a single ion, heralded by a telecom-converted photon is demonstrated in the last section.

6.1 Frequency Converter Setup

In this section the setup of the frequency converter is described in general. In the following sub-sections, parts of the setup are described in more detail. Also parts of the setup can be modified for certain experiments which then is explained in the corresponding section. Figure 6.1 shows a sketch of the optical setup. The signal photons at 854 nm are delivered to the converter via a single mode fiber (see sec. 6.1.2). After passing a manual polarization controller and a motorized half-wave plate, the photons arrive at a polarizing beam splitter. Only the vertically polarized component can interact in the nonlinear process. The signal photons are overlapped with the pump field on a dichroic mirror (Layertec 103472: HR@854 nm; HT@1.3 μm , 2.5 μm). The pump field, generated by the optical parametric oscillator (see chapter 4), passes a motorized half wave plate and a rutile polarizer. The beam then has a vertical polarization, necessary for the nonlinear process. Power control of the pump field is realized with the wave plate in combination with the polarizer. Both pump and signal beam are then coupled into the waveguide (see sec. 6.1.1). The waveguide is mounted on a three axis translation stage and temperature stabilized. Behind the waveguide its output is collimated. The frequency converted photons are vertically polarized. A dichroic mirror separates the residual signal beam which passes a bandpass filter and is then coupled into a single mode fiber. The telecom photons are transmitted through the dichroic mirror and pass several interference filters (bandpass filters: Edmund

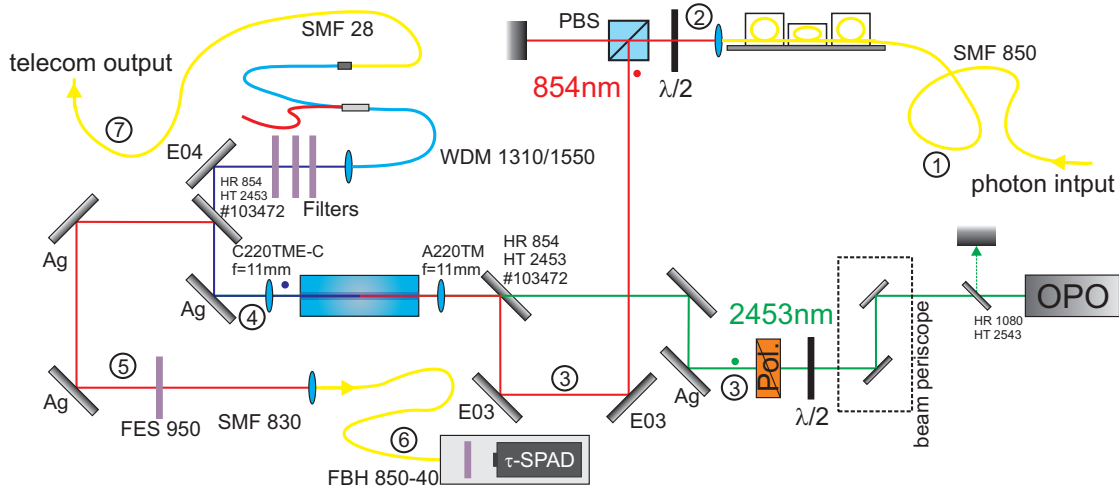


Figure 6.1: General optical setup of the frequency converter. Details are explained in the text.

Optics 1300-50 and 1325-50, Thorlabs FB 1310-12) before being coupled into a standard SMF28 telecom fiber. For further filtering a wavelength division multiplexer (WDM) is attached to the fiber. Finally, another SMF28 fiber can guide the telecom photons to the detectors. The pump field behind the waveguide suffers losses in the collimation lens, the second mirror and the bandpass filters and is thus separated from the telecom photons. Furthermore, residual pump photons will suffer high attenuation in SMF28 fibers.

The numbers in Fig. 6.1 mark positions where powers are measured. The pump power is measured at position 3. The waveguide coupling efficiency can be calculated by comparing the powers at position 4 and 3 and taking the transmission of the collimation lens into account.

6.1.1 Waveguide Characterization

Wavelength Tuning

The waveguide chip used (NTT WS-0854-000-A-C-C-S008) offers several slightly different waveguides. These waveguides are arranged in six groups with two waveguides each. The QPM period is the same in each group but the geometry slightly changes. The period is given as $22.60 \mu\text{m}$ for group one and increases in steps of 50 nm to $22.85 \mu\text{m}$ at group six (the period lengths significantly differ from the values for bulk LN). The details of the width and height of the waveguides are a business secret of NTT and were not measured later. Figure 6.4a shows a sketch of the chip cross section as given in the data sheet. The end facets of the chip are anti reflective coated around

854 nm, 1310 nm and 2453 nm ($R < 1\%$). The frequency conversion process under investigation later will be difference frequency generation according to the following scheme:

$$\frac{1}{854\text{nm}} - \frac{1}{2453\text{nm}} = \frac{1}{1310\text{nm}} \quad (6.1)$$

where the single input photons at 854 nm are converted to the telecom O-band around 1310 nm, stimulated by a strong pump field at 2453 nm. To find optimum operating conditions we investigate the process of SPDC that obeys the same phase matching as DFG. This means, a coherent field at 854 nm is coupled to the waveguide which spontaneously decays into signal and idler photons. Then the temperature of the chip is varied to find a tuning curve for the output photon wavelength.

However, tuning curves of DFG processes in lithium niobate including near infrared wavelengths can show an anomaly which has previously been observed with OPOs [143]. The wavelengths here are in a region where the curvature of the dispersion function changes its sign. This causes a so-called retracing behavior of the phase matching curve where two pairs of signal and idler wavelengths can be phase matched simultaneously. Such an effect can be applied for example to achieve large tuning bandwidths in OPOs [207]. Figure 6.2 shows calculated tuning curves for bulk PPLN. If we want

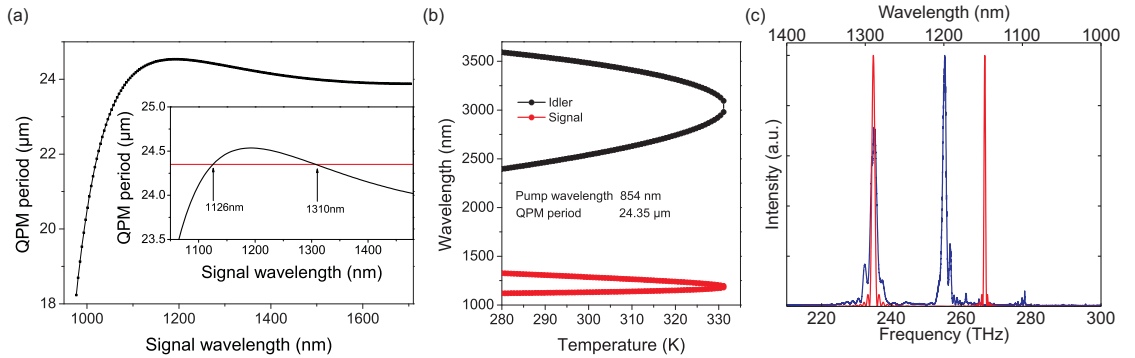


Figure 6.2: Tuning curves of LN for pumping with 854 nm and holding the crystal at room temperature. a) shows a calculation of the QPM period in bulk LN as a function of the signal wavelength to be generated. The inset shows a close-up of the region of interest. For a certain period, phase matching is fulfilled for two wavelength combinations simultaneously. This leads to a retracing behavior shown in b). c) shows a measured spectrum behind the waveguide (WG-4-1, $T=21^\circ\text{C}$), pumped at 854 nm (blue line) and a calculated spectrum for bulk LN (red line). For the calculation the QPM period was adjusted such that the low frequency peak is centered at the experimental peak.

to generate a 1310 nm photon out of 854 nm a QPM period of $24.35 \mu\text{m}$ is necessary to achieve phase matching around room temperature. In this case, phase matching also allows the generation of photons around 1128 nm. The calculated temperature dependent tuning curve for these parameters is illustrated in Fig. 6.2b. Furthermore, with the data of the dispersion curve from the Sellmeier equations the SPDC spectrum can be calculated. For comparison Fig. 6.2c illustrates such a calculated spectrum for bulk LN and a measured spectrum behind the waveguide. The difference can be attributed to the different phase matching in bulk and waveguide structures as in waveguides geometry-dependent effective refractive indices have to be taken into account. Obviously retracing is also present in the waveguides. In Fig. 6.3 more detailed spectra of the waveguides are presented. To measure these spectra the waveguide was pumped with approximately 5 mW of power at 854 nm. The light was generated by a diode laser which was actively stabilized to an atomic transition in calcium. Thus it has exactly the same wavelength as the single photons used in later experiments. The spectra were either recorded with a high sensitivity spectrometer (Princeton Instruments SP2500A) featuring a grating of 600 lines/mm and an InGaAs camera, or with an optical spectrum analyzer (OSA, Yokogawa AQ6370B). Figure 6.3a shows the SPDC spectrum of the waveguide used later for the conversion experiments. It is slightly broader than the calculated (bulk) spectrum which can be attributed to the different phase matching conditions in the waveguide structure. There is a slight asymmetry visible in the side lobes of the spectrum. This effect is even more prominent for other waveguides on the chip, as shown in Fig. 6.3b. It is known that a spatial variation of the refractive index

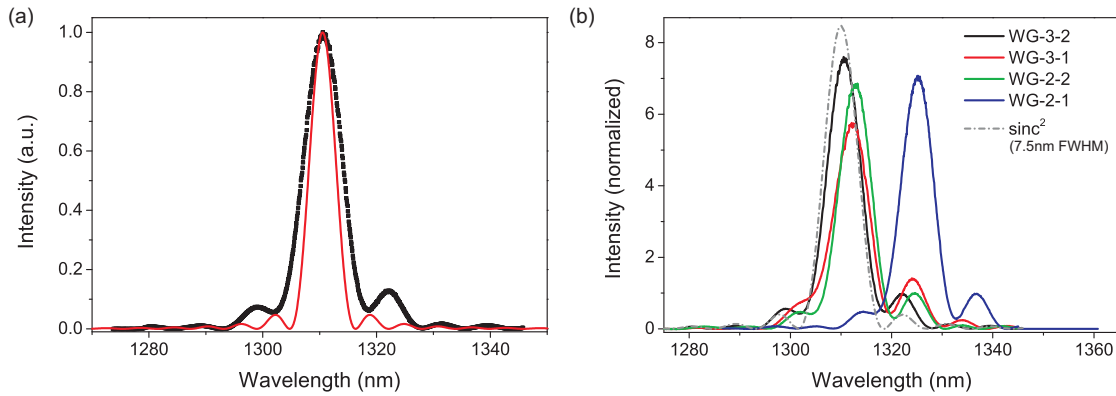


Figure 6.3: Measured SPDC spectra around 1310 nm of the waveguides. a) shows the measured spectrum of WG3-2 at 30.76°C (black dots) together with the calculated spectrum (red line). b) compares measured spectra of different waveguides at different temperatures with an ideal phase matching curve. All curves are normalized to have unity area resulting in different peak heights.

or the birefringence in the crystal will distort the phase of the propagating beams resulting in a modified phase matching curve [208]. A similar effect can be observed when the duty cycle of the poling period is not constant along the propagation path [170]. In the waveguides the propagation phase is described by the effective refractive index (eqn. 3.47) which also depends on the local geometry of the guiding structure. Hence in the waveguide system not only the quality of the QPM structure but also the material and fabrication quality affect the phase matching function. The structural change of the phase matching function also includes a change of the peak heights. This means the side lobes and peripheral regions are increased at the cost of the central peak. In the DFG experiments of narrowband photons presented later the signal bandwidth is much smaller than the phase matching bandwidth. Hence only the central part of the highest peak will be relevant. To achieve maximum efficiency this peak should be as high as possible. This condition can be examined in the SPDC spectra by normalizing these spectra to have the same area. Then the re-distribution of the intensity from the central peak becomes visible as shown in Fig. 6.3b. The experience from earlier experiments with other waveguides tells that the measured curve often largely differs from the ideal phase matching function. For the later experiments we thus chose the waveguide (WG-3-2) that offers a spectrum as close as possible to the ideal case and the highest central peak.

To fully characterize the chip, the temperature tuning curve was recorded as follows. The individual waveguides were pumped with the laser at 854 nm and the SPDC spectra at telecom wavelengths were recorded with the OSA. The tuning curve is defined as the position of the signal peak of the SPDC spectrum as a function of the temperature. The short wavelength peak (retracing effect) here was neglected. The results can be found in Fig. 6.4b. The nomenclature of the waveguides follows WG-x-y where x denotes the group (1–6) and y the number (1 or 2). The waveguides of group 6 are not shown as they show a very low transmission and can thus not be used for later applications. For the tuning curves shown in Fig. 6.4b we restricted the data points to the spectrum in the telecom O-band. As mentioned in the beginning of this section, phase matching is also fulfilled for another wavelength combination (cf. Fig. 6.2). This results in two peaks in the SPDC spectrum. For increasing temperature the peak in the telecom O-band shifts to shorter wavelengths while the other peak shifts to longer wavelengths. At a certain point these two peaks start to overlap. In this case the shape of the spectrum drastically changes and cannot be described by a sinc function any more and we are not able to clearly identify any peaks. The measurement of the tuning curve was thus not continued below 1200 nm. Anyway, frequency conversion should also be possible in this region. The temperature was limited between 15°C to avoid condensation of air humidity at the facets and approximately 50°C due to power limitations of the temperature control. The temperature is stabilized via a peltier module and a temperature controller (Thorlabs TED200C).

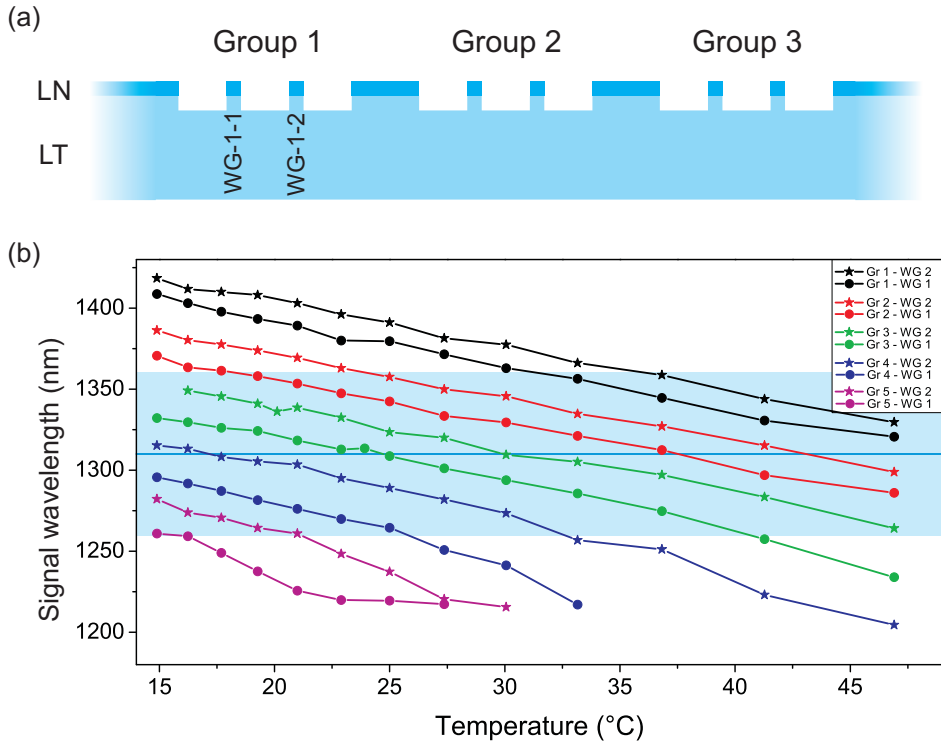


Figure 6.4: a) Cross sectional outline of the chip according to its data sheet. b) temperature tuning curve of the individual waveguides. The shaded area marks the telecom O-band.

With the pump wavelength fixed at 854 nm it is thus possible to cover the whole telecom O-band with this waveguide chip. The central wavelength of 1310 nm is accessible with five different waveguides. We chose waveguide WG-3-2 as it will offer the highest conversion efficiency according to its spectrum.

Coupling of Light into the Waveguide

As elaborated in section 3.3.1, high modal overlap is a prerequisite for high conversion efficiency. Coupling light into a waveguide is comparable to coupling light into a fiber. The spot size of the beam focus has to match the mode field distribution in the waveguide. In the case of a nonlinear interaction this is more complicated because two beams have to be coupled into the waveguide and the requirements have to be fulfilled simultaneously. Due to geometry of the beam path the in-coupling lens before the facet has to be passed by both beams. The coupling procedure in principle consists of the following steps. Both beams (signal and pump) are combined on a dichroic mirror and then overlapped to a common beam path defining the optical axis of the setup. Afterwards, an aspheric lens is inserted for focusing. Next the waveguide is inserted

into the beam. For practical reasons in a first instance the pump beam is blocked and the coupling is first realized with the signal beam only as it can be visualized with an infrared viewer. The waveguide is translated in the beam until a coupled mode is visible at the output. Measuring the power behind the waveguide while observing the mode structure helps to optimize coupling. Next the pump beam is unblocked and should also be coupled. Finally the waveguide position should stay fixed and coupling is optimized for both beams individually by varying the beam paths using steering mirrors and increasing the power behind the waveguide.

Ideally, the diameter and transverse profile of both beams is characterized first and optimal coupling is calculated. This in general involves beam shaping by a telescope before the waveguide. Unfortunately beam profiling devices or CCD cameras sensitive at the pump wavelength were not available. Thus the exact diameter of the pump beam is unknown. In a first step, coupling was optimized for the pump beam. The optimum coupling was found in practice by testing different lenses available off the shelf with the following results: In general, spherical lenses provided less coupling efficiency than aspheric lenses. From this we can conclude that the beam diameter is large enough to suffer spherical aberrations in standard lenses. For the aspheres a focal length around 11 mm turned out best. We thus chose the uncoated lens Thorlabs A220TM. Unfortunately there is another challenge. Standard glasses based on SiO_2 (like D-K59 used in the A220TM asphere) show an increase in absorption for wavelengths above $2 \mu\text{m}$. This is due to hydroxyl incorporation forming absorption bands especially around $2.2 \mu\text{m}$ and $2.7 \mu\text{m}$ [209] also hampering transmission around $2.5 \mu\text{m}$. Thus the transmission of the pump field through such components is significantly reduced. In our case it was measured to be at 72.6 %. Specialized infrared glass-materials like Infrasil (used as substrate for the OPO mirrors) offer reduced OH-content. Alternatively, other materials like calcium fluoride (used for the collimation lens behind the OPO), sapphire or zinc selenide have to be used. Spherical lenses of sapphire are readily available at standard focal lengths and indeed show high transmission for our pump laser and at 854 nm. However, due to its hardness, precision machining of sapphire is sophisticated making custom made aspheric lenses very expensive. Calcium fluoride has a low refractive index and shows birefringence which complicates the fabrication of custom aspheric lenses. Eventually, an aspheric lens made of zinc selenide with a focal length of 11 mm was custom made by II-VI Deutschland GmbH. Zinc selenide (ZnSe) is transparent from 600 nm to $16 \mu\text{m}$ and commonly used for infrared optics. The lens was covered with an anti reflection coating for 854 nm and $2.5 \mu\text{m}$ resulting in a measured transmission of $97.8 \pm 0.6 \%$ at the pump wavelength. Although the ZnSe lens has a significantly higher transmission, the coupled power is slightly smaller than for the case of the glass asphere. The glass asphere showed a coupling efficiency (ratio between power measured behind the waveguide and before the lens) of up to 38 %, while with the ZnSe lens an efficiency of 37 % was achieved. The glass lens

was specified at 633 nm and their properties (refractive index, focal length) at 2.5 μm deviate from that while the custom made ZnSe lens was optimized for the infrared region. The working distance between crystal facet and lens surface was approximately 6 mm shorter for the glass lens as compared to the ZnSe lens. We can conclude that it has much shorter effective focal length than specified, resulting in a smaller focus. For the rest of the chapter all results presented were achieved with the glass lens due to the better over-all performance while the ZnSe lens was not used further. However, it could be advantageous in future. An additional focusing element in the pump beam path before the asphere could reduce the effective focal length of the whole system increasing the coupling efficiency.

While up to now the coupling of the pump field was optimized, the next step is the input coupling of the 854 nm signal field. As the coupling lens is fixed by the optimization of the pump field the signal beam has to be shaped to fit accordingly. As the focus diameter depends on the beam diameter an easy way to adapt the spot size is to vary the beam width. Therefore an iris diaphragm was inserted in the beam and the coupling efficiency to the waveguide was measured while the aperture width was decreased. After the maximum efficiency was found, the beam diameter behind the iris was measured with a beam profiling device (Gentoo Beamscope). For beam shaping one has to consider that the signal photons are delivered to the frequency conversion setup by a single mode fiber. The choice of the collimation lens behind the fiber determines the beam diameter. Knowing the mode field diameter (Φ) in the fiber and the desired diameter (d), the focal length (f) for the fiber collimation lens can be calculated $f = \frac{\pi d \Phi}{4\lambda}$. With an aspheric lens of $f = 6.24$ mm a beam diameter of 600 μm FWHM was achieved. This results in a maximum coupling efficiency of 84.2 %. Optimum coupling for pump and signal field could be reached simultaneously. For comparison the maximum with the ZnSe asphere was 77.7 % and the working distance for optimum coupling of pump and signal differed by 174 μm .

The figure of merit of the whole setup is the conversion efficiency. Hence fine-tuning of the input coupling was realized by maximizing the power of the generated telecom field and thus the conversion efficiency. In this configuration the transverse beam profiles of signal and pump beam were recorded. These profiles are a measure for the intensity distribution inside the waveguide. The intensity of the signal field was measured with a CCD camera and is shown in Fig. 6.5. The elliptic shape is directly visible resulting from the rectangular, non-quadratic, geometry of the waveguide cross-section. Comparing the intensity with the 00-mode shows that a major fraction is guided in the fundamental spatial mode. Measurements of the mode before the waveguide confirmed the nearly ideal Gaussian shape due to the outcoupling from a single mode fiber. As mentioned earlier, there was no camera device available for the pump wavelength. To nevertheless get an impression of the intensity distribution, an InGaAs photo diode was mounted behind a slit of two razor blades and both slit and photo diode together

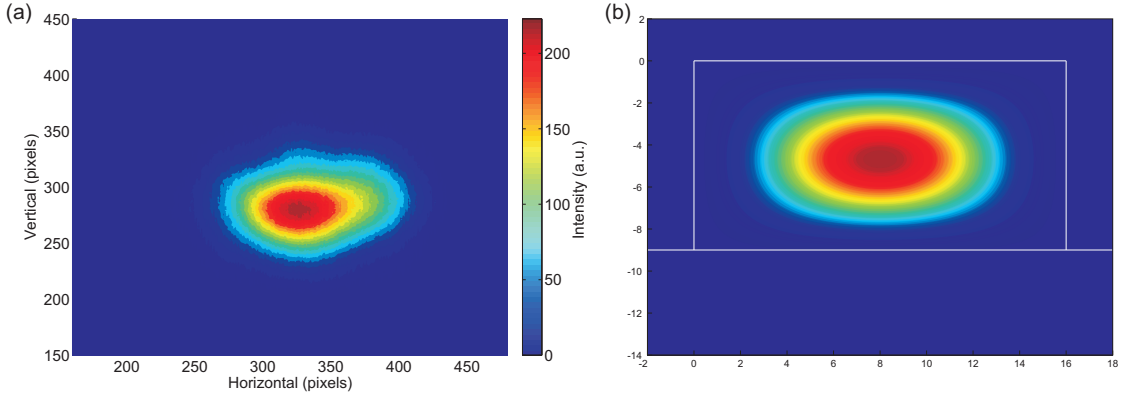


Figure 6.5: Transverse profile of the 854 nm mode. a) measured intensity distribution behind the waveguide. b) simulated, ideal profile of a 00-mode.

were scanned across the beam. To get the profile, the intensity was recorded at several positions as shown in Fig. 6.6. We can identify three peaks. Hence the pump field shows higher order mode content. We also performed this measurement directly behind the OPO with a similar result. This means the cross-sectional profile of the pump beam also shows a structure with three peaks already before coupling to the waveguide. This pump beam profile is the reason why a coupling to the fundamental spatial mode of the waveguide could not be realized. The fact that we achieved coupling to the fundamental mode with the signal beam shows that it is in principle possible to couple the pump beam to the same mode too with the precondition of an optimized input beam profile. In principle the coupling of shorter wavelengths to the fundamental mode should be more sensitive to beam deviations. The alignment of the OPO was optimized with regard to output power and single-frequency operation. The scanning slit measurements employed here were relatively time consuming and do not deliver a real-time signal which could be used for cavity alignment. If a camera was available for real-time imaging of the pump beam, further optimization of the OPO cavity should be possible to shape the output beam.

To get an initial estimation of the mode distribution in the waveguide a numerical simulation was performed. Therefore the intensity of the three lowest order modes (00, 01, 02) was overlapped including weighting factors. Then the intensity was integrated along the vertical axis to emulate the experimental measurement method as the scanning slit did not apply an aperture in this direction. The weighting factors were varied and the intensity profile was compared with the experimental data points. The best fit, shown in Fig. 6.6, is a mixture of 36.5 % mode-00, 15.9 % mode-01 and 47.6 % of mode-02. To estimate the consequences for the frequency conversion process we calculate the coupling integral. For this we assume the signal and telecom field in their fundamental modes and the pump field in the simulated mode distribution. In this case

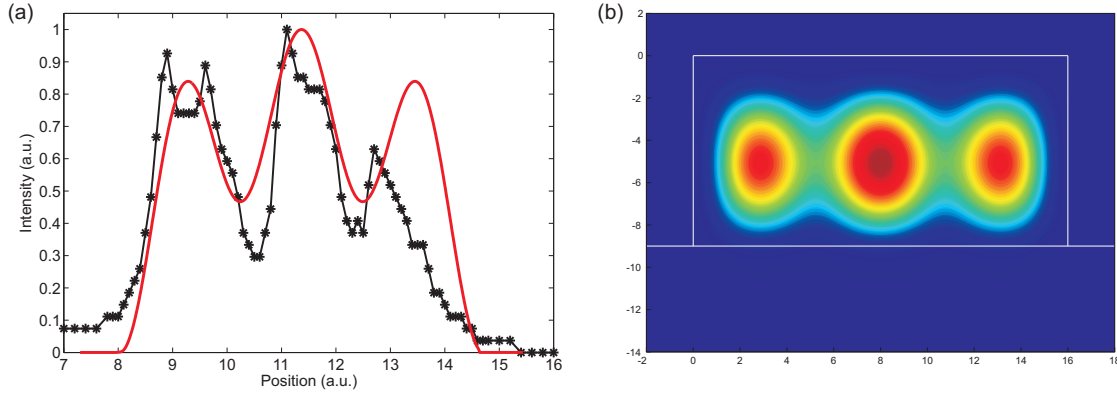


Figure 6.6: Transverse profile of the pump field. a) black curve shows the measured horizontal profile behind the waveguide. The red curve is a fit to the data. b) shows the calculated mode profile fitting best to the experimental data.

the coupling integral (eqn. 3.59) is reduced to $|J_1| = 1.978 \cdot 10^8 \text{ 1/m(V/A)}^{3/2}$. This is only 26.3 % of the value when all three fields are guided in their fundamental modes. The lower coupling integral affects the slope of the conversion efficiency curve. To reach the maximum conversion efficiency a pump power around 3 W would be necessary. In our setup the pump power coupled into the waveguide is limited around 280 mW. At this point we can only achieve 19 % of the efficiency compared to the ideal case. The reduction of the conversion efficiency is another argument to implement proper beam shaping before the waveguide to optimize the input coupling to the fundamental spatial mode.

Behind the waveguide, the generated telecom fields are collimated by an 11 mm aspheric lens (Thorlabs C220TME-C) with an AR coating for the telecom bands. This coating reduces the transmission for the signal and pump field which can be accepted as only the telecom photons have to be used later with low loss. This lens has more than 99 % transmission for the telecom photons, 22 % for pump and 90 % for the signal. The collimation lens is mounted on a three axis translation stage. In the following the beam is coupled into a single mode fiber by an identical lens. Ideally, the fiber and the waveguide have similar geometries and their facets are imaged in each other by this setup.

Finally, there is another way to overcome the problems with waveguide coupling in future setups. The waveguides devices in use have only a single guiding structure. However, two input waveguides could be combined with a directional coupler and each waveguide could be optimized in geometry to guide the fundamental mode of either pump or signal. With an adiabatic taper the size of the signal waveguide could be matched to the pump waveguide. The coupling to the waveguides can be realized independently. Such integrated optic devices were already demonstrated in the context

of experiments in the field of frequency conversion [26].

6.1.2 Linking the Labs

The quantum frequency conversion experiments involve work in two different labs. In one lab the converter is set up whereas the sources and the ion-trap are located in another lab. Hence there must be some channel linking the rooms. This channel consists of a telecom SMF28 fiber, a single mode fiber for 850 nm, one coaxial cable (RG 58) and an ethernet compatible cable (CAT 7). The fibers have a length of 90 m and the cables 100 m. A major part of the length is installed in a maintenance shaft and a lobby which don't have air condition and thus suffer temperature fluctuations. As the fibers are not polarization maintaining a measurement of the polarization stability was necessary. To this end, a linearly polarized and stabilized diode laser beam at 854 nm was coupled into one end of the fiber. At the output the fiber was inserted in a manual polarization controller and the polarization was adjusted close to vertical direction. The state of polarization was then continuously recorded with a polarimeter (Thorlabs PAX5710IR1-T). Figure 6.7 shows the long-term track of data points on the Poincaré sphere for two different measurements (the maximum number of data points was limited in the polarimeter control software, thus two measurements were necessary to cover one whole day of measurement time). Obviously, the state of polarization

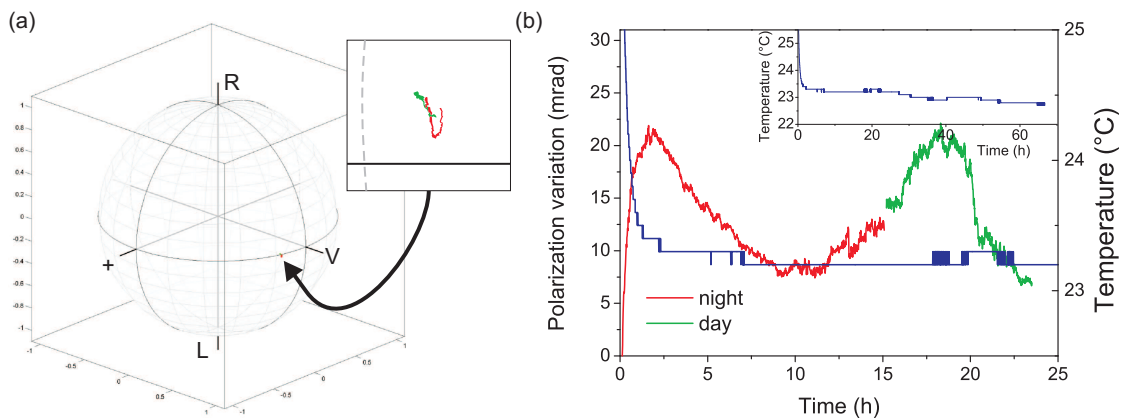


Figure 6.7: Long term measurement of polarization state behind fiber link. a) shows the Poincaré sphere for measurements over day (green curve) and night (red curve), respectively. b) shows the solid angles between the Stokes vectors and the temperature (blue curves) measured at the vicinity of the fiber. The state of polarization at the beginning of the measurements is used as a reference.

does not change significantly within a 10 h measurement period. There is also no significant difference between the curves measured over day and over night. To quantify the stability we use the first recorded data point as reference and calculate the solid angle between the measured Stokes vectors and this reference. The peak to peak fluctuation of the polarization state is below 23 mrad in this measurement. The results are illustrated in Figure 6.7b together with the ambient temperature in the maintenance shaft. In practice this means that the polarization was adjusted at the beginning of a measurement and can be taken as constant for the whole day. However, the precondition is that the fiber is left untouched as in a non polarization maintaining fiber the state of polarization is disturbed by moving the fiber and changing its bending due to strain-induced birefringence. For the transmission of the fiber at 854 nm a minimum value of 92.7 % was measured. For the experiments additional coupling losses have to be taken into account.

The BNC and CAT cables are necessary to exchange electronic signals between the labs. In particular these are pulses from detectors signaling a detection event. The coaxial cable can be used for general purposes. However the cables have significant loss (attenuation 4.6 dB/100m at 10 MHz according to datasheet) reducing the voltage level at the other end below one half of the initial value. This can be crucial for the setting of the voltage level discriminator of some time tagging modules. For this reason the ethernet cable can be used for transmitting digital signals. An electronics circuit board (developed by S. Kucera) transforms input pulses into a RS 485 compatible signal which is sent through the link. At the output this signal is converted into a standard TTL pulse. The cable has enough capacity to transmit two independent signals. A test of the timing jitter of the link with the delay generator as pulse source returned a value of 59 ps which is comparable to the intrinsic jitter of the generator. Thus the jitter of the channel is much smaller than the resolution limit of later experiments.

In summary there is a link available between the two labs containing optical and electronic channels. The influence of environmental conditions is negligible and should not disturb later experiments. Further actions like implementing an active polarization stabilization of the fiber are not necessary. The electronic channels can be used to either transmit analog signal as well as digital signals with very low timing jitter. Furthermore, the fibers can be used as a quantum channel and the cables as classical channel for the emulation of basic quantum network elements.

6.1.3 Telecom Photon Detection

In the beginning of this work, for telecom photon detection two single photon avalanche detectors (SPAD, IdQuantique id201) based on InGaAs APDs were available. Later two superconducting nanowire detectors (SSPD, Single Quantum EOS X10) were acquired. These devices are briefly introduced in the following.

The SPAD is based on a peltier cooled InGaAs/InP avalanche photodiode (APD). It can only be operated in gated Geiger mode with gate widths in the range 2.5 ns to 100 ns. The gates can be triggered internally or by an external signal with a frequency up to 8 MHz. However, in practice trigger rates above 1 MHz should be avoided due to excessive noise. APDs based on InGaAs suffer noise due to dark counts and afterpulsing [210]. The afterpulsing can be reduced by a long dead time in the microsecond range. Such a long dead time can lead to effects of count rate saturation at high photon rates. The noise can be reduced in general by adopting the gate width to the length of the signal of interest. The sensitivity of the detectors covers a spectrum between 900 nm and 1700 nm. The efficiency is 25 % at 1550 nm and 30 % around 1310 nm according to the data sheet. The timing jitter was measured as 243 ± 13 ps (1/e time).

The operation principle of the nanowire detectors is different. The active area is covered with a meander of a NbTiN nanowire. The temperature is reduced until superconductivity is reached in the detector (operating temperature 2.5 K). Then a constant electrical current is sent through the nanowire. In this state the voltage drop across the detector should be zero. When a photon is absorbed by the wire it heats up and the superconductivity is quenched locally. This results in a voltage pulse which can be used as the signature for a detection event [211]. After absorption the detector recovers very fast (dead time < 10 ns). This technique also allows for the lowest timing jitter which is below 50 ps for our detection system. In principle all particles that carry heat and reach the nanowire can trigger a detection event [212–214]. This also allows the detection of noise sources which are invisible for the SPAD system. Our detector contains two chips, housed in a closed-cycle cryostat and held around 2.5 K. Optical access is realized by two SMF28 fibers which limit the sensitivity range to 200–2000 nm. The detection efficiency depends on the absorption of the nanowire and thus also on layer thickness and fabrication parameters. Channel 1 (2) of our detector is specified with detection efficiencies of 27 % (25.8 %) at 1310 nm and 17.5 % (17.6 %) at 1550 nm, measured under the condition of less than 300 dark counts per second. However, these values are very sensitive to operation conditions and vary on a day by day basis. There is a dependence of efficiency on bias current which can be increased at the cost of higher dark counts. Unfortunately, the efficiency also depends on the vacuum pressure in the cryostat and the polarization of the light. The output pulses are also influenced by the external connections and cables due to an improper impedance matching. In preparation of any measurement the bias current was varied and the dark count rate recorded. Usually this is enough to set the bias current to the reference dark count rate of 300 s^{-1} and have comparable detection efficiencies day by day. Most errors can be identified in the change of the shape of this dark count curve. The quantum efficiency was measured with a continuous wave laser of known power coupled to a telecom fiber. The power of the laser beam was then attenuated to

the single photon level by calibrated neutral density filters. From this known photon rate and the detection rate the quantum efficiency can be estimated. Unfortunately we observed that there is a cross-talk between the two channels of our detector. This means that a detection event at one channel will cause a simultaneous event on the other channel with a certain (low) probability. We could not figure out if the origin of this cross-talk has optical or electrical reasons. In most experiments an additional delay fiber (50 m) was installed at the input of one detector channel. In correlation measurements the signal of interest is then shifted away (by 244 ns) from the cross-talk correlation peak.

The great advantage of the SSPD over the SPAD is the ability of free-running detection, hence an external trigger signal to open a gate is obsolete. Additionally, the internal noise rate is several orders of magnitude smaller than for the SPAD. However, depending on the experimental circumstances (e.g. heralded detection, many external noise photons) these advantages can become marginal.

6.2 Frequency Conversion of Coherent Fields

In the previous sections the optical setup was presented and it was explained how the process of SPDC can be used to find the operating point. Difference frequency generation (DFG) and spontaneous parametric down conversion (SPDC) are similar nonlinear processes with the main difference that an additional pump field with appropriate frequency stimulates the down conversion in the case of DFG. This effect is demonstrated in Fig. 6.8. The output of the frequency converter was connected to

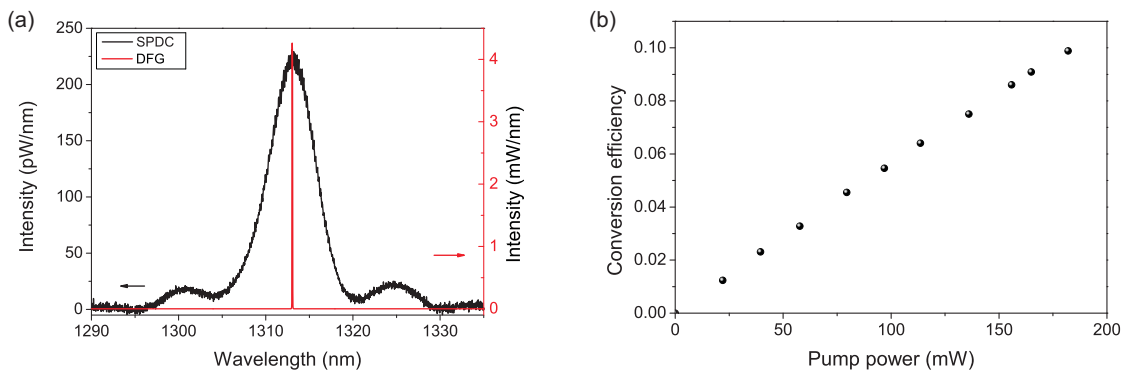


Figure 6.8: Frequency conversion of a laser field. a) shows the spectrum behind the converter measured with the OSA with pump beam blocked (SPDC, black curve) and with active pump beam (DFG, red curve). Please note the six orders of magnitude difference in scale. b) shows the conversion efficiency measured with the OSA.

the OSA. As a light source for the signal photons at 854 nm a diode laser (Toptica DL100) was used. The signal power coupled into the waveguide 3-2 was 4.68 mW. The chip was set to a temperature of 29.21°C which results in a SPDC spectrum centered around 1313 nm. The integrated intensity of the whole spectrum results in 1.78 nW. The shape and width of the SPDC spectrum as discussed earlier are clearly visible. When the pump field with a power of 182 mW at 2.45 μm is added, the spectrum completely changes. The width is reduced drastically and reaches the resolution limit of the OSA (20 pm) while the intensity increases to a total of 349 μW . This clearly demonstrates the stimulating effect of the pump field which increases the conversion efficiency by more than five orders of magnitude. The good overlap between DFG and SPDC intensity peak proves the equality of phase matching conditions for both processes.

To determine the conversion efficiency of the DFG process for such a strong signal field the following procedure can be used. As there was no power meter available with high enough sensitivity at the telecom band, the OSA was used. It has an option to record the spectrum in units of spectral power density which can later be integrated to calculate the power. In this way the spectra were recorded for different pump powers and the output power at the telecom O-band was calculated. The signal power was measured with a power meter verifying that it was constant during the measurement time. The over-all conversion efficiency is then given by the ratio between the signal and the output power. For the photon to photon conversion efficiency (which will be used from now on for the rest of the thesis) the different photon energies (frequencies) have to be taken into account (compare eqn. 3.22 for OPO). The resulting efficiency curve is shown in Fig. 6.8b. I call this efficiency over-all conversion efficiency because the output power is measured behind the frequency converter setup. Hence this value includes all transmission losses between waveguide and fiber output. These are in particular the transmission losses of the filtering elements, the loss due to coupling the free-space beam into a single mode fiber and the coupling losses between individual fiber components. If these losses are well known they can mathematically be eliminated and the internal conversion efficiency can be calculated (internally here denotes inside the crystal; in literature this value is often cited as conversion efficiency). The internal efficiency can be used to compare different waveguides or processes whereas the over-all (or external) efficiency is the value of interest in practice.

In the following, another method should be introduced to estimate the internal conversion efficiency. Assuming an ideal DFG process, every signal photon will be converted to the output mode with a certain probability. If a photon is not converted it will still be present in the signal mode behind the waveguide. As any converted signal photon generates a single telecom output photon the number of telecom photons is equivalent to the number of photons lost in the signal mode. Hence we can use the power of the signal field behind the waveguide in the case that no pump field is present

as reference value for the undisturbed signal field P_0 , subtract the signal power measured with pump field present P_i and normalize this difference by the reference value. We call this value signal depletion:

$$\eta_i = \frac{P_0 - P_i}{P_0} \quad (6.2)$$

If there are any linear losses in the setup between the waveguide and the point the power is measured, they will be included in the reference value and any measured power data point. Obviously these losses will cancel when the signal depletion is calculated. Under these ideal assumptions the signal depletion equals the internal conversion efficiency.

However, when we allow additional processes in the waveguide, e.g. Raman scattering of the pump field followed by downconversion or second harmonic generation of the pump field, additional photons at NIR wavelengths can be generated. Or we allow conversion of signal photons to another wavelength by higher order processes, reducing the output at the target wavelength. Such effects seem very weak and are usually far away from perfect phase matching. However, they can play a significant role when observing the signal field at the single photon level.

A measurement of the signal depletion at macroscopic powers is shown in Fig. 6.9. The data points are expected to follow the same curve as the conversion efficiency given in equation 2.60. As fit function

$$\eta(P) = A \sin^2 \left(\sqrt{\eta_{\text{nor}} PL} \right) \quad (6.3)$$

is used, where P is the pump power, A is an amplitude corresponding to the maximum efficiency, η_{nor} is an internal efficiency parameter and $L = 4$ cm is the waveguide length. The pump power was measured before waveguide coupling and the values

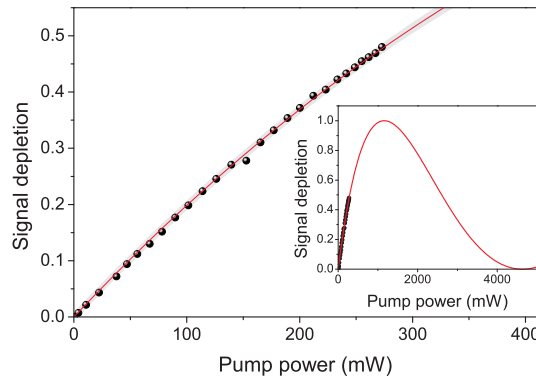


Figure 6.9: Measurement of signal depletion at a macroscopic power level ($139 \mu\text{W}$).

The red line shows a fit to the data and the grey shaded area shows the confidence interval of the fit.

shown in the graphs are corrected for the coupling efficiency. At macroscopic power levels (here $139 \mu\text{W}$) the signal depletion can easily be measured with a power meter. The fit results in a maximum depletion of $A = 1 \pm 0.11$ which is reached at a pump power around $P_{\text{max}} = 1165 \pm 145 \text{ mW}$. For the efficiency parameter we find $\eta_{\text{nor}} = 0.133 \pm 0.017 \text{ W}^{-1}\text{cm}^{-2}$. The errors are given by the 95 % confidence interval of the fit. This means the OPO must generate a power of at least 2.7 W to allow for maximum conversion efficiency including all losses. Unfortunately, such high power is not available. If all light from the OPO was coupled into the waveguide the maximum might be reached which again is an argument to further improve the coupling to the fundamental waveguide mode in future. The maximum depletion actually reached is 48 % at a pump power of 273 mW. As we performed this measurement at a macroscopic power level we can neglect noise processes on the single photon level. We can compare this measurement of pump depletion with the direct measurement of conversion efficiency. In Fig. 6.8b we can read a value of 9.9 % of external conversion efficiency for a pump power of 182 mW. To estimate the internal conversion efficiency we have to take the losses between waveguide and detector into account. We measured a transmission of 37 % through all interference filters and we achieve approximately 80 % coupling efficiency of the telecom photons into the fiber. This results in an internal efficiency of 33 %. For the signal depletion we can read a value of 33.2 % for a pump power of 177 mW from Fig. 6.9. Hence the results from both measurements perfectly match. As it is much more feasible to measure the signal depletion with our setup we can use this number as a figure of merit for the (internal) conversion efficiency.

As we now have a means to measure conversion efficiency, the phase matching bandwidth can be determined. Therefore signal and pump wavelength are kept fixed and the temperature of the waveguide is varied. For every temperature setting the power of the generated telecom light is measured which is proportional to the conversion efficiency. The result is shown in Fig. 6.10. For comparison the same curve was calculated with the help of sellmeier equations for bulk LN [129]. The experimental curve is slightly broader and has a width of 2.9 K (FWHM). The shape agrees very well with the simulation. The temperature dependent phase matching curve (Fig. 6.10) is related to the wavelength dependent curve (e.g. Fig. 6.3) via the dispersion of the waveguide. As dispersion does not change much in the small wavelength and temperature range of interest the shapes of both curves are similar. The crystal mount with the controller is capable to hold a certain temperature with 10 mK accuracy. This is enough to fix the phase matching curve at its maximum.

The measurements at a macroscopic power level allow for a first impression of the converter performance. For the conversion of quantum states, however, an initial characterization at the single photon power level is necessary. For signal depletion measurements the residual signal photons are separated from the telecom beam and coupled into a single mode fiber. The transmission between the waveguide and the fiber output

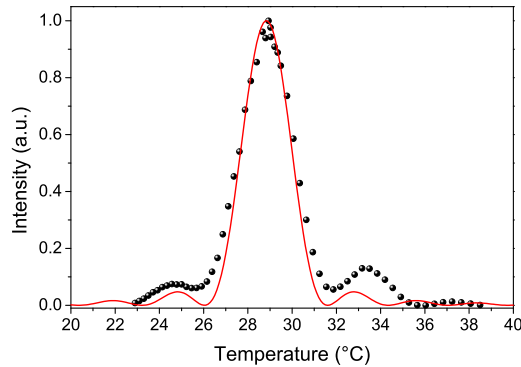


Figure 6.10: Phase matching curve for temperature tuning. Telecom wavelength 1314.152 nm. The solid line shows a calculated curve for bulk LN with Sellmeier equations [129].

(from 4 to 6 in Fig. 6.1) was measured with a laser first. Together with the collimation lens transmission we deduce that 19 % of the photons inside the waveguide reach the end of the single mode fiber. This number appears low, however the optical path behind the waveguide is optimized for telecom photons resulting in non perfect collimation for other wavelengths. The short pass filter (Thorlabs FES 950) is used to suppress residual 1080 nm photons stemming from the OPO pump laser traveling through the whole setup. Hence, by attaching this fiber to a silicon APD we can count the residual signal photons and calculate the number of input photons to yield the signal depletion.

Before attaching a single photon detector to the telecom output of the converter we measure the spectrum. Figure 6.11a shows the converter output when all spectral filters are removed. It was recorded with the spectrometer (grating of 600 lines/mm) and the InGaAs camera with 1 s integration time. The two prominent peaks saturated the camera and are cut-off in their intensity. Peak 1 can be found at 1079 nm which is the pump wavelength of the OPO. The fiber-laser has an output power in the Watt regime. It is partly transmitted through the dichroic mirror behind the OPO, coupled through the waveguide and reaches the final fiber coupler although it suffers high loss. The pedestal found in the spectrum around this peak is also mostly generated in the OPO as it can already be found in its output. Peak 2 in contrast is generated in the waveguide. This is the second harmonic of the DFG pump field. This process is not actively phase matched but the intensity in the waveguide is high enough to generate this field on the single photon level. There are many more small peaks visible with unclear origin. From earlier experiments we know that Raman scattering of the pump field can generate photons at the output wavelength [34]. The range of Raman peaks in lithium niobate seems limited to shifts below 1000 cm^{-1} [35]. For the pump wavelength

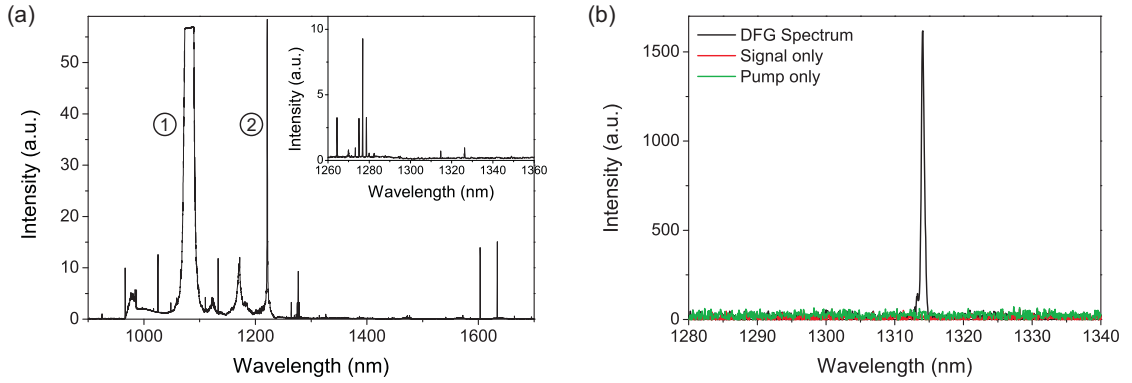


Figure 6.11: Spectra of the waveguide output. a) shows a spectrum without any filters, with high pump power coupled into the waveguide. Peak 1: 1079 nm, OPO-pump laser, Peak 2: second harmonic of pump field. The inset shows a close-up of the spectrum in the telecom O-band. b) shows the spectra with filtering. For comparison spectra are shown for coupling of the pump field only, coupling of the signal field only and simultaneous coupling of pump and signal fields, respectively.

used here this means approximately $1.97\text{--}3.25\ \mu\text{m}$. This is far away from the target wavelength range (telecom O-band) and can thus easily be separated. Another noise source that generally appears is SPDC of the pump field. This process only generates photons with energy lower than the pump photons. In our case the pump wavelength is longer than the target wavelength which avoids noise due to SPDC photons [32]. A third noise process observed in quantum frequency conversion is introduced by fabrication tolerances of the nonlinear medium. Random duty cycle errors in the QPM grating period will allow a broad band phase matching pedestal. This leads to a broad noise floor [32]. Furthermore, narrowband noise peaks can stem from nonlinear processes which are phase matched by higher-order QPM. Finally, there are a plethora of cascaded nonlinear process possible at which the efficiency reduces drastically with every additional conversion step.

Obviously in our spectrum there is a low noise window between $1.3\ \mu\text{m}$ and $1.6\ \mu\text{m}$ where the peaks nearly vanish. This circumstance is advantageous for converting to the telecom O-band. Nevertheless spectral filtering is necessary to suppress noise outside this window. Our superconducting detectors are sensitive for wavelengths between 200 nm and 2000 nm. Hence we have to suppress all noise photons of the spectrum except for a small window around 1310 nm where our target wavelength can be found. Therefore a total of three bandpass filters (Techspec 1300-50 and 1325-50, Thorlabs FB 1310-12) and a wavelength division multiplexer were added. The total transmission through this filtering stage is 37 %. The transmission of the filtering stage directly influences the external efficiency. Increasing its transmission directly increases the ratio

between external and internal conversion efficiency. Most of the loss is introduced by the narrow filter (FB 1310-12, transmission 45 %). The over-all transmission could be optimized by exchanging this filter with a high-transmission component. The combined suppression of these filters is high enough to suppress all the noise peaks in the whole spectrum and especially in the telecom O-band as Fig. 6.11b shows.

With these preliminary studies we can measure the conversion efficiency at the single photon level. The measurement scheme is similar to the measurement with higher power but here the powermeter is replaced by a silicon APD. The laser was attenuated by neutral density filters (OD 11) to have approximately 400 kcts./s on the Si-APD resulting in 2.3 kcts./s on the InGaAs-SPAD at maximum pump power. The count rates of signal and telecom field were recorded for different pump powers. The signal count rate in the case of the pump blocked is used as reference for the calculation of signal depletion, which is shown in Fig. 6.12a. The signal depletion reaches a maximum of 35 % at 283 mW pump power. The fit results in an efficiency parameter $\eta_{\text{nor}} = 0.106 \pm 0.069 \text{ W}^{-1}\text{cm}^{-2}$ which agrees with the macroscopic measurement within the error bar. To calculate the conversion efficiency from the measured count rates a few

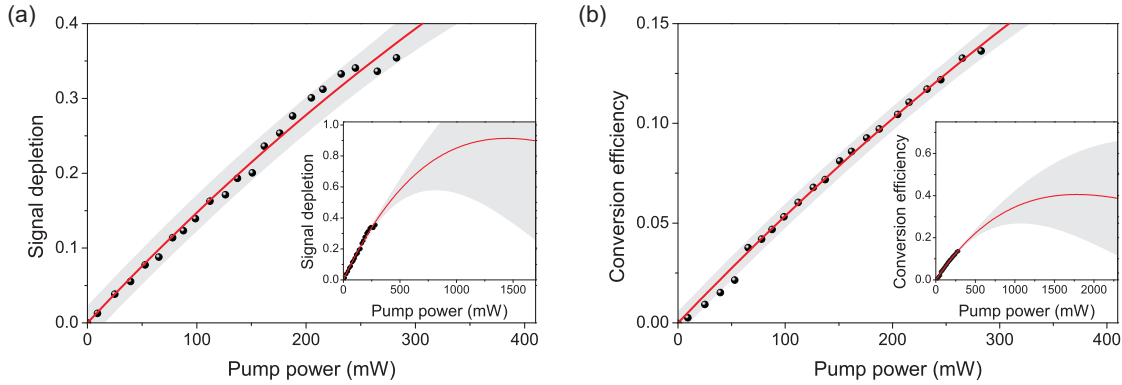


Figure 6.12: Frequency conversion of a coherent field at the single photon power level. a) shows a measurement of the signal depletion. b) shows the external conversion efficiency. The red curves show fits to the data and the shaded area corresponds to the fit confidence interval.

parameters of the setup have to be taken into account. The InGaAs-SPAD can only be operated in gated mode. Therefore a 1 MHz trigger which is not correlated to the generation of photons opens gates with 5 ns width. The deadtime was set to 10 μs . The detection efficiency is 30 %. The internal dark count rate for these setting was measured as 262 cts./s and subtracted from all data points. With the gate duty cycle and the detection efficiency we estimate that only the fraction of $1.5 \cdot 10^{-3}$ of the telecom

photons in the fiber is registered by the detector. In the signal branch we know that the detection efficiency is at 50 % for 854 nm, we have a transmission of 19 % from the waveguide to the APD and we additionally lose half of the photons as the APD used here was mounted in a HBT-setup. Thus the fraction of $47.5 \cdot 10^{-3}$ of the signal photons coupled into the waveguide is detected. We can now divide the count rates by the individual ratios to evaluate the photon rates. The ratio of these photon rates then is the external conversion efficiency as shown in Fig. 6.12b. The data reach a maximum of 13.6 % at the maximum pump power. The fit results in an efficiency parameter $\eta_{\text{nor}} = 0.032 \pm 0.018 \text{ W}^{-1} \text{ cm}^{-2}$. Obviously the fit curves at the single photon regime show larger errors than at macroscopic power levels. To calculate the internal conversion efficiency we have to correct the value for the losses between waveguide and detector which are approximately 37 % for the filters and 80 % for fiber coupling. This gives an estimate for the internal conversion efficiency of 46 % which is between the signal depletion values measured for single photon and macroscopic power levels. The same loss values can also be used to convert the η_{nor} -value between external and internal conversion efficiency. We can compare these results with previous measurements. For the external conversion efficiency we found a value of 9.9 % at a pump power of 182 mW for the measurement at macroscopic power levels (Fig. 6.8b). When the laser is attenuated to the single photon level we measured an external conversion efficiency of 9.7 % at a pump power of 187 mW (Fig. 6.12b). These values perfectly match although we used different signal power levels and different measurement devices. We can also compare the pump depletion results. At macroscopic power levels we find a maximum of 48 % (Fig. 6.9) whereas this value is slightly smaller for the measurement at single photon power level (35 %, Fig. 6.12a; 46 % derived from Fig. 6.12b). The values for the normalized efficiencies derived from the fits agree within their error bars. From these facts we can conclude that there is no fundamental difference in conversion efficiency between low or high signal power levels. From several months of operating the frequency converter there exist some data from frequent measurements of signal depletion or conversion efficiency. From this data we can claim that the signal depletion is typically 45 ± 10 % and the external conversion efficiency is around 9 ± 2 %. We can see day by day fluctuations of these values and can also identify different reason for the variations: One issue is the alignment of the beam path in the converter. This can be optimized regarding the generated telecom photon rate. On the other hand we can identify the OPO as source of efficiency fluctuations. Its output power decreases after a few days and re-optimization of the cavity becomes necessary. After that, the output wavelength changes by small amounts and it is not clear if the spatial profile of the output beam changes, too. Nevertheless reliable conversion efficiency can be reached.

Eventually, we can compare the conversion efficiencies of our converter with efficiencies from previous experiments. In these experiments higher values for the normalized and the internal efficiency (e.g. 738 nm \rightarrow 1550 nm: $\eta_{\text{nor}} = 0.61 \text{ W}^{-1} \text{ cm}^{-2}$,

$\eta_{\text{int}} > 0.73$ [34] and $710 \text{ nm} \rightarrow 1310 \text{ nm}$: $\eta_{\text{mor}} = 1.15 \text{ W}^{-1}\text{cm}^{-2}$, $\eta_{\text{int}} > 0.64$ [37]) have been measured. The deviation can be explained by the different coupling integrals which are significantly higher [175] for the older experiments. This is due to a different geometric outline of the waveguides and a smaller difference between the wavelengths involved in the conversion processes. The internal conversion efficiency measured within this thesis is lower just because the maximum of the conversion curve was not reached with the available pump power.

6.3 Frequency Conversion of SPDC Photons

The results from the previous section show that the converter can be used for frequency conversion of weak optical fields. To examine its compatibility with quantum states, the input has to be fed with non-classical light. Therefore we use photons generated by spontaneous parametric down conversion. The setup is shown schematically in Fig. 6.13. As first stage of the SPDC pump field a diode laser at 854 nm is used

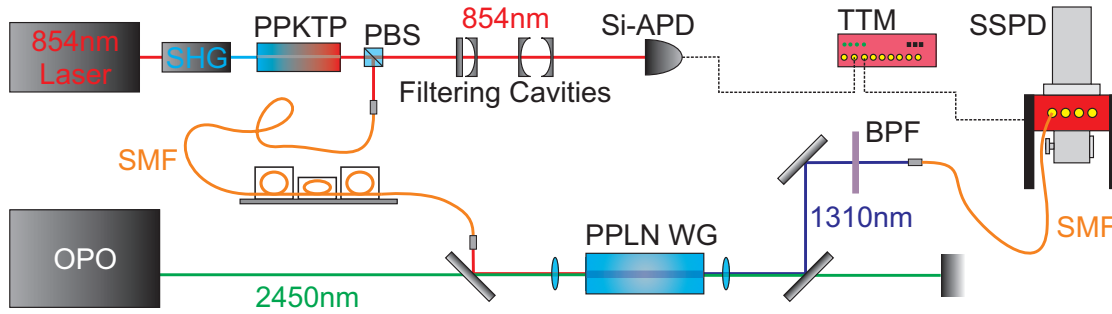


Figure 6.13: Setup for quantum frequency conversion of correlated photon pairs.

(this is the same laser used for alignment purpose, waveguide characterization and the conversion experiment with coherent field). The laser is frequency stabilized to a transition in calcium ions ($^{40}\text{Ca}^+$: $3^2D_{5/2} \leftrightarrow 4^2D_{3/2}$). In the next stage this laser is frequency doubled, resulting in an available pump power of up to 60 mW at 427 nm for the following SPDC process: It is based on Type-II phase matching in bulk periodically poled potassium titanyl phosphate (KTP). In the configuration of Type-II phase matching, output signal and idler fields have orthogonal polarization [98]. Furthermore the phase matching is set to generate frequency degenerate photons. In summary, this source generates polarization entangled and frequency degenerate photon pairs centered around the 854 nm transition in calcium ions. Behind the source a polarizing beam splitter is used to separate signal and idler mode. Thus we destroy the polariza-

tion entanglement as the paths become distinguishable. One of the photons is sent to the filtering cavities described earlier (see sec. 5.1.2), to cut out photons resonant with the calcium transition. The other photon is coupled to a single mode fiber and sent to the frequency converter. The source has been described in more details in several publications [183, 184, 215].

Figure 6.14a shows a measurement of signal depletion for frequency conversion of the SPDC photons. Obviously the curve of this measurement resulted in significantly

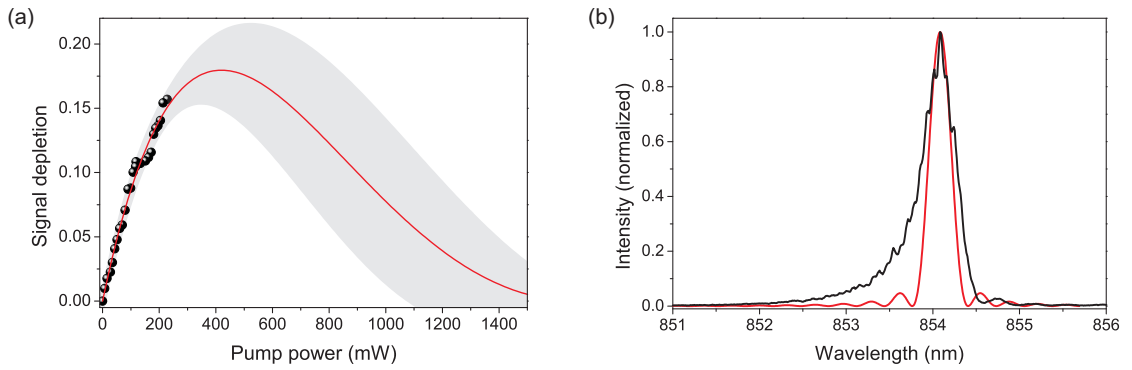


Figure 6.14: Frequency conversion of SPDC photons. a) shows a measurement of signal depletion. b) shows the spectrum of the signal photons (black line) and a calculated phase matching curve (red line) for comparison.

less signal photon depletion compared to the measurement with the attenuated laser field (Fig. 6.12). To explain this we have to take the spectral width of the sources into account. The laser has a linewidth in the MHz-range, much narrower than the acceptance bandwidth of the conversion process (118 GHz FWHM). However, the SPDC spectrum has a width of approximately 173 GHz (FWHM) as shown in Fig. 6.14b. Thus only the central part of the spectrum is perfectly phase matched whereas the outer wings suffer a phase mismatch resulting in reduced conversion efficiency. We send these unfiltered SPDC photons to the converter and detect the residual photons behind the converter for a calculation of the signal depletion, as explained in previous sections. Thus the count rate of 854 nm photons behind the converter corresponds to the rate of photons integrated over the whole NIR spectrum reaching the APD. This means that the calculation of the signal depletion value (Fig. 6.14a) is influenced by photons that are not affected by the conversion process due to their wavelength. Hence we derive a value for signal depletion averaged over the spectrum. The phase matching curve (cf. red curve in Fig. 6.14b) is a measure for the spectral dependence of the conversion efficiency. Not only the conversion efficiency but also the signal depletion is

reduced for the spectral components at the wings of the phase matching curve. From the original spectrum at 854 nm and the phase matching curve we can estimate the spectrum of the converted photons and the ratio of peak conversion efficiencies. For this end we multiply the signal spectrum and phase matching curve for any wavelength. The integration over the resulting curve delivers a value proportional to the total count rate. When we compare this with the integration over the original spectrum we find a ratio of 0.397. The maximum signal depletion reached for the conversion of SPDC photons here was 15.7 %. On the other hand, it was 33.3 % for the conversion of weak coherent light at the same pump power. The ratio between these two values of 0.47 is comparable to the estimation from the spectral mismatch. From this we can conclude that the peak signal depletion and conversion efficiency is the same for the weak laser and the SPDC photons.

Correlation of Converted Photons

As demonstrated in section. 5.1.2 there exists a temporal correlation between the photons of a pair produced by SPDC. These correlations show non-classical statistics and are a result of the quantum character of the pair generation process. Quantum frequency conversion with a continuous pump field should not alter the temporal properties of the photons during conversion. Thus these correlations should be preserved. As a reference, the correlation function between the original signal and idler photons, both at 854 nm was measured (i.e. without converter). The result is shown in Fig. 6.15a. The

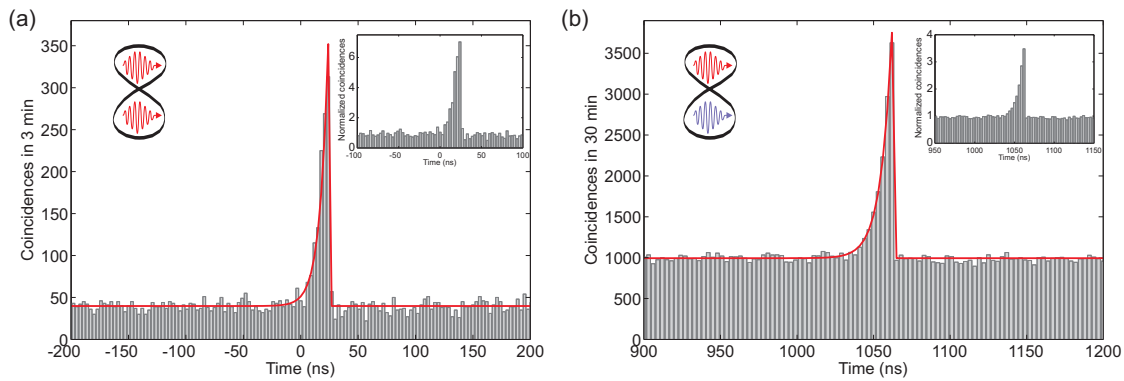


Figure 6.15: Coincidence measurements of SPDC photon pairs. a) shows the signal-idler correlation function for the 854 nm photon pairs. b) shows the correlation function after converting one photon to the telecom O-band. The red solid lines show fits to the data. The insets show the coincidences normalized to the background level.

exponential decay of the photon wave packet with a time constant of 7 ± 0.4 ns is clearly visible. This temporal shape corresponds to a spectral bandwidth of 22.9 ± 1.3 MHz. The design value for the bandwidth of the filtering system is 22 MHz, corresponding to 7.25 ns. The rise time of the correlation function should correspond to the temporal shape of the herald photon. The herald photon is not filtered and has thus a broad spectrum resulting in a time constant of 5 ps (cf. section 6.4). As this is far below the timing jitter of the detectors the rise time of the correlation function (664 ± 68 ps) is dominated by the detection timing jitter. The background coincidence rate is found by averaging the rate for time delays outside the coincidence peak. To determine the coincidences, we sum up the coincidence events under the fit curve over 10 time bins at 3 ns each. According to the temporal shape, there should be more than 98 % of the coincidence events in this 30 ns interval. From this coincidences the background (offset) is subtracted. This results in a coincidence rate of 4.97 cts./s. The data here was recorded with at a SPDC pump power of 2.85 mW. The noise-free coincidence rate scales linearly with the pump power thus we expect 96.1 cts./s at the maximum available pump power of 55 mW.

The coincidence measurement including quantum frequency conversion is shown in Fig. 6.15b. Here the pump power of the SPDC source was set to 55 mW and the pump power of the converter to 260 mW which were the maximum values reached, respectively. We again see the exponential decay with the same time constant of 7.3 ± 0.7 ns. Hence the frequency conversion did not alter the temporal shape of the photon wave packet. The rise time is here again 595 ± 42 ps as the same detector for the herald photon was used. With the same procedure as before we find a coincidence rate of 4.15 cts./s. Comparing this rate with the original rate without conversion and taking into account the different detection efficiencies of the Si-APD at 854 nm and the SSPD at 1310 nm, we find an over-all conversion efficiency of 7.8 %. For calibration purpose a measurement of the conversion efficiency with the attenuated laser was performed directly following the correlation measurement resulting in an external conversion efficiency of 8.3 % which is in good agreement with the value derived from the correlation functions and from earlier measurements.

If the coincidences in Fig. 6.15 are normalized with respect to the background level we see that the correlation peak reaches a maximum value of 7.03 in the original case and 3.48 including frequency conversion. This is a clear indication that the temporal correlation is preserved in the conversion process.

There have been reports on the frequency down conversion of NIR SPDC photons to telecom wavelengths and the conservation of their temporal correlation [28, 216, 217]. However, the coherence time of these photons was too short to reveal their temporal structure. As already mentioned, the continuous wave pump does not change the temporal shape of the photons during the conversion process. This has already been studied earlier in the conversion process of single photons emitted by a semiconduc-

tor quantum dot [37]. In contrary, a pulsed pump source can be used to reshape the wave packet. The photon can only be converted when the wavefunctions of signal and idler photon overlap inside the nonlinear medium. Thus an ultra-short pump pulse can be used to cut out a piece of the single photon and generate an ultra-short idler photon. This effect was used as a quantum eraser technique [42] to reduce the effective timing jitter of single photon detection. In other experiments the pump pulse has been shaped to modulate the amplitude of the photon under conversion [218] which simultaneously changes its temporal shape. Furthermore, modulating the phase of the pump pulse [219] or even introducing a chirp [40] can be used to tailor the spectral and temporal shape of the photons. Such a technique can be useful to adapt photons to a certain optical transition or to make photons from different sources indistinguishable [220].

As one photon of the pair can be converted successfully to the telecom O-band we can use it for long-range transmission in a fiber. Results from such a measurement are presented in Fig. 6.16. First, a reference measurement of the correlation function was performed and then the measurement was repeated with additionally 20 km delay fiber (Corning SMF-28). From the fit data we derive an additional delay of 100044 ± 3 ns.

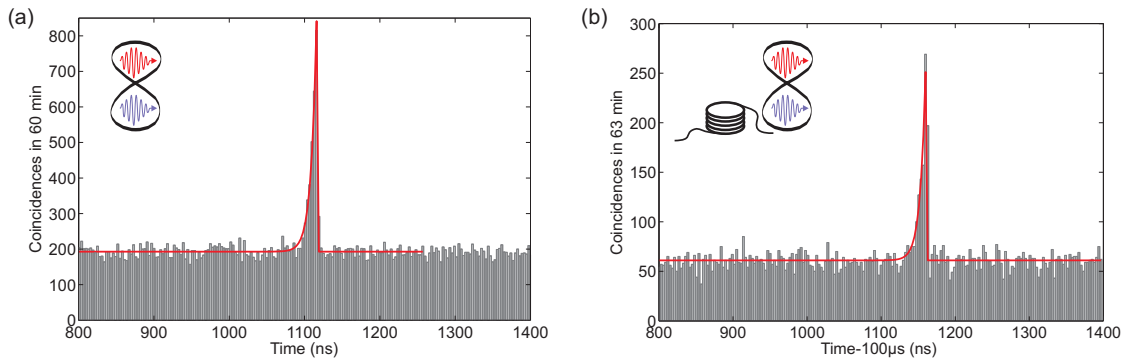


Figure 6.16: Correlation measurement of SPDC photons, one original (854 nm) and one converted (1310 nm) with long delay. a) shows a reference measurement without delay, b) shows the same measurement with additional 20 km delay fiber. Please note the shifted time axis.

According to the refractive index given in the data sheet [221], this corresponds to a length of 20444.7 ± 0.6 m. We can again see that the temporal shape of the wave packet is left untouched and the decay constant did not change. When we compare the coincidence rates, we see that it is reduced to a fraction of 0.32 by the additional

delay fiber. According to the data sheet [221], the maximum loss is 0.35 dB/km at 1310 nm. For our fiber this results in an attenuation of -7.16 dB or a transmission of 0.19. The fiber in use shows a better performance than this worst-case values. We can estimate an attenuation of 0.247 dB/km. However, in these calculations we neglected the losses introduced by coupling the fiber into the already existing fiber link. For this we use butt-coupling via mating adapters which can cause additional loss depending on the individual connector fabrication tolerances. For comparison in literature [144] an attenuation factor around 2 dB/km can be found for 850 nm which would result in a transmission of $8 \cdot 10^{-5}$ for our fiber. This shows the benefit of frequency converting the photons before sending them through a long fiber. Taking into account the finite conversion efficiency, still two orders of magnitude more photons would arrive at the end of the fiber.

Heralded $g^{(2)}$

In this section we want to focus on heralded single photons. Per definition, a single photon is in a pure photon number state $|1\rangle$ with $n = 1$. As discussed earlier in this thesis (see sec. 2.2.1), the second order correlation function of one light mode with itself can be used to distinguish different classes of light. Single photons will show anti-bunching in the second order correlation function. A heralded single photon source generates photons which show single photon statistics conditioned on the detection of a heralding event. Such a source can be realized by an atomic emission cascade where the first emitted photon serves as herald for the second photon (e.g. in [222]). Both photons are temporally correlated and are in a single photon state, respectively, due to their generation process. The process of SPDC also generates pairs of correlated photons. The difference between these two methods is the statistics of pair generation. As can be seen in equation 2.80 the state generated by SPDC contains contributions from higher order pairs. If there is no photon number resolving detector available we can not distinguish between a single pair and multiple pairs. Hence a heralding event may go along with several photons and not only a single one. However, these higher order contributions depend on the pump power of the SPDC process. If we operate our source at low enough powers we can in principle generate a state as close to an ideal heralded single photon state as desired. In literature it is thus well accepted to consider such a SPDC source as heralded single photon source [223], i.e. the slight deviations in photon number statistics are neglected. We want to follow this definition and investigate the application of the NIR SPDC source in combination with QFC as source for heralded telecom single photons. The second order correlation of the photons can then be measured with a Hanbury-Brown Twiss (HBT) interferometer when the heralding event is taken into account. The signature for heralded single photons then is the observation of anti-bunching in this correlation function. The setup in our case is

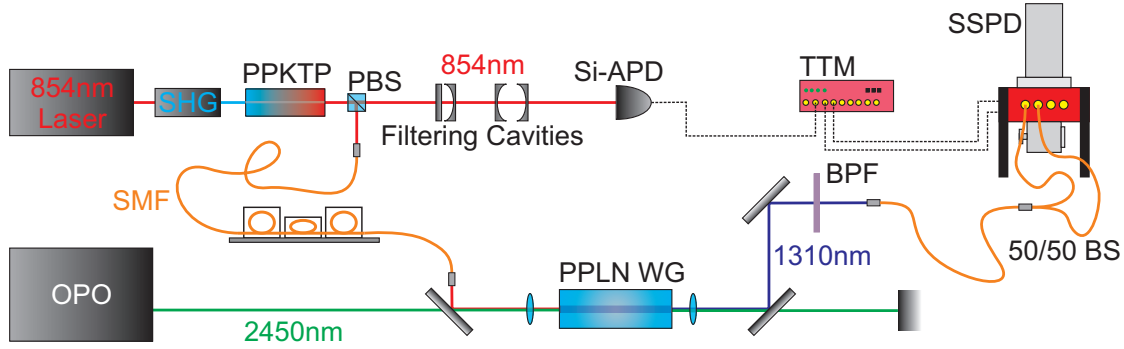


Figure 6.17: Setup to measure heralded second order correlation function of telecom-converted photons.

shown in Fig. 6.17.

As described earlier, one photon of the pair is used as herald. In the first experiments to be presented, the herald photon is narrowband filtered. The other (unfiltered) one is sent through the frequency converter and translated to the telecom O-band. The converter output is coupled to a fiber based beam splitter with each output connected to one channel of the SSPD. This add-on serves as HBT interferometer. Both SSPD channels and the herald are recorded by a time tagging module (AIT TTM8000). The heralding procedure is realized in the post processing. An event in the list of time tags of the heralding detector can be used to cut out a certain time window in the lists of the HBT interferometer. In the measurements with photons from the OPO (see sec. 5.1.1) the temporal structure of the second order correlation function was lost as the detector jitter exceeds by far the photons' coherence time. This is not the case here. However, there is another problem: In the previous section we calculated a coincidence rate of 4.15 cts./s. As we here introduced a beam splitter, the coincidence rate for each detector will cut in half. The signal to noise ratio (SNR) will reduce by a factor of four. A measurement of the temporal shape of the second order correlation function will thus take hours of integration time. The herald count rate for this measurement was 784 cts./s while the rate on each SSPD channel was around 30 kcts./s. If we neglect the temporal structure and are only interested in multi-photon probabilities there exist more efficient ways of data analysis. A few prerequisites have to be met. As elaborated in equation 2.51, the value of the second order correlation function at zero delay depends on the average photon number. If we assume a perfect single photon source ($\langle \hat{n} \rangle = 1$) and add a source of uncorrelated noise photons, the effective photon number will increase $\langle \hat{n}_{\text{eff}} \rangle \geq 1$. This will also increase the value of $g^{(2)}(0)$ towards one. From equation 2.51 we can expect a value of:

$$g^{(2)}(0) = 1 - \frac{1}{n} \quad (6.4)$$

In the case of solid state single photon sources, n is often identified as the number of unresolved, individual emitters contributing to the optical field under investigation [224]. In analogy, an equation can be derived that gives a lower boundary for the $g^{(2)}(0)$ -value in the presence of uncorrelated noise photons. In literature equations can be found to correct the $g^{(2)}(\tau)$ -functions [225]:

$$g_b^{(2)}(\tau) = 1 + \rho^2 (g^{(2)}(\tau) - 1) \quad (6.5)$$

Where g and g_b are the noise-free and the noise-degraded correlation functions, respectively. The factor $\rho = \frac{S}{S+B}$ is the ratio between signal photons and the total number of photons. For an ideal single photon source we find $g^{(2)}(0) = 0$. We can now express the previous equation with the $SBR = \frac{S}{B}$ and find:

$$g^{(2)}(0) = 1 - \left(\frac{SBR}{SBR + 1} \right)^2 \quad (6.6)$$

We will use this equation to estimate the $g^{(2)}(0)$ -value for different operating conditions of our heralded single photon source (c.f. Fig. 6.20c).

In the case of heralded single photons the choice of the gate's temporal position and width will influence how much signal and noise photons will be detected. The resulting value for $g^{(2)}(0)$ will thus also depend on the parameters of the detection gate. We can use the above relation to optimize the SBR via the gate width to achieve the lowest possible value for the correlation. However, the SNR is better suited here as it takes into account the actually collected number of events while the SBR should be independent of measurement time. The second order correlation between the herald photon and one channel of the SSPD is shown in Fig. 6.18a. On the right side it shows a step edge limited by the detection timing jitter while on the left there is an exponentially decaying tail with a decay time of 7.2 ns corresponding to the temporal width of the filtered photons. The background count rate is constant and the signal is largest close to the step edge. Thus the signal to background ratio will decrease when the width of the gate window is increased. However, a narrow window contains only few detection events and is thus more susceptible to detection noise. We have to look at the signal to noise ratio which considers both effects. To find an optimal gate, we varied the gate offset and width and calculated the SNR for each combination. The result is shown in Fig. 6.18b, showing an island of high SNR values. The gate width is similar to the decay time of the photons. We find an optimum value of 8 ns. This procedure was repeated for the other SSPD channel.

As explained, in the post-processing each herald event can trigger a gate with the above determined offsets and widths to cut out detection events in the lists of the SSPDs. In the resulting lists only few events are left which then can be correlated with the usual procedures. With these data we can calculate the anti-correlation parameter

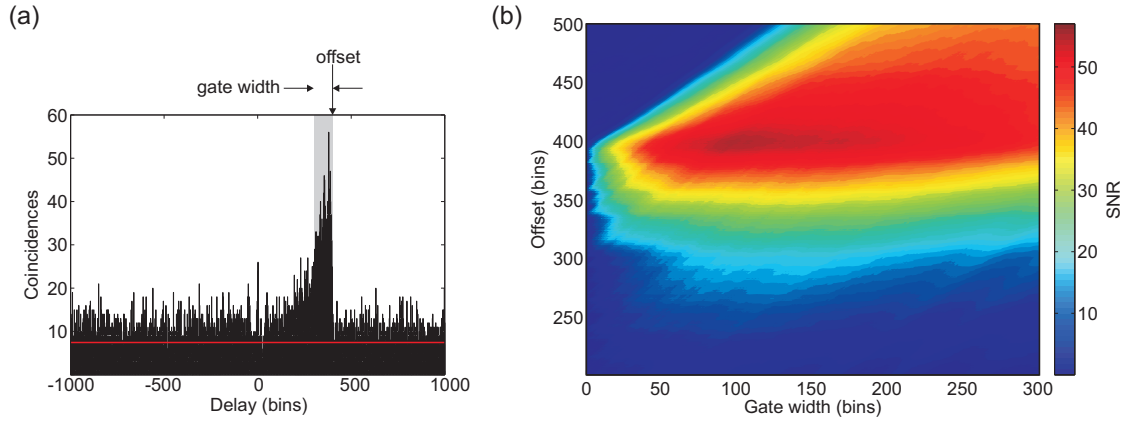


Figure 6.18: Data post-processing for heralded $g^{(2)}$ measurement. a) shows a correlation measurement between the herald photon and one channel of the SSPD. The red line indicates the average background level. A gate window was defined and its offset and width varied while the SNR was calculated. b) shows the result of this variation. Here the values for maximum SNR can be found. The grey shaded area in a) shows the optimal gate. The time units are bins of 82.0345 ps each.

α (see eqn. 2.85) and an approximation for the $g^{(2)}(0)$ value (see eqn. 2.86): $\alpha = 0.771$ and $g^{(2)}(0) = 0.621$.

There is another method to calculate the heralded second order correlation where the data is efficiently used, but with the drawback that the temporal information is lost. The method was introduced by Fasel [65] and a software was developed to analyze our data with this method by Bock [199]. The basic procedure behind this method is as follows: For every heralding event the software checks for each signal channel individually if there is a detection event within a certain time window (gate). In our case this results in a list of zeros and ones for each SSPD channel indicating if there was a signal photon detection event coinciding with the current herald. In the next step these two lists will be compared. The software starts with the first event in the first list and checks how many heralding events it takes to find the next event in the second list. Then the pointer in the first list advances to the next event. In the end this results in a histogram showing how many herald detections can be found between consecutive heralded signal photon detection events in both SSPD channels. In the case of an ideal single photon source there should always be at least one herald between two photon detections and thus the bin at zero should not contain any data. In the case of coherent photons the time delay between two photons is uncorrelated and equally distributed and thus all bins should contain the same number of events. The ratio between the height of the bin at zero and the surrounding bins equals the $g^{(2)}(0)$ -value. For this analysis we recorded 20027506 heralding events in a total measurement time

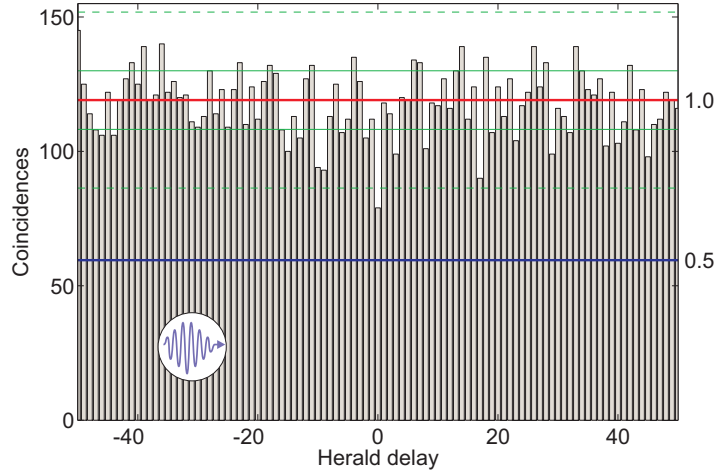


Figure 6.19: Heralded second order correlation of telecom-converted photons. The red line shows the average coincidence value and the green lines the error intervals around this level (solid green lines \sqrt{N} -noise, dashed green lines three times \sqrt{N} -noise). The blue line indicates the $g^{(2)} = 0.5$ boundary for non-classical states of light.

of 426 min. The pump power of the SPDC source was set to the maximum available power of 55 mW. The resulting histogram for our measurement is shown in Fig. 6.19. There is a clear anti-bunching visible as the central bin is significantly smaller than the noise level (less than three times detection noise). If the average value of the time bins is normalized to one, we find a value of $g^{(2)}(0) = 0.663$. This is in good agreement with the value derived earlier by the approximative method. In the whole section we used the filter cavities to herald narrowband single photons. As a result, the device can be used as a heralded narrowband single photon source at telecom wavelengths.

For the following experiment we remove the filters from the heralding beam path and use full bandwidth, broadband photons as herald. The previously introduced procedure to determine the $g^{(2)}(0)$ -value can also be applied for these short-coherence length photons. We use the same measurement setup (except for the removal of the filter cavity) and the same software for data analysis. In the software, each detection event is analyzed individually and sorted to the appropriate histogram bin without regard to the exact timing delay between successive detections at the SSPDs. As the time between two consecutive heralding events is on average much longer than the timing jitter, this procedure is nearly insensitive for the jitter. This allows us to reveal the single photon character of the converted photons with unfiltered herald. The results are summarized in Fig. 6.20. For reference, two measurements of heralded $g^{(2)}(0)$ were performed with the original 854 nm photon pair, i.e. without frequency conversion. We chose a high pump power of 9.3 mW, where the heralding detector starts to saturate

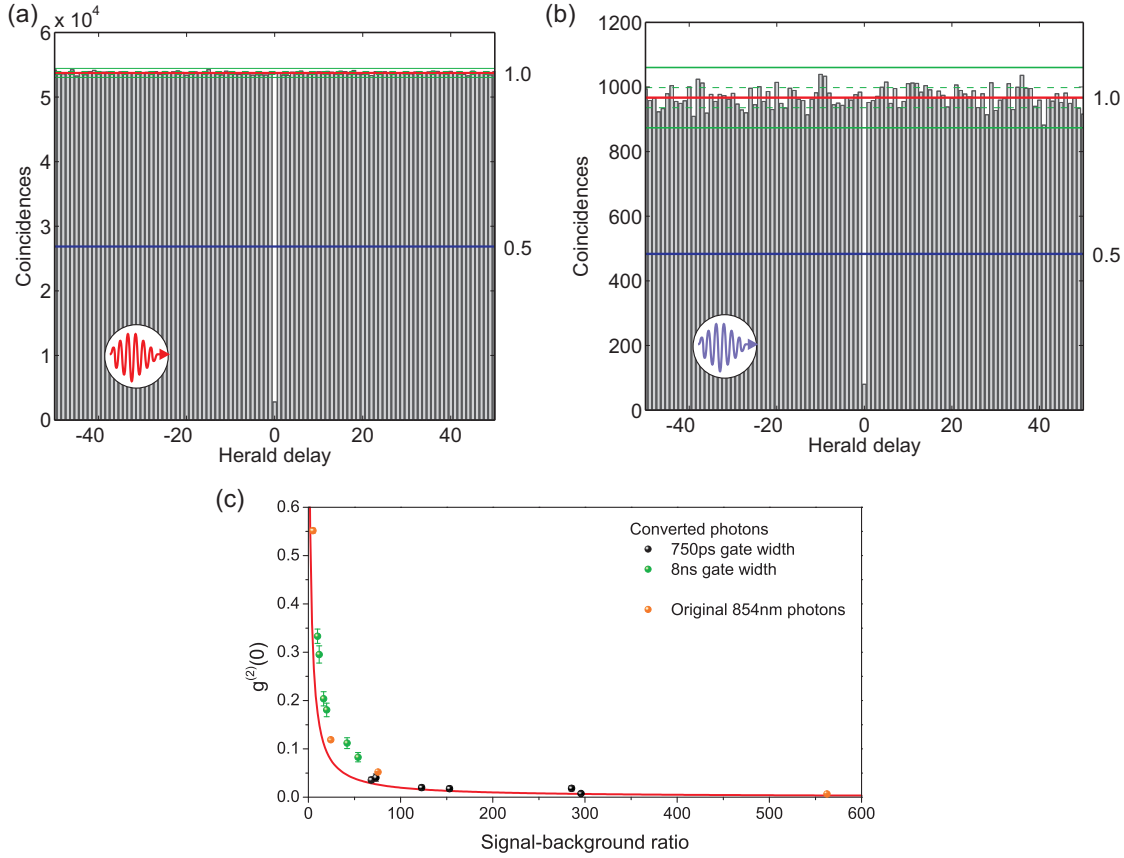


Figure 6.20: Heralded $g^{(2)}$ -measurement of unfiltered photons. a), b) show the resulting histogram at the lowest pump power of 0.5 mW and 8 ns gate width, for the original 854 nm photons a) and the telecom converted photons b), respectively. c) shows the measured values as a function of the SBR. The solid line indicates the values expected theoretically.

and a low power of 0.5 mW. We want to compare the results for two different gate widths: 8 ns was found as optimal value for the filtered photons; 750 ps is the optimal value for the unfiltered photons. The result for the low power measurement with a gate time of 8 ns is displayed in Fig. 6.20a. As a result we find $\text{SBR}=75.5$ from the raw data and $g^{(2)}(0) = 0.052 \pm 0.001$ from the histogram. If we reduce the gate width to 750 ps the SBR increases to $\text{SBR}=563$ and we find $g^{(2)}(0) = 0.007$. This effect of the gate width becomes more prominent when we look at the data at high pump powers: for 8 ns gate we find $\text{SBR}=4.9$ and $g^{(2)}(0) = 0.552 \pm 0.005$ and for 750 ps gate this changes to $\text{SBR}=24.3$ and $g^{(2)}(0) = 0.119 \pm 0.004$. The results are plotted in Fig. 6.20c (orange curve). The increase in pump power results in increased high-order pair generation rate which contributes to the background as seen in the experimental data.

Next we introduce QFC to convert one photon of the pair to the telecom O-band and use the other 854 nm photon as herald. Due to the phase matching curve being narrower than the signal photon bandwidth, there will be herald events without a corresponding telecom partner, contributing to the background. The heralded- $g^{(2)}$ was measured for different pump powers of the SPDC source. The histogram in Fig. 6.20b was measured at 0.5 mW and calculated with a gate width of 8 ns. We find a SBR=53.9 and the histogram shows a clear antibunching dip of $g^{(2)}(0) = 0.083 \pm 0.01$. If we compare this with the original 854 nm measurement, we see a decrease in SBR and an increase in the $g^{(2)}(0)$ -value, accordingly. This is consistent with our expectations, as QFC reduces the signal rate due to the finite conversion efficiency and additionally adds uncorrelated noise photons. In an ideal process the SBR would not change. The influence of SPDC pump power on the SBR due to multi-pair generation can be investigated by power-dependent measurements. These are shown in Fig.6.20c. All data points follow the expected dependence of the $g^{(2)}(0)$ -value on the SBR. We can further compare the results for different gate widths (green and black curves in Fig. 6.20c). We increase the gate from 750 ps to 8 ns (ratio 10.7). This decreases the SBR on average by a factor of 6.8. This can be explained by the shape of the background which is constant in time while the signal is time correlated with the herald. The width of the signal is resolution limited and thus determined by the detection timing jitter (approx. 600 ps). When the gate width is increased from 750 ps, the background rate increases thus linearly but the signal rate only slightly increases further. The $g^{(2)}(0)$ -values for these two gate widths increase by a factor 9.2, on average.

We can summarize the results as follows: As the low $g^{(2)}(0)$ -values demonstrate, the combination of a NIR SPDC source and QFC can be used as heralded single photons source in the telecom O-band. We can herald narrowband photons which suffer noise due to uncorrelated, converted unfiltered photons. In future this could be optimized by inserting an additional filter before or after the converter and thus filter both photons, herald and signal, symmetrically. On the other hand no such issues are observed in the experiments with unfiltered source pairs. In this case very low $g^{(2)}(0)$ -values were observed. However, these values actually depend on the chosen gate width. Using a small, optimized gate width the highest SBR and lowest $g^{(2)}(0)$ -value can be reached. The results from all different measurements follow the expected dependence between $g^{(2)}(0)$ -value and SBR. In practice, this means for our source: If we want to operate the system as heralded single photon source for the unfiltered case, we can define a time window of 750 ps width, correlated to the herald detection, where we find a telecom photon. In this window we have a very low probability to find another photon. The results, regarding $g^{(2)}(0)$ -values and SBR of our source based on SPDC+QFC are comparable to integrated waveguide SPDC sources with NIR herald and telecom signal photon [64].

In this section the conversion of correlated photons from a pair source was presented. The comparison of the correlation function without conversion and including frequency conversion (Fig. 6.15) shows that the temporal correlation is preserved in the conversion process. Furthermore, there is still a bunching of the coincidences visible. Additionally, it was shown that the combination of NIR SPDC source and QFC can be used as a source of heralded single photons in the telecom O-band. Both narrowband and broadband heralding was demonstrated. The coincidence rate was determined as 4.15 cts./s. This can be expressed as $3.43 \cdot 10^{-3}$ coinc./(s·mW·MHz) or a generation rate of $25.4 \cdot 10^{-3}$ pairs/(s·mW·MHz) for the narrowband case, when we take into account the pump power of the SPDC source and its bandwidth, as well as the detection efficiencies.

6.4 Franson Interferometry of Converted Photons

In the previous section we could prove that the original temporal correlation between the photons of the pair is preserved in the frequency conversion process. We know that the generation process of the photons co-occurs with a time-energy entanglement. Hence the next step is to demonstrate that this entanglement is also preserved in QFC. This can be detected via Franson interferometry. The setup for this experiment is shown in Fig. 6.21. The coherence time of the filtered photons is longer than the

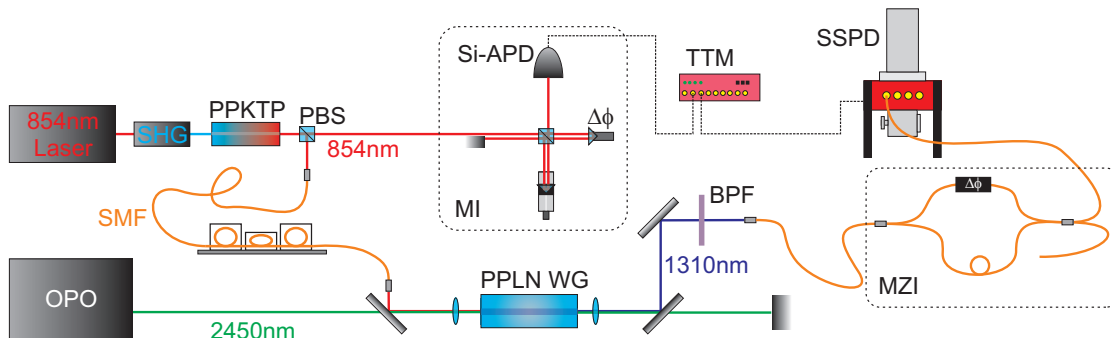


Figure 6.21: Setup for Franson interferometry including quantum frequency conversion.

maximum available delay in our interferometers. Thus we decided to bypass the filtering cavities and use the unfiltered photons. This has the advantageous side-effect of increased coincidence rate. The 854 nm photons are still separated by a polarizing beam splitter which destroys the polarization entanglement. One of the photons is directly coupled to the bulk Michelson interferometer (MI) while its partner photon is

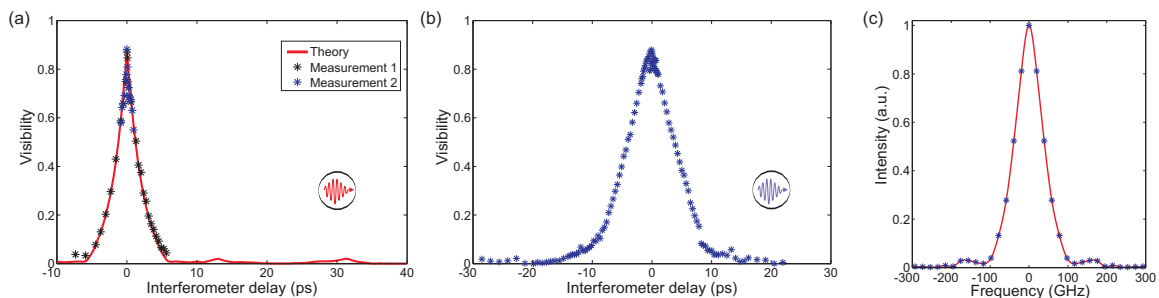


Figure 6.22: Coherence measurements. a) shows the $g^{(1)}$ -function the 854 nm photons measured with the MI. The red solid line shows the theoretical curve calculated from the spectrum of the photons. b) shows the coherence function of the converted (unfiltered) photons measured with the MI. c) shows the spectrum calculated by Fourier transform of the data shown in b). The solid line is an interpolation of the data-points and drawn as a guide to the eye.

sent to the frequency converter followed by the fiber-based Mach-Zehnder interferometer (MZI). Both interferometers are the same as used earlier with the OPO photon pair source (see sec. 5.3). To detect the telecom photons behind the MZI we use one channel of the SSPD. In contrast to the measurement with the OPO, gating of the detectors via heralding is not necessary this time as the SSPD is operated in a free-running mode.

In a preparatory study we measured the first order coherence of the 854 nm photons. For this, the visibility was measured for different delays of the MI. The frequency conversion was not used for this measurement. We could achieve a maximum visibility of 88 %. In first approximation we can fit an exponential function to the data with a decay constant of $\tau_c = 2.37 \pm 0.16$ ps which we identify as coherence time. An alternative definition for the coherence time [102]:

$$\tilde{\tau}_c = \int_{-\infty}^{\infty} d\tau |g^{(1)}(\tau)|^2 \quad (6.7)$$

is independent of the particular shape of the coherence function. For the 854 nm photons we find $\tilde{\tau}_c = 3.7$ ps. The theoretical shape of the coherence function is determined by the spectrum of the photons. We can calculate it by Fourier transformation of the spectrum (Fig. 6.14). The result is shown in Fig. 6.22 together with data from two independent measurements. The experimental data is in very good agreement with the expected coherence function.

In another preparatory study, performed independently, we measured the first order coherence of the converted photons. Therefore the optical elements in the MI were exchanged for telecom-wavelength compatible parts. The photons were detected with the SSPD and the measurement procedure is the same as for the 854 nm photons.

The resulting coherence function is shown in Fig. 6.22b. To estimate a value for the coherence time we can fit an exponentially decaying function to the data resulting in $\tau_c = 5.0 \pm 0.1$ ps, or $\tilde{\tau}_c = 10.5$ ps according to the alternative definition. In a first approximation the central part has a triangular shape. We know that the Fourier transform of a triangular function is a sinc^2 -function. Hence this is what we would expect from a spectrum dominated by the phase matching function. Despite the fact that we were not able to measure a high-resolution spectrum of the converted photons we are now able to compute the spectrum. Therefore the data from the coherence measurement was Fourier transformed. The result is shown in Fig. 6.22c. The computed spectrum has a FWHM of 82 GHz which is smaller than the acceptance bandwidth and the width of the unfiltered 854 nm photons (compare Fig. 6.14b), as expected. A similar argument holds for the coherence function. The coherence time of the converted photons is larger than for the original photons as the phase matching curve of the frequency converter is narrower than the spectrum and acts as a spectral filter.

With this knowledge we can perform the Franson interferometry including QFC in one interferometer arm. First, the phase is only varied by the MI while the MZI is kept static. A coincidence measurement between the outputs of the two interferometers reveals the temporal correlation of the photons, as shown in Fig. 6.23a. The signature for balanced paths is clearly visible in the three peaks. The height of the central peak should be twice the outer peaks which is well met. Due to the timing jitter of the Si-APD (Perkin Elmer SPCM-AQR-14) the peaks slightly overlap, reducing the visibility. This effect is reduced by choosing a narrow coincidence window of 512 ps as shown in Fig. 6.23a. The coincidences are recorded over time while the phase is changed by applying a ramp voltage to the piezo in the MI. The visibility is found by fitting the coincidence fringes with a sine-function and calculating the contrast from the fit data. This procedure was repeated for different interferometer detunings, corresponding to a coarse shift of the phase. These detunings were set by translating the mirror in the MI mounted on a motorized translation stage. The theoretical shape of this function can be found by convoluting the first order coherence functions of both wavelength modes of the pair state (see eqn. 5.11). The resulting function together with the experimental data is shown in Fig. 6.23b. In the theoretical curve the height was normalized to fit the experimental data. Comparing the shape and especially the width of the curve we find a good overlap of the data. With this comparison we bridge the gap between independent measurements concerning the single photon wave functions and the pair state wave function. Deviations can partly emerge from the finite number of data points and measurement range put into the numerical calculations afterwards. This numerical procedure also causes a slightly asymmetric shape of the pair coherence function. For the Franson coherence time of the pair wave function we find a value of $\tau_F = 5.8 \pm 0.5$ ps (decay time of an exponential fit to the data) or $\tilde{\tau}_F = 12.4$ ps. For the MZI we find a maximum visibility of 95 %, measured with a laser, which will limit the visibility

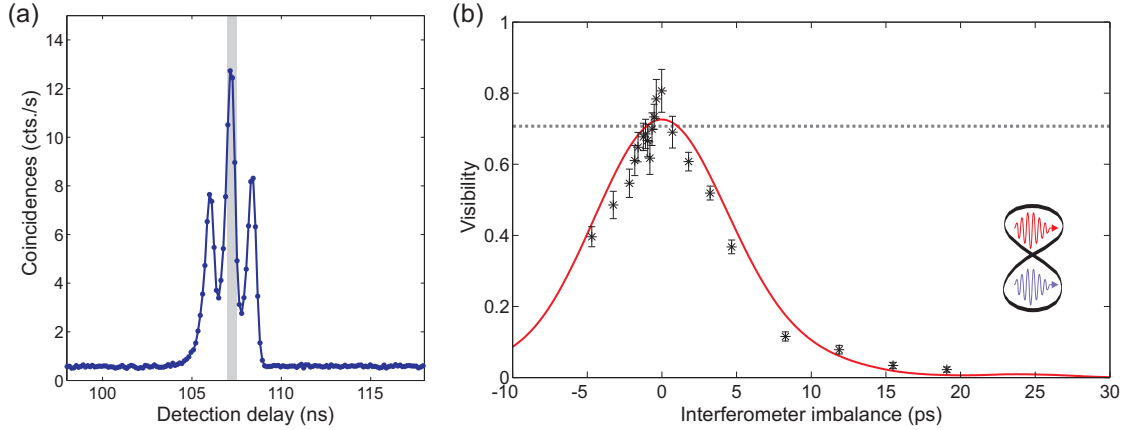


Figure 6.23: a) shows the correlation function for the Franson setup. The grey shaded area illustrates the coincidence window. b) shows the Franson visibility as a function of the delay. The red solid line shows a theoretical calculation. The dotted line indicates the visibility limit of the Bell inequality.

of the Franson experiment to $V_{\max} = 0.88 \cdot 0.95 = 84\%$. The maximum visibility of the Franson fringes was found as $80.7 \pm 6\%$. When the background coincidences are subtracted this value increases to $83.7 \pm 7.7\%$. The corrected value thus equals the maximum of $V_{\max} = 84\%$ derived earlier. Additionally, we here see a clear violation of the Bell inequalities as the visibility significantly exceeds the boundary value of 70.7% by 1.66 error margins.

The occurrence of interference fringes results from the relative phase between the two interferometers. Up to now we intentionally varied the phase only in one interferometer while the other was left untouched. In the next experiment we start as before, scanning only the phase in the MI. After a while we additionally applied a ramp voltage to the modulator in the MZI now changing the phase in both interferometers. Some time later the piezo in the MI was switched off and the phase was scanned in the MZI only. The time trace of the fringes is shown in Fig. 6.24a. The insets show close-ups of the fringes with sinusoidal fits clearly showing the expected shape. In the case when both phases vary, the shape of the fringes changes (Fig. 6.24b). The solid line in this figure shows the trace of the coincidences as expected by adding the two sine-fits with different periodicity. The experimental findings support this assumption. Comparing the minimum and maximum values of the coincidence rate in the case when both interferometers scan we again find a visibility above 80% in good agreement with the results found scanning the MI alone. Please note that there appear jumps in the trace of fringes (Fig. 6.24). This is because the voltage ramps of piezo or modulator arrive a turning point and change their direction. The observation of fringes in the above measurement prove that only the relative phase between the interferometers is impor-

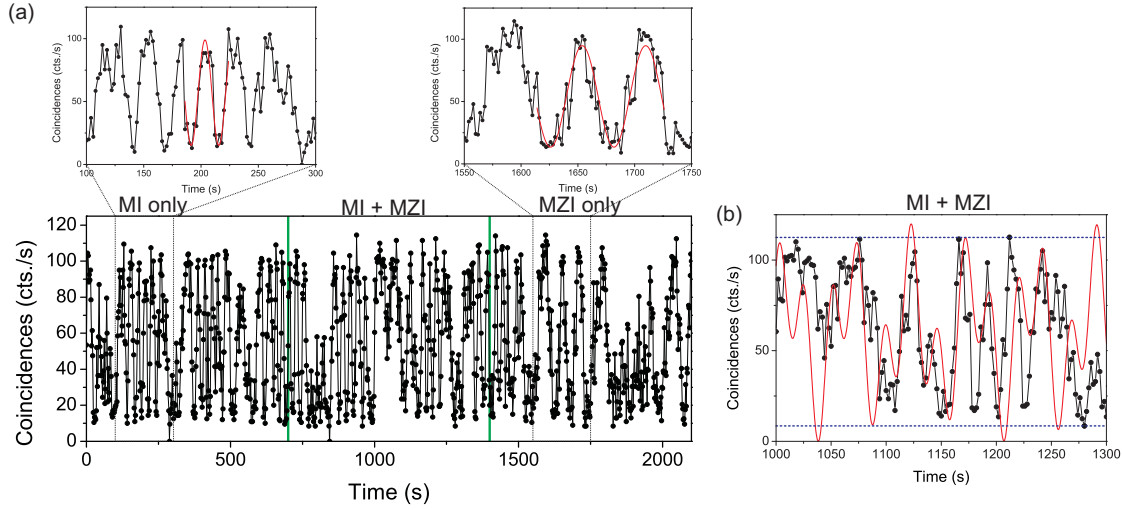


Figure 6.24: Franson fringes with both interferometers scanning their phase. a) shows a long term measurement where first only the MI phase is scanned then both interferometers are scanned and finally only the phase of the MZI is scanned. b) shows a close-up of the region where the phase in both interferometers is varied. The dashed blue lines indicate the minimum and maximum values. The red line shows the expected visibility calculated from the fit functions of a).

tant. When both phases are varied the shape of the fringes becomes more complex and can not be described by a simple sine function any more. However the visibility is not affected.

The successful observation of Franson interference between one photon of the original pair and the frequency converted partner shows the conservation of time-energy entanglement in the frequency conversion process. This has first been demonstrated by Tanzilli and coworkers [28] for the upconversion process and it was first demonstrated here in this thesis for downconversion. This means we can use QFC to transfer the time-energy entanglement from the original NIR photon pair system to the NIR-telecom photon pair system. We can also look at an alternative aspect of the experiment, following the interpretation in [28]: We assume that the original 854 nm photon pair is in a nearly maximally entangled state with an initial entanglement fidelity $F_i := 1$. With the Franson experiment we can now determine the influence of the conversion process on the entanglement fidelity. According to [28] the transfer fidelity can be calculated with the help of the interference visibility via:

$$F = \frac{1 + V_{\text{net}}}{2} \quad (6.8)$$

Where V_{net} is the noise-corrected visibility, in our case. From this follows, that we

find an entanglement transfer fidelity of $F = 91.9 \pm 3.9 \%$. We can further argue that this measurement result is limited to $F_{\max} = 92 \%$ by the maximum visibility of our setup $V_{\max} = 84 \%$. In any case we can claim that our frequency converter can transfer an entangled state from NIR photon pairs to NIR-telecom photon pairs with nearly perfect fidelity.

6.5 Telecom-Converted Heralded Absorption

From the previous sections we know that temporal correlations and even time-energy entanglement is preserved in the frequency conversion process. We will use these facts to herald the absorption of a single photon at 854 nm by a single trapped calcium ion via a telecom photon. The photon that is absorbed will be one of a pair and its partner will be converted to the telecom band. The success of this heralding process can be demonstrated by correlating the onset of quantum jumps of the ion with the detection of the telecom herald photon. The experimental setup is sketched in Fig. 6.25.

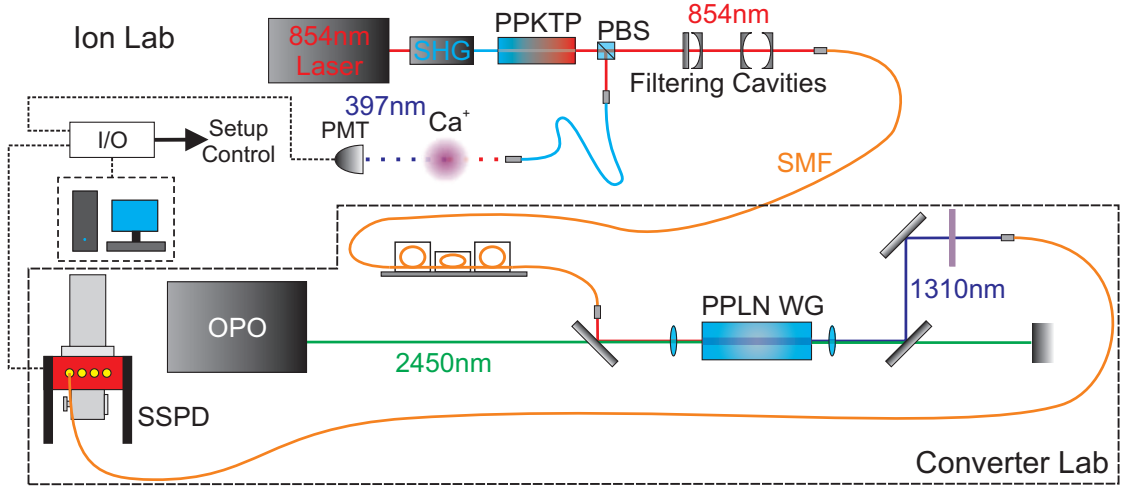


Figure 6.25: Setup for telecom-heralded absorption experiment with converted photons.

We again use the source of entangled photon pairs at 854 nm. One photon of the pair is directly sent to the ion while its partner is sent through the filtering cavities. The filters are actively stabilized to emulate the transition in calcium ($^{40}\text{Ca}^+$: $3^2D_{5/2} \leftrightarrow 4^2P_{3/2}$). As the photon pairs are generated in a frequency degenerate process the photon passing the filter can be used as a herald for the other photon being resonant with the calcium transition. The filtered photon is then sent to the frequency converter and translated to the telecom O-band. Due to the preservation of temporal

correlation, this telecom photon heralds the existence of the resonant 854 nm photon. The telecom photon is detected with the SSPD and its detection signal is sent to the ion lab for recording. The ion is prepared with the same procedure described earlier (see sec. 5.2.1): We find the ion in the $3^2D_{5/2}$ state following the sequence shown in Fig. 5.12. After absorption of a resonant photon at 854 nm the ion is excited to the $4^2P_{3/2}$ state which can decay to the $4^2S_{1/2}$ ground state with 93 % probability. When the ion is in the ground state it can scatter blue photons from a laser at 397 nm. These scattered photons are detected as a signature for the absorption of the 854 nm photon earlier in this cycle. The detection times of the blue photons are recorded. In the data post processing the time of the onset of scattering is taken as absorption time. This can then be correlated with the arrival time of the telecom photon. The result of this correlation is shown in Fig. 6.26. The central peak at zero delay significantly

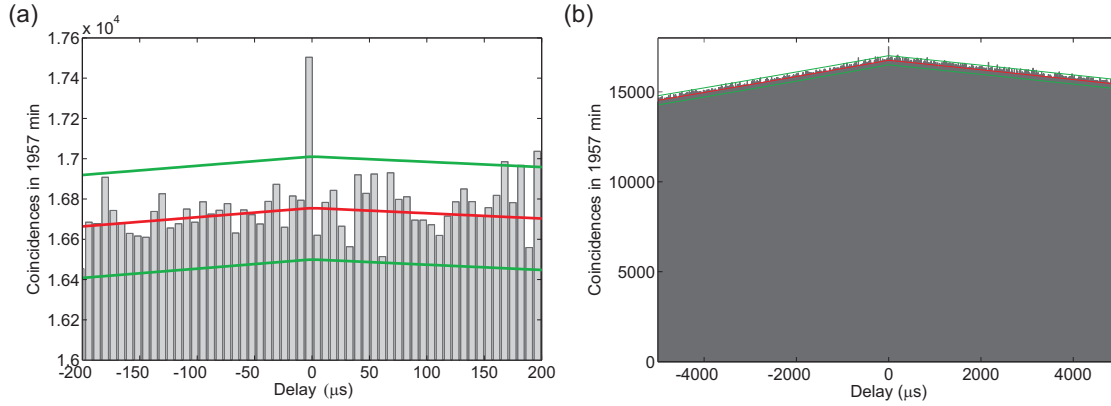


Figure 6.26: Correlation measurement between quantum jumps and telecom herald photon. a) shows the central region while b) shows a larger time window. The red line shows the calculated average background level while the green lines indicate the noise interval.

exceeds the surrounding noise floor and is thus a clear proof for a temporal correlation between the telecom photon and the quantum jumps in the calcium ion. The detection events were integrated for 1957 min and 786 coincidences were found corresponding to $6.69 \cdot 10^{-3}$ coincidences per second. However, this signal sits upon 16722 background coincidences (per $7.1 \mu\text{s}$ time bin) resulting in a SBR of 0.047 and a signal to noise ratio (SNR) of 6.08. The temporal shape of the background coincidences can be modeled with the following assumptions: First the quantum jumps are correlated with the timing trigger of the preparation sequence. This function corresponds to a cut-off exponential decay of the effective lifetime. The second step is then the correlation of

the sequence trigger with the converted channel, resulting in a step-like function. The cut-offs in both functions stem from the temporal gating of the detection path of the sequence. The correlation of both functions is then the modeled background. As seen in Fig. 6.26b the background level is well described by this simple model.

Compared to the heralded absorption experiment with the OPO pair source (see sec. 5.2.2) the QFC scheme has a lower coincidence rate and thus needs a longer integration time. On the other hand, the SBR is higher by one order of magnitude. Hence the same SNR was reached with lower background count rate. This shows that the bottleneck in the present setup is not the frequency converter. Using a 854 nm pair source with higher coincidence rate will increase the SBR and decrease measurement time as the background count rate is mainly determined by the converter and will not change.

In summary, we found an alternative approach to establish a temporal correlation between a telecom photon and the ion via the absorption process and QFC of the herald photon. Compared to earlier heralded absorption experiments [184] this is a step forward to the implementation in quantum network technologies. In the former experiment with the 854 nm pair source [184] a coincidence rate of 1.57 s^{-1} was reported. In the meantime between that experiment and ours the performance of the source deteriorated (heralding rate $3000 \text{ s}^{-1} \rightarrow 800 \text{ s}^{-1}$) and we here have additional losses due to the conversion efficiency. If we correct the coincidence rate for these parameters $R = 1.57 \text{ s}^{-1} \cdot \left(\frac{800}{3000}\right)^2 \cdot 0.08 = 8.9 \cdot 10^{-3} \text{ s}^{-1}$, we find a value which is pretty close to our experimental result. This again supports the conclusion that the temporal correlation is preserved in the QFC process.

6.6 Summary

In this chapter a setup for quantum frequency down conversion from 854 nm to the telecom O-band at 1310 nm was presented and characterized. The QFC was mainly focused on the conversion of photons from a SPDC source. The results show that the conversion process with a continuous wave pump field does not alter the shape of the temporal wave packet of narrowband-filtered photons. However, the phase matching bandwidth acts as a spectral filter for the unfiltered 854 nm photons in the conversion process which could be observed in the increase of coherence time. In both cases the temporal correlations between the photons are preserved in the QFC process. As a side effect we can use our device as a heralded single photon source for the telecom regime. In the narrow-band case the single photon purity suffers from uncorrelated noise due to asymmetric filtering and noise photons generated in the converter. For the unfiltered case, high rates at low $g^{(2)}(0)$ -values can be achieved. The SPDC photons are time-energy entangled. With the observation of Franson interference we prove that this

entanglement is preserved in our frequency converter. Furthermore, the observed raw visibility was high enough to violate the Bell inequalities proving fundamental aspects of quantum mechanics, i.e. that the results do not obey a local-realistic theory. The transfer of the entanglement between the NIR photon pairs and the NIR-telecom pair can be realized with a fidelity around 92 %.

The temporal correlation and time-energy entanglement are pre-conditions to demonstrate atom-photon interaction with a telecom-compatible heralding photon. This result is also a basic demonstration of an elementary quantum repeater node.

In future there are a few aspects that can be optimized for the frequency converter. There is a ZnSe-lens available that offers low transmission losses for all wavelengths involved in the conversion process. First tests showed that the mode matching is not optimal reducing the coupling efficiency into the waveguide. However, with detailed measurements of the beam parameters behind the OPO a beam shaping stage can be implemented that increases coupling efficiency in combination with the ZnSe-lens. Such a higher coupling efficiency will directly increase the conversion efficiency. At the same time, a higher pump power will give rise to a higher background level. Hence the next point which can be improved is the spectral filtering behind the converter. At the moment three band-pass interference filters are used. One of them shows a poor transmission. This element could be replaced by a tailored fiber Bragg grating. Such a FBG has a high efficiency and narrow filtering characteristics. This could improve the signal count rate and especially increase the SBR. A long-term objective is upgrading the converter for polarization independent QFC which allows the conversion of polarization qubits. Concepts for this will be presented in the next chapter (section 7.2). Another modification is the reverse of the conversion process, i.e. upconversion of telecom light towards the calcium transition. This would allow the direct interaction of telecom signals with the calcium ion without the intermediate step of the SPDC source.

7 Quantum Networks

Most of the work presented in this thesis was done in the framework of the projects "QuOReP" and "Q.com-Q" which intend to develop basic building blocks for quantum repeaters in Germany. In particular, QFC was identified as a key technology for interfaces between locally generated qubits and long-range quantum communication links. In this chapter I will briefly put the results of QFC and telecom pair generation into the context of quantum networks. I will show how such technologies, e.g. quantum repeaters and quantum communication, will benefit from the findings presented in previous chapters.

As there exists no technical realization of a quantum network yet it is still topic of current research what technologies turn out most advantageous. However, we can already identify some basic preconditions for such an architecture (cf. [13, 226–228]). There will be quantum nodes which provide different functionalities like performing quantum gate operations, storing quantum information and mapping information between different qubits. The qubits used in these nodes are called stationary. The nodes are connected via quantum channels, i.e. there must be a capability to share so-called flying qubits between the nodes to transfer quantum states. It is well accepted that photons are the most promising candidates for that purpose. In this context, free-space channels were successfully tested with NIR photons. While in the first experimental demonstration of quantum key distribution (QKD) the distance was only 32 cm [6] such channels now can exceed 100 km [229] and are also suitable for quantum teleportation [230, 231]. The flexibility of free-space links even allows QKD with flying airplanes [232]. However, an obvious drawback is the need for a free line-of-sight beam path. The losses can be as low as 0.2 dB/km but also reach 0.55 dB/km depending on apparatus and weather conditions [230, 231]. It is worth mentioning that the distances demonstrated yet for free-space quantum channels are far enough to reach satellites in earth's orbit, at least in principle [233]. For the purpose of classical communication, free-space links were already demonstrated to bridge the distance of $3.8 \cdot 10^5$ km to the moon [234].

To overcome the need for a free line of sight, one can use fiber links for optical communication. The attenuation can be as low as 0.19 dB/km at a wavelength of 1550 nm and thus comparable to free-space links. The advantage is that these fibers can be installed underground and connect nodes without direct line of sight. This is

a prerequisite to setup metropolitan optical networks. Such networks are well established for classical communication. Ideally, a quantum network would make use of this already existing infrastructure. Similar to the experiments with free-space links, there have been many demonstrations of fiber-based quantum channels. In state of the art realizations, QKD is possible over 336 km [235] and entanglement distribution was demonstrated with lengths up to 300 km [236]. Such high-loss channels became possible with the development of low-noise detectors [237]. Hence, QKD over existing fiber networks in urban areas has been demonstrated [238–240] as well as entanglement distribution [195] and teleportation [241].

The above mentioned attenuation of 0.19 dB/km in optical fibers is only valid for 1550 nm. In general there is a strong dependence on the wavelength. One effect hampering fiber communication at visible wavelengths is Rayleigh scattering. The scattered intensity depends on wavelength as $1/\lambda^4$ and is the major contribution for loss in the visible and near infrared regions. Standard fibers are made of fused silica which has increased absorption for infrared wavelengths above 1600 nm. Hence there is a region in between with minimal losses. The spectral dependence of the attenuation coefficient is illustrated in Fig. 7.1a. Around the wavelength of 1.4 μm there is a peak visible which stems from absorption of OH impurities in the glass. Modern fabrication methods reduce these impurities so effectively that this peak disappears in current fibers (c.f. SMF-28e standard [221]). The low-loss region is divided into the so-called telecom bands. The lowest loss (< 0.20 dB/km [221]) can be found in the telecom C-band (1530-1565 nm). In the telecom O-band (1260-1360 nm) the loss is slightly higher (< 0.35 dB/km [221]) but the dispersion is minimal here. These two bands are commonly used in optical communications today. For these reasons it seems advantageous to use telecom O-band or C-band photons as flying qubits in quantum

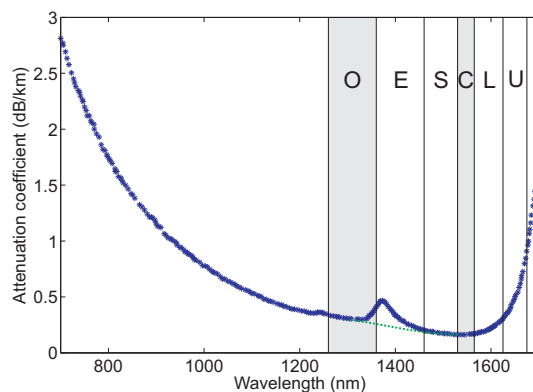


Figure 7.1: Attenuation in single mode fibers in dependence of wavelength. The green dotted line indicates the slope for fibers with reduced OH-content. The plot is adapted from [144].

networks.

Another important point is the question where these flying qubits are generated. There must be some kind of interaction between the flying and stationary qubits for information transfer. In general two mechanisms can be identified: Either a single photon is generated directly in the node carrying the quantum state of the emitter or there is a source of entangled photons where one photon is sent to the node for interaction and the state is swapped to the other photon on successful interaction [227]. As shown, QFC is compatible with both approaches and SPDC sources are ideally used for the entanglement swapping approach.

7.1 Telecom Single Photon Sources

Up to now there have only been few reports on true single photon sources emitting at telecom wavelengths. Although there exist optical transitions in atoms with telecom wavelength (e.g. in Rb [53]), most sources today are based on semiconductor quantum dots. These can emit in the O-band [242,243] as well as the C-band [244,245]. There are also possibilities for the generation of entangled states based on telecom photons [78].

In contrast, there is a vast number of single photon sources based on parametric down conversion. Usually, the signal photon is used as a herald for the idler photon in the telecom band. The herald can be in the NIR wavelength range (e.g. [64]) for highly efficient detection, or both photons of the pair can be in the telecom region (e.g. [246]). Such sources may also allow for additional degrees of entanglement like polarization or time-bin entanglement [247–249].

In this thesis two different approaches were investigated. An optical parametric oscillator was set up as parametric down-conversion source. This device can be used as a heralded single photon source (sections 5.1.1 and 5.1.2). The heralding efficiency is commonly defined as

$$\eta_{\text{her}} = \frac{R_c}{R_{\text{her}} \cdot \eta_{d,i}} \quad (7.1)$$

Here R_c , R_{her} are the detected rates for coincidences and herald photons and $\eta_{d,i}$ is the detector efficiency at the idler wavelength. Phenomenologically, η_{her} is the probability of having a photon in the idler mode when there is a photon in the heralding mode, including all losses. For the unfiltered case we can derive a value of $\eta_{\text{her}} = 119\%$ for low pump powers (see data in table 5.1; the efficiency can exceed 100% when the losses for the herald photon are much higher than for the other one). In the case of narrowband filtered operation the value is $\eta_{\text{her}} = 0.036\%$ (derived from the data shown in Fig. 5.7). It is much lower due to the additional losses introduced by the filtering. Over a large range the coincidence rate and the rate of heralds are linear functions of the pump power (compare Fig. 5.8) and hence the heralding efficiency is constant. The pump power can thus be used to adjust the single photon generation rate. These heralding

rates are competitive to state of the art reports (e.g. 60 % in [64]) for the broadband photons but much lower than recently reported for narrowband photons (13 % in [185]). We attribute this low efficiency to the losses and poor coupling to the filtering stage. An additional outstanding feature of our OPO is the wide spectral tunability due to six different poling periods which allows to cover the telecom O, E, S and C-band. Other SPDC sources reported so far operate on a single design wavelength.

The other approach is to convert the wavelength of a NIR single photon source to the telecom band. This was first realized with a quantum dot emitting at 710 nm converted to the telecom O-band [37]. This particular scheme allowed to generate more than 60,000 telecom photons per second with a spectral bandwidth of 131 GHz. In the sense of an on-demand or heralded single photon source we have to take into account the rate of excitation pulses for the quantum dot (80 MHz). Thus we generated $7.5 \cdot 10^{-4}$ telecom photons per excitation pulse. We also demonstrated the application of a SPDC process as source for heralded single photons (at 854 nm) before converting them to the telecom O-band (c.f. sec. 6.3). With this scheme we reach a heralding efficiency of $\eta_{\text{her}} = 1.5$ % for telecom photons with 22 MHz bandwidth. For the unfiltered case a heralding efficiency of $\eta_{\text{her}} = 1.1$ % can be derived. For the original 854 nm pairs we find $\eta_{\text{her}} = 18$ %. If we multiply this with the conversion efficiency we expect a value of 1.4 % which is close to the actually measured value. From this we can conclude, that the different efficiencies mostly result from the finite conversion efficiency. Comparing both approaches (OPO source and QFC) realized in the scope of this thesis, the QFC scheme is much more efficient than the OPO to generate narrowband single photons.

One parameter we did not take into account yet is the purity of the single photon state which can be expressed by the $g^{(2)}(0)$ -value. For the converted quantum dot photons it was 0.24 [37]. As discussed in detail in [175], reasons for $g^{(2)}(0)$ -values exceeding 0 are on the one hand, emission of uncorrelated photons from neighboring emitters at the original wavelength and on the other hand noise photons from the conversion process due to anti-Stokes Raman scattering of the pump field. In the case of SPDC sources the background depends on the pump power. The coincidence rate depends linearly on the pump power but there is a polynomial dependence of higher order pair states on the pump power (see eqn. 2.80). Hence SBR and single photon purity will decrease with power. For the OPO source $g^{(2)}(0)$ -values as low as $5 \cdot 10^{-3}$ were reached (see table 5.1). For the frequency conversion experiments we also saw this dependence of $g^{(2)}(0)$ -value on the pump power of the source (c.f. sec. 6.3). As these higher-order pairs are converted with the same efficiency, this kind of background will be transferred to the telecom wavelength accordingly. In addition the conversion process adds uncorrelated noise photons. As the results show, all these noise sources have low effect on the heralded single photon state. In the experiments with the QFC scheme we found $g^{(2)}(0)$ -values of 0.01 for broadband and 0.66 for narrowband photons (for 8 ns heralding gate). In all cases we find a clear signature for sub-Poissonian statistics.

The photons generated via SPDC are nearly Fourier-limited as their measured coherence function equals the corresponding temporal wave packet. Furthermore, the QFC did not alter the temporal shape and we do not expect any change in the spectrum of the narrowband photons. This is because of the high coherence of the QFC pump field. When each photon is fourier-limited in such a way one can expect that successively generated photons will be indistinguishable. This could not be proved in the framework of this thesis. However two-photon interference after QFC was demonstrated [38] which shows that QFC can be used to render dissimilar photons indistinguishable [220].

7.2 Quantum Communication

The field of quantum communication describes the distribution of quantum information over quantum channels. This includes techniques like quantum key distribution (QKD) and quantum repeaters based on effects like teleportation or entanglement swapping. QKD means that quantum physics offers techniques to establish a secret key between two or more parties which can later be used to encrypt a message and sent it via an insecure classical channel. The first and most prominent idea for that is the so-called BB84-protocol [4]. The information is encoded in the state of polarization of a single photon which can be generated and detected independently in one of two conjugated bases. For the implementation of the original idea, single photons with a pure polarization state are necessary. Up to now there has been a vast number of demonstrations of QKD (e.g. the first one reported [6]; quantum dots as single photon source, compatible with demonstrated QFC schemes [250]) as well as the teleportation of the state of an atom to another mediated via photons [251]. Review articles of QKD can be found in [7, 227, 252, 253].

The experiments mentioned were performed with single photons at visible to NIR wavelengths on short free-space or fiber links. Here the same limitations apply as discussed in the beginning of this chapter and for the same reasons it seems desirable to perform long-range quantum communication over fiber links. Figure 7.2 shows the transmission of photons through a fiber link as a function of fiber length. As shown earlier the attenuation strongly depends on photon wavelength. The red line highlights the transmission for a wavelength of 854 nm. The green line includes QFC in the transmission process. This means, the photons are first converted to the telecom O-band and then transmitted through the fiber. At short distances this results in a reduced transmission due to the finite over-all efficiency of the converter (here assumed to be 8 %, c.f. sec. 6.3). The telecom photons suffer significantly less attenuation in the fiber. Hence there exists a point where the lower transmission losses compensate the conversion losses. This is reached after approximately 10 km for the 854 nm scenario. For comparison, curves for different single photon sources are drawn in the figure (quantum dots: 710 nm, 905 nm; SiV-centers in diamond: 738 nm). Obviously,

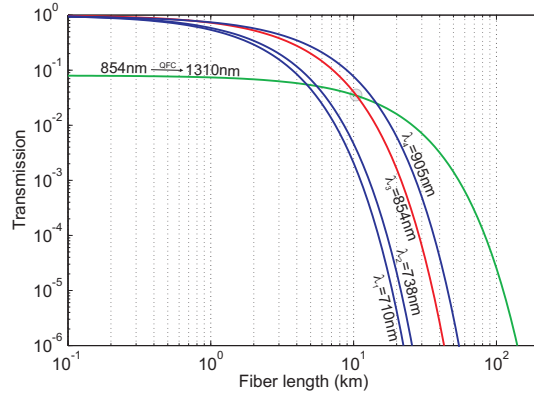


Figure 7.2: Fraction of photons transmitted through a fiber link as a function of its lengths. The green line assumes QFC to telecom O-band while the other lines show the direct transmission for different wavelengths.

adding a QFC process for long-range fiber transmission outperforms direct transmission already at distances of a few kilometers. There is another drawback of fiber links, as standard single mode fibers are not polarization maintaining. That means the state of polarization could randomly change during transmission. An encoding scheme that is more robust against decoherence in fibers are time-bin qubits where the state is mapped into a superposition of two time-bins. With such time-bin entangled states teleportation was demonstrated over fiber links of several kilometers of length [241].

Second order nonlinear processes as SPDC or QFC used throughout the thesis are intrinsically polarization dependent. This means the choice of the process and the design of the nonlinear medium define the polarization states of the involved fields. In the case of the OPO, signal and idler photons have the same polarization (s-polarization with respect to the experimental setup). Hence there is no polarization entanglement. On the other hand this makes the OPO a single photon source with a high degree of polarization. To implement quantum communication via polarization qubits following the BB84 protocol for example two electro-optic modulators could be added behind the OPO idler output, one modulator to define the bit-value of the qubit (i.e. polarization rotation of 0 or $\frac{\pi}{2}$) the other one defines the basis (rotation of 0 or $\frac{\pi}{4}$). In the QFC setup the input and output photons also have the same state of polarization which is s-polarized in the beam path. This will also destroy polarization entanglement and the same restrictions apply as outlined above for the OPO photons.

When we use time correlated photon pairs as presented with the OPO or the QFC experiments there is a more feasible way to define entangled states. The scheme is based on Franson interference and requires two equally unbalanced interferometers [194]. One can be used locally for the NIR photons with a defined detuning of $0, \frac{\pi}{2}, \pi, \frac{3\pi}{2}$ defining two orthogonal states in two bases. The photons can be sent to the remote interfer-

ometer via a long fiber link where the same detunings can be set independently. If a single pair is sent the sum of the phases defines between which outputs of the interferometers a coincidence will be measured. From this coincidence and the knowledge of the phase in one interferometer the phase in the other can be inferred. Hence a BB84 protocol could be implemented with such phase qubits. One technical challenge is that the phase-detuning in the interferometers has to be stable with respect to each other.

In the case of time-bin qubits QFC can directly be used to transfer the qubits to telecom wavelengths. There are also schemes where polarization qubits can be converted to time-bin qubits by sending them through a polarization dependent, unbalanced interferometer. After converting the polarization state to a time-bin state the photon wavelength can be converted. Such a scheme has already been demonstrated in experiment and its feasibility proved by state tomography [216].

However, most atomic stationary qubits are encoded in Zeeman- or hyperfine states of atoms or ions. The emission of a photon maps this state onto the polarization state of the photon due to the polarization selection rules. One way to handle this polarization qubit is to first convert the polarization state into a time-bin state, then frequency-convert it and finally convert the time-bin state back to a polarization state (see Fig. 7.3b) [254]. However, in each of the interferometers necessary to convert between polarization and time-bin states half of the photons is lost due to not-deterministic coupling to a certain output port or detection gate (c.f. [216]). Therefore it seems desirable to directly handle polarization qubits. The most basic idea would be to separate the polarization state into perpendicular components, convert each of them independently and afterwards recombine them (see Fig. 7.3a) [255]. Ideally no photons are lost, with the drawback that two waveguides will be necessary. To overcome this, the frequency converter presented in chapter 6 can be expanded for polarization independent conversion in a future setup. Figure 7.3c shows a proposal for such a device. The idea is based on the fact that the waveguide can guide optical fields of any polarization. In earlier experiments we were able to demonstrate that such waveguide devices can be used for frequency conversion in both directions independently [256]. In particular, here the pump field has to be set to a 45° polarization which involves that only half of the power can be used for the conversion process. In the forward direction the s-polarization component is converted from 854 nm to 1310 nm as usual. Behind the waveguide all three fields pass a quarter wave plate, are reflected on a mirror and pass the wave plate again. The double-pass of the wave plate makes them act as a half wave plate which can be set to introduce a 90° rotation of the polarization. This means all polarization components change their role before passing the waveguide the second time. Now the originally p-component is converted. As phase matching is fulfilled for a certain polarization direction only, the perpendicular components will be left untouched. After the second pass of the waveguide, both (orthogonal) polarization

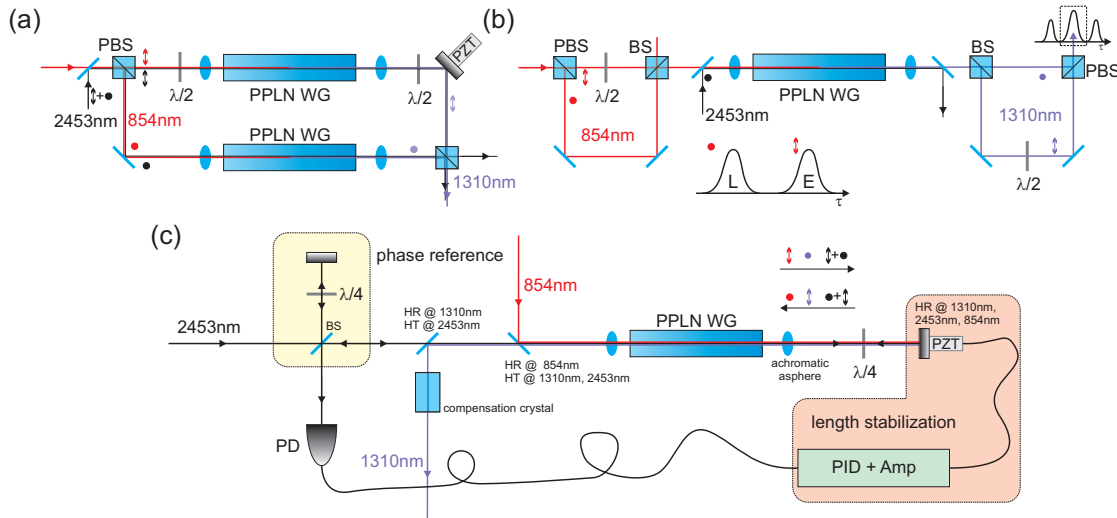


Figure 7.3: Setups for polarization-independent quantum frequency conversion. a) parallel conversion of the two polarization components. b) transfer of polarization qubit to time-bin qubit, frequency conversion and transfer back to polarization qubit. c) polarization independent frequency conversion with a single crystal.

states have been converted. However, they might have experienced different phases in the setup. Lithium niobate is a birefringent material and hence the orthogonal components travel the waveguide with different speed. Furthermore, in the first pass the p-component crosses the crystal at 854 nm and therefore slower than the s-component which is converted to 1310 nm. For the second pass similar considerations apply. Thus behind the converter a birefringent material must be included to rebalance this phase difference. To not introduce further phase variations between these three fields, the length of the setup between the two passes of the waveguide has to be stabilized. For that, a Michelson interferometer can be introduced into the pump beam path and before the waveguide. This means the converter is completely implemented into one interferometer arm. The fringes at the output of the interferometer can be measured to stabilize the length of the converter arm. The second arm of the interferometer serves as reference. Here a double-pass quarter wave plate compensates the polarization rotation in the other arm. In this scheme ideally no photons are lost and only a single waveguide device is necessary, however twice the pump power is needed. A similar setup has already been demonstrated [257].

Quantum and Classical Channel in a Single Fiber

Today's internet traffic that is distributed over fibers mainly concentrates on the telecom C and L-band because in-line active amplifiers based on erbium doped fibers offer a

feasible way to build repeaters for the signals. Hence there exist some frequency bands which are not used, being available for quantum communication. The BB84 protocol for example involves an exchange of data via both quantum and a classical channel to establish the final secret key. Realizing both channels in a single fiber could reduce the device complexity. In first experimental demonstrations, weak coherent pulses at the single photon power level in the telecom O-band were multiplexed with a common data channel in the C-band and sent via several kilometers of installed fiber [258] with an acceptable error rate at the quantum channel. The dominant noise source in that scheme is anti-Stokes Raman scattering of the strong classical pulses into the quantum channel [259]. Furthermore, it is also possible to transmit the O-band photons through a fiber link equipped with active erbium amplifiers. The spontaneous emission of the amplifiers at O-band wavelengths is quite low and the amount of additional noise photons in the quantum channel can be neglected after narrow spectral filtering [260]. However, each amplifier attenuates the O-band photons (e.g. 11 dB loss in [260]). In such a configuration the distribution of entangled states was demonstrated [260].

The telecom C-band is divided into a grid of equally spaced channels for dense wavelength multiplexing (12.5 GHz - 100 GHz spacing in ITU-grid [261]). Each of these channels can be used independently for classical communication and filters are available to separate and demultiplex individual channels. However, the suppression of such common filters is not high enough (20-40 dB) to protect a quantum channel from neighboring classical states of light. If such a fiber link includes an amplifier, a quantum channel in the C-band will also be classically amplified which destroys its quantum state. From these considerations, transmitting the quantum channel in the O-band (taking losses into account) and classical data in the C-band seems the best solution. We can also think of sending several quantum channels in parallel through the O-band at slightly different frequencies, similar to the frequency grid defined for the C-band.

The single photon sources demonstrated in this thesis (OPO and QFC based) mainly work in the telecom O-band. The OPO tuning range can cover several telecom bands while the tuning range of the QFC setup is large enough to cover the whole O-band. Hence these sources are in principal ready for the above mentioned schemes multiplexing quantum channels with classical channels in the C-band.

To examine the different properties of fibers in the O- and C-band we used correlated photon pairs in each of these bands. For this purpose, we pump a waveguide [37] at a wavelength of 708 nm to generate photons at 1535 nm and 1313 nm via SPDC (details about SPDC in this particular device can be found in [262]). The photons have a bandwidth of 983 GHz corresponding to a coherence time of 162 fs. Both photons are sent through long single mode fibers (SMF-28e) before separating them with a wavelength division multiplexer and detecting them. The fiber has a different refractive index in the O- and C-band and thus the delay between the photons will depend on the length

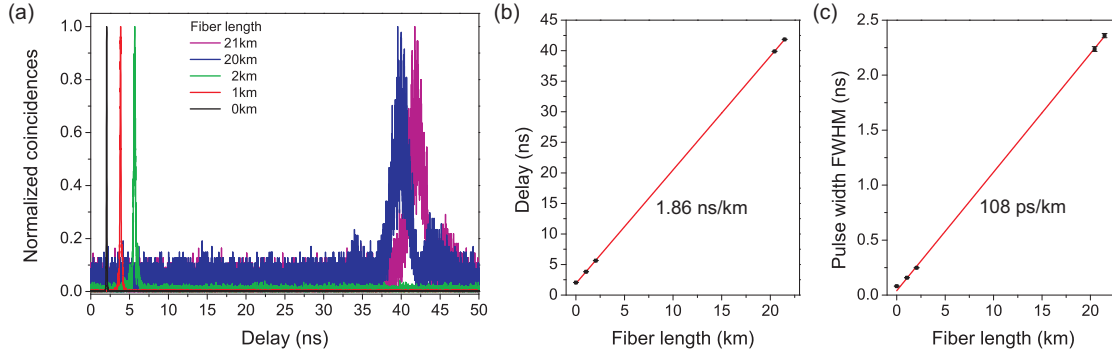


Figure 7.4: Dispersion effects in telecom fiber. a) shows correlation measurements between O-band and C-band photon pairs sent through different fibers. b) shows the shift of coincidence peak and c) the broadening of this peak for the different fibers.

of the fiber. Hence the position of the coincidence peak will move. The result is shown in Fig. 7.4. Furthermore, even the individual spectral components of each photon will experience different phase velocities leading to pulse broadening. The dispersion minimum of SMF-28 fibers is in the telecom O-band ($1310 < \lambda_0 < 1324$ nm, [221]). Hence we expect negligible pulse broadening there but the temporal shape of the C-band photon will significantly broaden due to dispersion. The results of the correlation measurement show that the delay between the O-band and C-band photons increases by 1.861 ± 0.004 ns/km. This value was measured at the peak positions and thus holds for every pulse-pair with 1535 nm and 1313 nm central wavelength. For the pulse broadening of the C-band photons we find a value of 108 ± 0.8 ps/km which depends on the particular spectral shape. In practical realizations such effects can hamper the applicability. For example in the Franson experiments described in this thesis a broadening of the single photon pulse to the nanosecond range will cause an overlap of neighboring time-bins which reduces the visibility. In internet communication the link between two nodes can be reconfigured on demand to reduce data traffic in certain channels and optimize speed and workload. Hence the optical distance between two nodes might change. For the idea of multiplexing quantum and classical channels this means the delay between these data packets might also change. For example if we use the InGaAs-SPAD as detector for the quantum channel, derive a gate trigger from the classical channel and use a gate width of 5 ns (standard setting of the SPAD) then a change of only 3 km is enough to completely lose the signal. There are techniques to track the signal via correlation measurements [263] which then need to be implemented, increasing complexity.

To demonstrate the multiplexing of two optical signals in a single fiber (SMF-28e), we implemented the experiment described in the following. We use the 854 nm SPDC

source and convert one photon of the pair, while its partner is detected as a herald (compare sec. 6.3). However, this time the heralding detector (Si-APD) is directly connected to a diode laser (Thorlabs LPSC-1550-DC) emitting at 1550 nm in the telecom C-band. In detail the diode was biased with DC current of 11 mA and the TTL-pulses were added via a bias-T and a 50 Ohm load resistor. This is enough to drive the diode above threshold (36 mA). The shape of the generated optical pulse follows the electrical pulse. The laser pulse is transmitted through 1550 nm bandpass-filters to suppress noise at other telecom wavelengths. A set of neutral density filters is used here to reduce the power. Then the pulses are sent to the lab where the converter is hosted. Here the laser pulses are combined with the converted photons via a wavelength division multiplexer (WDM) as shown in Fig. 7.5. After combination,

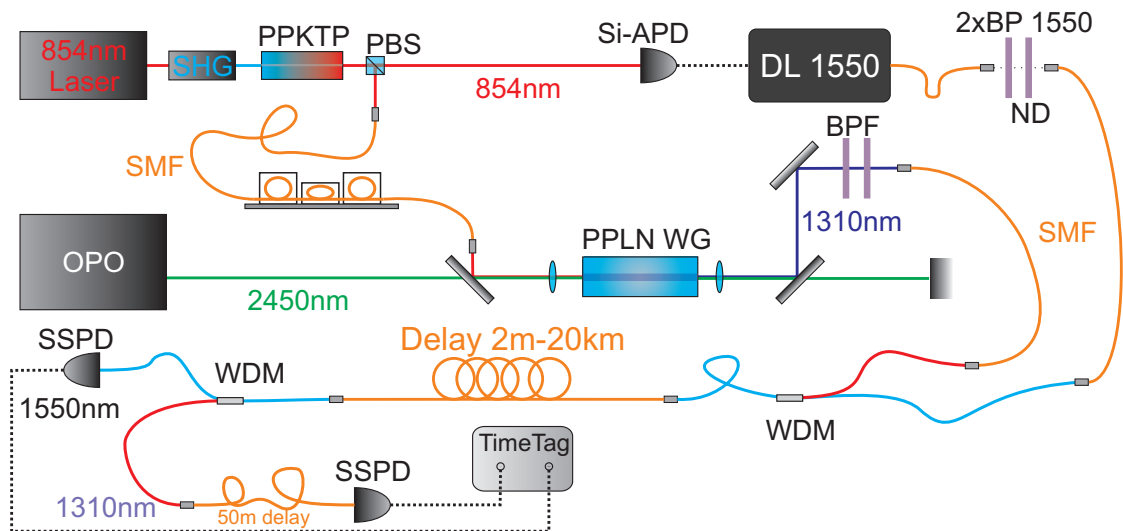


Figure 7.5: Experimental setup for correlation measurements between converted photons and an optical clock signal.

both optical fields travel in the same delay fiber which has a length between 2 m and 20 km. After this fiber link both fields are again separated by a single WDM. These WDMs (Thorlabs WD202B-FC) have a minimal isolation of 16 dB between the two bands. Both output channels are connected to the SSPDs. The O-band channel has an additional delay of 50 m of fiber to reduce cross-talk effects in detection. In a preparatory measurement the rate of herald events was measured directly at the Si-APD. Then the laser pulses were attenuated by six orders of magnitude which, for the heralding channel, resulted in a comparable count rate on the SSPD as on the Si-APD before. We collect the detection events on both SSPD in a list of time-stamps

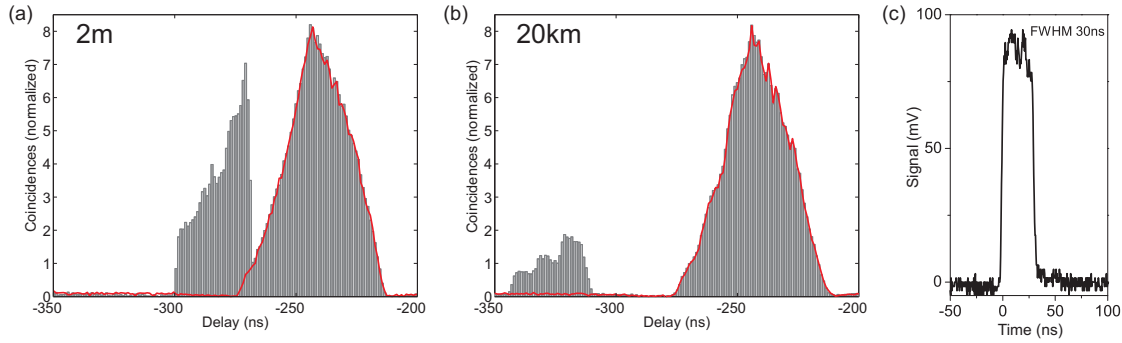


Figure 7.6: Converted single photons at telecom O-band and laser herald pulses in the telecom C-band multiplexed in a single fiber. a) shows the results for 2 m of delay, as reference and b) shows the long-range measurement over 20 km. The red solid lines show measurements of the background. c) shows a measurement of the laser pulse intensity with a standard photo diode and an oscilloscope (2 m fiber delay).

and correlate both later. For comparison a background measurement was performed by blocking the input of 854 nm photons in the converter and repeating the measurements with the same settings. The laser pulses have a rectangular shape of 30 ns width (see Fig. 7.6c). Hence we expect a triangular auto-correlation with a width of 60 ns at the base. This corresponds well with the experimental width of 62 ns. The results for the shortest and longest available fibers are shown in Fig. 7.6. In both examples we can identify two coincidence peaks. We inserted a 50 m delay between the two SSPD channels (measured to introduce 244 ns delay). Hence we can identify the peak around -250 ns to be the copy of the C-band laser pulse leaking into the O-band detection channel. This is proved by the background coincidence rate (red lines in Fig. 7.6) which shows that this peak is completely independent of the frequency converted photons. The neighboring peak really stems from the correlation between the laser pulses and the converted single photons. The center of mass of this peak shifts by 43 ns which is comparable to the shift expected from the earlier results (37.2 ns for 20 km, see Fig. 7.4). For the correlation signal of interest we expect a convolution between the short photon pulse (coherence time 5 ps) and the laser pulse, which corresponds in first approximation to the shape of the laser pulse itself. The measured width at the base of the 20 km delayed pulse is 34 ns, corresponding well with the estimated value ($30 \text{ ns} + 20 \text{ km} \cdot 108 \text{ ps/km} = 32 \text{ ns}$). We can attribute the modulation of the pulse height to saturation and dead-time effects in the detectors. The coherent laser pulse consists of more than one photon on average which means that possibly more than one detection event can be triggered by a single pulse on the SSPD. Especially the dead time of the SSPD is around 10 ns which is smaller than the pulse width. To summarize the results, we can claim that this basic experiment demonstrates a way

to multiplex classical and quantum channels in a single fiber. We could demonstrate the correlation of the SPDC photons by transmitting the timing information by an optical clock pulse. In the sense of an application we should use gated detection and chose the gate width and position to cut out the coincidence peak with the true signal only. For fibers with several kilometers of length the delay is large enough to make this feasible. We also performed this measurement with not-attenuated laser pulses and additional filters before the single photon detector. In this case we were able to detect the laser pulses with a standard photodiode (Thorlabs DET10C), single photon sensitivity was not necessary. However, the background on the single-photon channel drastically increases. The experimental setup could be optimized in both cases by including narrowband filters, like FBG and WDMs with higher isolation. A further improvement is to use much shorter laser pulses that either decrease timing jitter and reduce dead time effects in detection.

7.3 Quantum Repeaters

We already saw in the beginning of this chapter that losses grow exponentially with transmission distance which seems to ultimately limit the length of a quantum channel. These losses include the absorption of photons as well as the depolarization. If we use single photons as flying qubits this means the number of trials we need to transmit the photons over the complete distance grows exponentially with the length whereas the entanglement fidelity of a transmitted state decreases exponentially. In classical communication channels the losses can be overcome by inserting repeater stations in between two nodes. At these repeaters the light pulses are amplified to compensate for the attenuation. Unfortunately, classical amplification is not compatible with qubits as the quantum state cannot be cloned [5]. But the idea of repeating signals can be adapted to quantum communication. The first proposal for a quantum repeater was described by Briegel and coworkers [18]. They assume that a link of length L connecting node A and B is divided into N nodes with elementary EPR pairs as shown in Fig. 7.7a. In a first step entanglement is established between neighboring nodes, e. g. via sending photons and projecting them via a Bell state measurement, except for the nodes $C_k, C_{2k}, C_{3k}, \dots$ where $N = k^n$. After this first step there are N/k entangled pairs bridging a distance of k nodes each. This is repeated for a number M of copies of these pairs. With the help of these auxiliary pairs the state can be purified to increase its fidelity. In the next step entanglement is established over larger distances, i.e. between neighboring nodes except between the nodes $C_{k^2}, C_{2k^2}, C_{3k^2}, \dots$. Then the states are purified again with the help of auxiliary pairs. These steps are continued until there is a gap-less chain of entangled pairs between the end nodes A and B . The whole scheme is based on the effects of entanglement swapping and teleportation [264]. The over-all losses of the link are reduced by dividing it in short

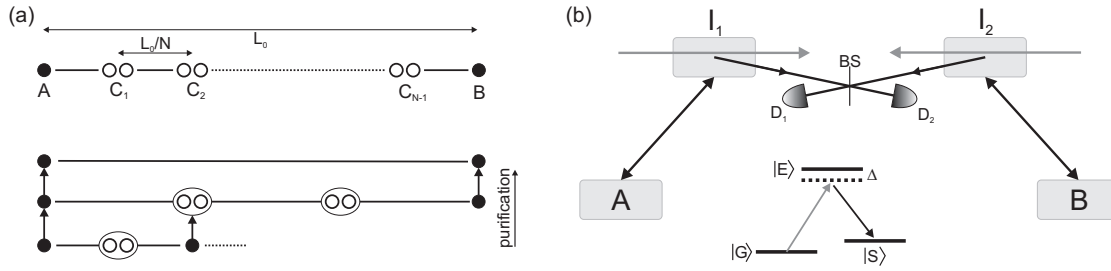


Figure 7.7: Protocols for quantum repeaters. a) reproduced after [18]. A, B, C_n : repeater nodes. b) Entanglement connection in DLCZ protocol, reproduced from [226]. $D_{1,2}$: detectors; BS: beam splitter; A, B are remote nodes implemented by atomic ensembles, the intermediate ensembles $I_{1,2}$ are used for storage. The inset illustrates the energy level structure of the ensembles with $|G\rangle, |E\rangle$ ground and excited state, respectively; $|S\rangle$ is the intermediate state used for storage.

segments and purifying the state after each segment. However this involves to work with several links in parallel to have copies of the states available for the purification protocol. In summary this means the losses growing exponentially with the channel length can be compensated by investing a polynomially growing number of resources.

Another famous proposal is known as the DLCZ-protocol [226]. Here the authors suppose the nodes are based on atomic ensembles which can also act as quantum memories. Without memory for the purification process the ancilla states have to be established probabilistically which can lead to exponential time dependence while a memory is useful to store successfully purified states and only the purification of unsuccessful parts needs to be repeated. The quantum state of the ensembles can efficiently be transferred to a photonic qubit triggered by a laser pulse. Neighboring nodes can be entangled via a Bell state measurement between these photons as shown in Fig.7.7b. In this case the entanglement is also transferred step by step by means of entanglement swapping. The authors also showed theoretically that a quantum channel based on this repeater scheme is capable of quantum teleportation, communication and Bell inequality detection [226]. It can be shown that the over-all fidelity of state transfer can be arbitrarily large at the cost of speed. Hence inefficiency of detectors or attenuation of photons do not limit the final fidelity but increase the time T_{tot} for transferring a single state. To derive this time we assume that the channel of length L is divided into 2^n segments of length L_0 , which is the typical attenuation length (transmission reduced to $\exp(-1)$ after L_0). At each node there is a success probability of p_i for entanglement transfer and there is an additional over-all probability factor p_a and a photon loss factor η_p . The fidelity imperfection is accounted for by ΔF . The

the total transfer time can be calculated by [226]:

$$T_{\text{tot}} \approx \frac{2(L/L_0)^2}{\eta_p p_a \Delta F \prod_i^n p_i} \quad (7.2)$$

We can use this formula to estimate the impact of QFC for the quantum repeater scheme. We assume to connect two remote calcium ions via a quantum channel equipped with quantum repeaters connected by fibers. The ions interact via photons at 854 nm. We assume the whole channel is designed for 854 nm which will be the operating wavelengths of all nodes. In the first scenario the transmission wavelength is 854 nm. The fiber attenuation for this wavelength is about 1.4 dB/km (see Fig. 7.1) corresponding to an attenuation length of $L_0 = 3.11$ km. We assume all other parameters above as fixed and can derive T_{tot} . In the second scenario we convert the photons from the ion to the telecom O-band with efficiency η_c and back at every node and transfer the quantum information between the nodes via telecom photons. Hence we have a longer attenuation length of $\tilde{L}_0 = 12.4$ km (attenuation 0.35 dB/km at 1310 nm) which reduces the number of nodes to $\tilde{n} = n \cdot L_0 / \tilde{L}_0 \approx n/4$. The efficiency of every node is reduced by these two conversion steps to $\tilde{p}_i = \eta_c^2 \cdot p_i$. The ratio

$$\frac{\tilde{T}_{\text{tot}}}{T_{\text{tot}}} = \left(\frac{L_0}{\tilde{L}_0} \right)^2 \cdot \frac{\prod_i^n p_i}{\prod_j^{\tilde{n}} \eta_c^2 p_j} \quad (7.3)$$

can be used to describe the speed benefit of scenario 2. If it is smaller than 1 the transfer needs less time including conversion. On the one hand, with telecom wavelengths the attenuation length is longer which means a smaller number of nodes is necessary. Every node has imperfect efficiency (described by p_i). Hence with less nodes the overall efficiency increases. On the other hand, with two frequency conversion steps at each node the efficiency of the nodes is reduced. In the end we expect an optimum solution for this trade-off depending on the particular efficiency parameters. We can look for which parameters equation 7.3 becomes ≤ 1 . For different channel lengths and node efficiencies we derive the minimum conversion efficiency to solve the inequality. The results are shown in Fig. 7.8. For a channel of zero length (or close to zero) the solution is trivial and an efficiency of 1 is necessary to not introduce additional losses. This holds as long the the number of nodes (n, \tilde{n}) is small. Then the critical value for conversion efficiency quickly decreases and reaches a steady state independent of length but depending on node efficiency. For a fixed length (e.g. at 2000 km where the steady state is reached), using the same equation the dependence of conversion efficiency on node efficiency can be calculated (Fig. 7.8b). This curve shows us, which minimum conversion efficiency is necessary that the scenario including QFC outperforms the original scenario, regarding channel transfer time, for a certain efficiency of the node. A discussion about the efficiency of a repeater node will follow in the next paragraph.

A more general variant to realize a quantum repeater was proposed by Simon and coworkers [265] based on the ideas of the DLCZ protocol. There, each node consists of

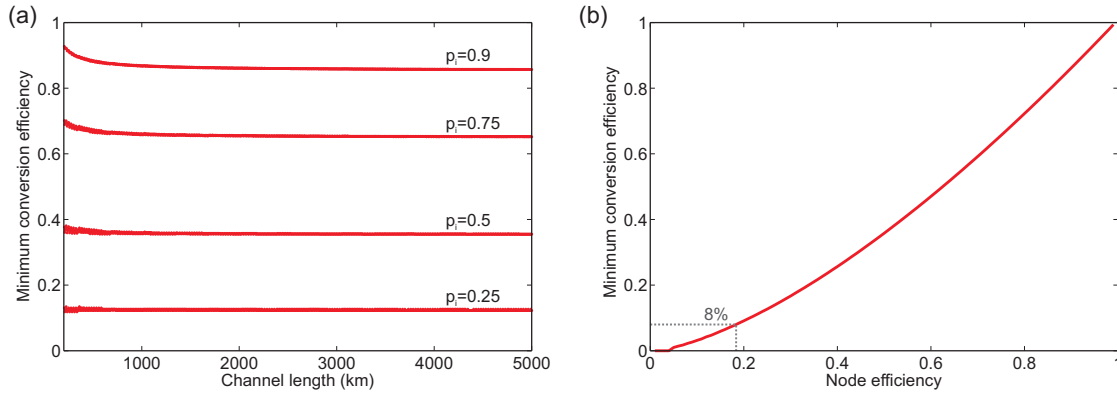


Figure 7.8: Minimum conversion efficiency necessary to achieve the same channel transfer time for the scenarios with and without QFC. a) shows the minimum conversion efficiency necessary to beat the direct transmission versus channel length for different node efficiencies. b) shows this minimum as a function of the node efficiency for 2000 km channel length.

a photon pair source where one photon is sent to a quantum memory for storage while the other one is available for entanglement transfer via Bell state measurement. This has the advantage that the pair does not need to be frequency degenerate. One can design a source that entangles photons optimized for quantum memories with telecom photons. Such a source was demonstrated in this thesis with the OPO heralding the absorption of a photon in a calcium ion via a telecom photon. Such an interaction can in principle be used for photon-atom entanglement [266] and the photonic state stored in the state of the ion. Quantum memories can be realized with several techniques [267]. One can use long-lived states in single atoms [268], atomic frequency combs in rare-earth-metal-doped crystals [206,269] or spins in atomic ensembles [270,271]. The read and write efficiencies reported are usually around 10 % or below but can reach up to 78 % [270]. The efficiency factor for a node not only includes memory efficiency but also the efficiency for entanglement swapping, i.e. Bell state measurement (30 % detector efficiency, 75 % loss due to partial BSM). This means, even for the best memories we expect the over-all efficiency of a node far below 10 %. If we now look at the curve in Fig. 7.8 we find a minimum conversion efficiency of 3 % (70 %) for 10 % (78 %) node efficiency. In this thesis a conversion efficiency of about 8 % was realized which makes scenario 2 (including QFC) competitive to the first one (direct 854 nm operation) when the efficiency of the nodes is below 18 % on average. This condition is fulfilled for realistic devices today when we take memory efficiency and efficiency of Bell state measurement into account. In general, two aspects have to be taken into account: QFC helps to reduce the number of repeater nodes due to larger distance between the nodes resulting from lower transmission losses. QFC introduces additional losses in

each node due to the finite conversion efficiency. If a certain quantum channel benefits from QFC hence depends on the efficiency of each node. The minimum efficiency when QFC pays off can be read from Fig. 7.8b. Future developments will increase both the efficiency of QFC and of the repeater nodes, but with state of the art technology quantum repeaters will benefit from quantum frequency conversion techniques. To give a numerical example: if we assume the same node efficiency of $\eta_i = 10\%$, a conversion efficiency of $\eta_c = 8\%$ and a total length of 100 km for an urban network, then the original scenario needs 286379 times more transfer time than the QFC scenario (eqn. 7.3). There are $n = 33$ repeater nodes necessary for scenario 1 but only $\tilde{n} = 9$ repeater nodes for scenario 2 and the losses grow exponentially with the number of nodes.

There is another feasible scheme for quantum repeaters based on quantum memories and single photon sources, proposed by Sangouard and coworkers [272]. The scheme is sketched in Fig. 7.9a. The single photons, synchronously generated at sites A and

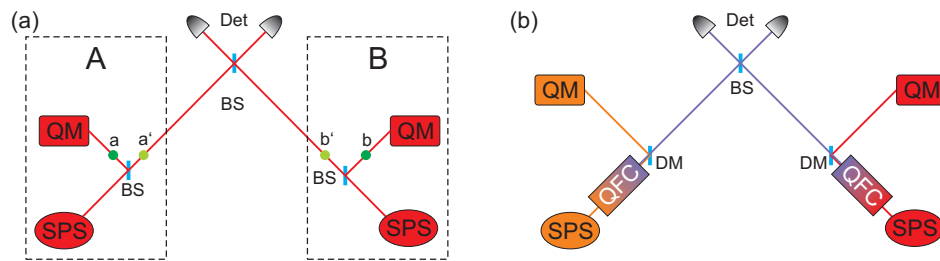


Figure 7.9: Repeater scheme based on single photon sources (SPS) and quantum memories (QM). a) shows the original setup proposed in [272]. b) shows the modified scheme with QFC. BS: beam splitter, DM: dichroic mirror, Det: detectors.

B, each hit identical beam splitters. With a certain probability they are reflected towards the quantum memory or transmitted to an intermediate site for a coincidence measurement. Behind the beam splitter each photon is in a superposition state of the two possible paths. The detection of a single photon (not a coincidence) at the center detectors corresponds to the case that one memory contains a single photon state while the other is empty and it cannot be distinguished from which site the photon arrived. This entangles the memories. To avoid coincidences at the central site the reflectivities of the beam splitters should be rather high. This protocol is faster than the DLCZ protocol when efficient single photon sources are used with an emission probability $p > 0.67$ [272]. One drawback of the scheme is that the photon has either to interact with the memory or is used for transmission. Hence it has either a wavelength with increased transmission loss or a telecom compatible memory is necessary, which

does not exist yet. However, we propose that QFC can be introduced to solve this contradiction. The frequency conversion process can be regarded as a beam splitter (cf. equations 2.56, 2.57) where an input photon is prepared in a superposition between the signal and idler frequency modes at the output of the converter. The conversion efficiency determines the content of the idler mode in this superposition. Hence in the repeater scheme we can replace the beam splitter behind the single photon source with a frequency converter and a dichroic mirror. The single photon source emits a photon that is resonant with the memory transition. In the QFC process it is either left untouched, reflected at the mirror and guided to the memory or it is converted to the telecom band, passes the mirror and is sent to the central interaction node. Behind the converter the photon is in a superposition of frequency modes which is transferred to the superposition of paths like in the original proposal. As most of the photons should be sent towards the memory (e.g. 89 % in the example in [272]) only a rather small conversion efficiency is necessary. The addition of QFC offers even more benefits. The splitting ratio, i.e. the conversion efficiency, can be varied continuously via pump power and thus adapted to the other efficiencies in the repeater node to maximize over-all performance. But the most interesting advantage is that the single photon sources at the sites A and B do not need to operate at the same wavelength. Hence the scheme can be used to connect dissimilar systems. The precondition is that the photons arriving at the central beam splitter are indistinguishable which can be established via QFC. In summary, replacing the beam splitter by a QFC process does not introduce additional losses or reduce the efficiency of the protocol but increases the flexibility and reduces transmission losses.

7.4 Networks of Dissimilar Nodes

In the previous sections basic building blocks for quantum networks have been introduced. With these tools we can think of a lot of different realizations of quantum networks. Here I want to focus on a few ideas how networks could be demonstrated in near future. I will restrict myself to quantum systems and process steps that are available in Saarbrücken, or are probably available in near future. We can identify three basic requirements: First, the state of the stationary quantum system is mapped onto a photonic qubit. Next, the wavelength of the photon is transferred to the telecom band for long-range transmission. Finally, the remote telecom photons interact on a beam splitter to perform a Bell state measurement for entanglement swapping. The network design is sketched in Fig. 7.10. One network node (denoted as B in the figure) could consist of a single trapped calcium ion and a resonant SPDC source at 854 nm. At this node we could perform a heralded absorption experiment as described in section 6.5. To improve performance, the filtering cavities have been replaced by solid-state etalon filters as described earlier (sec. 5.4, c.f. [201]). Trapped ions seem

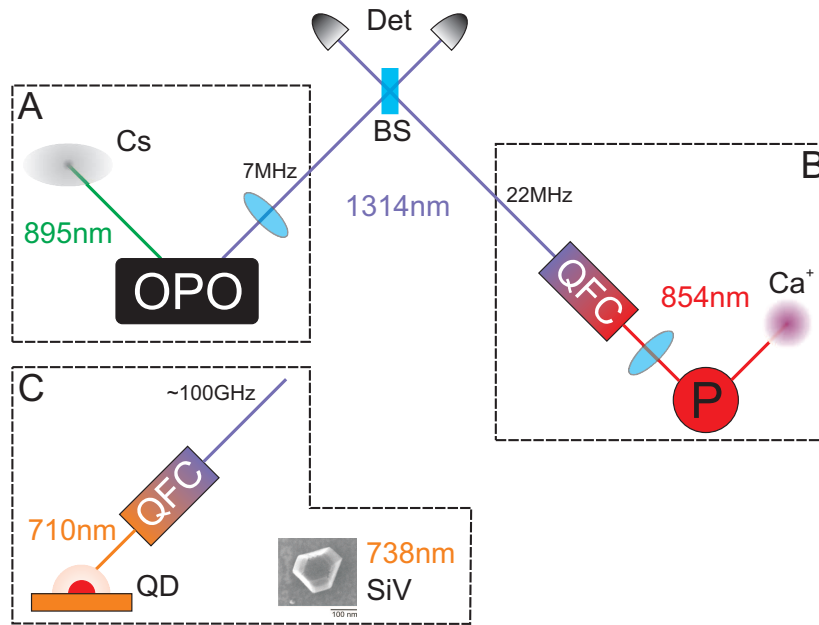


Figure 7.10: Basic quantum networks. A,B and C illustrate different possible nodes for the network. P: photon pair source, QD: quantum dot, SiV: silicon vacancy color center in diamond, BS: beam splitter, Det: detectors, Ca^+ : single trapped calcium ion, Cs: atomic cloud of cesium.

to be ideal candidates for quantum networks as many basic applications have already been realized [15, 273]. In combination with polarization-independent conversion we could create atom-photon entanglement between a telecom photon and the ion. It has recently been shown that such a polarization qubit can be stored in the state of the ion [274]. This gives rise for future quantum repeater and computing applications. Another node (A) could use the OPO pair source (see section 5.2). The OPO is set to the D1 transition in cesium at 895 nm. The corresponding idler photon is in the telecom O-band. Here a filter is necessary to cut out a single idler mode. The signal photon is sent to a cesium gas cell. With additional control lasers the cesium can be prepared to work as a hot atomic vapor quantum memory for the 895 nm photons. These can be based on a Raman process [275] or on electromagnetically induced transparency [276–278]. After an arbitrary delay time the excitation photon can be read out of the memory. On successful entanglement swapping with the telecom photons there should be a correlation between the quantum jumps in the calcium and the photon retrieved from the cesium memory. A few drawbacks of this design can be identified. There is a bandwidth mismatch of the two telecom photons which makes them partially distinguishable at the beam splitter. Hence symmetric filtering is necessary which will result in a reduction of the absorption rate. The natural linewidth of the cesium D1

transition is 4.6 MHz [204]. By increasing the lengths of the OPO cavity the width of each longitudinal mode can be decreased and the photons matched to the transition. Filtering of the photon bandwidth at node B is necessary accordingly. Another experimental drawback is that both pair sources involved in this scheme are operated continuous wave. Hence there is no synchronization between the absorption events at the two nodes.

One can also consider the case of solid-state emitters as local nodes: Here, the conversion of single photons from a quantum dot (QD) at 710 nm to the telecom O-band has been demonstrated [37]. Comparing its emission with the above mentioned examples for quantum nodes there is a massive mismatch in bandwidth. Filtering the QD emission to the MHz range will drastically reduce the photon rate. Coupling of solid-state emitters to a cavity was shown to channel the emission of the emitter into a narrow bandwidth [279]. However, the quantum dots are excited by optical pulses which makes a synchronization with the ion or memory feasible.

Another process that could be realized soon is the conversion of single photons from silicon vacancy (SiV) color centers in diamond [280] at 738 nm to the telecom O-band. The necessary mixing field of 1690 nm is available as signal wavelength of the OPO presented in this thesis (see section 4). At the time writing this thesis an appropriate waveguide chip was already available. From the SiV center similar results as with the quantum dot can be expected. Also the same drawbacks apply when we try to interface the SiV center with calcium or cesium network nodes. However, the similarity with the QD makes an interaction between QD and SiV feasible. Both can be excited with the same laser pulse and are thus synchronized. The bandwidths are comparable and can be further filtered symmetrically. It has been demonstrated that the spin state of a QD can be transferred to a photonic qubit [281] and entanglement transfer to telecom wavelength by QFC is possible [42], too. The entanglement between an atomic spin and a photon could also be demonstrated with color centers in diamond (nitrogen vacancy center [282]), but not with the SiV-center yet. The internal electronic [283] and spin [284,285] structure of the SiV is in the focus of current research. The entanglement between the atomic state of a SiV and a photon has not been demonstrated yet.

A prerequisite for all above approaches is a Bell state measurement which involves that both photons at the beam splitter are indistinguishable. There exist schemes how to make photons indistinguishable by temporal and spectral tailoring, including QFC [38,220]. Hence one next step is to check whether our frequency converter worsens indistinguishability of originally indistinguishable photons and to check if the OPO SPDC source indeed delivers indistinguishable photons. Therefore Hong-Ou-Mandel interference [110] between succeeding photons should be measured [286], as the contrast is a measure for the distinguishability of the photons.

8 Summary and Conclusion

In this thesis we have experimentally studied techniques to establish interfaces for photons between the near infrared and telecom spectral region. The schemes are based on nonlinear optical effects. We can distinguish the experiments mainly in two approaches: Photon pairs generated by spontaneous parametric downconversion (SPDC) in an optical parametric oscillator (OPO) and quantum frequency conversion (QFC).

For the first approach we have set up an optical parametric oscillator operated far below its oscillation threshold as photon pair source. The lithium tantalate crystal is pumped at 532 nm which allows to generate signal photons in the NIR between 806–954 nm and idler photons in the telecom bands between 1202–1564 nm. This wide tuning range is possible due to six different QPM periods in the crystal and broadband coated cavity mirrors. The signal wavelengths cover a region with many atomic transitions which is an outstanding feature of the OPO compared to state-of-the-art SPDC sources. The singly resonant OPO cavity shapes the photons spectrally and temporally which was investigated in detail via time-correlated photon counting and interference experiments. It turned out that a single mode of the spectrum ideally fits to atomic transitions (7 MHz line width). In particular, we aimed at a transition in calcium ions at 854 nm ($4^2P_{3/2} \leftrightarrow 3^2D_{5/2}$). The corresponding idler wavelength is around 1411 nm in the telecom region. We employed a custom-made fiber Bragg grating to cut out a single idler mode while there were stabilized cavity filters available for the signal wavelength. The temporal correlation of these narrow-band filtered photons could be observed. After this preparatory characterization, we investigated the interaction of the photons with a single trapped calcium ion. As a means to observe the interaction, we measured the effective life time of the ion's $D_{5/2}$ metastable state or detected the onset of quantum jumps to the $S_{1/2} \leftrightarrow P_{1/2}$ cycling transition. Experimentally, we had to implement a stabilization scheme to tune the OPO to resonance. To demonstrate the applicability of the pair source for resonant excitation of atomic transitions we performed single photon spectroscopy of the $P_{3/2} \leftrightarrow D_{5/2}$ transition using the signal photons. If we include the fluctuations of the OPO, the measurement result of the linewidth agrees well with the literature values. To maximize absorption, we set the wavelength to the line center. We then correlated the onset of quantum jumps in the ion with the detection of the OPO idler photons. Due to this temporal correlation we can use this telecom-compatible photon as a herald for the absorption process. This has been the first demonstration for telecom-heralded absorption of a single photon

by a single atom and constitutes a basic building block for many quantum repeater and network schemes. To prove quantum correlations between signal and idler photons we performed Franson interferometry. The results prove the time-energy entanglement between the signal and idler photons. Furthermore, the visibility of the interference fringes was high enough to significantly violate a Bell inequality and thus discard local-realistic theories for our experiment.

The second approach is based on quantum frequency conversion. Here photons resonant with an atomic transition ($4^2P_{3/2} \leftrightarrow 3^2D_{5/2}$ in $^{40}\text{Ca}^+$, 854 nm) should be interfaced to a telecom wavelength in the O-band (1310 nm). Such an interface can be based on nonlinear difference frequency generation with a strong mixing field at 2453 nm: $854 \text{ nm} - 2453 \text{ nm} \rightarrow 1310 \text{ nm}$. As there was no suitable laser source at the mixing wavelength available, an optical parametric oscillator was developed. This OPO was planned and designed in detail as a high power and high stability source for experiments in nonlinear optics. It is based on lithium niobate, housed in a singly resonant ring cavity. With seven available QPM periods a tuning range from 2311–2870 nm for the idler field could be demonstrated where tuning to even longer wavelengths is still possible. Over the whole tuning range a single-mode, single-frequency operation with output power exceeding 1 W was observed. Detailed long-term measurements of output power (0.9 % RMS fluctuations) and frequency (64 MHz RMS) proved the suitability for future experiments. In particular, we set the OPO to a wavelength around 2453 nm which is the pump wavelength for the following QFC process. The frequency converter was planned, set up in the lab and characterized in detail. The heart of the converter is a chip of lithium niobate ridge waveguides with different phase matching conditions. An approximative model was used to numerically simulate the field distribution in the waveguides and derive important operation parameters. The measured shape of the phase matching fits to the expectations. The tuning range is broad enough to cover the whole O-band starting with calcium resonant photons. Different coupling optics were investigated. However, coupling to the fundamental mode is hardly achievable due to the waveguide geometry. The current setup suffers from absorption losses in the coupling lens and coupling of the pump field to a higher waveguide mode, which is a principal starting point for future optimization. The frequency conversion itself was first characterized with attenuated coherent fields. Over-all conversion efficiencies of up to 8 % were achieved (48 % signal depletion). Due to lack of power and reduced overlap in the waveguide the efficiency maximum could not be reached, yet. The conversion scheme discards most noise sources and we are left with a continuous noise floor. This allows to use standard interference filters reducing device complexity. To verify operation of the quantum frequency converter at the single photon level we converted entangled photons from a SPDC source. We here reach comparable conversion efficiencies as for the laser. The temporal correlation between the photons is preserved

in the conversion process. We hence can use the combination of SPDC source and QFC as heralded single photon source. This could be proved in heralded- $g^{(2)}$ measurements for broadband and narrowband ($g^{(2)}(0) = 0.66$) photons. All measured curves show a clear antibunching. For optimized parameters in the broadband case very low values of $g^{(2)}(0) < 0.1$ can be reached resulting from low noise level. The applicability for long-range quantum channels could be proved in correlation measurements including long fibers. The temporal correlations and the temporal shape of the photon wave packet are preserved in the transmission through 20 km of standard telecom fiber. Furthermore, the herald signal could be transferred to a laser pulse which was multiplexed with the converted photon and transmitted through a single fiber demonstrating the simultaneous transmission of classical and quantum signals over the same fiber channel. Still the temporal correlation is preserved. Furthermore we used Franson interferometry to prove preservation of quantum correlations during QFC. In a first step, the first-order single photon interference was measured before and after frequency conversion. The coherence time of the broadband photons is increased in QFC as the converter acts as a spectral filter. These coherence functions are sufficient to model the interferogram of the pair state. In the Franson experiment this interferogram was measured, agreeing well to the modeled data. Such a detailed interference experiment, including QFC could be demonstrated for the first time. Again we see here a significant violation of the Bell inequality, after the QFC step. From the resulting visibility of the Franson experiment we can derive an entanglement transfer fidelity of 91.9 % for our frequency converter in the case of time-energy entangled photon pairs. The fidelity value is limited by the measurement devices. Finally we were able to apply the QFC technique to another heralded absorption experiment. One photon of a SPDC source was absorbed by a single calcium ion, while the herald was converted to the telecom O-band. We here see a temporal correlation between the telecom photon and the onset of quantum jumps. We could show that the initial correlation of the near infrared photon pair can be transferred to the ion-telecom photon system. This clearly proves the applicability of QFC for quantum networking schemes.

In a final chapter the former results were put into the context of QIP scenarios. Simulations clearly show that the technology, as presented in this thesis for the first time, allows for a great benefit for quantum repeater and quantum networking schemes. Including QFC into quantum repeater nodes can drastically reduce the transfer time. This chapter also addresses future advancements of the presented results.

Future Prospects

As a next short-term goal, the conversion of single photons emitted by the calcium ion is feasible. In principle, the converter is already capable of this process, however the

photon generation rate is quite low at the ion due to the absence of a certain excitation laser. At the moment a sequence including three optical transitions ($4^2S_{1/2} \rightarrow 4^2P_{1/2} \rightarrow 3^2D_{3/2} \rightarrow 4^2P_{3/2}$) is necessary to populate the upper state of the 854 nm transition ($4^2P_{3/2} \rightarrow 3^2D_{5/2}$). Direct population of the upper state from the ground state would be possible with the help of a laser source at 393 nm ($4^2S_{1/2} \rightarrow 4^2P_{3/2}$) which drastically increases the photon generation rate. This laser is currently being installed in the ion setup.

As a general outlook, I think the main goal will be to modify the frequency converter for polarization independent conversion. This will for the first time allow to convert a polarization qubit with a single device. Schemes to transfer entanglement to the calcium ion via the polarization state of a 854 nm photon have already been demonstrated. Another modification of the converter is to reverse the process, i.e. to allow upconversion of telecom photons to 854 nm. We could generate telecom single photons or even qubits with experimental schemes already demonstrated (e.g. OPO SPDC source, chapter 5; conversion of quantum dot emission [37]; waveguide SPDC source [262]) and then convert them to the resonance wavelength of calcium. A mid-term goal would then be to generate a single photon with a quantum emitter (e.g. SiV, quantum dot) and in a first step convert this photon to the telecom O-band. The telecom photon is transferred in a fiber and then upconverted to the calcium wavelength. This would for the first time demonstrate the interaction of two dissimilar quantum systems via QFC. Saarbrücken here turns out to be an outstanding location for these kind of experiments, combining labs with research focuses on solid state emitters, single atoms and solid state memories with research in quantum nonlinear optics.

For the OPO SPDC source a short-term goal is to improve the efficiency of filtering of a single mode, e.g. by the use of monolithic filtering cavities. A mid-term goal could be to address the D_1 line in cesium with a signal photon, which is correlated with an O-band idler photon. Apart from that, the OPO can be used as an efficient source for heralded, single telecom photons.

On a long-term time scale, all necessary elements to set up a quantum network or a quantum repeater node could be available in Saarbrücken. Hence it would be an interesting research task to demonstrate such an architecture.

Bibliography

- [1] M. Fox, "Quantum Optics," Oxford University Press (2006).
- [2] S. Singh, "Geheime Botschaften - Die Kunst der Verschlüsselung von der Antike bis in die Zeiten des Internet," 8th edition, Deutscher Taschenbuch Verlag, München (2008).
- [3] P. W. Shor, "Algorithms for quantum computation: discrete logarithms and factoring," Proceedings of the 35th Annual Symposium on Foundations of Computer Science, 124-134 (1994).
- [4] C. H. Bennett and G. Brassard, "Quantum cryptography: Public key distribution and coin tossing," Proc. IEEE International Conference on Computers, Systems and Signal Processing **175**, 8-12 (1984).
- [5] W. K. Wootters, and W. H. Zurek, "A single quantum cannot be cloned," Nature **299**, 802-803 (1982).
- [6] C. H. Bennett, F. Bessette, G. Brassard, L. Salvail, and J. Smolin, "Experimental Quantum Cryptography," J. Cryptology **5** 3-28 (1992).
- [7] N. Gisin, G. Ribordy, W. Tittel, and H. Zbinden, "Quantum cryptography," Rev. Mod. Phys. **74**, 145-195 (2002).
- [8] R. P. Feynman, "Simulating Physics with Computers," Int. J. Theor. Phys. **21**, 467-488 (1982).
- [9] I. M. Georgescu, S. Ashhab, and Franco Nori, "Quantum simulation," Rev. Mod. Phys. **86**, 153-185 (2010).
- [10] D. Deutsch, "Quantum Theory, the Church-Turing Principle and the Universal Quantum Computer," Proc. R. Soc. London A, **400**, 97-117 (1985).
- [11] M. A. Nielsen, and I. L. Chuang, "Quantum Computation and Quantum Information," 8th edition, Cambridge University Press (2005).
- [12] J. I. Cirac, P. Zoller, H. J. Kimble, and H. Mabuchi, "Quantum State Transfer and Entanglement Distribution among Distant Nodes in a Quantum Network," Phys. Rev. Lett. **78**, 3221-3224 (1997).

- [13] H. J. Kimble, "The quantum internet," *Nature* **453**, 1023-1030 (2008).
- [14] T. D. Ladd, F. Jelezko, R. Laflamme, Y. Nakamura, C. Monroe, and J. L. O'Brien, "Quantum computers," *Nature* **464**, 45-53 (2010).
- [15] L.-M. Duan, and C. Monroe, "Colloquium: Quantum networks with trapped ions," *Rev. Mod. Phys.* **82**, 1209-1224 (2010).
- [16] B. B. Blinov, D. L. Moehring, L.-M. Duan, and C. Monroe, "Observation of entanglement between a single trapped atom and a single photon," *Nature* **428**, 153-157 (2004).
- [17] T. E. Northup, and R. Blatt, "Quantum information transfer using photons," *Nature Photon.* **8**, 356-363 (2014).
- [18] H.-J. Briegel, W. Dür, J. I. Cirac, and P. Zoller, "Quantum Repeaters: The Role of Imperfect Local Operations in Quantum Communication," *Phys. Rev. Lett.* **81**, 5932-5935 (1998).
- [19] L. D. Landau, and E. M. Lifschitz, "Lehrbuch der Theoretischen Physik, Band 8: Elektrodynamik der Kontinua," 5th edition, Akademie-Verlag, Berlin (1990).
- [20] P. A. Franken, A. E. Hill, C. W. Peters, and G. Weinreich, "Generation of Optical Harmonics," *Phys. Rev. Lett.* **7**, 118-119 (1961).
- [21] R. S. Weis, and T. K. Gaylord, "Lithium Niobate: Summary of Physical Properties and Crystal Structure," *Appl. Phys. A* **37**, 191-203 (1985).
- [22] M. M. Fejer, G. A. Magel, D. H. Jundt, and R. L. Byer, "Quasi-Phase-Matched Second Harmonic Generation: Tuning and Tolerances," *IEEE J. Quantum. Electron.* **28**, 2631-2654 (1992).
- [23] P. Kumar, "Quantum frequency conversion," *Opt. Lett.* **15**, 1476-1478 (1990).
- [24] J. Huang, and P. Kumar, "Observation of quantum frequency conversion," *Phys. Rev. Lett.* **68**, 2153-2156 (1992).
- [25] M. A. Albota, and F. N. C. Wong, "Efficient single-photon counting at $1.55\mu\text{m}$ by means of frequency upconversion," *Opt. Lett.* **29**, 1449-1451 (2004).
- [26] M. H. Chou, J. Hauden, M. A. Arbore, and M. M. Fejer, "1.5- μm -band wavelength conversion based on difference-frequency generation in LiNbO_3 waveguides with integrated coupling structures," *Opt. Lett.* **23**, 1004-1006 (1998).

-
- [27] C. Langrock, E. Diamanti, R. V. Roussev, Y. Yamamoto, H. Takesue, and M. M. Fejer, "Highly efficient single-photon detection at communication wavelengths by use of upconversion in reverse-proton-exchanged periodically poled LiNbO₃ waveguides," *Opt. Lett.* **30**, 1725-1727 (2005).
- [28] S. Tanzilli, W. Tittel, M. Halder, O. Alibart, P. Baldi, N. Gisin, and H. Zbinden, "A photonic quantum information interface," *Nature* **437**, 116-120 (2005).
- [29] J. D. Franson, "Bell Inequality for Position and Time," *Phys. Rev. Lett.* **62**, 2205-2208 (1989).
- [30] M. T. Rakher, L. Ma, O. Slattery, X. Tang, and K. Srinivasan, "Quantum transduction of telecommunicationsband single photons from a quantum dot by frequency upconversion," *Nature Photon.* **4**, 786-791 (2010).
- [31] Z. Y. Ou, "Efficient conversion between photons and between photon and atom by stimulated emission," *Phys. Rev. A* **78**, 023819 (2008).
- [32] J. S. Pelc, C. Langrock, Q. Zhang, and M. M. Fejer, "Influence of domain disorder on parametric noise in quasi-phase-matched quantum frequency converters," *Opt. Lett.* **35**, 2804-2806 (2008).
- [33] J. S. Pelc, Q. Zhang, C. R. Phillips, L. Yu, Y. Yamamoto, and M. M. Fejer, "Cascaded frequency upconversion for high-speed single-photon detection at 1550 nm," *Opt. Lett.* **37**, 476-478 (2012).
- [34] S. Zaske, A. Lenhard, and C. Becher, "Efficient frequency downconversion at the single photon level from the red spectral range to the telecommunications C-band," *Opt. Express* **19**, 12825-12836 (2011).
- [35] J. S. Pelc, L. Ma, C. R. Phillips, Q. Zhang, C. Langrock, O. Slattery, X. Tang, and M. M. Fejer, "Long-wavelength-pumped upconversion single-photon detector at 1550 nm: performance and noise analysis," *Opt. Express* **19**, 21445-21456 (2011).
- [36] S. Blum, G. A. Olivares-Renteria, C. Ottaviani, C. Becher, and G. Morigi, "Single-photon frequency conversion in nonlinear crystals," *Phys. Rev. A* **88**, 053807 (2013).
- [37] S. Zaske, A. Lenhard, C. A. Keßler, J. Kettler, C. Hepp, C. Arend, R. Albrecht, W.-M. Schulz, M. Jetter, P. Michler, and C. Becher, "Visible-to-Telecom Quantum Frequency Conversion of Light from a Single Quantum Emitter," *Phys. Rev. Lett.* **109**, 147404 (2012).

- [38] S. Ates, I. Agha, A. Gulinatti, I. Rech, M. T. Rakher, A. Badolato, and K. Srinivasan, "Two-Photon Interference Using Background-Free Quantum Frequency Conversion of Single Photons Emitted by an InAs Quantum Dot," *Phys. Rev. Lett.* **109**, 147405 (2012).
- [39] S. V. Polyakov, A. Muller, E. B. Flagg, A. Ling, N. Borjemscaia, E. Van Keuren, A. Migdall, and G. S. Solomon, "Coalescence of Single Photons Emitted by Disparate Single-Photon Sources: The Example of InAs Quantum Dots and Parametric Down-Conversion Sources," *Phys. Rev. Lett.* **107**, 157402 (2011).
- [40] J. Lavoie, J. M. Donohue, L. G. Wright, A. Fedrizzi, and K. J. Resch, "Spectral compression of single photons," *Nature Photon.* **7**, 363-366 (2013).
- [41] J. M. Donohue, M. Agnew, J. Lavoie, and K. J. Resch, "Coherent Ultrafast Measurement of Time-Bin Encoded Photons," *Phys. Rev. Lett.* **111**, 153602 (2013).
- [42] K. De Greve, L. Yu, P. L. McMahon, J. S. Pelc, C. M. Natarajan, N. Y. Kim, E. Abe, S. Maier, C. Schneider, M. Kamp, S. Höfling, R. H. Hadfield, A. Forchel, M. M. Fejer, and Y. Yamamoto, "Quantum-dot spin-photon entanglement via frequency downconversion to telecom wavelength," *Nature* **491**, 421-425 (2012).
- [43] H. J. McGuinness, M. G. Raymer, C. J. McKinstrie, and S. Radic, "Quantum Frequency Translation of Single-Photon States in a Photonic Crystal Fiber," *Phys. Rev. Lett.* **105**, 093604 (2010).
- [44] H. J. McGuinness, M. G. Raymer, and C. J. McKinstrie, "Theory of quantum frequency translation of light in optical fiber: application to interference of two photons of different color," *Opt. Express* **19**, 17876-17907 (2011).
- [45] A. S. Clark, S. Shahnia, M. J. Collins, C. Xiong, and B. J. Eggleton, "High-efficiency frequency conversion in the single-photon regime," *Opt. Lett.* **38**, 947-949 (2013).
- [46] I. Agha, M. Davanco, B. Thurston, and K. Srinivasan, "Low-noise chip-based frequency conversion by four-wave-mixing Bragg scattering in SiN_x waveguides," *Opt. Lett.* **37**, 2997-2999 (2012).
- [47] I. Agha, S. Ates, M. Davanco, and K. Srinivasan, "A chip-scale, telecommunications-band frequency conversion interface for quantum emitters," *Opt. Express* **21**, 21628-21638 (2013).

-
- [48] J. T. Hill, A. H. Safavi-Naeini, J. Chan, and O. Painter, "Coherent optical wavelength conversion via cavity optomechanics," *Nature Commun.* **3**, 1196 (2012).
- [49] M. W. McCutcheon, D. E. Chang, Y. Zhang, M. D. Lukin, and M. Loncar, "Broadband frequency conversion and shaping of single photons emitted from a nonlinear cavity," *Opt. Express* **17**, 22689-22703 (2009).
- [50] M. Davanco, J. Chan, A. H. Safavi-Naeini, O. Painter, and K. Srinivasan, "Slot-mode-coupled optomechanical crystals," *Opt. Express* **20**, 24394-24410 (2012).
- [51] M. Notomi, H. Taniyama, S. Mitsugi, and E. Kuramochi, "Optomechanical Wavelength and Energy Conversion in High-Q Double-Layer Cavities of Photonic Crystal Slabs," *Phys. Rev. Lett.* **97**, 023903 (2006).
- [52] Y. Liu, M. Davanco, V. Aksyuk, and K. Srinivasan, "Electromagnetically Induced Transparency and Wideband Wavelength Conversion in Silicon Nitride Microdisk Optomechanical Resonators," *Phys. Rev. Lett.* **110**, 223603 (2013).
- [53] A. G. Radnaev, Y. O. Dudin, R. Zhao, H. H. Jen, S. D. Jenkins, A. Kuzmich, and T. A. B. Kennedy, "A quantum memory with telecom-wavelength conversion," *Nature Phys.* **6**, 894-899 (2010).
- [54] D. N. Klyshko, "Coherent Photon Decay in a Nonlinear Medium," *Sov. Phys. JETP Lett.* **6**, 490-492 (1967).
- [55] S. E. Harris, M. K. Oshman, and R. L. Byer, "Observation of Tunable Optical Parametric Fluorescence," *Phys. Rev. Lett.* **18**, 732-734 (1967).
- [56] D. C. Burnham, and D. L. Weinberg, "Observation of Simultaneity in Parametric Production of Optical Photon Pairs," *Phys. Rev. Lett.* **25**, 84-87 (1970).
- [57] A. Einstein, B. Podolsky, and N. Rosen, "Can Quantum-Mechanical Description of Physical Reality Be Considered Complete?" *Phys. Rev.* **47**, 777-780 (1935).
- [58] Y. H. Shih and C. O. Alley, "New Type of Einstein-Podolsky-Rosen-Bohm Experiment Using Pairs of Light Quanta Produced by Optical Parametric Down Conversion," *Phys. Rev. Lett.* **61**, 2921 (1988).
- [59] P. G. Kwiat, K. Mattle, H. Weinfurter, A. Zeilinger, A. V. Sergienko, and Y. Shih, "New High-Intensity Source of Polarization-Entangled Photon Pairs," *Phys. Rev. Lett.* **75**, 4337-4341 (1995).

- [60] Z. Y. Ou, and Y. J. Lu, "Cavity Enhanced Spontaneous Parametric Down-Conversion for the Prolongation of Correlation Time between Conjugate Photons," *Phys. Rev. Lett.* **83**, 2556-2559 (1999).
- [61] C. K. Hong, and L. Mandel, "Experimental Realization of a Localized One-Photon State," *Phys. Rev. Lett.* **56**, 58-60 (1988).
- [62] G. Brida, I. P. Degiovanni, M. Genovese, F. Piacentini, P. Traina, A. Della Frera, A. Tosi, A. Bahgat Shehata, C. Scarcella, A. Gulinatti, M. Ghioni, S. V. Polyakov, A. Migdall, and A. Giudice, "An extremely low-noise heralded single-photon source: A breakthrough for quantum technologies," *Appl. Phys. Lett.* **101**, 221112 (2012).
- [63] E. Pomarico, B. Sanguinetti, T. Guerreiro, R. Thew, and H. Zbinden, "MHz rate and efficient synchronous heralding of single photons at telecom wavelengths," *Opt. Express* **20**, 23846-23855 (2012).
- [64] S. Krapick, H. Herrmann, V. Quiring, B. Brecht, H. Suche, and Ch. Silberhorn, "An efficient integrated two-color source for heralded single photons," *New J. Phys.* **15**, 033010 (2013).
- [65] S. Fasel, O. Alibart, S. Tanzilli, P. Baldi, A. Beveratos, N. Gisin, and H. Zbinden, "High-quality asynchronous heralded single-photon source at telecom wavelength," *New J. Phys.* **6**, 163 (2004).
- [66] E. Pomarico, B. Sanguinetti, N. Gisin, R. Thew, H. Zbinden, G. Schreiber, A. Thomas, and W. Sohler, "Waveguide-based OPO source of entangled photon pairs," *New J. Phys.* **11**, 113042 (2009).
- [67] M. Förtsch, J. U. Fürst, C. Wittmann, D. Strekalov, A. Aiello, M. V. Chekhova, C. Silberhorn, G. Leuchs, and C. Marquardt, "A versatile source of single photons for quantum information processing," *Nat. Commun.* **4**, 1818 (2013).
- [68] X. Li, P. L. Voss, J. E. Sharping, and P. Kumar, "Optical-Fiber Source of Polarization-Entangled Photons in the 1550 nm Telecom Band," *Phys. Rev. Lett.* **94**, 053601 (2005).
- [69] J. G. Rarity, J. Fulconis, J. Duligall, W. J. Wadsworth, and P. St. J. Russell, "Photonic crystal fiber source of correlated photon pairs," *Opt. Express* **13**, 534-544 (2005).
- [70] J. E. Sharping, K. F. Lee, M. A. Foster, A. C. Turner, B. S. Schmidt, M. Lipson, A. L. Gaeta, and P. Kumar, "Generation of correlated photons in nanoscale silicon waveguides," *Opt. Express* **14**, 12388-12393 (2006).

-
- [71] S. Azzini, D. Grassani, M. J. Strain, M. Sorel, L. G. Helt, J. E. Sipe, M. Lisicidini, M. Galli, and D. Bajoni, "Ultra-low power generation of twin photons in a compact silicon ring resonator," *Opt. Express* **20**, 23100-23107 (2012).
- [72] N. Matsuda, T. Kato, K.-I. Harada, H. Takesue, E. Kuramochi, H. Taniyama, and M. Notomi, "Slow light enhanced optical nonlinearity in a silicon photonic crystal coupled-resonator optical waveguide," *Opt. Express* **19**, 19861-19874 (2011).
- [73] M. Davanco, J. R. Ong, A. B. Shehata, A. Tosi, I. Agha, S. Assefa, F. Xia, W. M. J. Green, S. Mookherjea, and K. Srinivasan, "Telecommunications-band heralded single photons from a silicon nanophotonic chip," *Appl. Phys. Lett.* **100**, 261104 (2012).
- [74] M. J. Collins, C. Xiong, I. H. Rey, T. D. Vo, J. He, S. Shahnian, C. Reardon, T. F. Krauss, M. J. Steel, A. S. Clark, and B. J. Eggleton, "Integrated spatial multiplexing of heralded single-photon sources," *Nature Commun.* **4**, 2582 (2013).
- [75] H. Takesue, N. Matsuda, E. Kuramochi, W. J. Munro, and M. Notomi, "An on-chip coupled resonator optical waveguide single-photon buffer," *Nature Commun.* **4**, 2725 (2013).
- [76] C. A. Kocher, and E. D. Commins, "Polarization Correlation of Photons Emitted in an Atomic Cascade," *Phys. Rev. Lett.* **18**, 575-577 (1967).
- [77] A. Aspect, P. Grangier, and G. Roger, "Experimental Realization of Einstein-Podolsky-Rosen-Bohm Gedankenexperiment: A New Violation of Bell's Inequalities," *Phys. Rev. Lett.* **49**, 91-94 (1982).
- [78] M. B. Ward, M. C. Dean, R. M. Stevenson, A. J. Bennett, D. J. P. Ellis, K. Cooper, I. Farrer, C. A. Nicoll, D. A. Ritchie, and A. J. Shields, "Coherent dynamics of a telecom-wavelength entangled photon source," *Nature Commun.* **5**, 3316 (2014).
- [79] H. Hübel, D. R. Hamel, A. Fedrizzi, S. Ramelow, K. J. Resch, and T. Jennewein, "Direct generation of photon triplets using cascaded photon-pair sources," *Nature* **466**, 601-603 (2010).
- [80] D. P. DiVincenzo, and D. Loss, "Quantum information is physical," *Superlattice. Microst.* **23**, 419-432 (1998).
- [81] W. Paul, and H. Steinwedel, "Ein neues Massenspektrometer ohne Magnetfeld," *Z. Naturforschg.* **8a**, 448-450 (1953).

- [82] W. Paul, O. Osberghaus, and E. Fischer, "Ein Ionenkäfig," *Forschungsberichte des Wirtschafts- und Verkehrsministeriums Nordrhein-Westfalen* **415** (1958).
- [83] W. Neuhauser, M. Hohenstatt, P. E. Toschek, and H. Dehmelt, "Localized visible Ba^+ mono-ion oscillator," *Phys. Rev. A* **22**, 1137-1140 (1980).
- [84] D. J. Wineland, J. C. Bergquist, W. M. Itano, and R. E. Drullinger, "Double-resonance and optical-pumping experiments on electromagnetically confined, laser-cooled ions," *Opt. Lett.* **5**, 245-247 (1980).
- [85] Th. Sauter, W. Neuhauser, R. Blatt, and P. E. Toschek, "Observation of Quantum Jumps," *Phys. Rev. Lett.* **57**, 1696-1698 (1986).
- [86] J. J. Bollinger, D. J. Heizen, W. M. Itano, S. L. Gilbert, D. J. Wineland, "A 303-MHz frequency standard based on trapped Be^+ ions," *IEEE Trans. Instrum. Meas.* **40**, 126-128 (1991).
- [87] M. G. Raizen, J. M. Gilligan, J. C. Bergquist, W. M. Itano, and D. J. Wineland, "Ionic crystals in a linear Paul trap," *Phys. Rev. A* **45**, 6493-6501 (1992).
- [88] J. I. Cirac, and P. Zoller, "Quantum Computations with Cold Trapped Ions," *Phys. Rev. Lett.* **74**, 4091-4094 (1995).
- [89] F. Schmidt-Kaler, H. Häffner, M. Riebe, S. Gulde, G. P. T. Lancaster, T. Deuschle, C. Becher, C. F. Roos, J. Eschner, and R. Blatt, "Realization of the Cirac-Zoller controlled-NOT quantum gate," *Nature* **422**, 408-411 (2003).
- [90] C. A. Sackett, D. Kielpinski, B. E. King, C. Langer, V. Meyer, C. J. Myatt, M. Rowe, Q. A. Turchette, W. M. Itano, D. J. Wineland, and C. Monroe, "Experimental entanglement of four particles," *Nature* **404**, 256-259 (2000).
- [91] F. Schmidt-Kaler, H. Häffner, S. Gulde, M. Riebe, G. P. T. Lancaster, T. Deuschle, C. Becher, W. Hänsel, J. Eschner, C. F. Roos, and R. Blatt, "How to realize a universal quantum gate with trapped ions," *Appl. Phys. B* **77**, 789-796 (2003).
- [92] D. Leibfried, B. DeMarco, V. Meyer, D. Lucas, M. Barrett, J. Britton, W. M. Itano, B. Jelenkovic, C. Langer, T. Rosenband, and D. J. Wineland, "Experimental demonstration of a robust, high-fidelity geometric two ion-qubit phase gate," *Nature* **422**, 412-415 (2003).

-
- [93] S. Gulde, M. Riebe, G. P. T. Lancaster, C. Becher, J. Eschner, H. Häffner, F. Schmidt-Kaler, I. L. Chuang, and R. Blatt, "Implementation of the Deutsch-Jozsa algorithm on an ion-trap quantum computer," *Nature* **421**, 48-50 (2003).
- [94] K.-A. Brickman, P. C. Haljan, P. J. Lee, M. Acton, L. Deslauriers, and C. Monroe, "Implementation of Grover's quantum search algorithm in a scalable system," *Phys. Rev. A* **72**, 050306(R) (2005).
- [95] M. Riebe, H. Häffner, C. F. Roos, W. Hänsel, J. Benhelm, G. P. T. Lancaster, T. W. Kärber, C. Becher, F. Schmidt-Kaler, D. F. V. James, and R. Blatt, "Deterministic quantum teleportation with atoms," *Nature* **429**, 734-737 (2004).
- [96] M. D. Barrett, J. Chiaverini, T. Schaetz, J. Britton, W. M. Itano, J. D. Jost, E. Knill, C. Langer, D. Leibfried, R. Ozeri, and D. J. Wineland, "Deterministic quantum teleportation of atomic qubits," *Nature* **429**, 737-739 (2004).
- [97] D. L. Moehring, P. Maunz, S. Olmschenk, K. C. Younge, D. N. Matsukevich, L.-M. Duan, and C. Monroe, "Entanglement of single-atom qubits at a distance," *Nature* **449**, 68-71 (2007).
- [98] R. W. Boyd, "Nonlinear Optics," 3rd edition, Academic Press, Elsevier, (2008).
- [99] D. A. Kleinman, "Nonlinear Dielectric Polarization in Optical Media," *Phys. Rev.* **126**, 1977-1979 (1962).
- [100] R. L. Sutherland, "Handbook of nonlinear optics," Marcel Dekker, New York (1996).
- [101] F. Zernike, J. E. Midwinter, "Applied Nonlinear Optics," Dover Publications, Mineola, New York (2006).
- [102] R. Loudon, "The Quantum Theory of Light," 3rd edition, Oxford University Press (2000).
- [103] O. Thomas, Z. L. Yuan, and A. J. Shields, "Practical photon number detection with electric field-modulated silicon avalanche photodiodes," *Nat. Commun.* **3**, 644 (2012).
- [104] A. R. Rossi, S. Olivares, and M. G. A. Paris, "Photon statistics without counting photons," *Phys. Rev. A* **70**, 055801 (2004).

- [105] S. E. E. Blum, "Theoretische und experimentelle Untersuchungen der nicht-linearen Frequenzkonversion einzelner Photonen," Diploma thesis, Universität des Saarlandes, Saarbrücken (2011).
- [106] G. A. Steudle, S. Schietinger, D. Höckel, S. N. Dorenbos, I. E. Zadeh, V. Zwiller, and O. Benson, "Measuring the quantum nature of light with a single source and a single detector," *Phys. Rev. A* **86**, 053814 (2012).
- [107] R. Hanbury Brown, R. Q. Twiss, "Correlation of photons in two coherent beams of light," *Nature* **177**, 27-29 (1956).
- [108] B. Brecht, A. Eckstein, A. Christ, H. Suche, and C. Silberhorn, "From quantum pulse gate to quantum pulse shaper - engineered frequency conversion in nonlinear optical waveguides," *New J. Phys.* **13**, 065029 (2011).
- [109] A. Lenhard, S. Zaske, S. Blum, G. Morigi, and C. Becher, "Low-Noise Frequency Down-Conversion at the Single Photon Level," in *CLEO:2012 (Optical Society of America, Washington, DC, 2012)*, paper **JTh1K.4**.
- [110] Z. Y. J. Ou, "Multi-Photon Quantum Interference," Springer Science+Business Media, New York (2007).
- [111] M. W. Mitchel, "Parametric down-conversion from a wave-equation approach: Geometry and absolute brightness," *Phys. Rev. A* **79**, 043835 (2009).
- [112] B. Yurke, and M. Potasek, "Obtainment of thermal noise from a pure quantum state," *Phys. Rev. A* **36**, 3464-3466 (1987).
- [113] B. Blauensteiner, I. Herbauts, S. Bettelli, A. Poppe, and H. Hübel, "Photon bunching in parametric down-conversion with continuous-wave excitation," *Phys. Rev. A* **79**, 063846 (2009).
- [114] P. Grangier, G. Roger and A. Aspect, "Experimental Evidence for a Photon Anticorrelation Effect on a Beam Splitter: A New Light on Single-Photon Interferences," *Europhys. Lett.* **1**, 173-179 (1986).
- [115] D. N. Nikogosyan, "Nonlinear Optical Crystals: A Complete Survey," Springer Science + Business Media Inc., New York (2005).
- [116] P. Lerner, C. Legras, and J. P. Dumas, "Stoechiometrie des monocristaux de metaniobate de lithium," *J. Crystal Growth* **3-4**, 231-235 (1968).
- [117] A. Ashkin, G. D. Boyd, J. M. Dziedzic, R. G. Smith, A. A. Ballman, J. J. Levinstein, and K. Nassau, "Optically-induced refractive index inhomogeneities in LiNbO_3 and LiTaO_3 ," *Appl. Phys. Lett.* **9**, 72 (1966).

-
- [118] S. Zelt, "Erzeugung von periodischen Domänen in ferroelektrischen Kristallen und deren Anwendung in der nichtlinearen Optik," Ph.D. thesis, TU Kaiserslautern (2003).
- [119] J. Hirohashi, V. Pasiskevicius, S. Wang, and F. Laurell, "Picosecond blue-light-induced infrared absorption in single-domain and periodically poled ferroelectrics," *J. Appl. Phys.* **101**, 033105 (2007).
- [120] Y. Furukawa, K. Kitamura, A. Alexandrovski, R. K. Route, M. M. Fejer, and G. Foulon, "Green-induced infrared absorption in MgO doped LiNbO₃," *Appl. Phys. Lett.* **78**, 1970-1972 (2001).
- [121] Y. Furukawa, K. Kitamura, S. Takekawa, A. Miyamoto, M. Terao, and N. Suda, "Photorefraction in LiNbO₃ as a function of [Li]/[Nb] and MgO concentrations," *Appl. Phys. Lett.* **77**, 2494-2496 (2000).
- [122] T. R. Volk, V. I. Pryalkin, and N. M. Rubinina, "Optical-damage-resistant LiNbO₃:Zn crystal," *Opt. Lett.* **15**, 996-998 (1990).
- [123] H. Ibach, and H. Lüth, "Festkörperphysik," 6th edition, Springer Verlag, Berlin Heidelberg (2002).
- [124] T. Suhara, M. Fujimura, "Waveguide Nonlinear-Optic Devices," Springer, Berlin Heidelberg (2003).
- [125] T. Andres, P. Haag, S. Zelt, J.-P. Meyn, A. Borsutzky, R. Beigang, and R. Wallenstein, "Synchronously pumped femtosecond optical parametric oscillator of congruent and stoichiometric MgO-doped periodically poled lithium niobate," *Appl. Phys. B* **76**, 241-244 (2003).
- [126] J. R. Schwesyg, C. R. Phillips, K. Ioakeimidi, M. C. C. Kajiyama, M. Falk, D. H. Jundt, K. Buse, and M. M. Fejer, "Suppression of mid-infrared light absorption in undoped congruent lithium niobate crystals," *Opt. Lett.* **35**, 1070-1072 (2010).
- [127] O. Gayer, Z. Sacks, E. Galun, and A. Arie, "Temperature and wavelength dependent refractive index equations for MgO-doped congruent and stoichiometric LiNbO₃," *Appl. Phys. B* **91**, 343-348 (2008).
- [128] Yoshiki Nishida, NTT electronics, personal communication.
- [129] D. H. Jundt, "Temperature-dependent Sellmeier equation for the index of refraction, n_e , in congruent lithium niobate," *Opt. Lett.* **22**, 1553-1555 (1997).

- [130] R. C. Miller, "Optical second harmonic generation in piezoelectric crystals," *Appl. Phys. Lett.* **5**, 17-19 (1964).
- [131] I. Shoji, T. Kondo, A. Kitamoto, M. Shirane, and R. Ito, "Absolute scale of second-order nonlinear-optical coefficients," *J. Opt. Soc. Am. B* **14**, 2268-2294 (1997).
- [132] R. C. Miller, W. A. Nordland, and P. M. Bridenbaugh, "Dependence of Second-Harmonic-Generation Coefficients of LiNbO_3 on Melt Composition," *J. Appl. Phys.* **42**, 4145-4147 (1971).
- [133] J. A. Giordmaine, and R. C. Miller, "Tunable Coherent Parametric Oscillation in LiNbO_3 at Optical Frequencies," *Phys. Rev. Lett.* **14**, 973-976 (1965).
- [134] R. C. Smith, J. E. Ceusic, H. J. Levinstein, J. J. Rubin, S. Singh, and L. C. Van Uitert, "Continuous Optical Parametric Oscillation in $\text{Ba}_2\text{NaNb}_5\text{O}_{15}$," *Appl. Phys. Lett.* **12**, 308-310 (1968).
- [135] L. E. Myers, R. C. Eckardt, M. M. Fejer, R. L. Byer, W. R. Bosenberg, and J. W. Pierce, "Quasi-phase-matched optical parametric oscillators in bulk periodically poled LiNbO_3 ," *J. Opt. Soc. Am. B* **12**, 2102-2116 (1995).
- [136] M. E. Klein, D.-H. Lee, J.-P. Meyn, B. Beier, K.-J. Boller, and R. Wallenstein, "Diode-pumped continuous-wave widely tunable optical parametric oscillator based on periodically poled lithium tantalate," *Opt. Lett.* **23**, 831-833 (1998).
- [137] G. D. Boyd, and D. A. Kleinman, "Parametric Interaction of Focused Gaussian Light Beams," *J. Appl. Phys.* **39**, 3597-3639 (1968).
- [138] H. Kogelnik, and T. Li, "Laser Beams and Resonators," *Appl. Opt.* **5**, 1550-1567 (1966).
- [139] M. Vainio, J. Peltola, S. Persijn, F. J. M. Harren, and L. Halonen, "Thermal effects in singly resonant continuous-wave optical parametric oscillators," *Appl. Phys. B* **94**, 411-427 (2009).
- [140] M. E. Klein, "Wavelength tunable, diode laser pumped optical parametric oscillators based on quasi-phase-matching," PhD thesis, University of Kaiserslautern (2000).
- [141] C. Warschburger, S. Zaske, A. Lenhard, M. Schug, J. Eschner, and C. Becher, "Analysis of Frequency Noise Properties of a CW Optical Parametric Oscillator using an Optical Frequency Comb," manuscript in preparation (2014).

-
- [142] S. Zaske, D.-H. Lee, and C. Becher, "Green-pumped cw singly resonant optical parametric oscillator based on MgO:PPLN with frequency stabilization to an atomic resonance," *Appl. Phys. B* **98**, 729-735 (2010).
- [143] A. Lenhard, S. Zaske, J. A. L'huillier, and C. Becher, "Stabilized diode laser pumped, idler resonant cw optical parametric oscillator," *Appl. Phys. B* **102**, 757-764 (2011).
- [144] B. E. A. Saleh, and M. C. Teich, "Fundamentals of Photonics," 2nd edition, John Wiley and Sons, Hoboken, New Jersey (2007).
- [145] B. Weigand, "Modellierung, Herstellung und Charakterisierung von Kantenwellenleitern in Lithiumniobat (LiNbO_3)," Diploma thesis, TU Kaiserslautern (2011).
- [146] D. Marcuse, "Theory of Dielectric Optical Waveguides," 2nd edition, Academic Press, Boston (1974).
- [147] J. Bures, "Guided Optics," Wiley-VCH, Weinheim (2009).
- [148] I. Dolev, A. Ganany-Padowicz, O. Gayer, A. Arie, J. Mangin, and G. Gadret, "Linear and nonlinear optical properties of MgO:LiTaO₃," *Appl. Phys. B* **96**, 423-432 (2009).
- [149] R. V. Schmidt, and I. P. Kaminow, "Metaldiffused optical waveguides in LiNbO₃," *Appl. Phys. Lett.* **25**, 458-460 (1974).
- [150] N. Uesugi, "Parametric difference frequency generation in a threedimensional LiNbO₃ optical waveguide," *Appl. Phys. Lett.* **36**, 178-180 (1980).
- [151] V. Gericke, P. Hertel, E. Krätzig, J. P. Nisius, and R. Sommerfeldt, "Light-Induced Refractive Index Changes in LiNbO₃:Ti Waveguides," *Appl. Phys. B* **44**, 155-162 (1987).
- [152] E. L. Wooten, K. M. Kissa, A. Yi-Yan, E. J. Murphy, D. A. Lafaw, P. F. Hallemeier, D. Maack, D. V. Attanasio, D. J. Fritz, G. J. McBrien, and D. E. Bossi, "A Review of Lithium Niobate Modulators for Fiber-Optic Communications Systems," *IEEE J. Sel. Top. QE* **6**, 69-82 (2000).
- [153] J. L. Jackel, C. E. Rice, and J. J. Veselka, "Proton exchange for highindex waveguides in LiNbO₃," *Appl. Phys. Lett.* **41**, 607-608 (1982).
- [154] O. Yavuzcetin, N. R. Perry, S. T. Malley, R. L. Dally, H. P. Novikov, B. Ozturk, and S. Sridhar, "Fabrication and characterization of single mode annealed proton exchanged waveguides in -x-cut lithium niobate," *Opt. Mater.* **36**, 372-375 (2013).

- [155] F. Chen, "Photonic guiding structures in lithium niobate crystals produced by energetic ion beams," *J. Appl. Phys.* **106**, 081101 (2009).
- [156] Y. Nishida, H. Miyazawa, M. Asobe, O. Tadanaga, and H. Suzuki, "Direct-bonded QPM-LN ridge waveguide with high damage resistance at room temperature," *Electron. Lett.* **39**, 609-611 (2003).
- [157] O. Tadanaga, T. Yanagawa, Y. Nishida, H. Miyazawa, K. Magari, M. Asobe, and H. Suzuki, "Efficient $3\mu\text{m}$ difference frequency generation using direct-bonded quasi-phase-matched LiNbO_3 ridge waveguides," *Appl. Phys. Lett.* **88**, 061101 (2006).
- [158] T. Nishikawa, A. Ozawa, Y. Nishida, M. Asobe, F.-L. Hong, and T. W. Hänsch, "Efficient 494 mW sum-frequency generation of sodium resonance radiation at 589 nm by using a periodically poled Zn:LiNbO_3 ridge waveguide," *Opt. Express* **17**, 17792-17800 (2009).
- [159] J. Thomas, M. Heinrich, P. Zeil, V. Hilbert, K. Rademaker, R. Riedel, S. Ringleb, C. Dubs, J.-P. Ruske, S. Nolte, and A. Tünnermann, "Laser direct writing: Enabling monolithic and hybrid integrated solutions on the lithium niobate platform," *Phys. Status Solidi A* **208**, 276-283 (2011).
- [160] D. W. Ward, E. R. Statz, and K. A. Nelson, "Fabrication of polaritonic structures in LiNbO_3 and LiTaO_3 using femtosecond laser machining," *Appl. Phys. A* **86**, 49-54 (2007).
- [161] F. Laurell, J. Webjorn, G. Arvidsson, and J. Holmberg, "Wet Etching of Proton-exchanged Lithium Niobate - A Novel Processing Technique," *J. Lightwave Tech.* **10**, 1606-1609 (1992).
- [162] I. E. Barry, G. W. Ross, P. G. R. Smith, and R. W. Eason, "Ridge waveguides in lithium niobate fabricated by differential etching following spatially selective domain inversion," *Appl. Phys. Lett.* **74**, 1487-1488 (1999).
- [163] M. Stolze, T. Herrmann und J. A. L'huillier, "Investigations on Microstructuring of Ferroelectric Materials by Picosecond UV Laser Pulses," 30th International Congress on Applications of Lasers and Electro-Optics (ICALEO) 2011, Orlando/FL, October 23-27, paper **M1006** (2011).
- [164] M. Stolze, T. Herrmann, B. Weigand und J. L'huillier, "Laser Microstructuring of Congruent Lithium Niobate by UV ps-pulses," ISAF ECAPD PFM 2012, Aveiro/Portugal, July 9-13, paper **109** (2012).

-
- [165] N. M. Bulgakova, R. Stoian, and A. Rosenfeld, "Laser-induced modification of transparent crystals and glasses," *Quant. Electronics* **40**, 966-985 (2011).
- [166] M. Stolze, Photonik Zentrum Kaiserslautern, personal communication (2014).
- [167] M. Roussey, M.-P. Bernal, N. Courjal, and F. I. Baida, "Experimental and theoretical characterization of a lithium niobate photonic crystal," *Appl. Phys. Lett.* **87**, 241101 (2005).
- [168] P. Fuchs, "Herstellung und Charakterisierung von Indiumzinnoxid-Schichten zur Optimierung optischer Kantenwellenleiter aus Lithiumniobat," Bachelor thesis, Universität des Saarlandes, Saarbrücken (2013).
- [169] E. Zscherpel, "Aufbau von optisch parametrischen Oszillatoren im infraroten Spektralbereich als Strahlquellen für die Frequenzkonversion einzelner Photonen," Master thesis, Universität des Saarlandes, Saarbrücken (2013).
- [170] C. R. Phillips, J. S. Pelc, and M. M. Fejer, "Parametric processes in quasi-phases-matching gratings with random duty cycle errors," *J. Opt. Soc. Am. B* **30**, 982-993 (2013).
- [171] I. Breunig, D. Haertle, and K. Buse, "Continuous-wave optical parametric oscillators: recent developments and prospects," *Appl. Phys. B* **105**, 99-111 (2011).
- [172] F. Riehle, "Frequency Standards: Basics and Applications," Wiley-VCH Verlag, Weinheim (2004).
- [173] J. Rutman, "Characterization of Phase and Frequency Instabilities in Precision Frequency Sources: Fifteen Years of Progress," *Proc. IEEE* **66**, 1048-1075 (1978).
- [174] C. Warschburger, "Aufbau eines Optisch Parametrischen Oszillators basierend auf PPLT für Experimente zur Frequenzkonversion von Einzelphotonen," Diploma thesis, Universität des Saarlandes, Saarbrücken (2010).
- [175] S. Zaske, "Quantum Frequency Down-Conversion of Single Photons in Nonlinear Optical Waveguides," PhD thesis, Universität des Saarlandes, Saarbrücken (2013).
- [176] J. Hirohashi, T. Tago, O. Nakamura, A. Miyamoto, Y. Furukawa, "Characterization of GRIIRA properties in LiNbO_3 and LiTaO_3 with different compositions and doping," *Proc. SPIE* 6875, 687516 (2008).

- [177] Y. J. Lu, and Z. Y. Ou, "Optical parametric oscillator far below threshold: Experiment versus theory," *Phys. Rev. A* **62**, 033804 (2000).
- [178] U. Herzog, M. Scholz, O. Benson, "Theory of biphoton generation in a single-resonant optical parametric oscillator far below threshold", *Phys. Rev. A* **77**, 023826 (2008).
- [179] R. Nelz, "Aufbau eines Michelson-Interferometers für die Fourier-Transform-Spektroskopie an Farbzentren in Diamant," Bachelor thesis, Universität des Saarlandes, Saarbrücken (2013).
- [180] A. Othonos, "Fiber Bragg gratings," *Rev. Sci. Instrum.* **69**, 4309-4341 (1997).
- [181] G. P. Agrawal, S. Radic, "Phase-Shifted Fiber Bragg Gratings and their Application for Wavelength Demultiplexing," *IEEE Photonic. Tech. Lett.* **6**, 995-997 (1994).
- [182] T. Erdogan, "Fiber Grating Spectra," *J. Lightwave Technol.* **15**, 1277-1294 (1997).
- [183] A. Haase, N. Piro, J. Eschner, and M. W. Mitchell, "Tunable narrowband entangled photon pair source for resonant single-photon single-atom interaction," *Opt. Lett.* **34**, 55-57 (2009).
- [184] N. Piro, F. Rohde, C. Schuck, M. Almendros, J. Huwer, J. Ghosh, A. Haase, M. Hennrich, F. Dubin, J. Eschner, "Heralded single-photon absorption by a single atom", *Nat. Phys.* **7**, 17-20 (2010).
- [185] J. Fekete, D. Rieländer, M. Cristiani, and H. de Riedmatten, "Ultrananrow-Band Photon-Pair Source Compatible with Solid State Quantum Memories and Telecommunication Networks," *Phys. Rev. Lett.* **110**, 220502 (2013).
- [186] C. Schuck, F. Rohde, N. Piro, M. Almendros, J. Huwer, M. W. Mitchell, M. Hennrich, A. Haase, F. Dubin, and J. Eschner, "Resonant interaction of a single atom with single photons from a down-conversion source," *Phys. Rev. A* **81**, 011802 (2010).
- [187] J. Benhelm, "Precision Spectroscopy and Quantum Information Processing with Trapped Calcium Ions," PhD thesis, University of Innsbruck (2008).
- [188] J. Jin and D. A. Church, "Precision Lifetimes for the Ca^+ $4p^2P$ Levels: Experiment Challenges Theory at the 1 % Level," *Phys. Rev. Lett.* **70**, 3213-3216 (1993).

- [189] J. D. Franson, "Violations of a Simple Inequality for Classical Fields," *Phys. Rev. Lett.* **91**, 290-293 (1991).
- [190] J. S. Bell, "On the Einstein Podolski Rosen paradox," *Physics* **1**, 195-200 (1964).
- [191] J. F. Clauser, M. A. Horne, A. Shimony, and R. A. Holt, "Proposed experiment to test local hidden-variable theories," *Phys. Rev. Lett.* **23**, 880-884 (1969).
- [192] A. Aspect, P. Grangier, and Gerard Roger, "Experimental Tests of Realistic Local Theories via Bell's Theorem," *Phys. Rev. Lett.* **47**, 460-463 (1981).
- [193] P. G. Kwiat, E. Waks, A. G. White, I. Appelbaum, and P. H. Eberhard, "Ultrabright source of polarization-entangled photons," *Phys. Rev. A* **60**, R773(R) (1999).
- [194] W. Tittel, J. Brendel, N. Gisin, and H. Zbinden, "Long-distance Bell-type tests using energy-time entangled photons," *Phys. Rev. A* **59**, 4150-4163 (1999).
- [195] W. Tittel, J. Brendel, H. Zbinden, and N. Gisin, "Violation of Bell Inequalities by Photons More Than 10 km Apart," *Phys. Rev. Lett.* **81** 3563-3566 (1998).
- [196] J.-A. Larsson, "Bell's inequality and detector inefficiency," *Phys. Rev. A* **57**, 3304-3308
- [197] M. A. Rowe, D. Kielpinski, V. Meyer, C. A. Sackett, W. M. Itano, C. Monroe, and D. J. Wineland, "Experimental violation of a Bell's inequality with efficient detection," *Nature* **409**, 791-794 (2001).
- [198] B. G. Christensen, K. T. McCusker, J. B. Altepeter, B. Calkins, T. Gerrits, A. E. Lita, A. Miller, L. K. Shalm, Y. Zhang, S.W. Nam, N. Brunner, C. C.W. Lim, N. Gisin, and P. G. Kwiat, "Detection-Loophole-Free Test of Quantum Nonlocality, and Applications," *Phys. Rev. Lett.* **111**, 130406 (2013).
- [199] M. Bock, "Aufbau und Charakterisierung einer Photonenpaarquelle," Master thesis, Universität des Saarlandes, Saarbrücken (2014).
- [200] P. G. Kwiat, A. M. Steinberg, and R. Y. Chiao, "High-visibility interference in a Bell-inequality experiment for energy and time," *Phys. Rev. A* **47**, 2472-2475 (1993).

- [201] P. Palittapongarnpim, A. MacRae, and A. I. Lvovsky, "Note: A monolithic filter cavity for experiments in quantum optics," *Rev. Sci. Instrum.* **83**, 066101 (2012).
- [202] C. Matthiesen, A. N. Vamivakas, and M. Atatüre, "Subnatural Linewidth Single Photons from a Quantum Dot," *Phys. Rev. Lett.* **108**, 093602 (2012).
- [203] A. Ulhaq, S. Weiler, S. M. Ulrich, R. Roßbach, M. Jetter, and P. Michler, "Cascaded single-photon emission from the Mollow triplet sidebands of a quantum dot", *Nat. Photon.* **6**, 238-242 (2012).
- [204] D. A. Steck, "Cesium D Line Data," available online at <http://steck.us/alkalidata> (revision 2.1.4, 23 December 2010).
- [205] K. F. Reim, P. Michelberger, K. C. Lee, J. Nunn, N. K. Langford, and I. A. Walmsley, "Single-Photon-Level Quantum Memory at Room Temperature," *Phys. Rev. Lett.* **107**, 053603 (2011).
- [206] C. Clausen, I. Usmani, F. Bussières, N. Sangouard, M. Afzelius, H. de Riedmatten, and N. Gisin, "Quantum storage of photonic entanglement in a crystal," *Nature* **469**, 508-511 (2011).
- [207] M. E. Klein, A. Robertson, M. A. Tremont, R. Wallenstein, and K.-J. Boller, "Rapid infrared wavelength access with a picosecond PPLN OPO synchronously pumped by a mode-locked diode laser," *Appl. Phys. B* **73**, 1-10 (2001).
- [208] F. R. Nash, G. D. Boyd, M. Sargent, and P. M. Bridenbaugh, "Effect of Optical Inhomogeneities on Phase Matching in Nonlinear Crystals," *J. Appl. Phys.* **41**, 2564-2576 (1970).
- [209] O. Humbach, H. Fabian, U. Grzesik, U. Haken, and W. Heitmann, "Analysis of OH absorption bands in synthetic silica," *J. Non-Cryst. Solids* **203**, 19-26 (2003).
- [210] G. Ribordy, N. Gisin, O. Guinnard, D. Stucki, M. Wegmuller, and H. Zbinden, "Photon counting at telecom wavelengths with commercial InGaAs/InP avalanche photodiodes: current performance," *J. Mod. Optics* **51**, 1381-1398 (2004).
- [211] C. M. Natarajan, M. G. Tanner, and R. H. Hadfield, "Superconducting nanowire single-photon detectors: physics and applications," *Supercond. Sci. Technol.* **25**, 063001 (2012).

-
- [212] H. Azzouz, S. N. Dorenbos, D. De Vries, E. B. Urena, and V. Zwiller, "Efficient single particle detection with a superconducting nanowire," *AIP Adv.* **2**, 032124 (2012).
- [213] R. W. Heeres, L. P. Kouwenhoven, and V. Zwiller, "Quantum interference in plasmonic circuits," *Nature Nano.* **8**, 719-722 (2013).
- [214] C. M. Natarajan, L. Zhang, H. Coldenstrodt-Ronge, G. Donati, S. N. Dorenbos, V. Zwiller, I. A. Walmsley, and R. H. Hadfield, "Quantum detector tomography of a time-multiplexed superconducting nanowire single-photon detector at telecom wavelengths," *Opt. Express* **21**, 893-902 (2013).
- [215] N. Prio, "Controlled absorption of heralded single photons by a single atom: Towards entanglement distribution in quantum networks," PhD thesis, Universitat Politècnica de Catalunya, Barcelona (2010).
- [216] R. Ikuta, H. Kato, Y. Kusaka, S. Miki, T. Yamashita, H. Terai, M. Fujiwara, T. Yamamoto, M. Koashi, M. Sasaki, Z. Wang, and N. Imoto, "High-fidelity conversion of photonic quantum information to telecommunication wavelength with superconducting single-photon detectors," *Phys. Rev. A* **87**, 010301 (2013).
- [217] R. Ikuta, T. Kobayashi, H. Kato, S. Miki, T. Yamashita, H. Terai, M. Fujiwara, T. Yamamoto, M. Koashi, M. Sasaki, Z. Wang, and N. Imoto, "Nonclassical two-photon interference between independent telecommunication light pulses converted by difference-frequency generation," *Phys. Rev. A* **88**, 042317 (2013).
- [218] M. T. Rakher, L. Ma, M. Davanco, O. Slattery, X. Tang, and K. Srinivasan, "Simultaneous Wavelength Translation and Amplitude Modulation of Single Photons from a Quantum Dot," *Phys. Rev. Lett.* **107**, 083602 (2011).
- [219] I. Agha, S. Ates, L. Sapienza, and K. Srinivasan, "Spectral broadening and shaping of nanosecond pulses: toward shaping of single photons from quantum emitters," *Optics Lett.* **39**, 5677-5680 (2014).
- [220] G. S. Solomon, E. B. Flagg, S. V. Polyakov, T. Thomay, and A. Muller, "Manipulating single photons from disparate quantum sources to be indistinguishable," *J. Opt. Soc. Am. B* **29**, 319-327 (2012).
- [221] Corning SMF-28e+ Optical Fiber with NexCor Technology - Product Information, Document PI1463, December 2007, Corning Inc.

- [222] A. Aspect, P. Grangier, and G. Roger, "Experimental Tests of Realistic Local Theories via Bell's Theorem," *Phys. Rev. Lett.* **47**, 460-463 (1981).
- [223] B. Lounis, and M. Orrit, "Single-photon sources," *Rep. Prog. Phys.* **68**, 1129-1179 (2005).
- [224] R. Brouri, A. Beveratos, J.-P. Poizat, and P. Grangier, "Photon antibunching in the fluorescence of individual color centers in diamond," *Opt. Lett.* **25** 1294-1296 (2000).
- [225] C. Becher, A. Kiraz, P. Michler, A. Imamoglu, W. V. Schoenfeld, P. M. Petroff, L. Zhang, and E. Hu, "Nonclassical radiation from a single self-assembled InAs quantum dot," *Phys. Rev. B* **63**, 121312(R) (2001).
- [226] L.-M. Duan, M. D. Lukin, J. I. Cirac, and P. Zoller, "Long-distance quantum communication with atomic ensembles and linear optics," *Nature* **414**, 413-418 (2001).
- [227] N. Gisin, and R. Thew, "Quantum communication," *Nature Photon.* **1**, 165-171 (2007).
- [228] S. Ritter, C. Nölleke, C. Hahn, A. Reiserer, A. Neuzner, M. Uphoff, M. Mücke, E. Figueroa, J. Bochmann, and G. Rempe, "An elementary quantum network of single atoms in optical cavities," *Nature* **484**, 195-200 (2012).
- [229] R. Ursin, F. Tiefenbacher, T. Schmitt-Manderbach, H. Weier, T. Scheidl, M. Lindenthal, B. Blauensteiner, T. Jennewein, J. Perdigues, P. Trojek, B. Ömer, M. Fürst, M. Meyenburg, J. Rarity, Z. Sodnik, C. Barbieri, H. Weinfurter, and A. Zeilinger, "Entanglement-based quantum communication over 144km," *Nature Phys.* **3**, 481-486 (2007).
- [230] J. Yin, J.-G. Ren, H. Lu, Y. Cao, H.-L. Yong, Y.-P. Wu, C. Liu, S.-K. Liao, F. Zhou, Y. Jiang, X.-D. Cai, P. Xu, G.-S. Pan, J.-J. Jia, Y.-M. Huang, H. Yin, J.-Y. Wang, Y.-A. Chen, C.-Z. Peng, and J.-W. Pan, "Quantum teleportation and entanglement distribution over 100-kilometre free-space channels," *Nature* **488**, 185-188 (2012).
- [231] X.-S. Ma, T. Herbst, T. Scheidl, D. Wang, S. Kropatschek, W. Naylor, B. Wittmann, A. Mech, J. Kofler, E. Anisimova, V. Makarov, T. Jennewein, R. Ursin, and A. Zeilinger, "Quantum teleportation over 143 kilometres using active feed-forward," *Nature* **489**, 269-273 (2012).
- [232] S. Nauerth, F. Moll, M. Rau, C. Fuchs, J. Horwath, S. Frick, and H. Weinfurter, "Air-to-ground quantum communication," *Nature Photon.* **7**, 382-386 (2013).

- [233] J.-Y. Wang, B. Yang, S.-K. Liao, L. Zhang, Q. Shen, X.-F. Hu, J.-C. Wu, S.-J. Yang, H. Jiang, Y.-L. Tang, B. Zhong, H. Liang, W.-Y. Liu, Y.-H. Hu, Y.-M. Huang, B. Qi, J.-G. Ren, G.-S. Pan, J. Yin, J.-J. Jia, Y.-A. Chen, K. Chen, C.-Z. Peng, and J.-W. Pan, "Direct and full-scale experimental verifications towards ground-satellite quantum key distribution," *Nature Photon.* **7**, 387-393 (2013).
- [234] X. Sun, D. R. Skillman, E. D. Hoffman, D. Mao, J. F. McGarry, L. McIntire, R. S. Zellar, F. M. Davidson, W. H. Fong, M. A. Krainak, G. A. Neumann, M. T. Zuber, and D. E. Smith, "Free space laser communication experiments from Earth to the Lunar Reconnaissance Orbiter in lunar orbit," *Opt. Express* **21**, 1865-1871 (2013).
- [235] H. Shibata, T. Honjo, and K. Shimizu, "Quantum key distribution over a 72 dB channel loss using ultralow dark count superconducting single-photon detectors," *Opt. Lett.* **39**, 5078-5081 (2014).
- [236] T. Inagaki, N. Matsuda, O. Tadanaga, M. Asobe, and H. Takesue, "Entanglement distribution over 300 km of fiber," *Opt. Express* **21**, 23241-23249 (2013).
- [237] H. Takesue, S. Nam, Q. Zhang, R. H. Hadfield, T. Honjo, K. Tamaki, and Y. Yamamoto, "Quantum key distribution over a 40-dB channel loss using superconducting single-photon detectors," *Nature Phot.* **1**, 343-348 (2007).
- [238] M. Peev, C. Pacher, R. Alleaume, C. Barreiro, J. Bouda, W. Boxleitner, T. Debuisschert, E. Diamanti, M. Dianati, J. F. Dynes, S. Fasel, S. Fossier, M. Fürst, J.-D. Gautier, O. Gay, N. Gisin, P. Grangier, A. Happe, Y. Hasani, M. Hentschel, H. Hübel, G. Humer, T. Länger, M. Legre, R. Lieger, J. Lodewyck, T. Lorünser, N. Lütkenhaus, A. Marhold, T. Matyus, O. Maurhart, L. Monat, S. Nauerth, J.-B. Page, A. Poppe, E. Querasser, G. Ribordy, S. Robyr, L. Salvail, A. W. Sharpe, A. J. Shields, D. Stucki, M. Suda, C. Tamas, T. Themel, R. T. Thew, Y. Thoma, A. Treiber, P. Trinkler, R. Tualle-Brouiri, F. Vannel, N. Walenta, H. Weier, H. Weinfurter, I. Wimberger, Z. L. Yuan, H. Zbinden and A. Zeilinger, "The SECOQC quantum key distribution network in Vienna," *New J. Phys.* **11**, 075001 (2009).
- [239] M. Sasaki, M. Fujiwara, H. Ishizuka, W. Klaus, K. Wakui, M. Takeoka, S. Miki, T. Yamashita, Z. Wang, A. Tanaka, K. Yoshino, Y. Nambu, S. Takahashi, A. Tajima, A. Tomita, T. Domeki, T. Hasegawa, Y. Sakai, H. Kobayashi, T. Asai, K. Shimizu, T. Tokura, T. Tsurumaru, M. Matsui, T. Honjo, K. Tamaki, H. Takesue, Y. Tokura, J. F. Dynes, A. R. Dixon, A. W.

- Sharpe, Z. L. Yuan, A. J. Shields, S. Uchikoga, M. Legre, S. Robyr, P. Trinkler, L. Monat, J.-B. Page, G. Ribordy, A. Poppe, A. Allacher, O. Maurhart, T. Langer, M. Peev, and A. Zeilinger, "Field test of quantum key distribution in the Tokyo QKD Network," *Opt. Express* **19**, 10387-10409 (2011).
- [240] A. Rubenok, J. A. Slater, P. Chan, I. Lucio-Martinez, and W. Tittel, "Real-World Two-Photon Interference and Proof-of-Principle Quantum Key Distribution Immune to Detector Attacks," *Phys. Rev. Lett.* **111**, 130501 (2013).
- [241] I. Marcikic, H. de Riedmatten, W. Tittel, H. Zbinden, and N. Gisin, "Long-distance teleportation of qubits at telecommunication wavelengths," *Nature* **421**, 509-513 (2003).
- [242] M. B. Ward, O. Z. Karimov, D. C. Unitt, Z. L. Yuan, P. See, D. G. Gevaux, A. J. Shields, P. Atkinson, and D. A. Ritchie, "On-demand single-photon source for $1.3\mu\text{m}$ telecom fiber," *Appl. Phys. Lett.* **86**, 201111 (2005).
- [243] M. B. Ward, T. Farrow, P. See, Z. L. Yuan, O. Z. Karimov, A. J. Bennett, A. J. Shields, P. Atkinson, K. Cooper, and D. A. Ritchie, "Electrically driven telecommunication wavelength single-photon source," *Appl. Phys. Lett.* **90**, 063512 (2007).
- [244] M. D. Birowosuto, H. Sumikura, S. Matsuo, H. Taniyama, P. J. van Veldhoven, R. Notzel, and M. Notomi, "Fast Purcell-enhanced single photon source in 1,550-nm telecom band from a resonant quantum dot-cavity coupling," *Sci. Rep.* **2**, 321 (2012).
- [245] M. Benyoucef, M. Yacob, J. P. Reithmaier, J. Kettler, and P. Michler, "Telecom-wavelength ($1.5\mu\text{m}$) single-photon emission from InP-based quantum dots," *Appl. Phys. Lett.* **103**, 162101 (2013).
- [246] O. Alibart, D. B. Ostrowsky, P. Baldi, and S. Tanzilli, "High-performance guided-wave asynchronous heralded single-photon source," *Opt. Lett.* **30**, 1539-1541 (2005).
- [247] H. Takesue, K. Inoue, O. Tadanaga, Y. Nishida, and M. Asobe, "Generation of pulsed polarization-entangled photon pairs in a $1.55\text{-}\mu\text{m}$ band with a periodically poled lithium niobate waveguide and an orthogonal polarization delay circuit," *Opt. Lett.* **30**, 293-295 (2005).
- [248] A. Martin, A. Issautier, H. Herrmann, W. Sohler, D. B. Ostrowsky, O. Alibart, and S. Tanzilli, "A polarization entangled photon-pair source based on a type-II PPLN waveguide emitting at a telecom wavelength," *New J. Phys.* **12**, 103005 (2010).

-
- [249] A. Yoshizawa, R. Kaji, and H. Tsuchida, "Generation of polarisation-entangled photon pairs at 1550 nm using two PPLN waveguides," *Electron. Lett.* **39**, 621-622 (2003).
- [250] T. Heindel, C. A. Kessler, M. Rau, C. Schneider, M. Fürst, F. Hargart, W.-M. Schulz, M. Eichfelder, R. Roßbach, S. Nauerth, M. Lermer, H. Weier, M. Jetter, M. Kamp, S. Reitzenstein, S. Höfling, P. Michler, H. Weinfurter, and A. Forchel, "Quantum key distribution using quantum dot single-photon emitting diodes in the red and near infrared spectral range," *New J. Phys.* **14**, 083001 (2012).
- [251] J. Hofmann, M. Krug, N. Ortegel, L. Gerard, M. Weber, W. Rosenfeld, H. Weinfurter, "Heralded Entanglement Between Widely Separated Atoms," *Science* **337**, 72-75 (2012).
- [252] W. Mauerer, W. Helwig, and C. Silberhorn, "Recent developments in quantum key distribution: Theory and practice," *Ann. Phys. (Berlin)* **17**, 158-175 (2008).
- [253] N. Lütkenhaus, and A. J. Shields, "Focus on Quantum Cryptography: Theory and Practice," *New J. Phys.* **11**, 045005 (2009).
- [254] R. Ikuta, Y. Kusaka, T. Kitano, H. Kato, T. Yamamoto, M. Koashi, and N. Imoto, "Wide-band quantum interface for visible-to-telecommunication wavelength conversion," *Nature Commun.* **2**, 537 (2011).
- [255] S. Ramelow, A. Fedrizzi, A. Poppe, N. K. Langford, and A. Zeilinger, "Polarization-entanglement-conserving frequency conversion of photons," *Phys. Rev. A* **85**, 013845 (2012).
- [256] A. Lenhard, S. Zaske, and C. Becher, "Lock-in detection of single photons after two-step frequency conversion," *Opt. Lett.* **37**, 4254-4256 (2012).
- [257] M. A. Albota, F. N. C. Wong, and J. H. Shapiro, "Polarization-independent frequency conversion for quantum optical communication," *J. Opt. Soc. Am. B* **23**, 918-924 (2006).
- [258] P.D. Townsend, "Simultaneous quantum cryptographic key distribution and conventional data transmission over installed fibre using wavelength-division multiplexing," *Electr. Lett.* **33**, 188-190 (1997).
- [259] T. E. Chapuran, P. Toliver, N. A. Peters, J. Jackel, M. S. Goodman, R. J. Runser, S. R. McNown, N. Dallmann, R. J. Hughes, K. P. McCabe, J. E.

- Nordholt, C. G. Peterson, K. T. Tyagi, L. Mercer, and H. Dardy, "Optical networking for quantum key distribution and quantum communications," *New J. Phys.* **11**, 105001 (2009).
- [260] M. A. Hall, J. B. Altepeter, and P. Kumar, "Drop-in compatible entanglement for optical-fiber networks," *Opt. Express* **17**, 14558-14566 (2009).
- [261] International Telecommunication Union, "Spectral grids for WDM applications: DWDM frequency grid, ITU-T G.694.1", version 02/2012.
- [262] M. Bock, A. Lenhard, and C. Becher, Manuscript in preparation, (2015).
- [263] C. Ho, A. Lamas-Linares, and C. Kurtsiefer, "Clock synchronization by remote detection of correlated photon pairs," *New J. Phys.* **11**, 045011 (2009).
- [264] C. H. Bennett, G. Brassard, C. Crepeau, R. Jozsa, A. Peres, and W. K. Wootters, "Teleporting an Unknown Quantum State via Dual Classical and Einstein-Podolsky-Rosen Channels," *Phys. Rev. Lett.* **70**, 1895-1899 (1993).
- [265] C. Simon, H. de Riedmatten, M. Afzelius, N. Sangouard, H. Zbinden, and N. Gisin, "Quantum Repeaters with Photon Pair Sources and Multimode Memories," *Phys. Rev. Lett.* **98** 190503 (2007).
- [266] A. Stute, B. Casabone, P. Schindler, T. Monz, P. O. Schmidt, B. Brandstätter, T. E. Northup, and R. Blatt, "Tunable ion-photon entanglement in an optical cavity," *Nature* **485**, 482-485 (2012).
- [267] A. I. Lvovsky, B. C. Sanders, and W. Tittel, "Optical quantum memory," *Nature Photon.* **3**, 706-714 (2009).
- [268] H. P. Specht, C. Nölleke, A. Reiserer, M. Uphoff, E. Figueroa, S. Ritter, and G. Rempe, "A single-atom quantum memory," *Nature* **473**, 190-193 (2011).
- [269] M. Gündogan, P. M. Ledingham, A. Almasi, M. Cristiani, and H. de Riedmatten, "Quantum Storage of a Photonic Polarization Qubit in a Solid," *Phys. Rev. Lett.* **108**, 190504 (2012).
- [270] Y.-H. Chen, M.-J. Lee, I.-C. Wang, S. Du, Y.-F. Chen, Y.-C. Chen, and I. A. Yu, "Coherent Optical Memory with High Storage Efficiency and Large Fractional Delay," *Phys. Rev. Lett.* **110**, 083601 (2013).
- [271] M. R. Sprague, P. S. Michelberger, T. F. M. Champion, D. G. England, J. Nunn, X.-M. Jin, W. S. Kolthammer, A. Abdolvand, P. St. J. Russell, and I. A. Walmsley, "Broadband single-photon-level memory in a hollow-core photonic crystal fibre," *Nature Photon.* **8**, 287-291 (2014).

-
- [272] N. Sangouard, C. Simon, J. Minar, H. Zbinden, H. de Riedmatten, and N. Gisin, "Long-distance entanglement distribution with single-photon sources," *Phys. Rev. A* **76**, 050301(R) (2007).
- [273] P. Schindler, D. Nigg, T. Monz, J. T. Barreiro, E. Martinez, S. X. Wang, S. Quint, M. F. Brandl, V. Nebendahl, C. F. Roos, M. Chwalla, M. Hennrich, and R. Blatt, "A quantum information processor with trapped ions," *New J. Phys.* **15**, 123012 (2013).
- [274] C. Kurz, M. Schug, P. Eich, J. Huwer, P. Müller, and J. Eschner, "Experimental protocol for high-fidelity heralded photon-to-atom quantum state transfer," *Nature Commun.* **5**, 5527 (2014).
- [275] K. F. Reim, J. Nunn, V. O. Lorenz, B. J. Sussman, K. C. Lee, N. K. Langford, D. Jaksch, and I. A. Walmsley, "Towards high-speed optical quantum memories," *Nature Photon.* **4**, 218-221 (2010).
- [276] K. S. Choi, H. Deng, J. Laurat, and H. J. Kimble, "Mapping photonic entanglement into and out of a quantum memory," *Nature* **452**, 67-71 (2008).
- [277] D. Höckel, and O. Benson, "Electromagnetically Induced Transparency in Cesium Vapor with Probe Pulses on the Single-Photon Level," *Phys. Rev. Lett.* **105**, 153605 (2010).
- [278] K. S. Choi, A. Goban, S. B. Papp, S. J. van Enk, and H. J. Kimble, "Entanglement of spin waves among four quantum memories," *Nature* **468**, 412-416 (2010).
- [279] R. Albrecht, A. Bommer, C. Deutsch, J. Reichel, and C. Becher, "Coupling of a Single Nitrogen-Vacancy Center in Diamond to a Fiber-Based Microcavity," *Phys. Rev. Lett.* **110**, 243602 (2013).
- [280] E. Neu, D. Steinmetz, J. Riedrich-Möller, S. Gsell, M. Fischer, M. Schreck, and C. Becher, "Single photon emission from silicon-vacancy colour centres in chemical vapour deposition nano-diamonds on iridium," *New J. Phys.* **13**, 025012 (2011).
- [281] W. B. Gao, P. Fallahi, E. Togan, J. Miguel-Sanchez, and A. Imamoglu, "Observation of entanglement between a quantum dot spin and a single photon," *Nature* **491**, 426-430 (2012).
- [282] E. Togan, Y. Chu, A. S. Trifonov, L. Jiang, J. Maze, L. Childress, M. V. G. Dutt, A. S. Sorensen, P. R. Hemmer, A. S. Zibrov, and M. D. Lukin, "Quantum entanglement between an optical photon and a solid-state spin qubit," *Nature* **466**, 730-734 (2010).

- [283] C. Hepp, T. Müller, V. Waselowski, J. N. Becker, B. Pingault, H. Sternschulte, D. Steinmüller-Nethl, A. Gali, J. R. Maze, M. Atatüre, and C. Becher, "Electronic Structure of the Silicon Vacancy Color Center in Diamond," *Phys. Rev. Lett.* **112**, 036405 (2014).
- [284] T. Müller, C. Hepp, B. Pingault, E. Neu, S. Gsell, M. Schreck, H. Sternschulte, D. Steinmüller-Nethl, C. Becher, and M. Atatüre, "Optical signatures of silicon-vacancy spins in diamond," *Nature Commun.* **5**, 3328 (2014).
- [285] B. Pingault, J. N. Becker, C. H. H. Schulte, C. Arend, C. Hepp, T. Godde, A. I. Tartakovskii, M. Markham, C. Becher, and M. Atatüre, "All-Optical Formation of Coherent Dark States of Silicon-Vacancy Spins in Diamond," *Phys. Rev. Lett.* **113**, 263601 (2014).
- [286] C. Santori, D. Fattal, J. Vuckovic, G. S. Solomon, Y. Yamamoto, "Indistinguishable photons from a single-photon device," *Nature* **419**, 594-597 (2002).

List of Publications

Journal Publications

1. A. Lenhard, M. Bock, S. Kucera, J. Brito, P. Eich, P. Müller, J. Eschner, and Christoph Becher, "Telecom-Heralded Single Photon Absorption by a Single Ion," manuscript in preparation (2015)
2. A. Lenhard, S. Zaske, and C. Becher, "Lock-in detection of single photons after two-step frequency conversion," *Opt. Lett.* **37**, 4254-4256 (2012), doi: 10.1364/OL.37.004254.
3. S. Zaske, A. Lenhard, C. A. Keßler, J. Kettler, C. Hepp, C. Arend, R. Albrecht, W.-M. Schulz, M. Jetter, P. Michler, and C. Becher, "Visible-to-Telecom Quantum Frequency Conversion of Light from a Single Quantum Emitter," *Phys. Rev. Lett.* **109**, 147404 (2012), doi: 10.1103/PhysRevLett.109.147404.
4. S. Zaske, A. Lenhard, and C. Becher, "Efficient frequency downconversion at the single photon level from the red spectral range to the telecommunications C-band," *Opt. Express* **19**, 12825-12836 (2011), doi: 10.1364/OE.19.012825.
5. A. Lenhard, S. Zaske, J. A. L'huillier, and C. Becher, "Stabilized diode laser pumped, idler resonant cw optical parametric oscillator," *Appl. Phys. B* **102**, 757-764 (2011), doi: 10.1007/s00340-011-4404-8.

Conference Papers¹

1. A. Lenhard, M. Bock, S. Kucera, J. Brito, P. Eich, P. Müller •, J. Eschner, and C. Becher, "Telecom-heralded single-ion single-photon quantum interface," European Conference on Trapped Ions ECTI, Mainz 2014.
2. A. Lenhard •, S. Kucera, J. Brito, J. Eschner, and C. Becher, "Frequency Conversion of Narrowband Single Photons from a SPDC Pair Source," in CLEO:2014 (Optical Society of America, Washington, DC, 2014), paper **FTu3A.2**.

¹A bullet • marks the presenter of the talk or poster

3. A. Lenhard •, S. Zaske, and C. Becher, "Quantum Frequency Conversion, invited talk," Single Photon Workshop 2013, Oak Ridge National Lab, TN (USA) 2013.
4. A. Lenhard •, S. Zaske, C. Kessler, J. Kettler, C. Arend, C. Hepp, R. Albrecht, W.-M. Schulz, M. Jetter, P. Michler, and C. Becher, "Quantum Frequency Conversion of Visible Single Photons from a Quantum Dot to a Telecom Band," in CLEO/Europe and EQEC 2013 Conference Digest, OSA Technical Digest (CD) (Optical Society of America, 2013), paper **IA3.5**.
5. C. Becher •, A. Lenhard, S. Zaske, C. Keßler, J. Kettler, C. Arend, C. Hepp, R. Albrecht, W.-M. Schulz, M. Jetter, and P. Michler, "Quantum Frequency Conversion of Single Photons from a Quantum Dot to the Telecom Band, invited talk," NOEKS 11, paper **Th1.1**, Stuttgart (2012).
6. B. Weigand •, M. Stolze, F. Rübel, S. Wolff, A. Lenhard, C. Becher, and J. L'huillier, "Fabrication of Ridge Waveguides in LiNbO₃," ISAF-ECAPD-PFM 2012, paper **182**, doi: 10.1109/ISAF.2012.6297792.
7. A. Lenhard •, S. Zaske, C. Keßler, J. Kettler, C. Arend, C. Hepp, R. Albrecht, W.-M. Schulz, M. Jetter, P. Michler, and C. Becher, "Quantum Frequency Down-Conversion of Single Photons from a Quantum Dot to the Telecom Band, post-deadline paper," in CLEO:2012 (Optical Society of America, Washington, DC, 2012), paper **QTh5B.6**.
8. A. Lenhard •, S. Zaske, S. Blum, G. Morigi, and C. Becher, "Low-Noise Frequency Down-Conversion at the Single Photon Level," in CLEO:2012 (Optical Society of America, Washington, DC, 2012), paper **JTh1K.4**.
9. S. Zaske •, A. Lenhard, and C. Becher, "Efficient Frequency Downconversion at the Single Photon Level from 738 nm to 1557 nm," in Nonlinear Optics: Materials, Fundamentals and Applications, OSA Technical Digest (CD) (Optical Society of America, 2011), paper **NMB3**.
10. S. Zaske •, A. Lenhard, and C. Becher, "Highly Efficient Frequency Downconversion at the Single Photon Level," EQEC 2011 Conference Digest, OSA Technical Digest (CD) (Optical Society of America, 2011), paper **EF4.4**.
11. A. Lenhard •, S. Zaske, and C. Becher, "Highly Efficient Frequency Conversion at the Single Photon Level for Quantum Communication," 1st GDR-IQFA Colloquium, Nizza (2011).
12. A. Lenhard, S. Zaske, J. A. L'huillier, and C. Becher •, "Highly Stable Diode-Laser Pumped, Idler Resonant CW OPO Based on MgO:PPLN," in Conference

on Lasers and Electro-Optics, OSA Technical Digest (CD) (Optical Society of America, 2010), paper **CThY5**.

13. S. Zaske, A. Lenhard •, H. Rütz, and C. Becher, "Single Photon Downconversion into the Telecom Band," 453. WE-Heraeus-Seminar - Quantum Communication based on Integrated Optics, Bad Honnef (2010).

Danksagung

Ich danke meinem Doktorvater Prof. Dr. Christoph Becher für die Möglichkeit an so einem interessanten Thema zu arbeiten, das er ganz am Anfang mit den Worten "Wir machen hier etwas abgefahrene Dinge" beschrieben hatte. Er gab mir die Möglichkeit selbständig zu arbeiten und eigene Ideen einzubringen. Ich danke Dr. Johannes L'huillier für die Arbeit als Zweitgutachter und die Kooperationen während der Promotion.

Solch eine Arbeit lässt sich natürlich nur mit der Unterstützung vieler weiterer Menschen realisieren. Jedem Einzelnen zu danken würde viele weitere Seiten füllen. Deshalb muss ich mich auf eine Auswahl beschränken:

Größten Dank schulde ich Sebastian Zaske. Er hat mich in Saarbrücken Willkommen geheißen und in die tiefen Weiten der Nichtlinearen Optik geführt. Seine Weisheiten zur Physik und dem Leben im Allgemeinen sowie die motivierenden Sprüche werden mir in Erinnerung bleiben. Ich kann mir ebenfalls keinen besseren Schreibtisch-Nachbarn vorstellen.

Es hat mir auch immer großen Spaß gemacht, meine Erfahrung an die nächste Generation weiter zu geben. Deshalb hat die Liste der Bachelor, Master und Diplomanden dann doch noch eine beachtliche Länge erreicht. Ihr alle habt einen Teil zu meiner Promotion beigetragen, dafür danke ich euch: Benjamin Weigand, Susanne Blum, Elisabeth Zscherpel, Richard Nelz, Philipp Fuchs und Matthias Bock. Ebenfalls erwähnt werden muss Claudia Warschburger, ohne deren OPO ein großer Teil dieser Arbeit nicht möglich gewesen wäre. Insbesondere Matthias war mir im letzten Jahr der Promotion eine große Hilfe. Letztlich wurde das NLO-Team noch durch Benjamin Kambs verstärkt. An ihn und Matthias werde ich nun das Staffelholz weiter reichen. Ich hoffe ihr könnt auf meine Arbeit aufbauen und werdet in euren Promotionen der Welt mal zeigen wie man anständig nichtlineare Optik mit einzelnen Photonen betreibt.

Auch außerhalb der Arbeitsgruppe durfte ich mit vielen Menschen erfolgreich zusammenarbeiten. Hierzu sei zuerst Jürgen Eschner mit seinem Team erwähnt. Ganz besonderer Dank gilt José Brito und Stephan Kucera, meinen nichtlinearen Leidensgenossen und Hütern der "Quelle". Sie haben dafür gesorgt, dass mein Aufbau immer mit genügend Photonen gefüttert werden konnte. Ich danke euch auch für die vielen Diskussionen und die ein oder andere unterhaltsame Messnacht im Ionenlabor. Ebenfalls

danke an die Herrscher des Ions, Philipp Müller und Pascal Eich.

Beim Photonikzentrum Kaiserslautern möchte ich mich bei Johannes L'huillier und Mareike Stolze bedanken. Die Kooperationen für diverse Abschlussarbeiten haben mir gefallen und waren ja auch erfolgreich. Ich drücke die Daumen dass daraus irgendwann noch nichtlineare Wellenleiter hervorgehen. Hier möchte ich auch nochmals Danke sagen für diverse Geräte und Komponenten die ich mir schnell und unbürokratisch ausleihen durfte.

Zuletzt möchte ich Peter Michler und seinem Team für die Kooperation bei den Quantenpunkt-Experimenten danken. Besonders Christian Keßler hat mit seiner Art nicht nur die Messungen mit dem QD aufgelockert, sondern auch die ein oder andere Konferenz. Ich bin gespannt auf zukünftige Resultate der Becher/Michler Allianz.

Christian Hepp, Carsten Arend, Elke Neu und Roland Albrecht danke ich für Gespräche und Unternehmungen nicht nur fachlicher Natur. An der Zeit in Saarbrücken habe ich vor Allem die gute Atmosphäre durch die netten Kollegen genossen (von denen die meisten bisher unerwähnt geblieben sind). Außerhalb der Uni wurde regelmäßig gefeiert und jeder hat auch mal ein echtes Pfälzer Weinfest miterlebt.

Das Beste kommt zum Schluss, und so möchte ich endlich die wichtigsten Menschen erwähnen: Meinen Freunden danke ich für die Ablenkungen am Wochenende und im Urlaub. Das wahre Leben findet nicht im Labor statt. Ich danke von ganzem Herzen meiner Familie, meinen Eltern und meinem Bruder für ihre stete Unterstützung. In den vielen frustrierenden Zeiten, in denen im Labor gar nichts funktionierte, haben sie immer an mich geglaubt und mich weiter motiviert. Auf sie kann ich immer zählen.

Vielen Dank!